

On-Surface Formation of Polymers and Molecular Networks

Abigail S. Browning

A thesis presented for the degree of
Doctor of Philosophy

July 2019



School of Physics & Astronomy
University of Nottingham
United Kingdom

Abstract

Self-assembly of ordered molecular structures on surfaces is of great interest in the formation of devices with novel properties. By utilising molecules that form ordered structures, structures can form spontaneously without the need for lithographic processes. The de-halogenation and polymerisation of 1,3,5-tris-(4-iodophenyl)benzene on the hBN surface was investigated with AFM, XPS and SIMS. The molecules were deposited both from solution and in vacuum in minor variations of the previously reported sine-wave structure. Above 100 °C, polymerisation was observed with AFM and confirmed with SIMS, which revealed that, after polymerisation, additional iodine was still present suggesting that dehalogenation had not fully taken place prior to polymerisation occurring as suggested by the XPS results.

Using a vacuum deposition method, the structures formed by melamine on the hBN surface were investigated with AFM. Thick film triangular islands suggested an alignment of the molecular structure with the hBN substrate. Two main structures were seen: a rhombic lattice 0.87 ± 0.01 nm by 0.89 ± 0.01 nm and a square lattice 2.22 ± 0.03 nm by 2.10 ± 0.10 nm. An additional structure was seen on the top of the thick islands of 2.02 ± 0.06 nm by 0.77 ± 0.03 nm which was deemed to be a variant of the rhombic structure with out-of-plane rows due to the transition into the bulk structure. The rhombic structure was also deemed to be the structure forming an observed moiré pattern with a period of 3.19 ± 0.03 nm.

The polymerisation of porphyrin monomers with varying numbers of reactive ethynyl groups on Ag(111) was investigated in vacuum using a novel indirect deposition method and STM. The 2R porphyrin was found to form chains when annealed to 120 °C for 15 min with an intra-chain porphyrin separation of 1.33 ± 0.05 nm and an inter-chain distance of 1.90 ± 0.10 nm. The 4R porphyrin was also observed to form a lattice of 1.53 ± 0.04 nm by 1.69 ± 0.02 nm which was rationalised to be partially reacted into chains containing Ag atoms in one direction after heating to 120 °C for a 15 min. The 3R porphyrin was observed to form short

chains without heating when imaged with a low temperature STM. The 4R porphyrin was also deposited onto HOPG using a solution deposition method and formed lines separated by 1.70 ± 0.20 nm.

Finally, mechanical transfer of hBN supported C_{60} islands was carried out. The C_{60} islands were found to be undamaged by soft deposit mechanical transfer process from a PPC/PDMS stamp. The transfer process using PPC/PDMS stamps was also used to form hBN/ C_{60} /hBN heterostructures and to transfer these to silicon nitride TEM grids for imaging although this step involved delaminating the PPC material at high temperature and subsequent cleaning.

Acknowledgements

Whilst this thesis is in my name, there are many people without who this body of work would not have been completed.

Firstly, I would like to thank my supervisor, Professor Peter Beton, for providing me the opportunity to carry out my PhD research and for welcoming me into his research group at the University of Nottingham. I would also like to thank Dr Alex Saywell for his guidance and assistance in the early stages of my PhD, particularly for helping me with the various UHV systems.

My thanks also go to the members of the Beton group past and present with special thanks to Dr Vladimir Korolkov, Dr James Kerfoot, and Dr Alex Summerfield for helping me get to grips with various research techniques and to everyone in the Nottingham nanoscience groups who have made my time during the PhD enjoyable and productive. I would also like to thank Dr David Scurr in the nmRC for giving me access to the OrbiSIMS instrument.

For their support even when I probably was making no sense to them, I want to thank my family, particularly my parents. I said I'd get there and I have!

Finally, this thesis would never have been completed without the unwavering emotional and technical support of one person. Jed, I cannot thank you enough for all of your help and support, particularly on the days when my hard drive died!

Glossary of Acronyms

AFM — Atomic Force Microscopy

AM-AFM — Amplitude Modulated Atomic Force Microscopy

BE — Binding Energy

DMF — Dimethylformamide

FM-AFM — Frequency Modulated Atomic Force Microscopy

FWHM — Full Width Half Maxima

GNR — Graphene Nano-Ribbon

hBN — hexagonal Boron Nitride

HOMO — Highest Occupied Molecular Orbital

HOPG — Highly Ordered Pyrolytic Graphite

KE — Kinetic Energy

LDOS — Local Density of States

LUMO — Lowest Unoccupied Molecular Orbital

ML — Monolayer

MD — Molecular Dynamics

PTCDI — Perylene tetracarboxylic diimide

RT — Room Temperature

SAMs — Self-Assembled Monolayers

SAMNs — Self-Assembled Molecular Networks

SIMS — Secondary Ion Mass Spectrometry

SPM — Scanning Probe Microscopy

STM — Scanning Tunnelling Microscopy

TBPB — 1,3,5-Tris-(4-bromophenyl)benzene

TEM — Transmission Electron Microscopy

TIPB — 1,3,5-Tris-(4-iodophenyl)benzene

TMA — 1,3,5-tricarboxylic acid (trimesic acid)

UHV — Ultra-High Vacuum

XPS — X-Ray Photoelectron Spectroscopy

0D/1D/2D/3D — Zero/One/Two/Three-Dimension

Contents

1	Overview	13
2	Background	15
2.1	Two-Dimensional Materials and van der Waals Heterostructures	15
2.1.1	Formation of Heterostructures	17
2.1.2	Moiré Patterns in Layered Materials	18
2.2	Molecular Self-Assembly at Surfaces	19
2.2.1	Hydrogen Bonding Stabilised Structures	20
2.2.2	Halogen Bonding Stabilised Structures	27
2.3	On-Surface Synthesis	29
2.3.1	Ullmann-Type Coupling	29
2.3.2	Glaser-Type Coupling	32
3	Techniques	35
3.1	Scanning Probe Microscopy	35
3.1.1	Scanning Tunnelling Microscopy	35
3.1.2	Atomic Force Microscopy	39
3.2	X-Ray Photoelectron Spectroscopy	47
3.2.1	Theory	47
3.2.2	Spectroscopic and X-ray Notation	50
3.2.3	Instrumentation	50
3.3	Secondary Ion Mass Spectrometry	54
3.3.1	Theory	54
3.3.2	Instrumentation	56
3.4	Transmission Electron Microscopy	59
3.4.1	Theory	59
3.4.2	Instrumentation	62
3.5	Deposition of Molecules	64

3.5.1	Vacuum Deposition of Molecules	64
3.5.2	Solution Deposition of Molecules	65
3.6	Sample Preparation Methods	65
3.6.1	Substrate Exfoliation	65
3.6.2	Vacuum Sublimation	66
3.6.3	Solution Deposition of Molecules	67
3.7	Instrumentation	67
3.7.1	AFM Systems	67
3.7.2	STM Systems	68
3.7.3	SPM Analysis	69
3.8	Summary	69
4	The de-halogenation and polymerisation of 1,3,5-tris-(4-iodophenyl)benzene	71
4.1	Temperature Dependence of TIPB on hBN	74
4.1.1	Solution Deposition onto hBN	74
4.1.2	Increased Anneal Temperature Results	75
4.1.3	XPS of TIPB on hBN	81
4.1.4	Mass Spectrometry of TIPB on hBN	84
4.2	Vacuum Deposition of TIPB onto hBN	89
4.2.1	Results	90
4.3	Deposition of TIPB onto HOPG	94
4.3.1	Results	95
4.4	Summary	96
5	The deposition of melamine on hexagonal boron nitride	99
5.1	Deposition of a Thick Film	101
5.2	Deposition of Thin Films	104
5.2.1	Square Lattice of Melamine on RT hBN	104
5.2.2	Rhombic Lattice of Melamine on room temperature hBN	112
5.2.3	Observed Moiré Pattern for Melamine on room temperature hBN	114
5.2.4	Melamine Grown at Elevated Substrate Temperature	117

<i>CONTENTS</i>	11
5.3 Summary	121
6 Deposition and Polymerisation of Porphyrins on Surfaces	123
6.1 Porphyrins with increasing number of Reactive Groups	123
6.2 Polymerisation of 2R Porphyrin on Ag(111) in UHV	126
6.3 Polymerisation of 4R Porphyrin on Ag(111) in UHV	131
6.4 Deposition of 3R Porphyrin on Ag(111) in UHV	135
6.5 Solution Deposition of 4R Porphyrin on HOPG in Ambient	137
6.6 Summary	140
7 Formation of Molecular/2D Hybrid Heterostructures by Mechanical Transfer	141
7.1 Flake Transfer Methodology	144
7.2 Preservation of C ₆₀ Islands During Mechanical Transfer	146
7.3 Preparation of hBN Encapsulated C ₆₀ islands	151
7.3.1 TEM of C ₆₀ Heterostructures	154
7.4 Summary	159
References	159
8 Appendix	171
8.1 Additional Data for Chapter 4	171
8.2 Appendix	173

1 Overview

The aim of this thesis is to investigate the formation of on-surface molecular networks and polymers on a variety of surfaces including hexagonal boron nitride, highly ordered pyrolytic graphite, and Ag(111). In Chapter 2, 2D materials such as graphene and hexagonal boron nitride are discussed including how they can be combined into stacked heterostructures and the potential uses of these. Different routes to molecular self-assembly on surfaces are then introduced including hydrogen bonding and halogen bonding, in addition to covalent bonding routes to on-surface synthesis. Chapter 3 gives an introduction to the various experimental techniques used including scanning probe microscopy, X-ray photoelectron spectroscopy, secondary ion mass spectrometry, and transmission electron microscopy.

In Chapter 4 the temperature dependence of the structures formed by solution deposited 1,3,5-tris-(4-iodophenyl)benzene is investigated to study the polymerisation on the hexagonal boron nitride surface by comparison with previous work on metallic surfaces. This involves investigation of the surface using AFM with characterisation of observed structures done through comparison with a range of previously published structures.

In Chapter 5 the vacuum deposition of melamine onto the hexagonal boron nitride surface and the molecular structures formed under different surface coverages and at an increased substrate temperature with AFM are discussed. The observed structures are compared to previously published structures observed on metallic substrates.

The deposition and polymerisation of various zinc-porphyrin molecules is investigated in Chapter 6 using a novel indirect deposition method. This explores the Glaser-type coupling of ethynyl in the presence of steric hinderance groups on Ag(111) surfaces for porphyrins with between 2 and 4 ethynyl modifications. The structure formed by the porphyrin with four ethynyl modifications on HOPG is also investigated.

Finally, Chapter 7 outlines a mechanical transfer method for formation of 2D-hybrid heterostructures in which molecular C_{60} islands are preserved. This process is used for the transfer of C_{60} on hBN flakes between SiO_2 substrates as well as to form hBN/ C_{60} /hBN heterostructures for TEM analysis.

2 Background

2.1 Two-Dimensional Materials and van der Waals Heterostructures

The study of two-dimensional (2D) materials changed in 2004 with the discovery of graphene which was further expanded into the study of other free-standing 2D materials such as boron nitride. These can be obtained on top of various substrates, in suspension, and as suspended membranes.¹

Graphene is a monolayer of carbon atoms bound in a 2D hexagonal lattice. Carbon can form fullerenes (0D), nanotubes (1D) or graphite (3D). The carbon atoms within the graphene sheet are sp^2 hybridised, which means the carbon atoms bond to their three neighbours via σ bonds between the three sp^2 orbitals with the final electron in a π orbital. The p_z orbitals are delocalised across the graphene to form the bonding π and anti-bonding π^* orbitals which correspond to graphene's valence and conduction bands. The structure of a sheet of graphene is shown in Figure 2.1 with the nearest neighbour distance a of 0.142 nm and a ring-to-ring distance b of 0.246 nm.

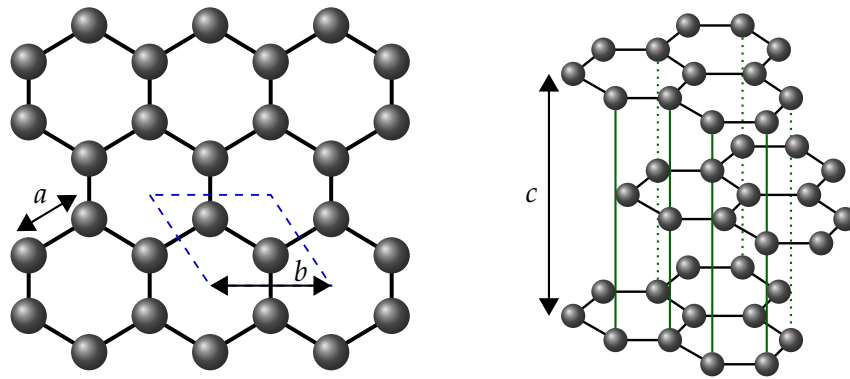


Figure 2.1 Left: The structure of a graphene sheet with unit cell shown by blue dashed line: nearest neighbour distance a is 0.142 nm and ring-to-ring distance b is 0.246 nm. Right: The interlayer structure of HOPG where c , the vertical lattice constant, is 0.670 nm.

Highly ordered pyrolytic graphite (HOPG) consists of graphene sheets stacked with a separation of 0.335 nm and held together by relatively weak van der Waals forces

arising from interactions between the π and π^* bands. Adjacent layers are shifted relative to each other leading to an ABAB stacking sequence and a c -axis lattice constant of 0.670 nm perpendicular to the layers as shown in Figure 2.1. This means that there are two non-equivalent carbon atom sites within the unit cell: the A-site has a carbon atom directly below in the next layer; and the B-site is located above the centre of a ring in the layer below.² The electronic screening length in graphite is ~ 0.5 nm which is less than two layers in thickness. Hence there is a difference in the properties of graphite depending on the number of layers with the electronic structure approaching the 3D electronic structure at 10 layers.¹

Hexagonal boron nitride (hBN) is an isoelectronic analogue of graphene consisting of an equal number of boron and nitrogen atoms bound covalently within layers and weakly between layers. As shown in Figure 2.2, the boron-nitrogen bond is 0.145 nm in length and the distance between ring centres is 0.250 nm which is similar to that for graphene. The boron nitride sheets stack into a crystal with neighbouring layers at a separation of 0.333 nm held by van der Waals forces.³ The hBN layers are stacked with the boron atoms above and beneath the nitrogen atoms in the corresponding ring position.⁴ Unlike the carbon atoms in graphene, the boron and nitrogen atoms are partially charged with a partial positive charge on the boron atoms and a partial negative charge on the nitrogen atoms. hBN has high temperature stability, intrinsic electrical insulation, and a band gap of 5.9 eV.⁵

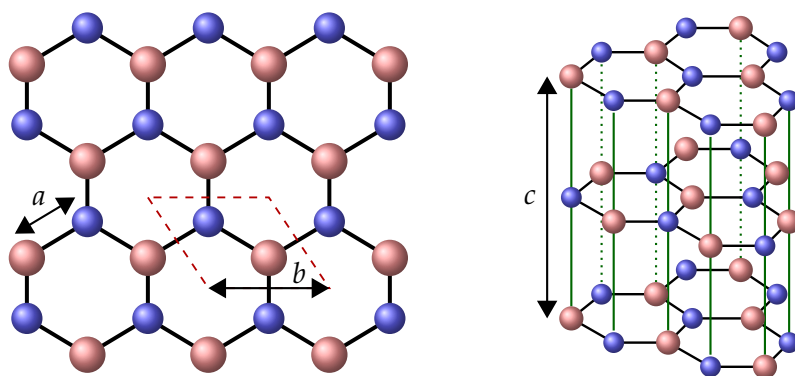


Figure 2.2 The structure of a boron nitride sheet (blue = nitrogen, pink = boron) with unit cell shown by red dashed line. Nearest neighbour distance a is 0.145 nm and ring-to-ring distance b is 0.250 nm.³

hBN flakes are often studied on a silicon wafer with 300 nm of silicon dioxide (SiO_2). The interaction of the hBN with the thick layer of silicon oxide shows a dependence of contrast and colour on thickness as shown in Figure 2.3.^{6,7} The zero-contrast wavelength shifts by 0.53 nm per hBN layer.⁷ The colour of the hBN flake is thus indicative of the thickness; pink/blue flakes are approximately 80 layers thick and pale green/orange flakes are typically less than 20 layers thick.⁶

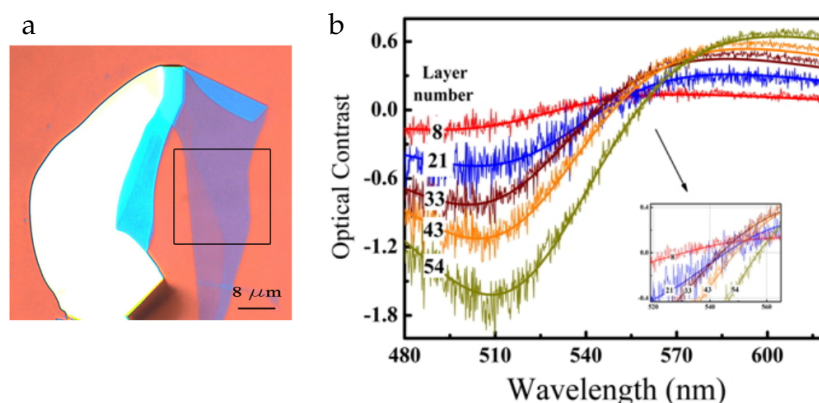


Figure 2.3 The relationship between hBN flake thickness and optical appearance: (a) optical microscopy image of a hBN flake of varying thickness on SiO_2/Si ; (b) optical contrast as a function of visible wavelength for various thickness hBN samples showing the different contrast for different thickness flakes- the inset shows the region of zero contrast. Adapted from reference 7.

2.1.1 Formation of Heterostructures

The formation of 2D heterostructure devices is of great interest in many different fields owing to their potential ability to produce novel properties and effects.⁸ Heterostructures consist of combinations of different 2D materials arranged into a stack held together by van der Waals forces. These heterostructures provide a route to tune the optical and electronic properties of the stack through control of the relative alignment, charge transfer, and proximity effects between layers. An example of a theoretically useful heterostructure is graphene sandwiched between dielectric layers (e.g. hBN or mica) and repeated; this structure would then be similar to superconducting copper oxides and has been proposed as a high temperature superconductor.⁹ Other potential uses for heterostructures include capacitive coupling between two graphene layers for Coulomb drag experiments,¹⁰

combining graphene with semiconducting and insulating materials to form field-effect tunneling transistors,¹¹ photovoltaic devices with photosensitive material sandwiched between conducting electrodes,¹² and plasmonic devices made by encapsulating graphene with hBN.^{8,13}

Mixed-dimensional heterostructures can also be formed by encapsulating 0D, 1D, or 3D materials within two 2D sheets. A recent example of this is the encapsulation of C_{60} between two sheets of graphene. The packing of the encapsulated C_{60} was different to that of bulk C_{60} with a smaller lattice spacing.¹⁴ The authors proposed that the graphene sandwich structure provided a nanoscale reaction chamber that also provided a level of damage protection when imaging in an electron microscope.

2.1.2 Moiré Patterns in Layered Materials

Layered materials can give rise to moiré patterns. A moiré pattern is a large scale interference pattern produced from two similar but non-identical periodic structures. These can arise from a rotated layer in a homogeneous material or by a difference in lattice dimensions between layers in a heterostructure as shown in Figure 2.4. The periodicity of a moiré pattern is sometimes referred to as the moiré wavelength or the moiré lattice constant as measured by the distance between neighbouring unit features.¹⁵ Moiré patterns are visible using many techniques including scanning probe microscopy (SPM) and transmission electron microscopy (TEM).

Moiré patterns have previously been observed for boron nitride nanosheet superstructures.¹⁵ For these samples, hBN powder was sonicated to separate the layers and a few drops of the sonicated solution were dropped onto a holey-carbon TEM grid. The resultant structures were observed to form mesoscale (up to 1 μm) hexagonal moiré patterns as shown in Figure 2.5. The maximum periodicity measured was $\sim 45\text{ nm}$ and the periodicity (D) was linked to the rotational angle, Φ , between the two sheets according to Equation 2.1 where d is the hexagonal lattice constant of hBN.¹⁵

$$D = \frac{d}{2 \sin(|\Phi|/2)} \quad (2.1)$$

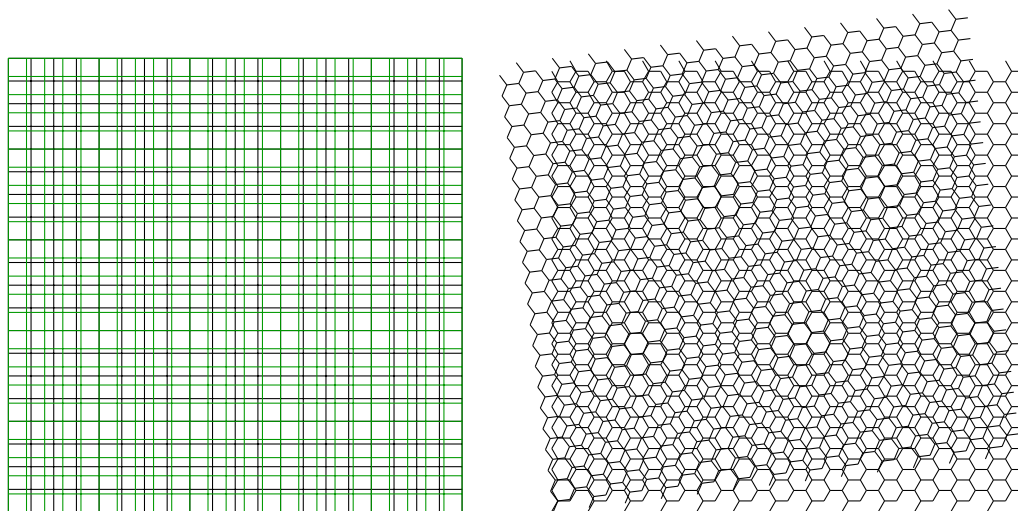


Figure 2.4 Two examples of moiré patterns: the square pattern is formed from two square grids with differing lattice dimensions (proportionally 1:0.8) and the hexagonal pattern is formed from two identical hexagonal grids with a rotation between layers of 7° .

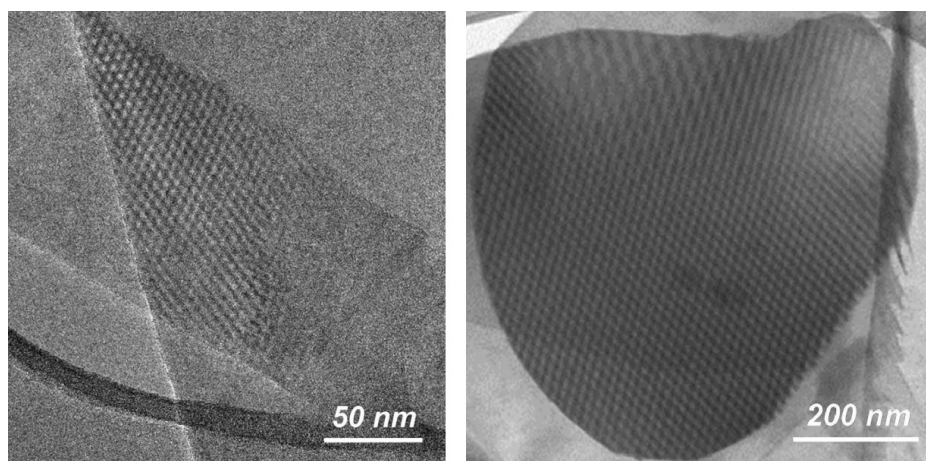


Figure 2.5 The moiré patterns formed from layered hBN sheets observed with TEM. The change in pattern across the image on the right is due to the tilt of the sample within the TEM. Adapted from reference 15.

Moiré patterns can also be formed by two non-identical layers although Equation 2.1 does not apply for layers with different lattice constants and these systems are mathematically more complex.

2.2 Molecular Self-Assembly at Surfaces

Self-assembled molecular networks (SAMNs) are of great interest for many reasons: they are relatively easy to prepare, have tunability via modification of molecular structure, and have the potential to stack into heterostructures.¹⁶ SAMNs can be grown

using many different methods including from solution, from vapour, and via molecular beam epitaxy. These can then form layers within a heterostructure system.

There are a variety of different ways that a surface assembly can be stabilised. The bonding mechanisms described in this work are: hydrogen bonding, halogen bonding, and covalent bonding. These are described in more depth below in Subsections 2.2.1, 2.2.2 and 2.3 respectively.

2.2.1 Hydrogen Bonding Stabilised Structures

Hydrogen bonding has been widely demonstrated to stabilise SAMNs. A hydrogen bond is an interaction between two molecular species in the form $A-H\cdots B$ where A and B are highly electronegative elements (generally nitrogen, oxygen and fluorine) and B possesses a lone pair of electrons. The formation of a hydrogen bond can be viewed as the interaction between a partial positive charge on the hydrogen and a partial negative charge on B.

The strength of the hydrogen bond is about 0.2 eV but depends on the specific atoms involved. As hydrogen bonding depends on orbital overlap, it is a contact-like interaction which decays quickly with distance. The distance between non-covalently bonded atoms has been seen to be less than their van der Waals contact distance which supports the theory that a strong attractive force is the dominating force. However, the strength of the interaction means that, when present, hydrogen bonding dominates other intermolecular interactions.¹⁷ For example, the properties of liquid and solid water are dominated by the hydrogen bonding between the H_2O molecules.

Commonly hydrogen bonds are asymmetric with the $A-H$ bond shorter than the $H\cdots B$. More rarely, symmetric hydrogen bonds can occur where the H atom lies halfway between the A and B atoms; this generally occurs between hydrogen fluoride molecules. These structures are shown in Figure 2.6. Electrostatic models which treat the $A-H\cdots B$ bond as an array of point charges with partial negative charges on A and B and partial positive charge on the H suggest that the lowest energy is achieved for a linear arrangement as the two partial negative charges are furthest apart.¹⁷

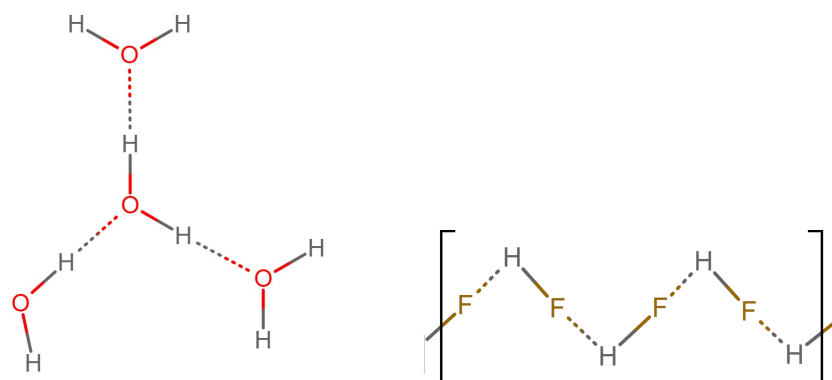


Figure 2.6 The hydrogen bonds between H₂O molecules showing a shorter O–H covalent bond than hydrogen bond and the hydrogen bonds between HF showing symmetric covalent and hydrogen bonds.

Initial studies of hydrogen bonding mediated assembly on surfaces were inspired by the selective pairing of nucleic bases.¹⁸ The four DNA bases (adenine, thymine, guanine, and cytosine) were observed to form 1D and 2D arrays on Cu(111).¹⁸ The authors used semiempirical molecular orbital calculations to justify their theory that the structures were stabilised by hydrogen bonding. Later work confirmed that adenine, guanine, and cytosine can form one or two dimensional structures on Cu(111) but found that thymine aggregates into small clusters.¹⁹ The work by Furukawa et al.¹⁹ also modelled the formation of thymine dimers and other ordered structures which were seen to be energetically unfavourable on the Cu(111) surface. Further work by Otero et al.²⁰ was carried out with guanine on a Au(111) surface and the molecule was observed in two different structures: a quartet unit cell with the guanine bound by two O···H and N···H to each of the neighbouring molecules giving six hydrogen bonds in total; and a higher density network seen at high temperatures also bound with six hydrogen bonds from each molecule. MD calculations found the quartet to be the only stable structure at room temperature.²⁰

Another frequently studied hydrogen bonded structure is that of trimesic acid (benzene-1,3,5-tricarboxylic acid). This is a highly symmetrical triangular molecule which has been observed to form large, ordered arrays on a wide array of substrates. This molecule can form hydrogen bonds between the carboxylic acid groups, leading to multiple possible structures. Two of these structures, as observed on HOPG, are shown in Figure 2.7.²¹ These structures were prepared by evaporating TMA at 181 °C followed

by annealing to 120 °C for 15 min to create large islands.²¹ The chickenwire structure was also observed on a Cu(100) surface for samples prepared with the substrate held at low temperatures (~ 200 K) and an alternative close-packed structure was observed when the sample was held at room temperature.²² The pores in these structures can accept TMA molecules in many different positions.²¹

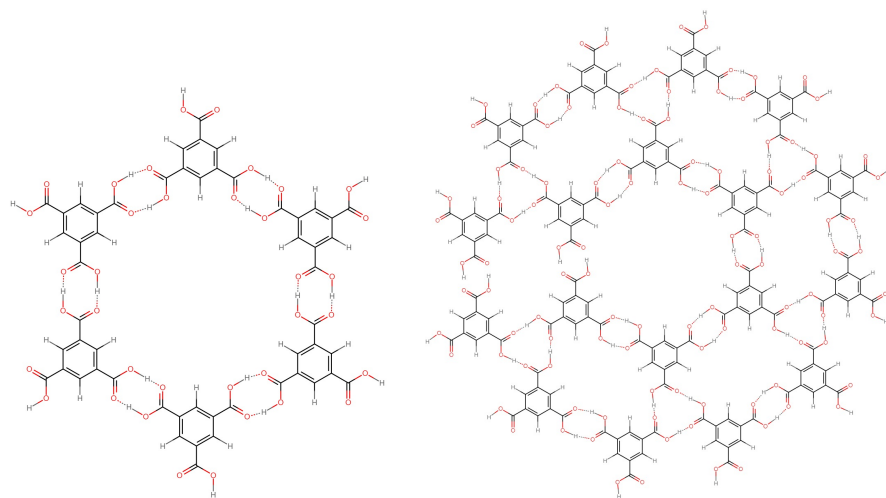


Figure 2.7 The hydrogen bonded structures trimesic acid can form (hydrogen bonds shown by dotted lines). The structure on the left is known as the chickenwire structure and the one on the right is known as the flower structure.²¹

The chickenwire structure of trimesic acid (TMA) on graphite has been observed to form moiré patterns. A preferential orientation was seen with the TMA structure at a relative rotation to the graphene sheet of $\sim 5^\circ$. The authors believed that this orientational preference is predetermined at an early stage of growth due to interactions between the TMA and the graphite surface. A small range of moiré pattern lattice periodicities were seen which suggests that the structure is kinetically stabilised rather than being in a thermodynamic equilibrium. However, the authors were unable to influence the moiré pattern formation by introducing thermal energy in the deposition stage.²³

Studies on trimesic acid led researchers to look at similar molecules such as melamine. One of the earliest molecular surface structures to be looked at which included melamine was the mixture of melamine and perylene tetra-carboxylic diimide (PTCDI) on the Au(111) surface.²⁴ In this work the researchers prepared the gold surface using sputtering and annealing to form the $22 \times \sqrt{3}$ chevron reconstruction.

The surface was then held at room temperature whilst the PTCDI and melamine were sublimed onto the surface. PTCDI was deposited first to form between 0.1 ML to 0.3 ML which was followed by approximately 0.5 ML of melamine. Prior to the deposition of melamine, the PTCDI was seen to form ordered islands with the molecules arranged in a head-to-tail arrangement, held together with hydrogen bonds. Once the melamine had been deposited, the PTCDI islands were observed to disrupt and form small areas of ordered arrays formed between the melamine and PTCDI. After the surface had been annealed to between 60 °C to 80 °C, a hexagonal network was formed. The authors theorised that annealing to this temperature removed the majority of the melamine molecules leaving only those held within the network by hydrogen bonds. The proposed structure was a honeycomb arrangement formed by a melamine molecule at the vertex and PTCDI molecules as the edges; this structure is shown in Figure 2.8.²⁴

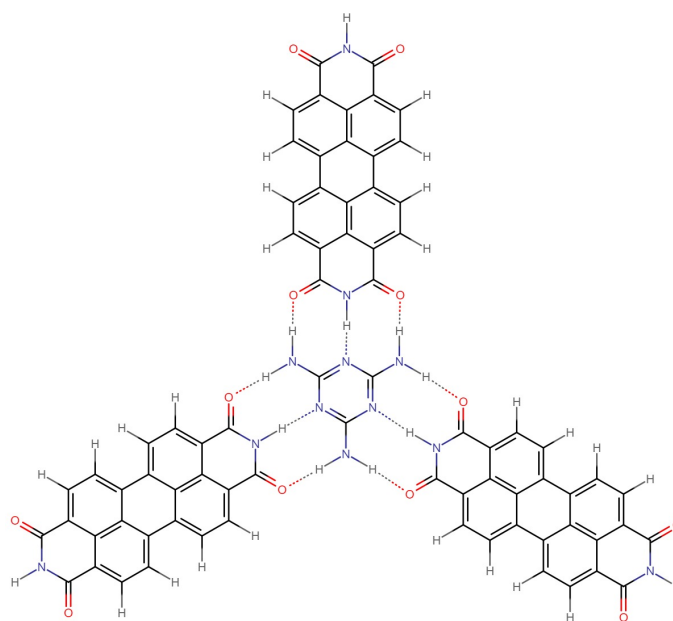


Figure 2.8 The hexagonal structure formed between melamine and PTCDI on the Au(111) surface.²⁴

The structure of melamine-PTCDI was then used to template molecular adsorption. Fullerene (C_{60}) molecules were sublimed onto the surface. After the deposition of approximately 0.1 ML, around 25% of the pores were filled with regular fullerene clusters with the other 75% of pores completely unoccupied. The authors explained

this as the fullerenes diffusing across the network and nucleating growth within the pores.²⁴

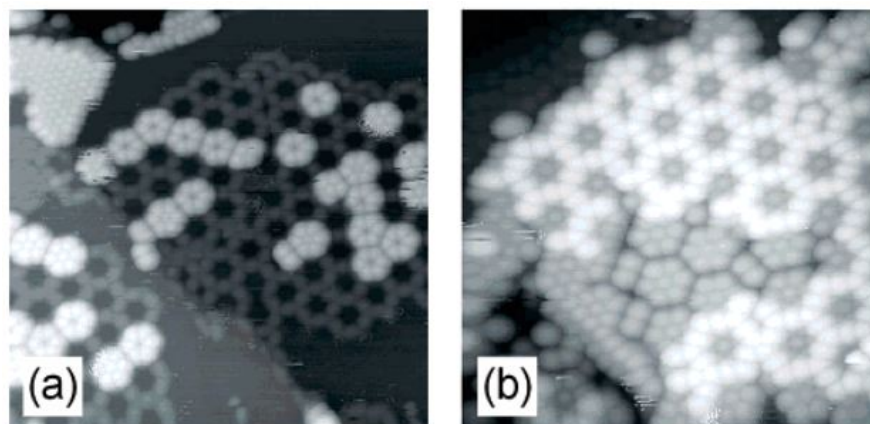


Figure 2.9 STM images of the templated absorption of fullerene into the melamine-PTCDI network: (a) shows the melamine-PTCDI network in the hexagonal structure from Figure 2.8 with an area at the top showing a different structure along with small areas of templated fullerene islands; (b) shows the higher coverage of fullerene with the templated fullerene structures as well as absorbed fullerene on top of the melamine-PTCDI structure. Image adapted from reference 24.

Following on from the melamine-PTCDI on Au(111) and Ag/Si(111) work, this bimolecular system has been formed on many other surfaces. An important development was the adsorption of the molecules from solution.²⁵ The melamine and PTCDI were prepared as dimethylformamide (DMF) solutions with relative concentrations of 0.66 mM and 0.5 μ M. Each sample was immersed in the solution then rinsed in fresh DMF and dried with N_2 . The bimolecular system was deposited onto HOPG (20 min immersion) and formed large islands (up to 0.5 μ m) with a lattice constant of 3.5 ± 0.1 nm, consistent with that seen on Au(111).²⁶ The network was also deposited onto hBN (1 min immersion) and MoS_2 (10 min immersion) to form extended layers which were seen to remain stable when stored under nitrogen.²⁶

Another melamine network was observed to form between melamine and cyanuric acid; this structure is sometimes referred to as melamine cyanurate.^{27,28} Unlike PTCDI, cyanuric acid is similar in structure to melamine with double-bonded oxygen in place of amine groups. The two molecules can interact through the formation of three hydrogen bonds to form a hexagonal structure as shown in Figure 2.10. This structure has been observed to form moiré patterns when on HOPG. This network has also

recently been shown to stabilise the highly reactive black phosphorus surface both microscopically and macroscopically.²⁹

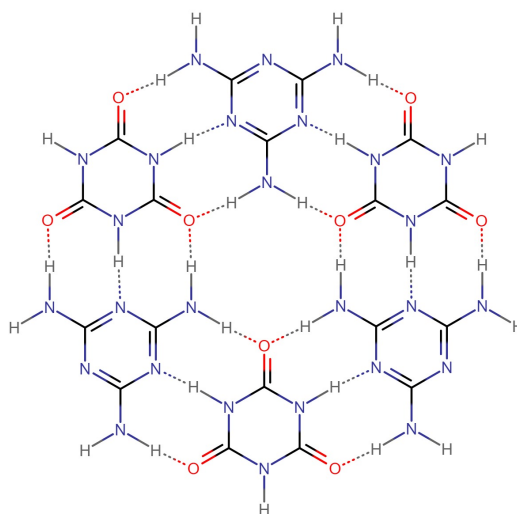


Figure 2.10 The hexagonal structure formed between melamine and cyanuric acid with the hydrogen bonds shown by dotted lines.²⁸

Melamine has also been studied as a monomolecular network.³⁰ Three different melamine assemblies have been reported on Au(111) and Ag(111) metal surfaces: α , β , and γ which are shown in Figure 2.11.^{30,31} The α assembly is hexagonal with central pores separated by 1.042 nm³¹. The β assembly forms rows and has an overall triangular symmetry with a ring-to-ring distance of 0.768 nm³⁰. The γ assembly is a combination of the α and β assemblies and can vary in structure with a larger or smaller proportion of β structure between the pores of the α structure; the simplest version is shown in Figure 2.11 and the lattice parameters are in Table 2.1. The main difference between the assemblies is the density of the melamine on the surface with two molecules per unit-cell in the α assembly and four molecules per unit-cell in the γ assembly.³¹ These assemblies can also be influenced by the size and orientation of the lattice of the supporting substrate. Melamine has also been seen to adsorb vertically on copper surfaces forming melamine-copper complexes.³²

	α	β	γ
a (nm)	1.042	1.20	1.042
b (nm)	1.042	0.77	1.733
θ (°)	120	65.3	106.1

Table 2.1 Lattice parameters for melamine structures shown in Figure 2.11.^{30,31}

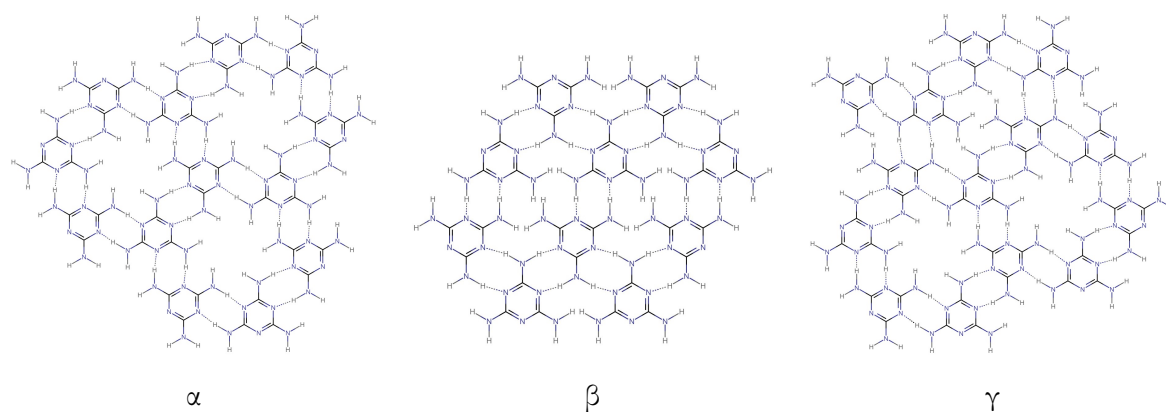


Figure 2.11 The alpha (α), beta (β), and gamma (γ) assemblies formed by melamine on Au(111) and Ag(111).^{30,31} Hydrogen bonds are denoted by dotted lines.

Another molecule that can form hydrogen bonded structures is melem which can be synthesised by thermal condensation of melamine.³³ Instead of a single azine ring, the structure consists of a heptazine group with three amino substituents. As with melamine, melem is stable in two different forms on the surface as well as forming chiral rings on the surface.³⁴ The structure of the three stable forms are shown in Figure 2.12. The chiral ring arrangement can take two forms – clockwise or anti-clockwise – with domain boundaries appearing between areas of differing chirality.

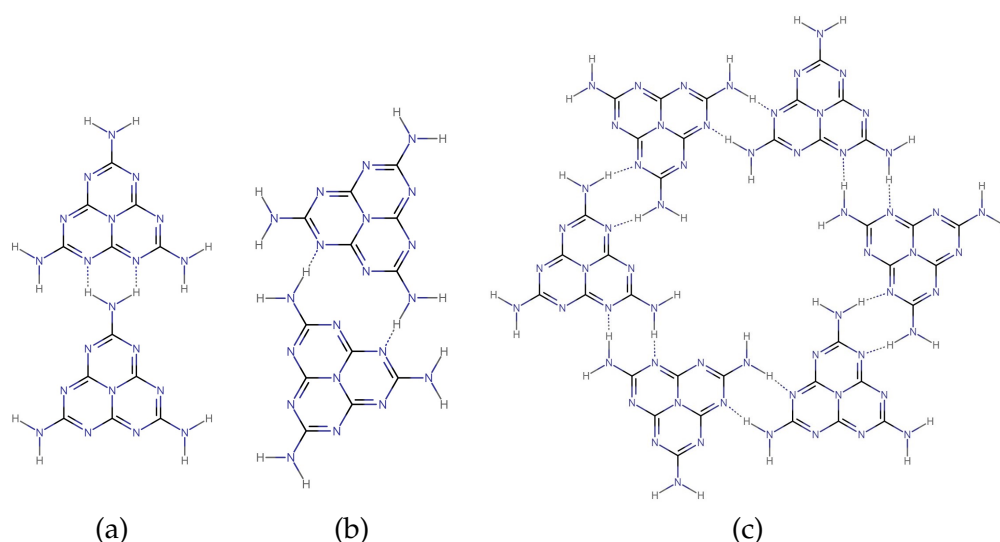


Figure 2.12 The different bonding schemes for melem with hydrogen bonds shown by dotted lines: (a) head-to-tail bonding, (b) side by side bonding, and (c) clockwise chiral bonding.³³

2.2.2 Halogen Bonding Stabilised Structures

Halogen bonding is similar to hydrogen bonding as it involves a difference in electrostatic potential along a bond. However, the bond, instead of being between a hydrogen atom and a more electronegative atom, involves a halogen atom in a halogen-carbon bond (X–C) or a halogen-nitrogen bond (X–N). This occurs because halogen atoms are highly polarisable and there is an electrostatic potential along the halogen-carbon bond. This creates an anisotropic charge distribution around the halogen atom with positive polarisation along the X–C axis and negative polarisation perpendicular to the axis as shown in Figure 2.13 (a).³⁵

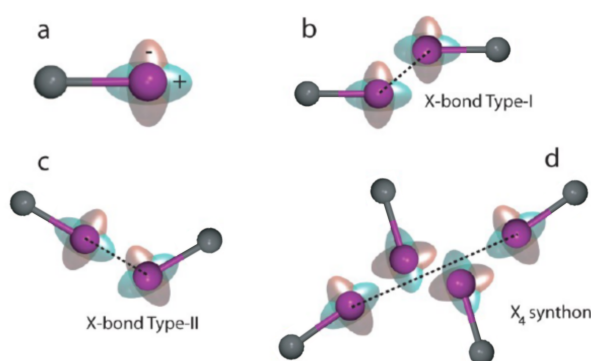


Figure 2.13 (a) The polarisation around the C–X bond, (b) type I bonding, (c) type II bonding, and (d) an X_4 synthon (iodine shown in purple and carbon in grey). Adapted from reference 35.

The bonding can be split into two types: type I are symmetrical and consist of van der Waals forces so occur when molecules are closely packed (Figure 2.13 (b)); type II are bent and consist of an attractive interaction between the nucleophilic and electrophilic areas of the halogen atom (Figure 2.13 (c)). The type I bond requires the angle between the two X–C bonds to be 180° whereas type II requires an angle between the bond axes of 90° to 120° . Also shown in Figure 2.13 (d) is an X_4 synthon which is a combination of type I and II bonds with a central type I interaction and two type II interactions at each end.³⁶

An example of a halogen bonded structure is that of 1,3,5-tris(4-bromophenyl)benzene (TBPB) on Au(111). This system forms several structures stabilised by halogen bonding at room temperature.³⁷ The halogen-bonded structures seen after a solution deposition

(either a 0.8 mg ml^{-1} solution in ethanol or a 0.2 mg ml^{-1} solution in butanol) are shown in Figure 2.14. The structures shown in Figure 2.14 have also been observed for the

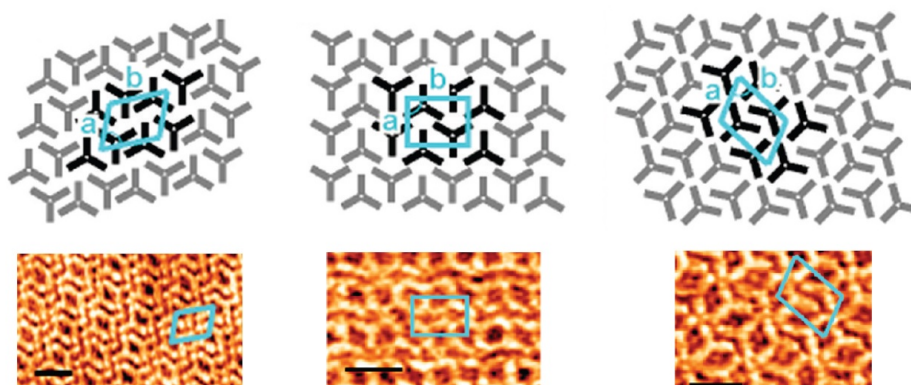


Figure 2.14 Three of the structures observed for TBPB on Au(111) by Russell et al. All scale bars are 2 nm. Image adapted from reference 37.

iodinated species – 1,3,5-tris(4-iodophenyl)benzene (TIPB). The structure in Figure 2.14 (c) has been theorised to be an X_4 synthon for the iodinated species as shown in Figure 2.15.³⁵

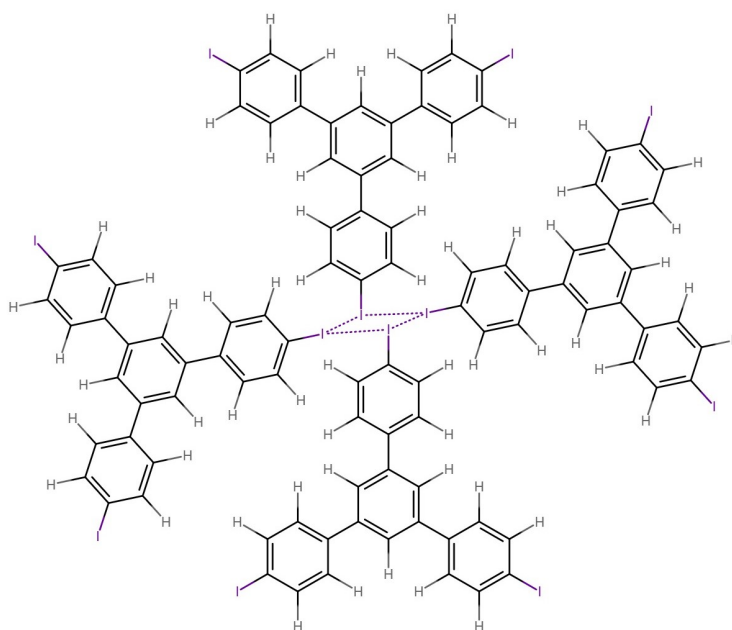


Figure 2.15 The X_4 synthon theorised to stabilise the structures formed by TIPB on various surfaces with the halogen bond area represented by the dotted lines.³⁵

Halogen bonding has the potential to stabilise many different molecules into 2D structures on surfaces however, unlike hydrogen bonding, it is not as well understood. One of the difficulties in studying halogen bonding on surfaces is the inherent

instability in the C–Br and C–I bonds which can give rise to the formation of covalently bonded structures.

2.3 On-Surface Synthesis

The previous self-assemblies discussed were stabilised by non-covalent interactions into assemblies so that the constituent molecules were unaltered. This may be contrasted with on-surface synthesis in which the precursor materials are covalently bonded into large assemblies or polymers. As this requires breaking and making bonds, an external source of energy is required to cross the activation energy barrier. The energy barrier can sometimes be sufficiently lowered by the surface so that the reaction occurs spontaneously at or below room temperature. There are many different routes for synthesis and it is generally determined by the reactive groups on the precursor molecules. A selection of mechanisms of particular relevance to the on-surface synthesis in this thesis are discussed below.

2.3.1 Ullmann-Type Coupling

Ullmann coupling is named after its discoverer Fritz Ullmann who worked on the synthesis of biphenyls from aryl halides in an acidic solution with a copper catalyst. In surface science, Ullmann-type coupling generally refers to C–C coupling of halogenated precursors on coinage metal (Cu, Ag, Au) surfaces which can catalyse the reaction.³⁸ An example of this work is the formation of graphene nano-ribbons (GNR). GNRs have been formed by Cai et al.³⁹ from 10,10'-dibromo-9,9'-bianthracene precursors on an Au(111) surface. First, Ullmann-type coupling takes place with the surface acting as a catalyst and activation energy provided by heating the surface to 200 °C to link the precursors into a 1D polyanthrylene chain then, with additional thermal energy provided by heating the surface to 400 °C, intramolecular cyclodehydrogenation takes place to create the planar GNR as shown in Figure 2.16.³⁹

Ullmann-type coupling has also been observed for the 1,3,5-tris(4-bromophenyl)benzene (TBPB) system mentioned above in Subsection 2.2.2. This system is bound by halogen bonds initially but, with the addition of thermal energy, the C–Br bond breaks which

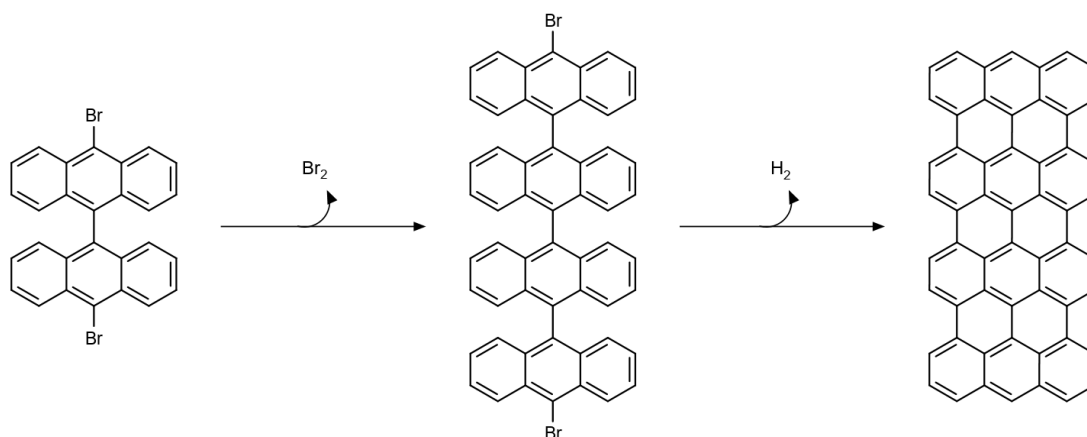


Figure 2.16 The reaction of 10,10'-dibromo-9,9'-bianthracene to form graphene nano-ribbons via Ullmann-type coupling followed by cyclodehydrogenation.³⁹

can lead to the formation of dimers, chains, or 2D hexagonal arrays. In work by Blunt et al.⁴⁰, the TBPB was sublimed onto a clean Au(111) thin film under UHV conditions. The samples were then imaged at room temperature with UHV STM. The effect of annealing the sample post-deposition was found to encourage debromination and covalent coupling between the molecules. After a 10 min anneal to 110 °C, dimers were found to form but the surface was seen to be mostly disordered. Further annealing led to an increase in the proportion of dimers and the formation of ordered regions however, additional annealing did not lead to the expected hexagonal pore structure. To achieve the hexagonal pore structure created by complete debromination and covalent coupling, the authors investigated heating the substrate during the deposition. They found that large ordered structures were formed by a repeated step of depositing 0.25 ML onto a surface held at 140 °C followed by a post-deposition anneal at 180 °C. A selection of the structures observed are shown in Figure 2.17.

The work on TBPB was then continued within this group to investigate solution deposition. The substrate was the same – Au(111) film on mica – but 10 μL TBPB was deposited from either a 0.8 mg ml^{-1} solution in ethanol or a 0.2 mg ml^{-1} solution in butanol. For a non-heated substrate, halogen-bonded structures were observed as shown above in Figure 2.14 however, for a substrate held at 150 °C some dimerisation events were observed and, for a substrate held at 200 °C ordered dimerised areas were observed as shown in Figure 2.18.³⁷

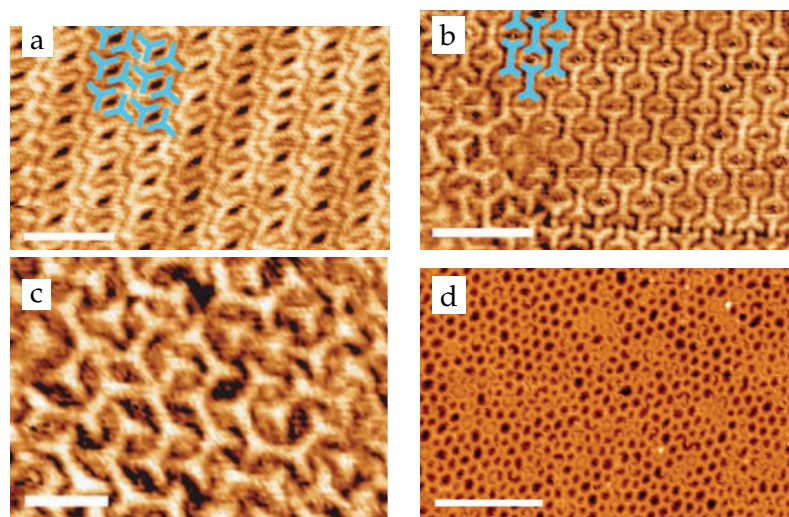


Figure 2.17 A selection of the structures reported for TBPB on Au(111): (a) a close-packed arrangement of the monomer with simplified monomers overlaid [scale bar is 4 nm]; (b) an ordered domain of dimers formed after heating to 110 °C with simplified dimers overlaid [scale bar is 5 nm]; (c) a multiply connected network seen when annealed at temperatures above 110 °C [scale bar is 2.5 nm]; and (d) the porous covalent network formed by deposition onto a heated substrate held at 140 °C [scale bar is 1.4 nm]. Images adapted from 40.

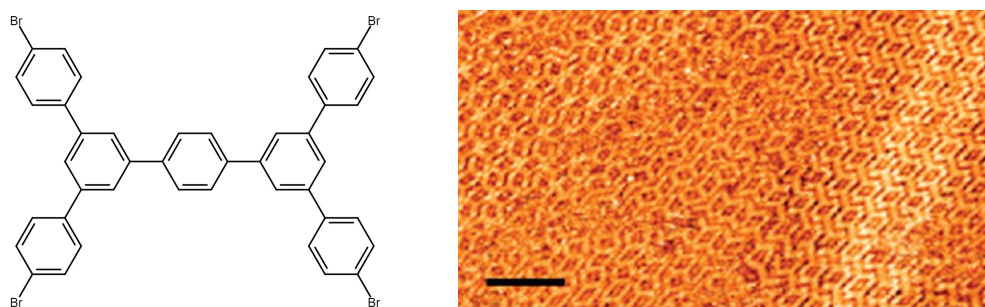


Figure 2.18 The dimer formed from two TBPB molecules and the structure observed to form at 200 °C. Right hand image is adapted from reference 37 with a scale bar of 5 nm.

The most important reaction parameters for Ullmann-type coupling are the halogen and the surface. According to catalysis theory, the more corrugated the surface the more reactive the surface so (110) surfaces for fcc metals should have the lowest dehalogenation temperatures. However, in practice the more densely packed (111) surface is used as flat areas are preferred for imaging. Coinage metal surfaces are generally used with the activation energy following: $\text{Cu} < \text{Ag} < \text{Au}$. The strength of the halogen-carbon bond follows: $\text{I} < \text{Br} < \text{Cl} < \text{F}$. Brominated precursors are the most common for Ullmann-type coupling as they require little activation energy but are stable against decomposition in the deposition process unlike some iodinated

species. Chlorinated species are also commonly used but require higher activation energies or more catalytically active surfaces. The high binding energy of the C–F bond prevents fluorinated species from being used.³⁸ The dehalogenation process in Ullmann-type coupling has also been observed for non-metallic surfaces however the reaction mechanism is currently unknown.^{41,42}

2.3.2 Glaser-Type Coupling

Another surface applicable type of covalent coupling is Glaser coupling. Glaser coupling is a copper catalysed oxidative coupling that links acetylenes into 1,3-diynes. More generally in surface science, Glaser-type coupling refers to the coupling of terminal alkynes on a metal surface to generate bisethynylarene products with a molecular hydrogen byproduct. An example of this bonding is that of 1,4-diethynylbenzene on various metal surfaces.⁴³ The reaction scheme for this molecule is shown in Figure 2.19. In work carried out by Gao et al.⁴³, the dimerisation of 1,4-diethynylbenzene was looked at on Au(111), Ag(111), and Cu(111) under UHV conditions. The authors determined that the copper substrate did not provide efficient on-surface coupling and that the silver substrate provided a lower proportion of side reactions so was the best surface to use for on-surface Glaser-type coupling. The authors also carried out density function theory (DFT) calculations to determine the most likely reaction pathways on the Au(111) and Ag(111) substrates. The DFT calculations found the alkyne activation by the metal surface was a high-energy pathway which was unlikely to be realised under their experimental conditions. The low-energy route comprises of interaction of the alkyne groups with the surface with the direct C–C bond formation as the rate-determining step. Their calculations also supported the observation that dimerisation is more efficient on the silver surface partially due to the greater stability of the dehydrogenated states on silver than gold.⁴³

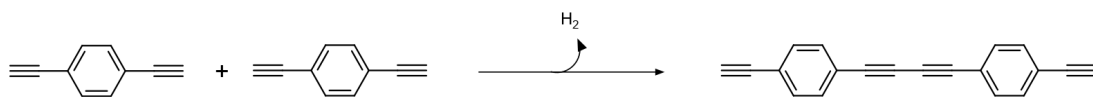


Figure 2.19 The dimerisation of 1,4-diethynylbenzene.⁴³

Glaser-type coupling can often result in many different structures. To improve the selectivity of surface-confined Glaser-type coupling, either the surface or the precursor needs modifying. Precursors are often modified by adding bulky side chains to provide steric hinderance for side reactions. Another strategy is to use the surface to limit the reaction products to the target product. An example of this is the growth of graphdiyne wires on an Ag(877) surface.⁴⁴ The molecule in this work – 4,4''-diethynyl-1,1':4', 1'' terphenyl – had previously been seen to undergo Glaser-type coupling on the Ag(111) surface when annealed to 400 K to form a wide range of structures due to the formation of branched junctions made from more than two monomers as shown in Figure 2.20. The authors limited this reaction using the surface geometry of an Ag(877) surface, which is a highly stepped surface with narrow terraces. The width of these terraces was used as a way of limiting the growth in one direction whilst not inhibiting growth along the terrace as shown in Figure 2.20. The resulting 1D graphdiyne wires were then electronically assessed and seen to have a simple band structure with a small energy gap.⁴⁴

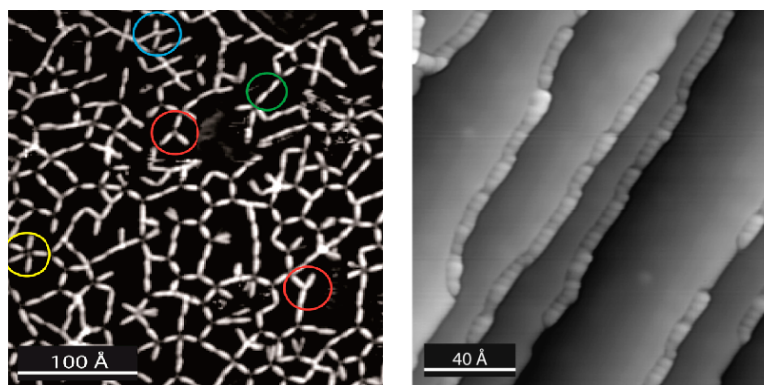


Figure 2.20 The resulting polymers of 4,4''-diethynyl-1,1':4', 1'' terphenyl on Ag(111) (left - with circled junctions) and on Ag(877) (right). Adapted from reference 44.

Glaser-type coupling is usually thermally activated but has also been reported that it can be activated by UV radiation on an Ag(111) surface for 1,4-diethynyl-2,5-dihexylbenzene.⁴⁵ A UV laser was used with the wavelength chosen using the UV-vis adsorption spectrum of the monomer to avoid direct photodissociation. The authors ensured that the laser did not heat the sample to induce coupling with thermal energy. It was also reported that photochemical coupling was not effective on the Au(111)

surface which the authors suggested was down to the reduced mobility of the aryl-alkynes on this surface.⁴⁵

All of the bonding mechanisms discussed in this chapter will be explored using various molecules and substrates in the experimental chapters later in this work.

3 Techniques

In this course of the work described in this thesis, a variety of techniques were used. A brief overview of the theory and instrumentation for SPM, XPS, SIMS, and TEM are included in this chapter. The main technique used in this thesis to investigate surfaces was atomic force microscopy which is described in the SPM section below. A section on experimental methods including flake exfoliation, sample cleaning and deposition of molecules is also included.

3.1 Scanning Probe Microscopy

Scanning probe microscopy (SPM) is frequently used to image molecular assemblies on various surfaces. The technique allows the topography and other properties of a surface to be resolved down to less than 0.1 nm. There are two main forms of SPM used: scanning tunnelling microscopy and atomic force microscopy.

3.1.1 Scanning Tunnelling Microscopy

Scanning tunnelling microscopy (STM) was the first type of SPM invented. In STM, an atomically sharp tip, typically platinum-iridium or tungsten wire, is brought near a sample. A bias voltage of V_t is applied between the tip and the sample such that when the distance between tip and sample is <1 nm a tunnelling current I_t can flow. If V_t is small compared to the work function of the surface, Φ , then the tunnelling barrier is rectangular with a width equal to the tip-sample separation z as shown in Figure 3.1. The tunnelling current is thus described by

$$I_t(z) = I_0 e^{-2\kappa_t z} \quad (3.1)$$

where $\kappa_t = \sqrt{2m_e\Phi}/\hbar$. This means that, for a metal with a work function of 4 eV, a change in tip-sample separation of 0.1 nm leads to a change in current of an order of magnitude making the technique extremely surface sensitive.⁴⁶

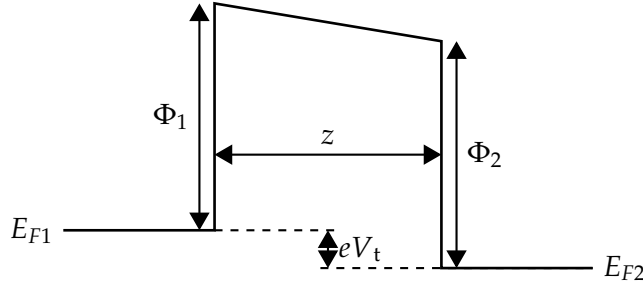


Figure 3.1 The barrier between two surfaces with work function Φ_1 and Φ_2 separated by z with an applied bias V_t between them.

Tersoff-Hamman theory is commonly used to interpret images obtained using STM. The theory has three assumptions: the STM tip is approximated by an atom with an s-orbital as the valence shell, the tip-sample interactions are negligible, and the bias voltage is small. These three assumptions allow the tip to be treated as a mathematical point, any structural modifications and the wavefunctions of the electrodes to be ignored, and only considers the sample electronic states at the Fermi level for the tunnelling. Using these assumptions, Tersoff-Hamman shows that the STM current I_t is proportional to the local density of states (LDOS) of the sample at the tip position \mathbf{r}_t according to

$$I_t \propto \sum_v |\psi_v(\mathbf{r}_t)|^2 \delta(E_s - E_f) \quad (3.2)$$

where ψ_v is the v electronic band orbital of the sample, E_s is the energy of the state v , and E_f is the Fermi energy.⁴⁷ The δ function ensures that only Fermi band orbitals contribute to the LDOS. For constant height STM measurements, the constant current contours represent $\rho(\mathbf{r}, E_f)$, the constant partial electron density of the sample surface at the Fermi level. The partial density is obtained by summing the density contributions of the band orbitals $\psi_v(\mathbf{r})$ of the sample:

$$\rho(\mathbf{r}, E_f) = \sum_{|E_v - E_f| \leq \Delta}^{E_f} \psi_v(\mathbf{r})^* \psi_v(\mathbf{r}) \quad (3.3)$$

where Δ is a small positive number, typically about 0.25 eV. For metals where the highest occupied and lowest occupied levels are degenerate, the summation includes all occupied band orbitals between E_f and $E_f - \Delta$ for sample-to-tip tunnelling and all unoccupied band orbitals between $E_f + \Delta$ and E_f for tip-to-sample tunnelling.⁴⁸

However, there are limitations to interpretations using Tersoff-Hamman. For example, the modelling of the tip as an atom with an s-orbital fails to explain observed atomic resolution for close-packed elemental metal surfaces as higher tip orbitals are involved in the interaction. Nevertheless, the Tersoff-Hamman model is useful to link observed current to the partial electron density at the surface.

Instrumentation

The basics of the STM equipment are shown in Figure 3.2. First, a voltage bias of 0.001 V to 5 V is applied between the tip and the sample. Then the STM tip is brought near to the surface until the tunnel current reaches a set level, usually between 0.1 nA and 40 nA. The tip-sample separation is typically <10 nm leading to significant tip-sample force interactions. These forces are generally strongest in ambient scanning due to the presence of a contamination layer which can transmit the tip force. The movement of the tip is controlled by a control loop which sends a voltage to three piezodrives allowing the tip to be moved in any direction.⁴⁸

The tip-sample separation is kept constant by a feedback loop controlled by measuring the difference between the actual and the set-point values for the tunnel current and adjusting to minimise this difference. The accuracy of the imaging depends on the conditions of the feedback loop; the use of small gains keeps the tip position constant and less able to respond to sudden surface height changes whereas high gains can create an unstable feedback circuit. For this reason, moderate gain values should be used with frequent adjustments needed for a new surface.⁴⁸

An ideal STM tip has a monoatomically sharp apex. However, in practice tips are usually prepared by mechanically cutting or electrochemically etching a metallic wire which leaves a poorly defined tip geometry. Platinum-iridium tips are typically used in ambient STM while tungsten tips are commonly used in UHV STM. These materials are used due to their relative stability under scanning and conductance. The tip geometry can also spontaneously change during scanning which can improve or reduce the STM quality.

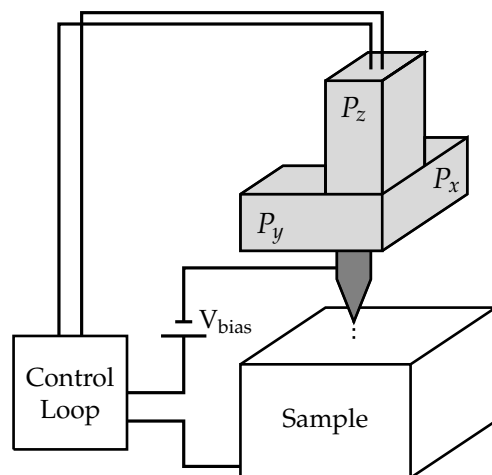


Figure 3.2 An overview of the STM tip controls. P_x , P_y , and P_z are the three piezodrives that control the direction of movement of the tip.

STM can be carried out in constant-current mode (also known as topographic) or constant-height mode. Topographic mode creates images by moving the tip in the xy plane and changing the z position to keep I_t constant. In constant-height mode, the z position of the tip is kept constant and the surface is measured as variations in I_t . As the tip does not have to adjust via a feedback loop, this technique is generally quicker but is only suitable for flat surfaces due to the risk of the tip crashing into the surface.⁴⁶

Some molecules are not stable enough to image under normal atmospheric conditions. There are two possible solutions to this: image in liquid or image in vacuum. To image under liquid conditions, the selected solvent is dropped onto the surface and the tip is approached as normal. Stable imaging of adsorbates at the liquid–solid interface requires optimum tunnelling conditions which can vary with the adsorbate and the solvent. The solvent also must be selected to reduce reactions with the tip, surface, molecules, or other materials within the sample mount.

Imaging under vacuum reduces the presence of the liquid contamination layer between the tip and sample which reduces the risk of unintended reactions and increases the stability of the surface, particularly for reactive metals which oxidise in atmosphere. Vacuum STM also allows for more directed tip modification and tip improvement by coating with a different material. For example, tips are often coated in coinage metal atoms by deliberately crashing the tip into a metal surface then slowly pulling the tip away from the surface. Vacuum conditions also allow the sample to

be cooled to extremely low temperatures. Low temperature (LT)–STM is carried out with either liquid nitrogen cooling (allowing a temperature of 77 K to be reached) or liquid helium cooling (allowing a temperature of 4 K to be reached). The benefit of LT–STM is that molecules, which would be highly mobile at RT, are fixed in place with the reduction of thermal energy.

STM is now widely used to image molecules on conducting and thin insulating surfaces,⁴⁹ to manipulate molecules and individual atoms,⁵⁰ and to investigate the properties of single molecules.⁵¹ The main limitation to STM is that the surface must be conducting. For work on metallic or silicon surfaces, even with a thin insulating layer, this is not a problem as long as tunnelling can occur. However, for thicker insulating layers or insulating substrates, STM cannot generally be used.

3.1.2 Atomic Force Microscopy

In order to study insulating surfaces, a different technique is required – atomic force microscopy (AFM). AFM is similar to STM except the force between the tip and the surface is measured instead of the tunnel current. This means that a greater range of materials can be studied as the substrate does not need to be conducting.

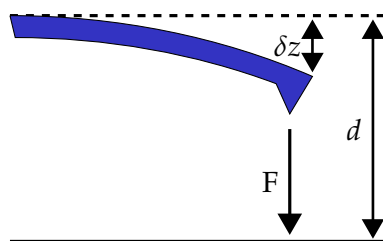


Figure 3.3 The deflection of a cantilever at height d above a surface experiencing an attractive force (F) causing a deflection of δz .

The AFM probe consists of a force sensor with a sharp tip. As the cantilever approaches the surface, the force between the two causes the cantilever to undergo a deflection as shown in Figure 3.3. There are several possible origins of the force between the tip and the surface, which can be long-range or short-range. Short-range contributions include chemical forces and long-range contributions include van der Waals, electrostatic and magnetic forces. Meniscus forces caused by adhesion layers of water or hydrocarbons on the tip or surface can also contribute if the AFM is in ambient

conditions.⁴⁶ The highest resolution images are generally obtained when measuring the differences in chemical forces but the long-range contributions are still present.

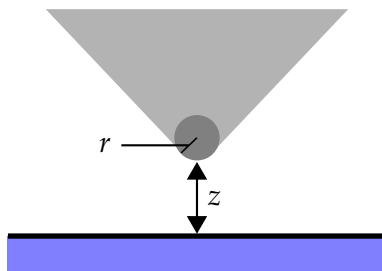


Figure 3.4 The tip-surface interaction for a tip with terminating sphere of radius r at separation z .

Generally the predominant long-range force is van der Waals. The van der Waals interaction is due to random fluctuations in the electric dipole moment of the atoms and the energy varies $\propto z^{-6}$ for two atoms separated by a distance z . Treating the tip as a terminating sphere of radius r and the surface as a semi-infinite plane as shown in Figure 3.4, the van der Waals interaction can be calculated using the Hamaker approach⁵² to give

$$F_{vdW} = -\frac{Hr}{6z^2} \quad (3.4)$$

where H is the Hamaker constant which is dependent on the material composition of the tip and surface.⁴⁶ The Lennard-Jones potential, shown in Figure 3.5, is formed to give a simplistic representation of the tip-surface relationship by combining the repulsive forces from Pauli repulsion and the attractive forces from van der Waals interactions between the tip and the surface.

AFM can be performed by measuring either the static response of a cantilever or the resonance of a dynamic cantilever. Contact mode uses static deflection of a cantilever. The deflection of the cantilever, z , is directly linked to the sum of the attractive and repulsive forces on the cantilever via the spring constant of the cantilever, k , as described by Equation 3.5.

$$F = -k\delta z \quad (3.5)$$

A soft cantilever is used to ensure that the measureable deflection of the cantilever is much larger than the deformation of the tip and sample. However, if the cantilever has too low a spring constant, thermal fluctuations will lead to a noisy scan. The root

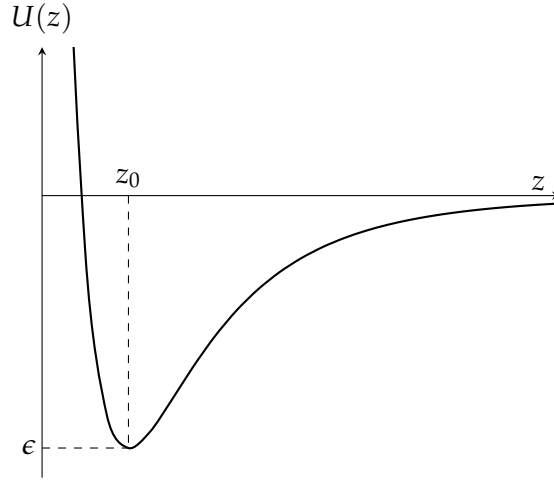


Figure 3.5 The Lennard-Jones potential described mathematically by $U(z) = \epsilon \left(z_0^{12}/z^{12} - 2z_0^6/z^6 \right)$ where ϵ is the depth of the energy well and z_0 is the point where the energy is at its minimum.

mean square of the thermal fluctuations, $\sqrt{\langle \delta z^2 \rangle}$, for a given spring constant and temperature can be calculated using the equivalence in Equation 3.6.

$$\sqrt{\langle \delta z^2 \rangle} = \sqrt{\frac{k_B T}{k}} \quad (3.6)$$

For soft cantilevers with spring constants of $\sim 0.1 \text{ N m}^{-1}$ at room temperature, this corresponds to thermal fluctuations of 0.2 nm which are not insignificant so generally higher k value cantilevers are required. Interpreting contact mode AFM images is relatively direct as the image is a map of the surface height profile, although changes in the surface chemistry can change the tip-surface interactions creating apparent height differences where there are none.⁴⁶

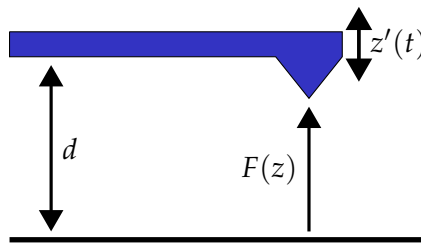


Figure 3.6 A driven cantilever at distance d experiencing a tip-surface force of $F(z)$ and undergoing oscillation $z'(t)$.

An alternative to static AFM is sinusoidal dynamic AFM (also called non-contact AFM). In the dynamic mode, cantilevers are driven by an external excitation at a

frequency ω , shown in Figure 3.6, so the system can be described by

$$m \frac{d^2 z}{dt^2} + \gamma \frac{dz}{dt} + k(z - d) = F(z) + F_0 \cos(\omega t) \quad (3.7)$$

where d is the undeflected tip-surface distance, and m and γ are constants relating to the mass and damping of the tip respectively. The free resonant frequency of the cantilever is given by $\omega = \sqrt{k/m}$. Without a driving force, the deflection matches that described by $F(z_0) = k(z_0 - d)$ where z_0 is defined as the static equilibrium position. If small oscillations around this position are considered, the time dependence of the system can be modelled so that $z \rightarrow z_0 + z'(t)$ which gives

$$F(z) \approx F(z_0) + z'(t) \frac{dF}{dz} + \dots \quad (3.8)$$

which can be substituted into Equation 3.7 and simplified to give

$$m \frac{d^2 z'}{dt^2} + \gamma \frac{dz'}{dt} + \left(k - \frac{dF}{dz} \right) z'(t) = F_0 \cos(\omega_0 t). \quad (3.9)$$

This equates to a system with a modified spring constant of $k_{eff} = k - dF/dz$ which leads to a modified resonant frequency of

$$\omega_0(z) = \sqrt{\frac{k_{eff}}{m}} = \sqrt{\frac{k}{m}} \sqrt{1 - \frac{1}{k} \frac{dF}{dz}} \approx \omega_0 - \frac{\omega_0}{2k} \frac{dF}{dz}. \quad (3.10)$$

This gives a shift in resonant frequency $\Delta\omega_0(z) \propto dF/dz$ in the limit $k \gg dF/dz$. These equations also show that in dynamic AFM the force gradient is measured not the force directly.

There are two dynamic AFM methods used to measure the force gradient: amplitude modulated (AM) and frequency modulated (FM). In AM-AFM, the cantilever tip is oscillated at ω_d , a fixed frequency near the resonant frequency. When the tip nears the surface, the presence of the tip-sample force field cause a change in the amplitude and the phase of the cantilever as shown in Figure 3.7. The oscillation amplitude is used as a feedback parameter to keep the tip-sample separation constant by altering the tip-sample separation with a piezoelectric. An important factor in

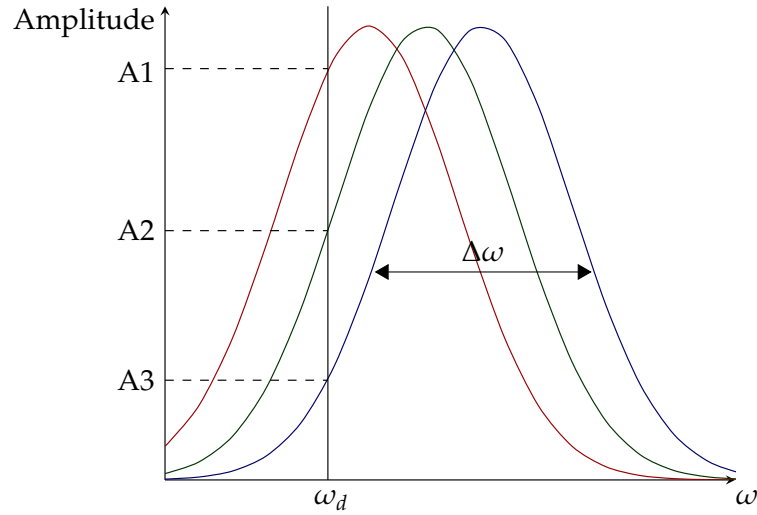


Figure 3.7 The frequency shift induces a change in oscillation amplitude. The amplitudes $A1$, $A2$ and $A3$ are measured at the drive frequency, ω_d , and allow the feedback loop to operate. The line $\Delta\omega$ is the full width at half maxima which relates to the Q factor of the cantilever.

AM-AFM is the quality factor, Q , defined for an oscillator by $Q = m\omega_0/\gamma$, which is approximated to be proportional to the width of the response curve as shown in Figure 3.7 according to $Q \approx \omega_0/\Delta\omega$. A large Q factor acts to increase the change in amplitude for a given dF/dz and typical silicon cantilevers have very high Q factors of 100-1000 in atmosphere. The disadvantage of a high Q factor is the response time. The timescale (τ) of the change in amplitude is determined by $\tau_{AM} \approx 2Q/f_0$.⁴⁶ The phase shift (ϕ) between the driving force and the tip oscillation can also be measured to give information on the material properties of the surface as described later in this section.

In FM-AFM, the cantilever is driven with fixed amplitude at its resonant frequency. The resonant frequency depends on the forces between the tip and surface so an image can be formed by scanning while maintaining a constant frequency shift.⁵³ The frequency is monitored by measuring the phase lag, $\phi(\omega)$, between the response and the driving term. The response of the cantilever is

$$z'(t) = z'_0(\omega) \cos(\omega t - \phi(\omega)) \quad (3.11)$$

where $z'_0(\omega)$ is the amplitude of oscillation. The frequency is then adjusted to ensure that $\omega = \omega_0 + C$ where C is a fixed constant. If the tip is being driven at the resonant

frequency, ω_0 , then $\phi = \pi/2$.⁵⁴ The timescale of response is quicker than for AM-AFM and is defined as $\tau_{FM} \approx 1/f_0$.⁴⁶

Another important aspect of AFM is phase, which can be measured concurrent to topography. Phase imaging can give a compositional or energy dissipation image of a heterogeneous material or provide a greater contrast image than a typical height image. The difference arises from the cause of the shift. The amplitude of oscillation depends on the topography and the composition of the surface whereas the phase shift signal depends on the energy transferred from the tip to the sample surface. There are two main theories regarding phase imaging AFM. The first theory holds where the steady-state oscillation of the tip can be described by

$$z(t) = z_0 + A \cos(\omega t - \phi) \quad (3.12)$$

which applies when a high Q factor tip is used with low adhesion forces between the tip and surface.⁵⁴ To maintain a steady oscillation, the energy per cycle supplied by the external excitation (E_{exc}) must equal the energy dissipated per cycle by the tip-surface forces (E_{dis}) and the damping in the scanning medium (E_{med}). When these are substituted, Equation 3.13 is produced.

$$\sin \phi = \frac{A\omega}{A_0\omega_0} \left(1 + \frac{E_{dis}}{E_{med}} \right) \quad (3.13)$$

Since the amplitude A remains constant in AM-AFM, changes to the phase shift ϕ reflect local changes in the mechanical energy transferred from the tip to the surface.⁵⁴ A complementary equation can be derived for the cosine of the phase. It can then be simplified to Equation 3.14 by assuming the tip is driven at the resonant frequency ω_0 and with an experimental observation that the mean deflection of the cantilever is negligible with respect to the oscillation amplitude.

$$\cos \phi \approx -\frac{2Q\langle F_{ts}z \rangle}{kAA_0} \quad (3.14)$$

For low Q values (<5), Equation 3.12 is not a valid description of tip motion as there are significant contributions from the higher harmonics and modes to the oscillation.⁵⁴ This means the other theory must be used to derive an analytical expression for the sine of the phase shift which shows a relationship between the phase shift and the energy dissipated per cycle as well as with the amplitude of the higher harmonics. This means that whenever the amplitudes of the higher harmonics is not negligible with respect to the primary oscillation, the phase shift is related to dissipative forces such as surface adhesion hysteresis and the viscoelasticity of the surface making the images more complex to analyse.

Instrumentation

An AFM usually consists of optical elements contained within a closed head unit and the sample is mounted on an xyz -stage in the base unit. The cantilever tip is usually mounted on alignment screws just above the sample on the base unit. The optical elements include a viewing-window (usually a camera connected to a computer), a laser diode with connected mirrors, and a four-quadrant positional photodetector. This set up is shown in Figure 3.8.

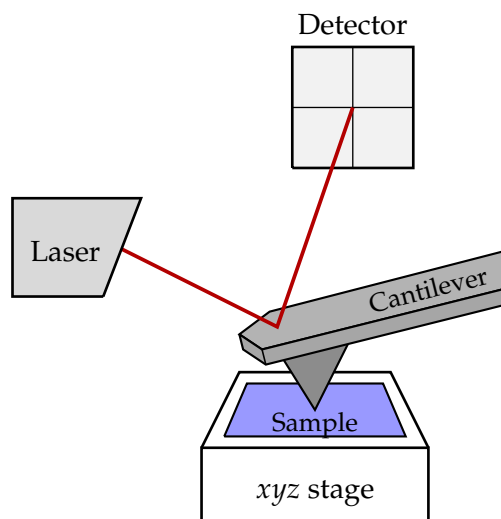


Figure 3.8 The general structure of the AFM instrument.

The force between the tip and surface is recorded by measuring the cantilever deflection, which depends on the spring constant k of the cantilever and the magnitude of the force between the tip and surface. There are two commonly used methods for

measuring the cantilever deflection. Firstly, there is reflection of laser light off the back of the cantilever onto a photodetector as shown in Figure 3.8. The photodetector typically has four quadrants which act independently and are positioned so the initial position of the photodetector has equal signal in each quadrant. The cantilever deflection is then measured as a difference in the signal from the four quadrants. This has the effect of multiplying the signal: for a cantilever of $100\text{ }\mu\text{m}$ to $200\text{ }\mu\text{m}$, the magnification factor is 750 to 1500 which means deflections of less than 0.1 nm can be detected. This method also has a relatively low signal-to-noise ratio.⁴⁸ The second method involves positioning an optical fibre above the cantilever. The light then undergoes a partial reflection at the glass/air interface then a reflection from the cantilever surface. These beams interfere as in a Michelson-Morley interferometer giving rise to an overall reflected intensity which depends on the fibre-cantilever separation.

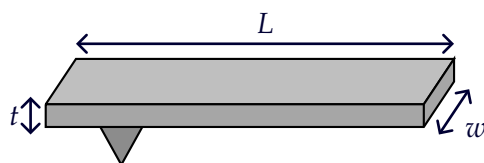


Figure 3.9 The structure and labelled dimensions of a rectangular AFM cantilever.

The most common probe type is a simple beam or cantilever with a sharp tip at one end and fixed at the other end. This structure is shown in Figure 3.9. The force between the tip and surface results in a deflection δz according to Hooke's law. The spring constant k of the cantilever is defined by $k = Ywt^3/4L^3$ where Y is the Young's modulus of the material. Most AFM cantilevers are micro-machined from silicon crystals with typical parameters: length (L) 10 to $100\text{ }\mu\text{m}$, width (w) 10 to $50\text{ }\mu\text{m}$, and radius of tip 5 to 30 nm . The spring constant of such cantilevers vary from 0.1 to 100 N m^{-1} . A typical van der Waals interaction of 10 pN would give a beam deflection of $\sim 10^{-10}\text{ m}$ for a soft cantilever.

3.2 X-Ray Photoelectron Spectroscopy

X-ray photoelectron spectroscopy (XPS) is a surface-sensitive technique that measures the elemental composition of a surface. It is also referred to as electron spectroscopy for chemical analysis (ESCA) although, as this does not adequately describe the technique, the term XPS will be used in this thesis. XPS involves irradiating a material with a beam of X-rays then measuring the kinetic energy and number of electrons that leave the surface.

3.2.1 Theory

The energy of a photon is given by the relation $E = h\nu$ where h is the Planck constant and ν is the frequency of the radiation. An atom is excited by the absorption of an excitation photon leading to ionisation and the emission of a core shell electron. The process of photoionisation can be considered as



Conservation of energy requires that

$$E_A + h\nu = E_{A^+} + E_{e^-} . \quad (3.16)$$

If the energy of the photoelectron is solely in the form of kinetic energy (KE), Equation 3.16 can be rearranged to give an expression for the KE.

$$KE = h\nu - (E_{A^+} - E_A) \quad (3.17)$$

The term $(E_{A^+} - E_A)$ is called the binding energy (BE) of the electron within the atom. This means that the KE of the electron can also be expressed as

$$KE = h\nu - BE. \quad (3.18)$$

A representation of this showing the electron being excited from a ground state into the vacuum state is shown in Figure 3.10.

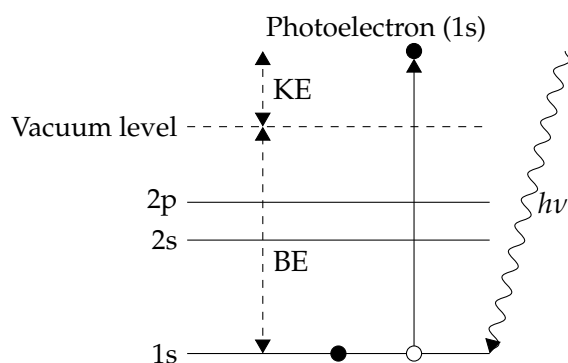


Figure 3.10 A schematic diagram of photoemission from a 1s orbital.

For every element, there is a characteristic binding energy associated with each atomic orbital so each element gives rise to a characteristic set of peaks at kinetic energies determined by Equation 3.18. This means that it can be shown that a sample contains a specific element by identifying the presence of known peaks for that element. Additionally, any changes in the binding energy and therefore the chemical environment of an atom can be observed at high resolution.⁵⁵

Emission from all levels with orbital angular momentum, l , greater than one does not give rise to a single peak; instead a closely spaced doublet is seen. The two states are different in energy because the unpaired electron left in an orbital after photoionisation can have spin and orbital angular momentum vectors parallel or anti-parallel.⁵⁶ This is known as spin-orbit coupling. The difference in energy between the peaks increases with atomic number for a given subshell and decreases with larger orbital angular momentum for constant principal quantum number n . The doublet peaks will have specific area ratios based on the number of different spin combinations that can give rise to the total spin. Thus the area ratio is 1:2 for the p-shell, 2:3 for the d-shell, and 3:4 for the f-shell.

The intensity of the observed peaks is related to the concentration of the elements within the sample. While in theory the surface concentration of an element can be calculated, in practice the method of relative sensitivity factors is used. This is because the relative intensity of different peaks depends on several factors including

the concentration, the probability of emission, the inelastic mean free path of electrons, and the efficiency of the spectrometer for the given kinetic energy. By determining the ratio of peaks within a single spectrum, the IMFP and the instrumental factors can be ignored and the relative concentrations of two elements A and B may be obtained using:

$$\frac{C_A}{C_B} = \frac{I_A}{I_B} \cdot \frac{\sigma_B}{\sigma_A} \quad (3.19)$$

where C_A and C_B are the concentrations of A and B , I_A and I_B are the peak areas for the core levels of A and B , and σ_A and σ_B are the photoemission cross-sections of the core level of A and B .⁵⁵ This means that either the concentration of one of the elements at the surface can be calculated if the other is known or the ratio between the two can be found.

As well as the main peaks due to core shell electron emission, Auger peaks are seen in the spectra. These peaks are due to the decay of a more energetic electron to fill the vacant hole created by the X-ray photon which makes available an energy equal to the difference in binding energy between the core hole and the electron that has filled it. This energy can either be released as a photon or through transfer to a third electron which can then escape into the vacuum with a kinetic energy related to the available energy caused by the electron decay. This process is shown in Figure 3.11. Unlike the photoelectron peaks, the kinetic energy of the Auger peaks is independent of the photon energy of the X-ray source.

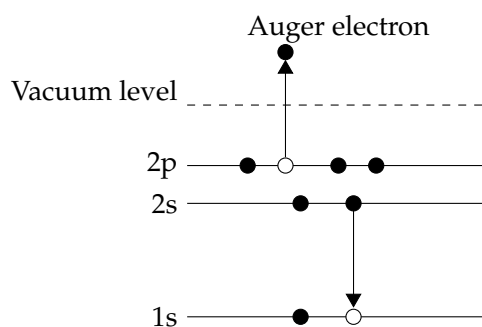


Figure 3.11 A diagram of an example Auger decay. An electron from the 2s shell decays into the hole formed by the XPS photoemission then an electron from a higher shell gains energy from this decay and is emitted.⁵⁵

XPS is surface sensitive if photoelectrons with the correct energy are used. This is because an electron with kinetic energy E moving through a solid matrix M has a specific probability of travelling a certain distance before losing all or part of its energy as a result of inelastic collisions. The average distance travelled before an inelastic collision is called the inelastic mean free path (IMFP, $\lambda_M(E)$). For the energy ranges typically used in XPS of 250 eV to 1500 eV, $\lambda_M(E)$ ranges from four to eight monolayers meaning electrons must originate in the top layers of a surface in order to be detected.

3.2.2 Spectroscopic and X-ray Notation

There are two different notations used in XPS: spectroscopic notation – used for the XPS spectra and X-ray notation – used for the excitation X-rays. The two are equivalent and based on the j-j coupling scheme. The j-j coupling scheme describes the orbital motion of an electron in which the total angular momentum is found by summing the individual electron spin (quantum number s) and angular momentum (quantum number l). This means that the total angular momentum (quantum number j) is given by $j = l + s$. Since l can take the values 0, 1, 2, and 3 and $s = \pm 1/2$, the total angular momentum is $j = 1/2, 3/2, 5/2$, etc. The other important quantum number is the principal quantum number n which has the values 1, 2, 3, 4, and so on.⁵⁷

In spectroscopic notation, states are defined first by their principal quantum number n then with the l state designated as s ($l = 0$), p ($l = 1$), d ($l = 2$), or f ($l = 3$). The j state is then added as a subscript. Therefore the states are: 1s, 2s, 2p_{1/2}, 2p_{3/2}, 3s, 3p_{1/2}, 3p_{3/2}, etc.

In X-ray notation, states are defined by the principal quantum number n designated as K ($n = 1$), L ($n = 2$), M ($n = 3$), N ($n = 4$), etc and then assigned a subscript for the combination of l and j . These are shown with their spectroscopic equivalent in Table 3.1.

3.2.3 Instrumentation

XPS is often carried out in an UHV chamber with a background pressure of the order 10^{-8} Pa. The UHV requirements mean that the system needs to be constructed from a

Quantum Numbers				Spectroscopic State	X-ray State
n	l	s	j		
1	0	$\pm 1/2$	$1/2$	1s	K ₁
2	0	$\pm 1/2$	$1/2$	2s	L ₁
2	1	$-1/2$	$1/2$	2p _{1/2}	L ₂
2	1	$+1/2$	$3/2$	2p _{3/2}	L ₃
3	0	$\pm 1/2$	$1/2$	3s	M ₁
3	1	$-1/2$	$1/2$	3p _{1/2}	M ₂
3	1	$+1/2$	$3/2$	3p _{3/2}	M ₃
3	2	$-1/2$	$3/2$	3d _{3/2}	M ₄
3	2	$+1/2$	$5/2$	3d _{5/2}	M ₅

Table 3.1 Spectroscopic and X-ray notations for the first nine states.⁵⁷

bakeable material such as stainless steel with metal, usually copper, seals. An example system is shown in Figure 3.12.

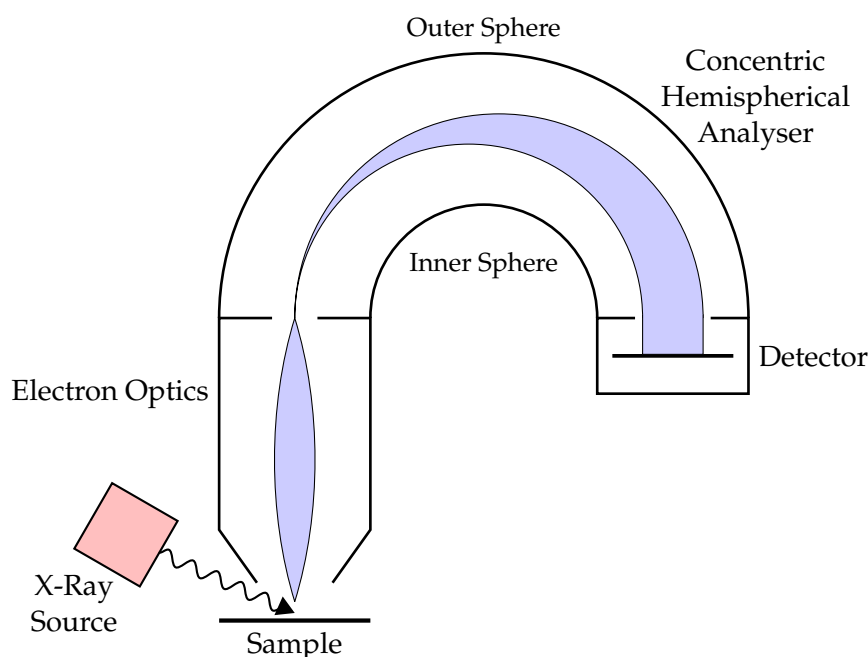


Figure 3.12 The layout of a laboratory XPS instrument.

In a laboratory-based system, a source of fixed-energy radiation is used as the X-ray source. The most important factor when choosing an X-ray source is the energy resolution. The energy spread (linewidth) of a core level electron is very small so the linewidth of the source is the determining factor for the observed spectral linewidth, assuming no broadening is introduced by the system. In order to identify elements, a linewidth of less than 1 eV is needed. The source material also needs to be a good thermal conductor for rapid heat removal and must be compatible with UHV. Given

these requirements, the most common X-ray sources are Mg K_α ($h\nu = 1253.6$ eV) and Al K_α ($h\nu = 1486.6$ eV).⁵⁸ These give emitted photoelectrons with kinetic energies of less than 1253.6 eV and 1486.6 eV and have linewidths of 0.70 eV and 0.85 eV respectively. These metals can be used as simple anodes. For efficient production of X-rays via electron bombardment, the exciting electron energies need to be an order of magnitude higher than the line energies. In Mg and Al sources, accelerating potentials of 15 eV are used. The optimum flux at the sample surface which gives the peak sensitivity in the spectra is obtained when the source anode is very close (≈ 2 cm). In order to protect the sample from stray electrons and from heating effects from the anode, a thin window is used between the anode and the sample, and the anode is placed on a retractable arm.

The X-rays emitted by Mg and Al sources are complex. The principal K_α lines are doublets and other satellite peaks are present. Monochromatisation is used to separate the K_α doublet and remove the satellite peaks along with removing the Bremsstrahlung background. This reduces the photon flux on the sample but gives a cleaner spectra with a better signal to noise ratio. Use of a monochromator also allows for the possibility of raster scanning a sample by directing the beam.⁵⁸

The emitted electrons are analysed in an electron energy analyser which can disperse the emitted electrons according to their kinetic energy. There are many different designs of electron energy analysers but, for photoemission experiments, the preferred design is a concentric hemispherical analyser (CHA) as shown in Figure 3.12. The energy analyser strongly influences the resolution of the spectra. The absolute resolution (ΔE) is the FWHM of a specific peak and the relative resolution (R) is defined as the ratio of the FWHM to the peak energy position ($R = \Delta E/E$). XPS requires that ΔE is constant at all energies such that closely spaced peaks at any energy can be resolved.⁵⁵

The CHA works by passing electrons between two hemispheres of radii r_1 (inner) and r_2 (outer) that have potentials $-V_1$ and $-V_2$ applied respectively where $V_2 > V_1$. The equipotential surface between the two hemispheres has a radius of r_0 and $\delta\alpha$ is the angular spread of the electrons away from the equipotential surface. The relative resolution for a system under these conditions is given in Equation 3.20, where w is the

width of the entrance and exit slits.

$$\frac{\Delta E}{E} = \frac{w}{2r_0} + (\delta\alpha)^2 \quad (3.20)$$

This equation also explains why the electrons are decelerated to a constant energy, the pass energy, before entering the entrance slit. If the electrons were not slowed, to obtain a resolution of 1 eV at the maximum kinetic energy for a Al K_α source of 1500 eV, a CHA with a slit size of 2 mm would need a radius of about 300 cm. However, with the common pass energies of 20 eV to 100 eV, the required radius is only 10 cm to 15 cm.⁵⁸

3.3 Secondary Ion Mass Spectrometry

Mass spectrometry is an analytical technique that measures the mass-to-charge (m/z) ratio of ions to identify the chemical species present. Secondary ion mass spectrometry (SIMS) is a type of static mass spectrometry that uses a primary ion beam to ionise surface molecules of a material then a mass analyser to separate the ions according to their m/z .

3.3.1 Theory

Mass spectrometry relies on the production of gas-phase ions of the compound to be studied. In SIMS, this is done with an ion beam which ionises surface molecules according to Equation 3.21.⁵⁹



The molecular ion A^+ can undergo fragmentation and these fragments can also undergo further fragmentation. The mass spectrometer detects the abundance of these ions and ion fragments to produce a mass spectrum. From the m/z , the mass of the ions can be calculated hence the mass of the original molecule can be found. The fragmentation pattern can also provide evidence for the structure of the molecule which can also be used to identify the structure of the original molecule.

In SIMS, the ionisation occurs at, or close to, the emission of the particles from the surface so the substrate and bulk material participate in the electronic processes involved. This means that the yield of ions is strongly influenced by the substrate. The current, as measured for a secondary ion m , depends on many factors as set out in Equation 3.22 where I_p is the primary particle flux, Y_m is the sputter yield, α^+ is the probability of forming positive ions, θ_m is the fractional concentration of m in the surface layer, and η is the transmission rate of the system.⁶⁰

$$I_m = I_p Y_m \alpha^+ \theta_m \eta \quad (3.22)$$

The sputter yield, Y_m , is the total yield of both neutral and ionic sputtered particles of species m per primary ion impact. This increases linearly with flux, I_p , and increases non-linearly with primary particle mass, charge, and energy. It is also affected by the crystallinity and topography of surface. The energy threshold for sputtering of the surface to begin is between 20 eV and 40 eV with the maximum yield generally occurring at 5 keV to 50 keV.⁶⁰ At higher energies, the beam penetrates into the bulk causing less energy to return to the surface and reducing the surface sensitivity of the technique. Sputtering also causes damage to the surface, particularly for organic material, making it difficult to measure the sputter rate. Under sputtering, molecules can have electrons removed and can fragment. Polymeric materials can break down into monomeric units or smaller polymeric chains.

Secondary ion formation is influenced by electron exchange process between the surface and the departing species, therefore the electronic state of the surface is important to consider. For organic molecules, secondary ion formation can occur via a number of mechanisms: ejection of an electron to form an ion M^+ ; undergoing acid–base reactions to form $[M + H]^+$ or $[M - H]^-$; or by cationisation or anionisation.⁶⁰

Surface charging occurs when samples are insulating and the charge is unable to dissipate. When a sample surface is bombarded with a positive ion beam, the potential of the surface rises due to the input of positive charge and the emission of secondary electrons. This results in the loss of the SIMS spectrum. There are two possible solutions: use a neutral beam or counter-charge the surface. The use of a neutral beam is known as fast atom bombardment. Counter-charging the surface is more applicable for the SIMS technique and can be done via two methods. The first method consists of irradiating the surface with a beam of relatively low energy electrons. This technique works well for positive-ion SIMS but can give rise to sample degradation and electron stimulated ion emission. In the alternative counter-charging method a metal grid is placed in close electrical contact with the sample to allow the surface potential to disperse.⁶⁰

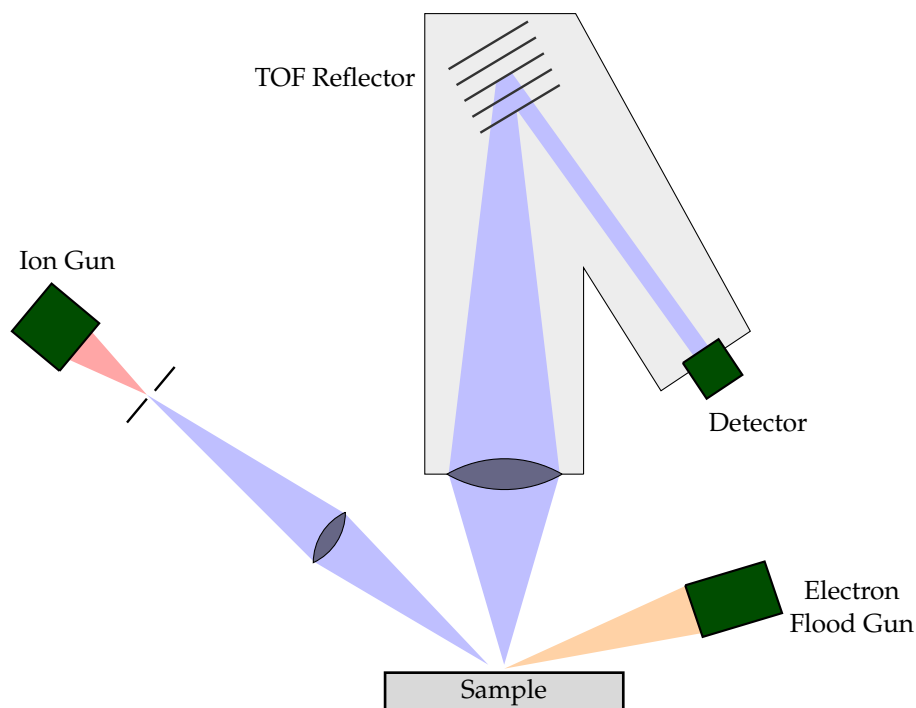


Figure 3.13 A diagram of the ToF-SIMS set up.

3.3.2 Instrumentation

SIMS typically involves ionising a beam of argon, xenon, bismuth or C_{60} clusters and accelerating them towards the sample surface. These ions then cause secondary ionisation of surface molecules. The primary ion beam can also be used to sputter the surface to give a depth profile or raster scanned across the surface to give 2D and 3D m/z data. The secondary ions from the surface are then accelerated into a mass analyser. A basic experimental set-up for a ToF-SIMS instrument is shown in Figure 3.13.

For time-of-flight (ToF) analysis, the secondary ions from the surface are then accelerated towards the ToF flight tube by a potential difference between an electrode and an extraction grid held in front of the sample. As the acceleration gives all ions approximately the same kinetic energy, the velocity of an ion is dependent on the charge to mass ratio, m/z . The detector arrival times are therefore also proportional to m/z . The m/z of the ions can be calculated according to

$$\frac{m}{z} = \frac{2t^2eV_s}{L^2} \quad (3.23)$$

where t is the arrival time at the detector, L is the path length of the ions in a field-free space, and V_s is the potential difference in the acceleration region. By calibrating the data using standard peaks, the molecular composition can be predicted from the m/z spectrum. In theory, there is no upper mass limit for TOF mass spectrometry and the technique is extremely surface sensitive with the correct parameters.⁶¹

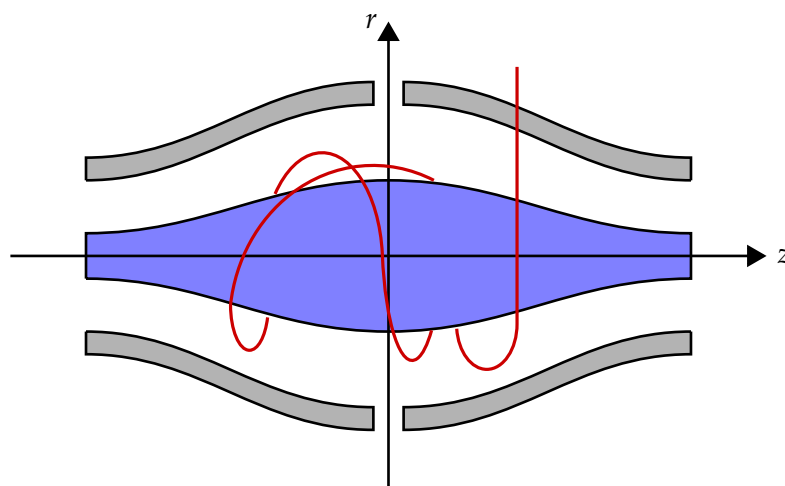


Figure 3.14 A diagram of the orbitrap mass analyser with the red line showing a possible path for the ions.

An alternative to the time-of-flight analyser is the orbitrap analyser. The orbitrap is an electrostatic ion trap as shown in Figure 3.14. The trap consists of an external barrel shaped electrode split at the centre and a central spindle shaped electrode. Ions are injected into the orbitrap with kinetic energy of several keV and oscillate around the central spindle in a complex helix under the influence of a quadro-logarithmic potential. Instead of separating ions along the path length and associating the time taken to travel to the m/z , the m/z is connected to the frequency of oscillation according to Equation 3.24 where k is the field curvature, which shows that the frequency is independent of the kinetic energy of the injected ions.⁵⁹

$$\omega = \sqrt{\frac{ze}{m}}k \quad (3.24)$$

The current induced by the oscillating ions is measured and converted by a Fourier transform to the individual ion frequencies and intensities to give the mass spectrum. As it is the ion current that is detected rather than the time taken for an ion to reach

a detection plate, the same ion can be measured multiple times which increases the resolution. As a single measurement is made to measure all of the ions generated, the signal-to-noise ratio is improved.

The main benefit of using an orbitrap compared to a time-of-flight analyser is the resolution. The orbitrap can achieve FWHM resolutions of up to 100000 at 1000 m/z compared to a TOF reflectron which can generally only achieve resolutions of 20000 at 1000 m/z .⁵⁹ The increase in resolution also allows isotopic fine structure to be investigated, although this technique is not used in this thesis.

3.4 Transmission Electron Microscopy

Transmission electron microscopy (TEM) is a technique that involves passing a beam of electrons through an electron transparent sample. As these electrons pass through the sample there are several possible outcomes for the electrons: if there is no interaction with the sample atoms the electrons remain undeflected; if there are interactions but no energy transfer the electrons are deflected by elastic scattering; if there are interactions involving energy transfer the electrons are deflected by inelastic scattering. TEM images are formed by separating these different electrons using an aperture to stop all electrons deflected by more than 0.5° .⁶²

3.4.1 Theory

The behaviour of the TEM beam can be broken down into the behaviour of individual electrons with the electron clouds of atoms in the sample. In scattering, an electron penetrating into the electron cloud of another atom is attracted by the positive potential of the nucleus and deflects towards the core. The coulombic force F between the nucleus and the electron is defined by

$$F = \frac{Q_1 Q_2}{4\pi\epsilon_0 r^2} \quad (3.25)$$

where r is the distance between the two charges Q_1 and Q_2 and ϵ_0 is the dielectric constant. The closer the electron comes to the nucleus, the larger the force is and the larger the scattering angle as shown in Figure 3.15. In some cases the force is large enough to lead to complete backscattering, generating back-scattered electrons (BSE). The force F depends on the charge of the nucleus hence the Coulomb force increases with increasing atomic number Z .

In reality, an electron passing through a sample interacts with many different atoms. The chance that an electron is scattered by the sample can be described by the probability of a scattering event determined by the interaction cross-section σ . The total interaction cross-section is a sum of the elastic σ_{elas} and the inelastic interactions $\sigma_{inelast}$. For each interaction the cross-section can be defined using an effective radius r

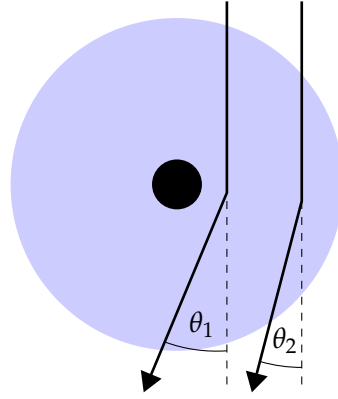


Figure 3.15 The closer the electrons come to atomic nuclei in the sample, the greater the angle of deflection.

to be $\sigma = \pi r^2$. For elastic scattering r_{elast} is defined as

$$r_{elast} = \frac{Ze}{U\Theta} \quad (3.26)$$

where Z is the atomic number, U is the electron beam potential and Θ is the scattering angle.¹⁷ This equation indicates that scattering is stronger for heavier atoms and that electrons scatter less at high voltages. A total scattering interaction cross-section Q_T can be calculated by considering that a sample contains N atoms per unit volume which gives

$$Q_T = N\sigma = \frac{N_A \sigma_T \rho}{A} \quad (3.27)$$

where N_A is the Avogadro number, A is the atomic mass and ρ is the density. The equation shows that doubling the density doubles Q_T . Another method to describe the interactions is by the mean free path λ_{mfp} which is the average distance that an electron travels between interactions and is related to the scattering cross-section by

$$\lambda_{mfp} = \frac{l}{Q_T}. \quad (3.28)$$

The probability p of scattering in a sample of thickness t is then defined by

$$p = \frac{t}{\lambda_{mfp}} = Q_T t. \quad (3.29)$$

This electron scattering model can explain the basic contrast mechanisms in TEM. Due to the increasing Coulomb force with atomic number, areas of the sample with heavy atoms will appear darker than areas of light atoms. Also, the probability of scattering depends on the sample thickness as shown above, therefore thicker areas appear darker than thin areas for the same material. These two effects are called mass-thickness contrast.

Generally, the scattering centres in a sample are arranged in an irregular way, especially in amorphous materials. If a sample is crystalline then coherent scattering takes place. Since the spacing between scattering centres in a crystal is regular, constructive interference of the scattered electrons can occur in certain directions to generate diffracted beams. This is known as Bragg diffraction. The conditions needed for constructive interference for electron waves diffracted at parallel lattice planes are described by the Bragg equation (Equation 3.30) where d is the distance between lattice planes, θ is the angle of incidence to the surface, λ is the wavelength of the beam, and n is a positive integer.

$$2d \sin \theta = n\lambda. \quad (3.30)$$

Each set of parallel lattice planes that occur in the crystal give rise to two spots in the diffraction pattern with a distance between them that is in reciprocal relation to that in real space. If a polycrystalline sample is observed where more than one crystal of a phase contributes, the diffraction patterns of all crystals are superimposed. This gives rise to a ring pattern.

Electron microscopy is associated with modification of the sample by the electron beam; this often limits the information about the sample that can be obtained. There are several different forms that sample damage can take. Phonons can be generated within the sample by the absorption of energy from the beam. This is equivalent to heating the sample so can be minimised by cooling the sample. The beam can also ionise atoms in the material which can cause the breaking of chemical bonds. Incoming electrons can also transfer large amounts of energy to an atom in a crystal lattice which can displace it to leave a Frenkel defect. This is common in metals. Finally electrons can be absorbed into the material. In conductive samples this charge is transported away but in non-

conductive samples it can lead to vibrations, drift and other effects that limit or prevent imaging.

3.4.2 Instrumentation

Many constituent parts in a TEM are analogous to the parts in an optical microscope as the basic principles of imaging apply to both; an important difference is that electron microscopy must be carried out in vacuum to remove the interactions between electrons and the air. The basics of instrumentation is shown in Figure 3.16.

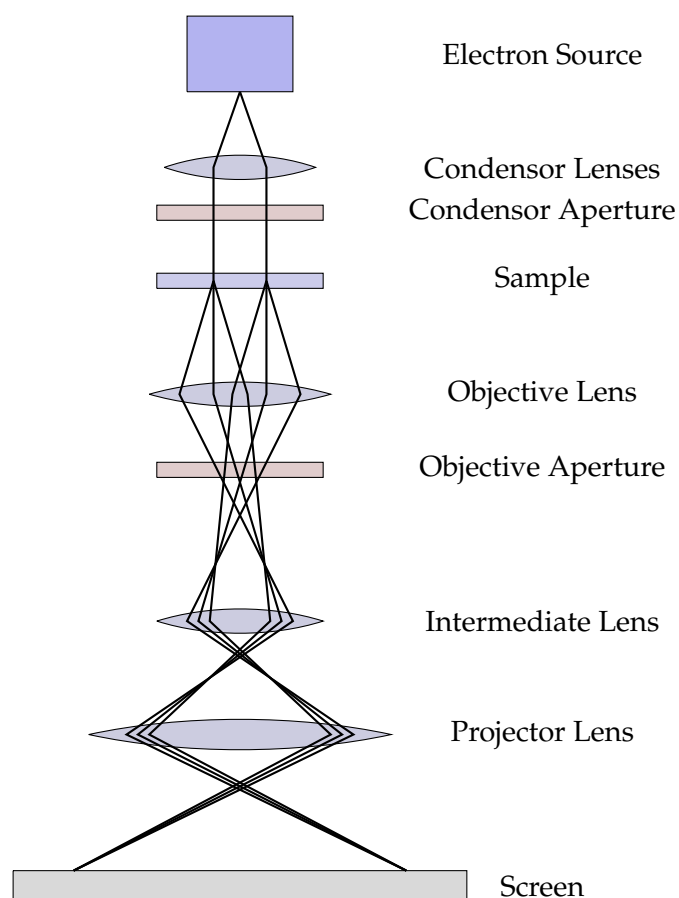


Figure 3.16 A diagram of the basic TEM instrumentation for imaging.

The TEM equivalent to a light source is an electron gun which consists of a cathode, usually a thin tungsten wire, to which an emission current is applied and a cathode cap (Wehnelt cylinder) to which an accelerating voltage is applied. There are a wide range of accelerating voltages that can be used from 40 kV to 120 kV. At high accelerating voltages there are more electrons with short wavelengths giving a brighter image, higher resolution, and greater penetration of the specimen but lower

amplitude contrast. This means that a compromise has to be made between contrast and resolution.⁶² Below the electron gun there is an anode plate which has a small hole through which the electrons are accelerated. This electron beam then passes through electromagnetic converging lenses made of tightly wound coils of copper wire. The condenser lens gathers the electrons and focuses them onto the specimen in the area of interest; this controls how strongly the beam is focused onto the specimen. The focal length of the lens, f , is determined by the field strength in the coil with

$$f = k \left(\frac{V}{I^2} \right) \quad (3.31)$$

where k is a constant based on geometry and number of turns in the coil, V is the accelerating voltage, and I is the current through the coil. A condenser aperture can be used to reduce spherical aberration. The objective lens is used to focus and as an initial magnifier and an objective aperture can be used to enhance specimen contrast. Other lenses can be used to further magnify the image before the projector lens which magnifies and projects the image onto the phosphorescent screen.⁶²

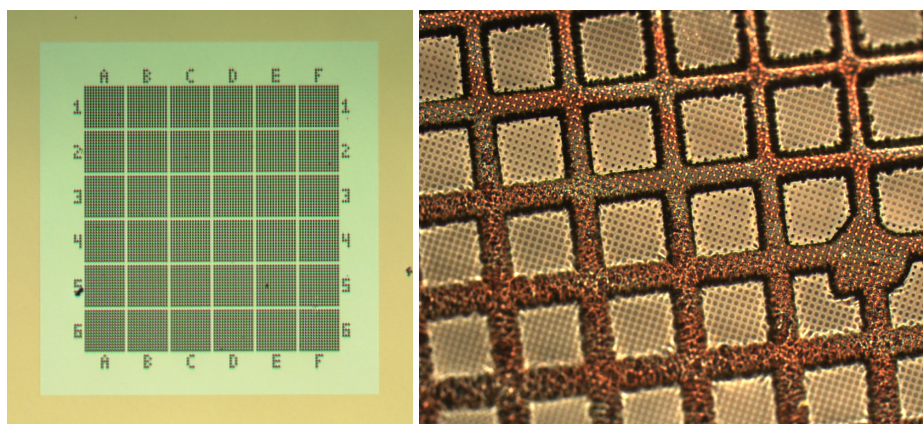


Figure 3.17 Optical microscope images of TEM Grids: (left) a silicon nitride grid and (right) a graphene on Quantifoil gold supported on a copper grid.

In order to be electron transparent a sample must be less than 200 nm thick otherwise all electrons are deflected. This means that thin samples are generally supported on grids made from metals or silicon nitride containing small holes that allow the electrons to pass through. Optical microscope images of two TEM grids are shown in Figure 3.17.

3.5 Deposition of Molecules

There are several methods that can be used to deposit molecules onto surfaces. The method must be chosen for the given combination of molecule and surface with many properties to be taken into account including the required coverage, volatility of molecules, and adhesion to the surface.

The bonding of molecules (adsorbates) to surfaces can be broadly classified as either physisorption or chemisorption. Chemisorption is characterised by an exchange of electrons between the molecule and the surface and is hence defined using the conventional classification into covalent, ionic, and metallic bonding. Physisorption is a much weaker adsorption that is associated with van der Waals interactions. Due to the lower energy of physisorbed systems, the adsorbate layer is always in equilibrium with molecules in the gas phase.⁵⁵

The probability of a molecule being associatively adsorbed is defined as the sticking probability, S .

$$S = \frac{\text{rate of adsorption of molecules by surface}}{\text{rate of incidence of molecules onto the surface}} \quad (3.32)$$

From this, it can be seen that both the surface and molecule as well as environmental factors will affect the sticking probability. The rate of collision of molecules with the surface can be changed by changing the environment in which the deposition takes place.

3.5.1 Vacuum Deposition of Molecules

Ultra-high vacuum (UHV) is commonly used in the sublimation of molecules onto surfaces. UHV is characterised by a pressure lower than 10^{-9} mbar. At this pressure, the mean free path (average distance a molecule moves before hitting another particle) is approximately 50 km, compared to approximately 64 nm at atmospheric pressure.⁶³ This means that a molecule sublimed inside the chamber has a high chance of moving ballistically to the sample surface. In UHV, the gases present in the system originate from the inner surfaces of the chamber when they diffuse out of or permeate through

the materials or by release from the UHV pumps themselves. This environment allows for thin layers of materials, including volatile materials, to be deposited. It also allows for reactive surfaces and molecules to be used, especially ones that would oxidise under ambient or liquid conditions.

Another use of UHV is in cleaning substrates prior to deposition. In UHV, this can be done by either heating the surface to remove contaminants or by sputtering the surface. Sputtering is used in conjunction with annealing for metal surfaces to restructure the surface into the required arrangement.

3.5.2 Solution Deposition of Molecules

Molecules can also be deposited from solution. Solution deposition offers an alternative deposition method, particularly for molecules which decompose when heated to sublimation point. There are two common solution deposition methods: drop-casting consists of placing a drop of solution onto the required surface and evaporating the solvent so requires a volatile solvent; immersion of the substrate into the solution can be used for less volatile solvents as the surface is generally dried with nitrogen post-immersion.

3.6 Sample Preparation Methods

3.6.1 Substrate Exfoliation

Exfoliation of hBN was used to create thin flakes that could be deposited onto various substrates. In the work described in this thesis, a commercial silicon sample with a 300 nm thick layer of thermally grown SiO_2 was cut into small squares to provide supporting substrates. Boron nitride flakes (grown at high pressure by Taniguchi and Watanabe⁶⁴) were then deposited using the Scotch tape method as shown in Figure 3.18. In this process, hBN flakes are placed onto tape then the tape is repeatedly folded over on itself and peeled apart until it is thinly covered with hBN. The tape was then placed onto the silicon samples, rubbed manually to ensure transfer of the hBN flakes, and peeled up slowly. The silicon samples were cleaned in toluene for up to

twelve hours to remove the glue from the tape. Finally the samples were heated in a furnace to 400 °C in an atmosphere of hydrogen and argon (5% : 95%) for 8 h.

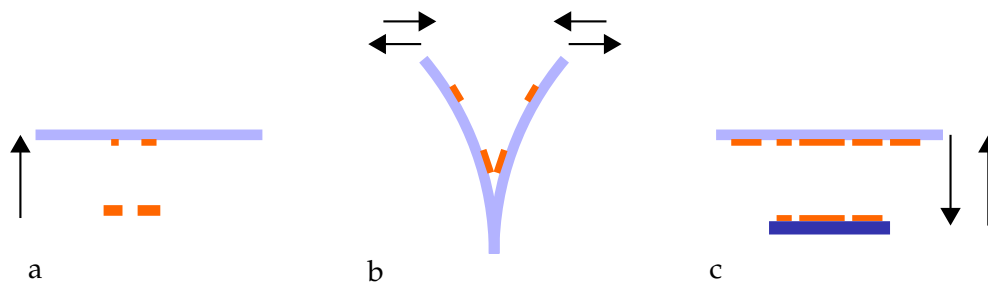


Figure 3.18 The exfoliation process for depositing hBN: (a) scotch tape picks up small hBN crystals; (b) the tape is separated repeatedly until the tape is covered; (c) the tape is pressed against a silicon sample then slowly peeled off to leave hBN flakes on the surface.

Graphite samples were also prepared using Scotch tape. However, for these samples, the top layer of highly ordered pyrolytic graphite was removed using the tape to leave a pristine surface on the bulk. No further cleaning or heating processes were required for these samples.

3.6.2 Vacuum Sublimation

Melamine and other molecules were deposited in vacuum from a Knudsen cell. A vacuum chamber held at a pressure of approximately 5×10^{-7} mbar was used to carry out the depositions. The sample holder was outgassed by heating to 400 °C for 1 h. This step was repeated each time a new sample entered the system. A hBN/SiO₂ sample, prepared as described in Subsection 3.6.1, was inserted into the system which was then pumped down to $\sim 5 \times 10^{-7}$ mbar. The sample was then heated to approximately 400 °C for 1 h to remove any remaining contaminants.

The source material was placed in a Knudsen cell and initially annealed to outgas any water or other reactive species present. This temperature was determined with consideration of the sublimation temperature of the particular source material. For the depositions, the Knudsen cell was heated to the required sublimation temperature and a shutter was used to control the amount of material reaching the sample surface. To measure the rate of deposition and determine the required exposure time, a quartz

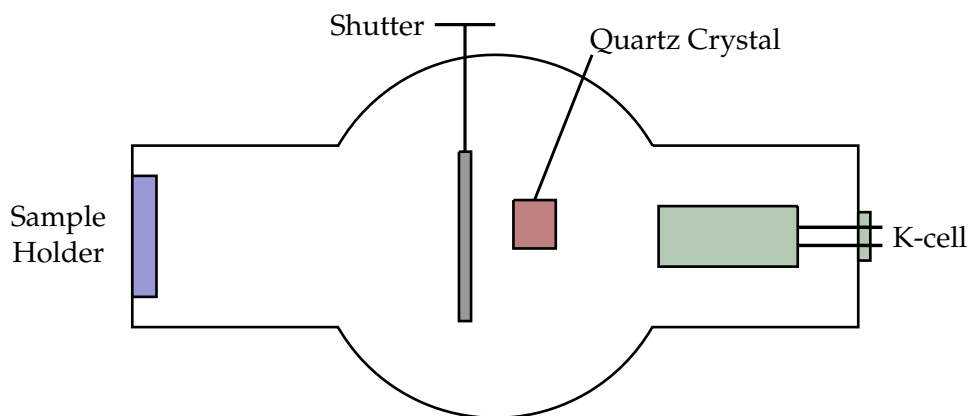


Figure 3.19 Vacuum chamber used for deposition with a single k-cell and a sample holder with the ability to indirectly heat the sample.

crystal thickness monitor was used. A modified sublimation method was used to deposit the porphyrin molecules which is discussed in depth in Section 6.2.

3.6.3 Solution Deposition of Molecules

Prior to solution deposition the substrates were prepared as described in Subsection 3.6.1. The hBN/SiO₂ substrates were flame annealed and cooled with nitrogen directly before to deposition. The solutions were prepared in either toluene or toluene with 1% pyridine to the required concentration. Either drop deposition or submersion was used to deposit the molecules from the solution. For drop deposition, a Pasteur pipette was used to deposit enough solution to cover the substrate surface and the sample was then left to allow the solvent to evaporate. In the submersion method, the substrate was left in the solution for the required period of time which was dependent on the molecule, solvent, and concentration before being removed and quickly dried with nitrogen.

3.7 Instrumentation

3.7.1 AFM Systems

The majority of the AFM work was carried out in ambient on an Asylum Research Cypher-S AFM which is shown in Figure 3.20. The instrument was set up as described below for all ambient samples. First, the sample was placed into the sample mount.

Then, a commercially available silicon cantilever (Multi75AL-G silicon cantilever from Budget Sensors) was placed in a holder in contact with a piezo to oscillate the tip, which was then mounted in the instrument head. The cantilever head was brought into close proximity to the sample by eye before the laser spot was aligned and the deflection was zeroed. The resonant frequency was found by sweeping a range of frequencies close to the predicted resonance. Once driven near the resonant frequency, the tip was coarsely approached and the z-piezo was extended until the set-point was reached. The tip then raster-scanned the surface to acquire images.

Additionally a vacuum AFM system (Omicron VT) with a base pressure of 1×10^{-9} mbar was used to image one of the TIPB samples. The tip was prepared slightly differently as the tip was used for both AFM and STM so could be improved as described below in Subsection 3.7.2. The sample mount matched that shown for STM in Figure 3.21 (b).

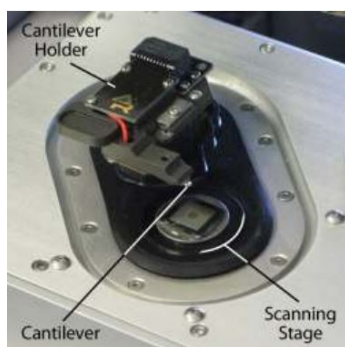


Figure 3.20 The sample and cantilever mount for the Cypher-S AFM. Adapted from reference 65.

3.7.2 STM Systems

The STM studies in this work on TIPB and some of the studies on porphyrin were carried out under ambient conditions. The instrument was set up as follows: firstly the tip was formed by holding a short length of Pt/Ir wire in pliers then cutting across the wire at an angle whilst pulling the wire apart; the tip was then inserted into the STM scanner head. The sample was then placed onto a glass slide on the sample stage and clipped in place with a conducting clip as shown in Figure 3.21 (a). The sample stage was magnetically held onto the scanner head and electrically connected. As with

AFM, the tip and sample were brought into close proximity by eye before the control computer was used to extend the z-piezo to test for the tunnel current and coarsely approach the surface. The tip was then raster-scanned the surface. It is also possible to deposit a drop of liquid onto the sample prior to mounting the head. This can stabilise some samples to allow them to be imaged using the same apparatus as for ambient conditions.

Several of the porphyrin studies were carried out using vacuum STM. The approach was the same as in ambient however the tip was prepared differently depending on the specific vacuum system.

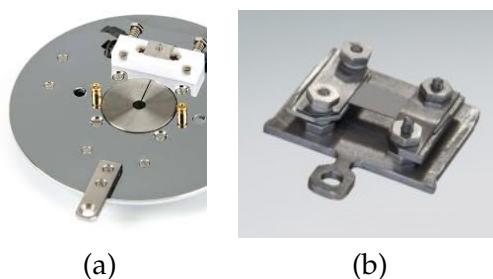


Figure 3.21 The apparatus used for STM: (a) the sample mount for ambient and liquid STM; (b) the sample mount for vacuum STM and AFM.⁶⁶

3.7.3 SPM Analysis

SPM images in this work were analysed using two standard SPM imaging programs - WSxM 5.0 Develop 8.0⁶⁷ and Gwyddion 2.5.1.⁶⁸ WSxM was used to find percentage coverage using the flooding tool. Gwyddion was used to find island heights using the profile tool, lattices using the measure lattice tool and to produce all the images included in this thesis. All island heights and lattices given in this thesis are averages with the island heights measured at multiple points within the image and the lattices taken as averages across the trace, retrace and phase images.

3.8 Summary

A wide range of techniques were used to obtain the results described in this thesis. The dominant analysis technique in this work is SPM with all samples imaged with either

STM or AFM prior to undergoing additional analysis with XPS or SIMS. TEM was used minimally in this work due to the challenge of preparing TEM suitable samples.

4 The de-halogenation and polymerisation of 1,3,5-tris-(4-iodophenyl)benzene

1,3,5-Tris-(4-iodophenyl)benzene (TIPB) and the brominated analogue (TBPB), shown in Figure 4.1, have been studied due to their propensity to undergo Ullmann-type coupling as described in Subsection 2.3.1.⁶⁹ Once bonded, the 2D polymers form strong conjugated networks with some rotational disorder of the rings. TIPB can be sublimed from a Knudsen cell onto a surface in vacuum, or deposited from solution by immersion or drop-casting depending on the sample substrate requirements. TIPB forms stabilised structures on different surfaces by covalent

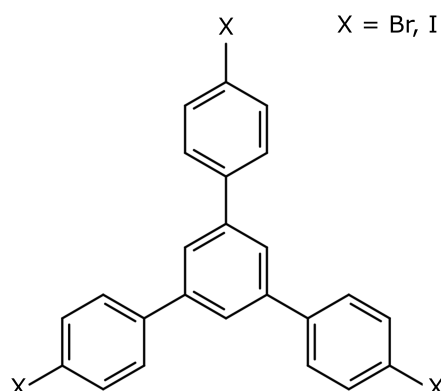


Figure 4.1 The structure of TBPB (X=Br) and TIPB (X=I).

and non-covalent interactions. Covalent bonding takes place through Ullmann-type coupling which involves carbon-carbon bonding following the dehalogenation of the TIPB. The dehalogenation can be induced by a catalytic surface, heat or other energy input.^{70–73} A wide range of covalent organic framework structures have been formed from TIPB and TBPB with varying pore sizes. The pore size and number of open pores for room temperature deposition of a related species (1,3-bis(4-bromophenyl)-5-(4-iodophenyl)benzene or BIB) on gold has been shown to depend on the final

annealing temperature with smaller pores more likely at higher temperatures.⁷⁴ The simplest structure that can be formed via covalent bonding is a dimer (3,3'',5,5''-tetra(4-iodophenyl)quatraphenyl – TBPQ) as shown in Figure 4.2 which is accompanied by the loss of I₂.

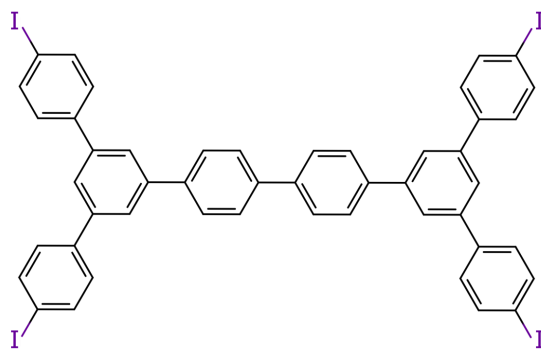


Figure 4.2 The structure of the TIPB dimer (3,3'',5,5''-tetra(4-iodophenyl)quatraphenyl – TBPQ).

One of the most important non-covalent interactions between TIPB molecules is halogen bonding, described fully in Subsection 2.2.2. Briefly, halogen bonding consists of a difference in electrostatic potential along either a carbon–halogen bond or a nitrogen–halogen bond. There are two types of halogen bond: type I has the bonds separated by 180° and type II has the bonds separated by an angle in the range 90° to 120°. For iodinated species like TIPB, type II bonding is most favoured due to the charge distribution around the iodine which is shown in Figure 4.3.⁷⁵

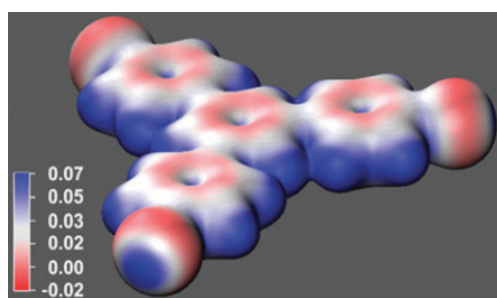


Figure 4.3 The distribution of charge within the TIPB molecule. Reproduced from reference 70.

For TIPB on various substrates, five different structures have been observed as shown in Table 4.1; two of the structures are entirely unreacted and are stabilised by halogen bonding, two are partially reacted containing one or two covalent bonds, and one is fully reacted in a covalent polygonal structure. The packing densities

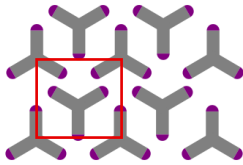
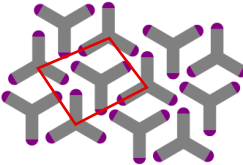
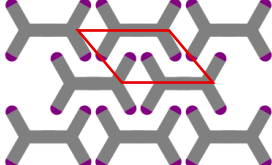
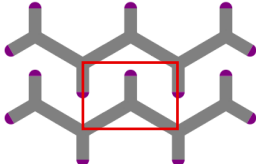
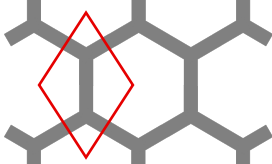
Arrangement	Observed Structure	Unit Cell	Packing Density on Cu ⁷⁶	Seen on
Sine-wave		2.1 ± 0.2 nm by 1.9 ± 0.2 nm (on Cu) ⁷⁶	0.50 ± 0.01 nm ⁻²	Cu ⁷⁶ , Au ^{37,77}
Bow-tie		2.2 ± 0.2 nm by 1.7 ± 0.2 nm (on Cu) ⁷⁶	0.55 ± 0.01 nm ⁻²	Cu ⁷⁶ , graphite ⁷⁸
Hybrid dimer		2.7 ± 0.2 nm by 1.7 ± 0.2 nm (on Cu) ⁷⁶	0.64 ± 0.01 nm ⁻²	Cu ⁷⁶ , Au ³⁷
Hybrid zig-zag		2.2 ± 0.2 nm by 1.6 ± 0.1 nm (on Cu) ⁷⁶	0.57 ± 0.01 nm ⁻²	Cu ⁷⁶ , Au ⁷¹
Covalent polygonal		Dependent on pore size and substrate	Dependent on pore size	Cu ^{76,78} , Au ⁷¹ , hBN/Ni(111) ⁷⁰

Table 4.1 The structures of TIPB and TBPB as seen on various substrates. [Note: the packing density is calculated for number of monomers per unit area.]

listed in Table 4.1 show that, for the unreacted structures, the bow-tie structure is the closest packed. The hybrid dimer is more densely packed than either of the other covalently bonded structures. The lower densities of the reacted species supports the observation by Peyrot and Silly⁷⁶ that at low coverage on gold, covalent polygonal structures dominate, whereas, at higher coverage, two dimensional halogen-bonded nanostructures grow preferentially with covalent structures at their domain boundaries. Above 1 ML coverage on gold, the surface has been observed to be terminated by a halogen-bonded layer on which covalently bonded structures form.⁷⁶

4.1 Temperature Dependence of TIPB on hBN

As described above, previous work has investigated polymerisation via Ullmann-type coupling on metal surfaces or metal supported surfaces.^{71,72,76} The work described in this chapter follows on from previous work and is an investigation of the polymerisation reaction on an insulating surface - hBN.

4.1.1 Solution Deposition onto hBN

Prior to deposition by immersion, a TIPB solution was prepared by dissolving a small quantity (typically 3.5 mg) of TIPB in toluene to form a 0.5 mg ml^{-1} solution. The TIPB did not dissolve readily so required manual agitation by shaking to break up the material. The solutions were stored in a dark cupboard but, due to the reactivity of the C–I bond, the TIPB solution degraded, colouring as the C–I bonds broke to leave iodine in the solution. Consequently, fresh solutions were prepared for every batch of samples and the solution was never more than 3 days old when used.

The hBN/SiO₂ samples, having been prepared as described in Subsection 3.6.1, were flame annealed and cooled with nitrogen prior to being immersed into the 0.5 mg ml^{-1} solution for 100 s and then dried with nitrogen to avoid drying effects. Initially, this deposition time and concentration was thought to result in the deposition of a monolayer of material, however, later results suggest multiple layers were deposited. This is discussed in the results below.

To investigate the effect of heat, the TIPB/hBN samples were heated to a range of temperatures (80 °C to 180 °C) in an argon flow furnace (flow rate 0.15 L min^{-1}) for 1 hour. The protocol consisted of heating to 20 °C below the target temperature at a rate of 10 °C min^{-1} then holding the temperature for 1 min before heating to the target temperature at a rate of 5 °C min^{-1} to reduce the risk of overshooting the temperature. The samples were removed from the argon flow once they had cooled to 45 °C or below and stored in the dark under nitrogen if not being immediately imaged to prevent degradation of the C–I bonds.

4.1.2 Increased Anneal Temperature Results

Following from the preparation steps described above, the samples were imaged in ambient with AFM on a Cypher-S (Asylum Research). Prior to annealing, the initial deposition left multilayers on the surface; the island height was measured to correspond to a 3 ML thick film albeit with high roughness in the surface. A selection of the unheated and the annealed sample AFM images are shown in Tables 4.2 and 4.3.

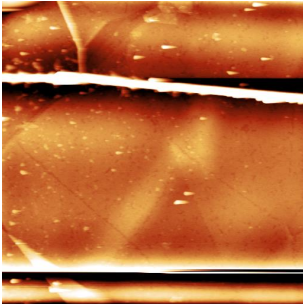
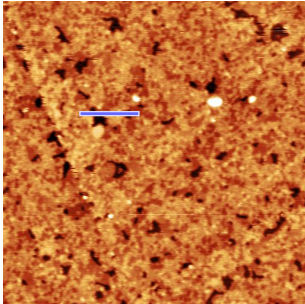
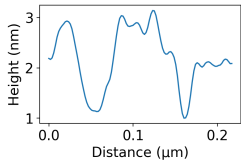
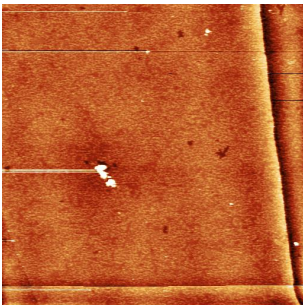
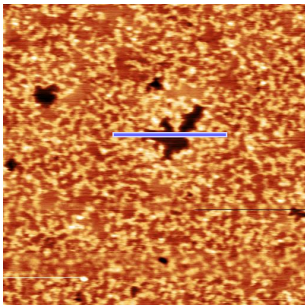
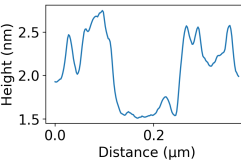
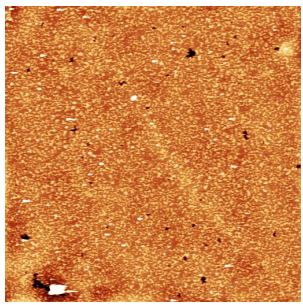
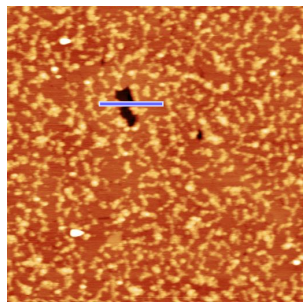
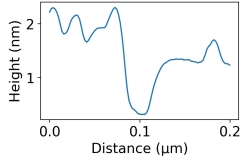
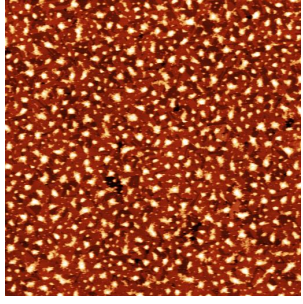
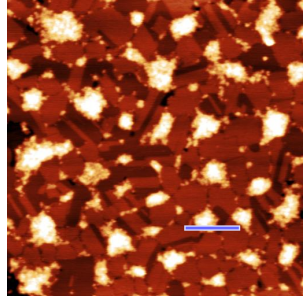
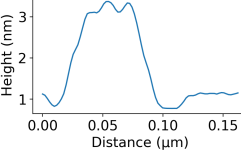
Temperature	4 μm	1 μm	
Unheated			
80 °C			
100 °C			
120 °C			

Table 4.2 Ambient AFM images of TIPB on hBN samples for an unheated sample and samples heated up to 120 °C with profiles along the blue line on the 1 μm image.

The results shown in Table 4.2 show little change in surface morphology for anneal temperatures of up to 100 °C with the small amounts of change connected to a reduction in material as expected. The pores in the surface are assumed to be defects in the hBN surface, around which the TIPB has not deposited. The coverage for the samples up to 100 °C, as measured with the flooding tool in the analysis program WSxM, is above 95% with the 120 °C sample having a second layer form on top of this background layer that covers a quarter of the sample surface. The islands for the samples up to 100 °C are 1.0 ± 0.1 nm high which would correspond to a multilayer coverage. For the 120 °C sample, the underlying islands are much lower (0.40 ± 0.04 nm) which could correspond to a monolayer of TIPB in an ordered structure. The second layer on this sample is much higher than the first layer (2.7 ± 0.3 nm) suggesting that it could be a 3D structure formed at the increased temperature.

For the higher anneal temperature samples shown in Table 4.3, changes to island morphology are seen. For the 130 °C sample, three distinct island types are seen, with the lowest assumed to be a thin layer of TIPB rather than the hBN surface. This underlying thin film of TIPB is then presumed to cover the surface entirely on the 140 °C and above samples. An additional layer of TIPB structure begins to appear on the 140 °C sample and is the majority structure on the 150 °C sample. These islands are very flat and likely ordered. The 4 μ m image for the 150 °C sample shows a range of island heights with steps of 0.40 ± 0.07 nm which would correspond to a monolayer of TIPB. Another substantial change is observed for this sample with the appearance of bright dendritic growth ~ 3 nm high. These features expand into wider features on the 180 °C sample where the large flat islands are nearly entirely gone.

These samples were challenging to image with AFM as the tip was readily damaged by picking up material from the sample, which affected the achievable resolution in the images. Additionally, the surface was easily contaminated by environmental macromolecules and by the adsorption of water. The environmental contamination was also seen on the melamine samples described in Chapter 5 and is believed to be long chain hydrocarbons from the tip and sample storage boxes. The adsorption

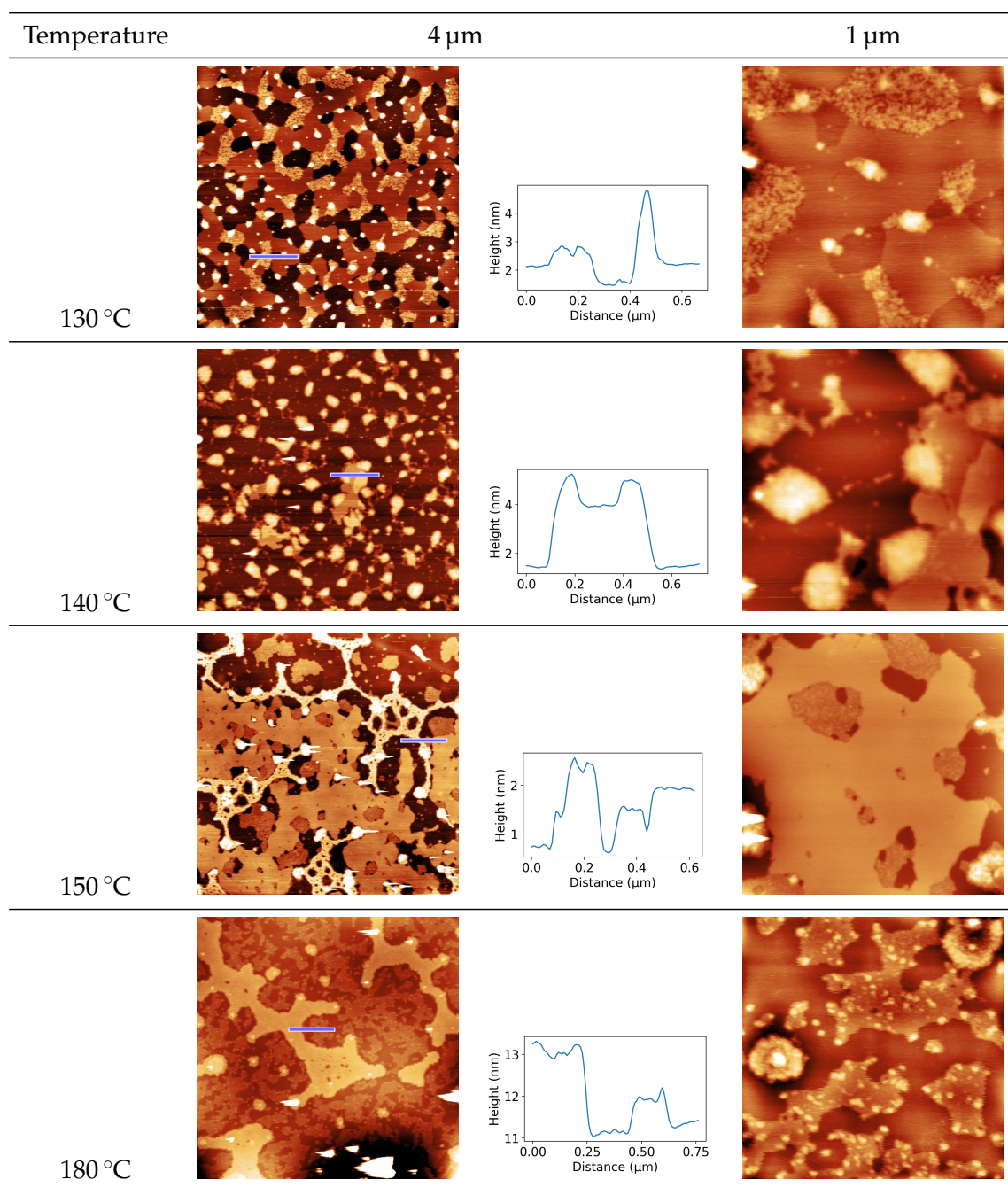


Table 4.3 Ambient AFM images of TIPB on hBN samples heated to temperatures from 130 °C to 180 °C with profiles along the blue line on the 4 μm image.

of water and degradation of the C–I bond also meant that the samples had to be imaged as soon as possible after leaving the furnace. Despite these problems, high resolution images were obtained for a selection of temperatures and these are shown in Figures 4.4, 4.5 and 4.6.

For the sample that had not undergone annealing, the lattice, shown in Figure 4.4 (a), was rhombic with a vectors of $2.00 \pm 0.05 \text{ nm}$ by $1.67 \pm 0.05 \text{ nm}$. These lattice

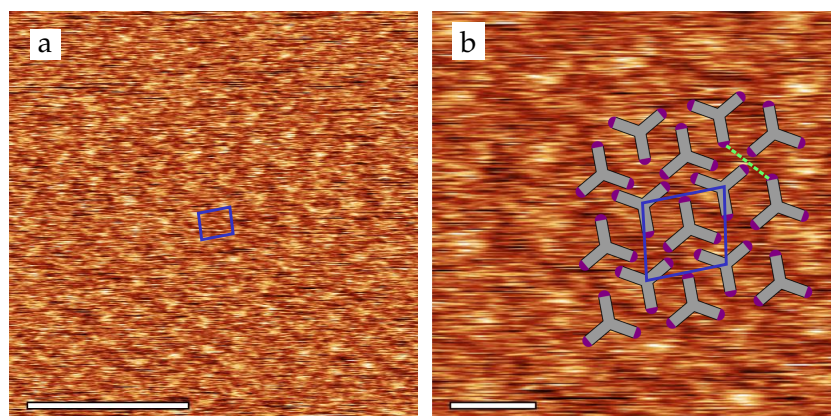


Figure 4.4 The structure resolved for the unheated TIPB on the hBN surface: (a) a lattice of 2.00 ± 0.05 nm by 1.67 ± 0.05 nm ($81 \pm 1^\circ$) shown in blue [scale bar is 10 nm]; (b) a fitted model of TIPB on (a) with a lattice of 2.0 ± 0.1 nm by 1.77 ± 0.05 nm ($80 \pm 5^\circ$) [scale bar is 2 nm].

dimensions are similar to, but do not match, those previously reported on metal surfaces, shown in Table 4.1. This suggests that the molecules adsorb in a different structure due to interactions with the substrate. The lack of detail in the AFM image makes fitting a model of TIPB challenging. A model was overlaid and is shown in Figure 4.4 (b). This lattice is very similar within each row to the sine-wave structure outlined in Table 4.1, however, the rows are offset and the molecules slightly rotated, which was not observed on the metal substrates. The packing density of this structure is $0.57 \pm 0.05 \text{ nm}^{-2}$ which is within the range of the bow-tie structure reported on metal surfaces. This packing structure has the molecules arranged with iodines in X_4 synthons, as marked by the dashed line on Figure 4.4 (b), which is known to be a stable structure.^{35,36}

High resolution images were also seen on a sample annealed to 120°C as shown in Figure 4.5. On the 120°C sample, two different lattices were seen one with 1.21 ± 0.01 nm by 1.73 ± 0.02 nm and the other 2.40 ± 0.01 nm by 1.69 ± 0.01 nm. The first lattice parameters do not match any of those previously reported however the second lattice is similar to the hybrid dimer shown in Table 4.1 although the dimensions are slightly different. These images were modelled as lattices of monomers and dimers as shown in Figure 4.5 (c-e). The monomer lattice in Figure 4.5 (c) is a closer packed version of the sine-wave lattice shown in Table 4.1 with a packing density of $0.69 \pm 0.04 \text{ nm}^{-2}$. This is higher than those previously reported or seen which could

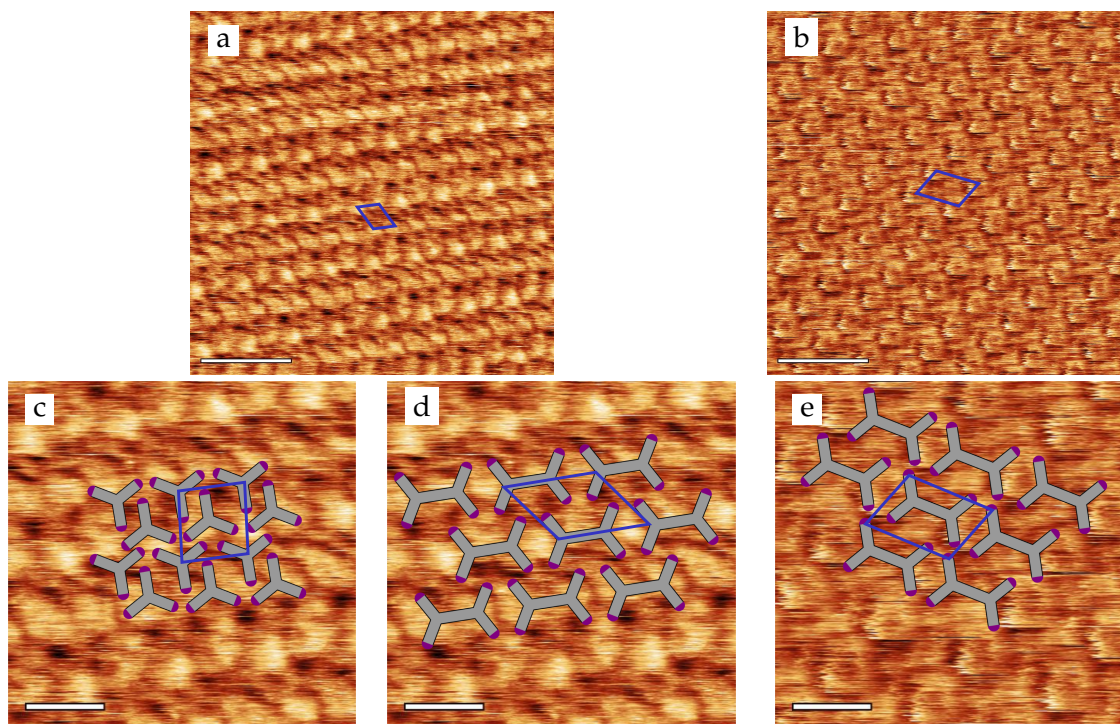


Figure 4.5 High resolution images for 120 °C sample of TIPB on hBN prepared from solution: (a) 120 °C sample with a lattice of 1.21 ± 0.01 nm by 1.73 ± 0.02 nm ($67.1 \pm 0.5^\circ$) shown in blue [scale bar is 5 nm]; (b) 120 °C sample with a lattice of 2.40 ± 0.01 nm by 1.69 ± 0.01 nm with $66.5 \pm 0.5^\circ$ shown in blue [scale bar is 5 nm]; (c) monomer model overlaid on (a) with lattice vectors of 1.80 ± 0.06 nm and 1.62 ± 0.04 nm ($86 \pm 4^\circ$) [scale bar is 2 nm]; (d) dimer model overlaid on (a) with lattice vectors of 2.39 ± 0.03 nm and 1.97 ± 0.04 nm ($52 \pm 1^\circ$) [scale bar is 2 nm]; (e) dimer model overlaid on (b) with lattice vectors of 2.34 ± 0.06 nm and 1.68 ± 0.04 nm ($69 \pm 3^\circ$) [scale bar is 2 nm].

suggest that the iodine has been lost allowing for a closer packed structure although it would be unlikely to see loss of iodine with no subsequent polymerisation unless the substrate or neighbouring molecules were stabilising the structure. Alternatively, this could be fitted to a structure formed from dimer units as in Figure 4.5 (d). This structure is similar to the hybrid dimer structure in Table 4.1 although the lattice is squarer with similar spacing between the rows but wider spacing along the rows. This structure has a packing density of $0.54 \pm 0.02 \text{ nm}^{-2}$ (calculated treating 1 dimer as two monomers), which, while less than that previously reported for the dimer structure, is similar to that seen on the unheated sample for monomers and the previously reported monomer and hybrid zig-zag structures. The second lattice, shown in Figure 4.5 (b) is similar in appearance to dimer lattices previously reported on metal surfaces so this was fitted as a packing of dimers in Figure 4.5 (e). This structure is a slightly

altered version of the hybrid dimer packing structure with a different offset between lines leading to a wider inter-row spacing. The packing density for the dimer structure is $0.55 \pm 0.03 \text{ nm}^{-2}$, which is similar to that previously found for monomer structures and the dimer structure in Figure 4.5 (d) although lower than that found for the hybrid dimer shown in Table 4.1.

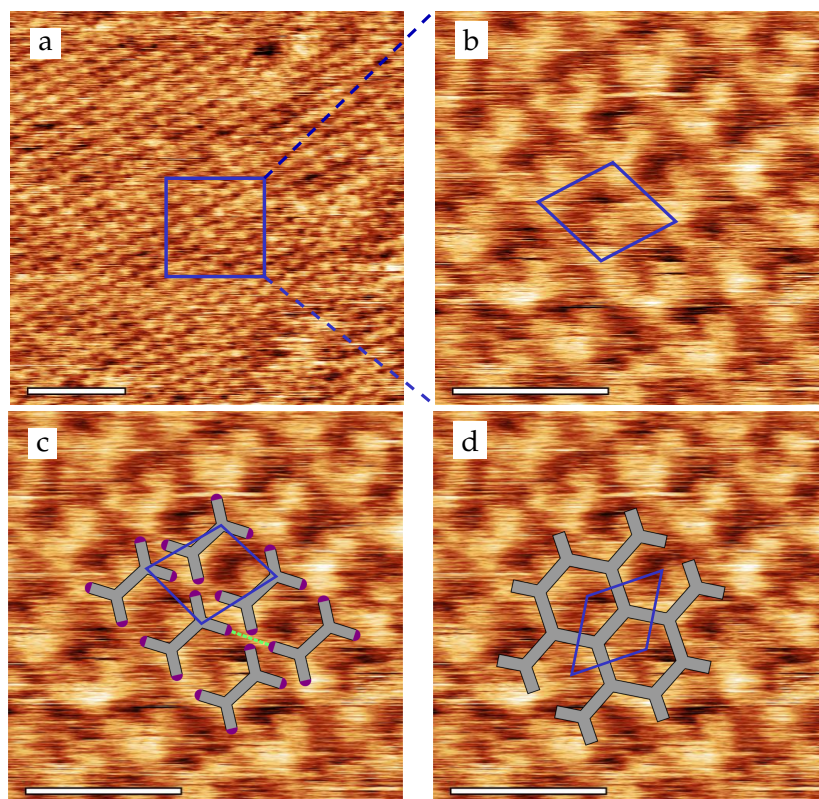


Figure 4.6 High resolution images for 140 °C sample TIPB on hBN prepared from solution: (a) 140 °C sample with a lattice of $1.64 \pm 0.01 \text{ nm}$ by $2.31 \pm 0.01 \text{ nm}$ ($70.7 \pm 0.5^\circ$) [scale bar is 10 nm]; (b) zoomed in on blue square in (a) showing a lattice of $1.88 \pm 0.04 \text{ nm}$ by $2.19 \pm 0.03 \text{ nm}$ ($72.2 \pm 0.6^\circ$) in blue [scale bar is 4 nm]; (c) model of dimers on (b) with lattice vectors of $2.27 \pm 0.02 \text{ nm}$ and $1.94 \pm 0.04 \text{ nm}$ ($75 \pm 1^\circ$) [scale bar is 4 nm]; (d) model of hexagonal polymeric structure on (b) with lattice vectors of $1.94 \pm 0.02 \text{ nm}$ and $1.99 \pm 0.02 \text{ nm}$ ($60 \pm 1^\circ$) [scale bar is 4 nm].

Only a single lattice structure was seen on the 140 °C sample, which is shown in Figure 4.6. The dimensions of the lattice, $1.88 \pm 0.04 \text{ nm}$ by $2.19 \pm 0.03 \text{ nm}$, do not agree with the structures in Table 4.1 or the previous structures shown in this section. The structure forming this lattice could be either a lattice of monomers, dimers, or polymeric; structures formed from dimers and fully reacted hexagonal polymers are shown overlaid on Figure 4.6 (b). The dimer structure in Figure 4.6 (c) is similar to that proposed for the 120 °C sample with the dimers packed into nearly aligned rows.

The ends of each dimer are arranged with the iodines in X_4 synthons, as shown by the dashed line on Figure 4.6 (c). The packing density of this structure is $0.47 \pm 0.01 \text{ nm}^{-2}$, which is a less dense structure than the dimer arrangement on the 120°C sample which may be connected with an overall reduction of material on the surface. The alternative structure comprised of a polymeric network is shown in Figure 4.6 (d). The packing density for this structure is higher than for the dimer structure at $0.60 \pm 0.01 \text{ nm}^{-2}$, which is close to the packing density for the hybrid dimer and hybrid zig-zag structures in Table 4.1 suggesting that this a better fit for the observed structure.

From the AFM images, it was clear that a change was occurring on the surface with some suggestions that this involved dimerisation and further polymerisation of the TIPB. However, due to the difficulty of interpreting high resolution images, a quantitative approach could not be taken. In order to obtain quantitative information about the chemical state of the TIPB, an alternative technique was needed.

4.1.3 XPS of TIPB on hBN

XPS was chosen as an alternative technique with which to investigate the samples as it can provide the elemental composition of materials. The limitation of the technique was the area from which the spectra were taken as this was larger than the average hBN flake size and it could not be confirmed that the spectra were obtained on hBN flakes. XPS was carried out on all samples shown in Tables 4.2 and 4.3 with multiple spectra taken on each sample. An overview spectra was taken first and then high resolution spectra were taken at specific points of interest; in this case, the important peaks were the I 3d peaks, the C 1s peak, and the Si 1s peak. An example set of these spectra are shown in Figure 4.7.

The wide view spectra shown in Figure 4.7 (a) show peaks for O 1s and 2s, C 1s, Si 2s and 2p, I 3d and 4d, and N 1s as expected for TIPB on SiO_2 supported hBN. Some smaller peaks are also present, which are mostly metals from contamination within the XPS system. There is a reduction in counts at increased temperatures, particularly for the I 3d ($\sim 620 \text{ eV}$) and I 4d ($\sim 50 \text{ eV}$) peaks. The presence and intensity of the

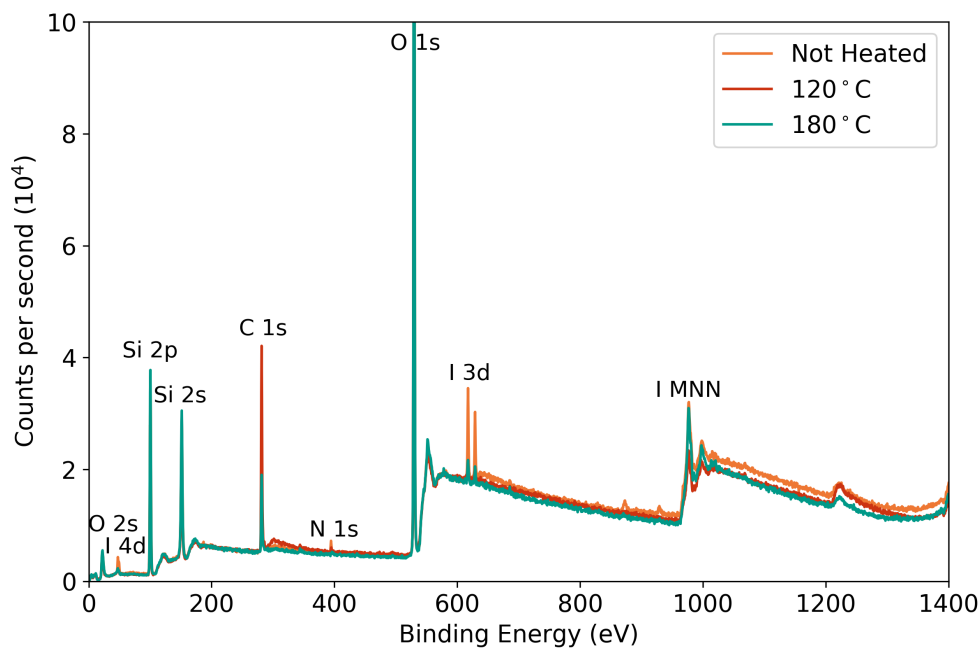


Figure 4.7 Wide view XPS spectra for the unheated sample, the 120 °C sample, and the 180 °C sample - the most intense peak (O 1s) has been cut off below maximum height to allow for better scaling.

oxygen and silicon peaks show that the XPS analysed large areas of surface without hBN present which is likely due to the large spot size of ~ 3 mm.

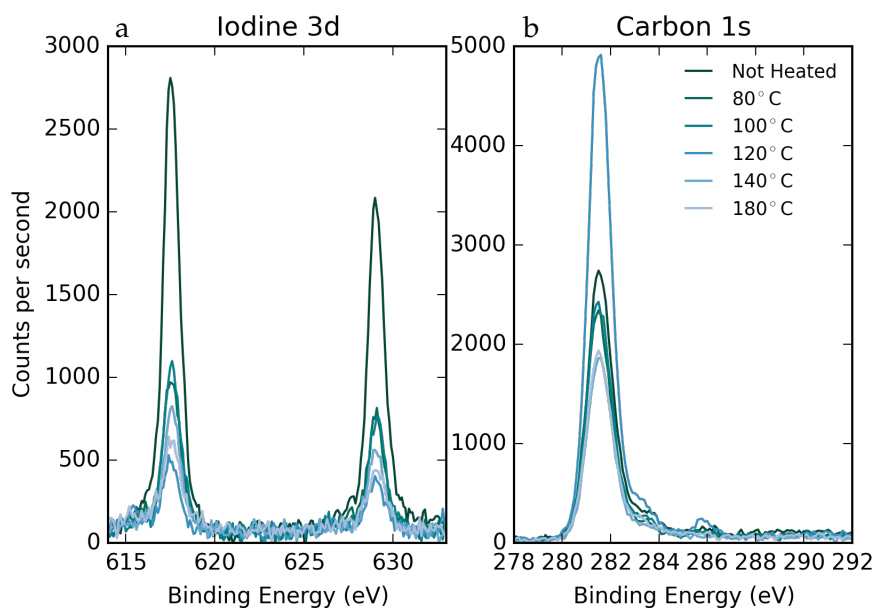


Figure 4.8 A selection of the XPS data: (a) iodine 3d and (b) carbon 1s peaks for a range of temperatures.

Higher resolution spectra were obtained for the I 3d and the C 1s peaks as shown in Figure 4.8. The higher resolution iodine spectra shown in Figure 4.8 (a) show a large reduction between the unheated sample and all the heated samples. This is not caused by a reduction of material on the surface as the carbon peaks shown in Figure 4.8 (b), with the exception of the 120 °C sample, are approximately unchanged in height. The area under the curve for the iodine spectra was taken for each peak then scaled to the area under the silicon peak and normalised to the unheated sample. These were then plotted against the anneal temperature for the samples as shown in Figure 4.9. The large error for the 80 °C sample is due to an anomalously large I 3d peak in one of the three spectra.

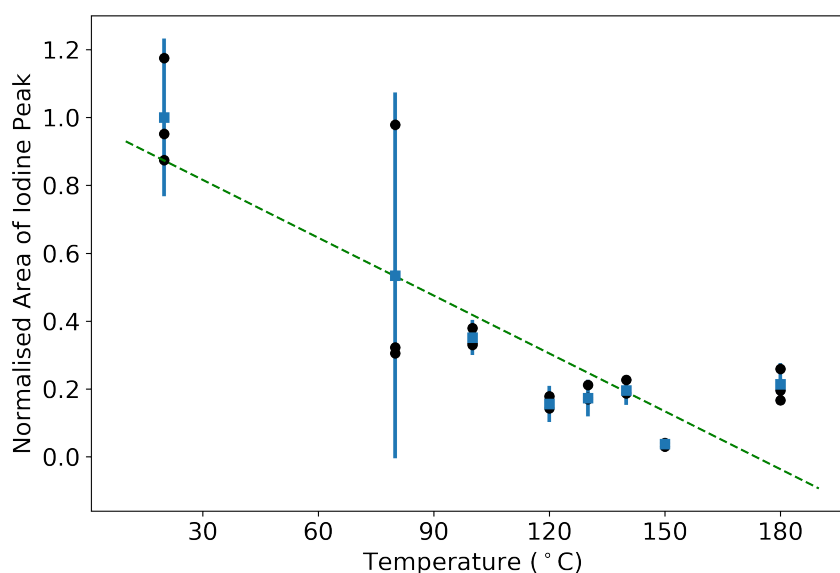


Figure 4.9 The normalised (first to the silicon peak for each spectra then to the average of the unheated samples) iodine peak area for the TIPB on hBN samples at increasing anneal temperatures. Error bars are shown on all samples and were calculated from the standard deviations of the three spectra taken on each sample. The trendline has the equation $y = 2.5383 - 5.68 \times 10^{-3}x$.

The data fits well with a model in which dimerisation occurs first, followed by complete loss of iodine from the molecules. The iodine leaves the surface, possibly as molecular iodine (I_2). From the trendline fitted to Figure 4.9, removal of 1/3 of the iodine would be expected at 56 °C with removal of 2/3 of the iodine seen at 115 °C and complete removal of iodine at 174 °C. The temperatures are lower than expected

given the AFM results however, the removal of iodine from TIPB is likely disordered so more than 1/3 of the iodine would need to be removed for complete dimerisation to occur. This would support the dimer structure for the 120 °C images in Figure 4.5 and either the dimer or the polymer structure for the 140 °C images in Figure 4.6. However, due to inherent limitations of the technique, the specific molecular species present on the surface were not discovered. The spot size for analysis also raises questions as to whether the iodine loss is the same on the hBN flakes or if the molecules react differently.

4.1.4 Mass Spectrometry of TIPB on hBN

In order to investigate the polymerised species present on the hBN surface, SIMS was used to identify the molecular species present for different temperature samples. This technique ionises surface species and analyses them; the mass-to-charge ratio (m/z) and observed fragmentation can be linked to specific structures. The SIMS instrument used was a hybrid time-of-flight/Orbitrap known as 3D OrbiSIMS developed by Passarelli et al.⁷⁹. This instrument has extremely high mass accuracy and resolution and is a surface sensitive technique making it ideal to look at the molecules formed on the surface during annealing. The 250 μm^2 area analysed is selected optically which allowed an area containing hBN flakes to be targeted. The TIPB species are seen as positive ions after ionisation with argon clusters.

The wide view positive ion spectra are shown in Figure 4.10. A larger range was measured than is shown here but no peaks were observed above 1900 m/z that could be distinguished from noise. The first observation is that the absolute amount of material coming off the surface is highly varied between samples. This suggests some inconsistency in the preparation method or some variation in the surface composition for the area selected. The area analysed on the different samples may have contained variable amounts of hBN flakes which would alter the amount of material present. The peak at 831.86 m/z is unassigned but is likely a fragment of the dimer structure consisting of the monomer with extra phenyl groups attached.

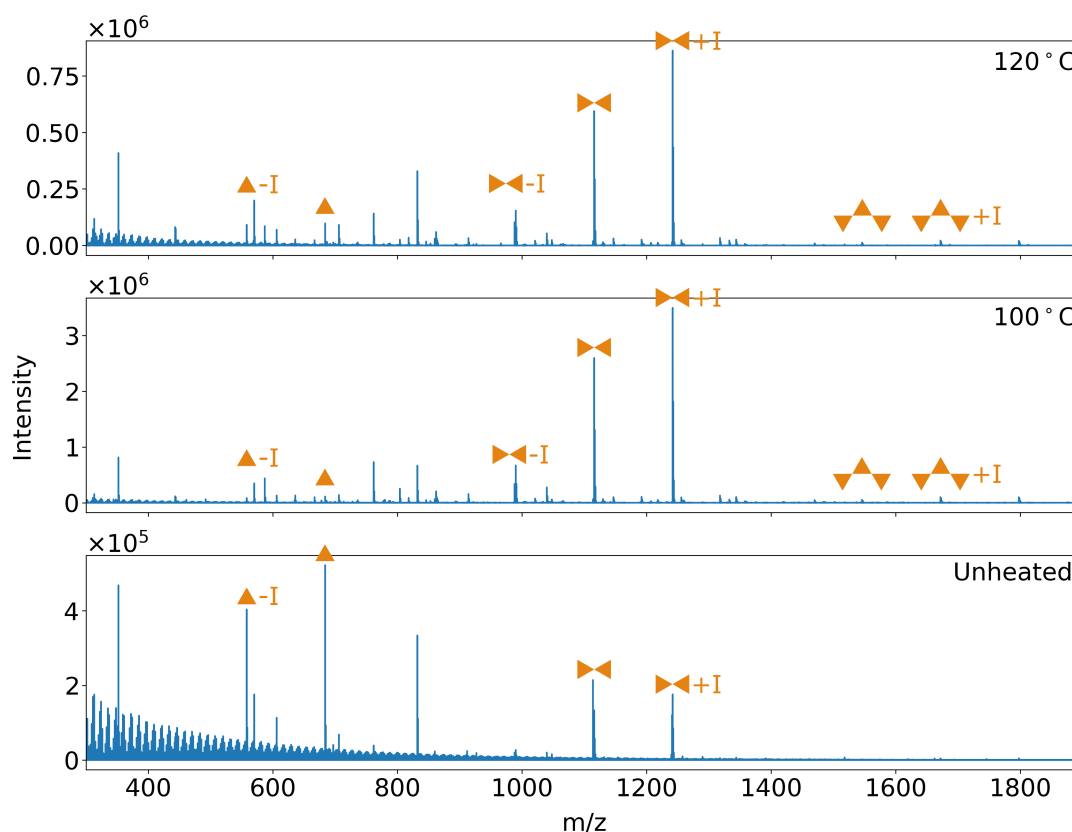


Figure 4.10 Labeled positive ion mass spectrometry results for all three samples. The monomer is denoted with a single triangle, dimer with two, and trimer with three. [Range measured was 300 to 3000 m/z .]

The spectra have a large amount of material at relatively low mass, particularly for the unheated sample. The low mass range is shown in detail in Figure 4.11 which reveals two sets of overlapping periodic peaks. These peaks are difficult to assign, however, there are features that can inform an assignment. The prominent peaks highlighted in orange suggest that the structure producing these peaks contains bromine or chlorine as these have two isotopes that are equally common so would produce this splitting. The most intense peaks in each group are separated by two different m/z s (10.99 and 13.01) which correspond to the addition of carbon at the same time as the removal of a hydrogen (10.992 u) and the addition of a carbon alongside a hydrogen (13.008 u) which would suggest that these peaks are from alkyl contaminants. Alternatively, these peaks could be caused by the hBN substrate as the separation between every other peak is 24.00 u which corresponds to the addition of BN with the removal of a hydrogen (24.004 u).

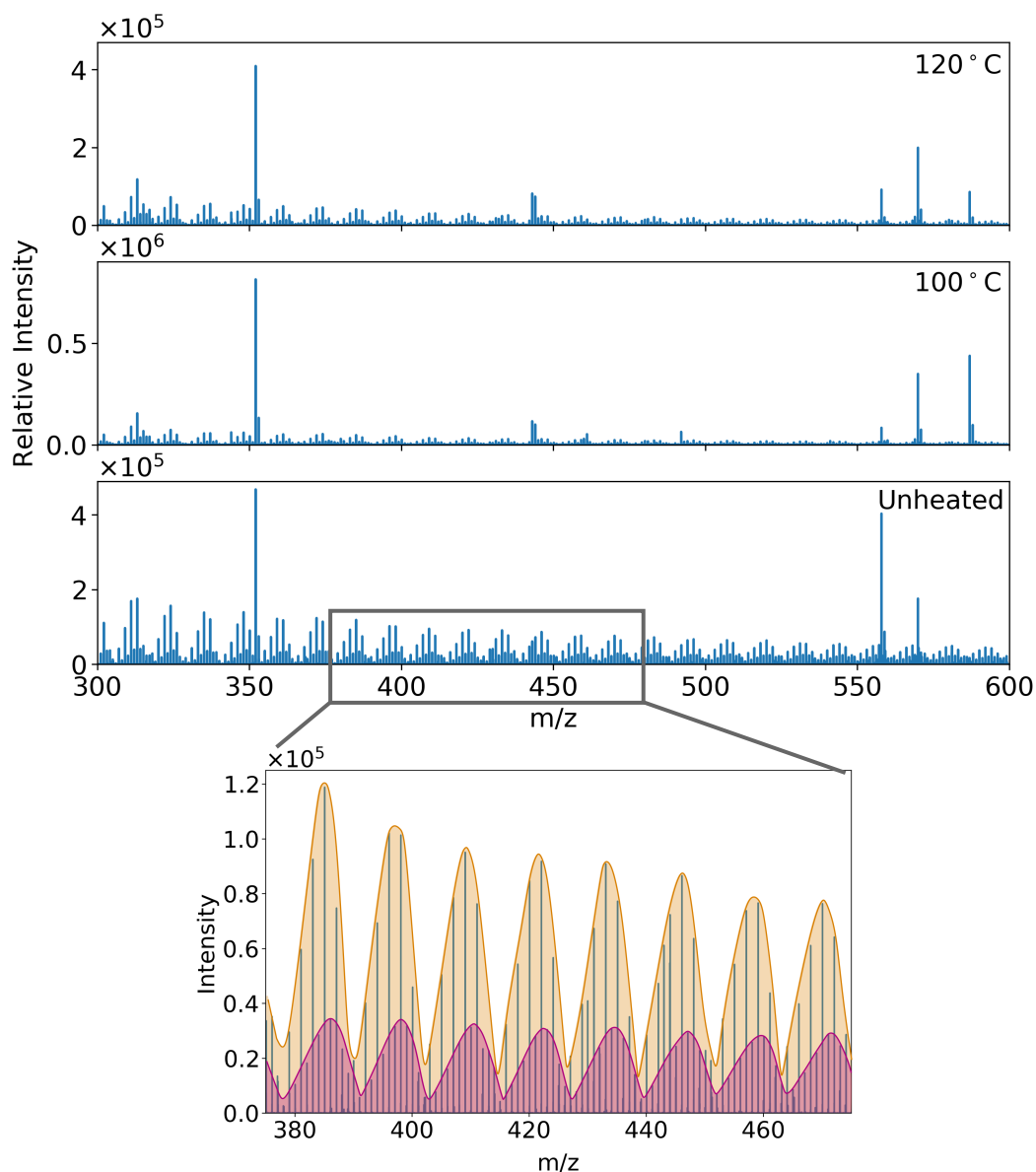


Figure 4.11 Positive ion mass spectrometry results: (a) the low mass range showing periodic peaks for all three samples. The peak at ~ 352 m/z is a contaminant from the instrument; (b) the mass range 375 to 475 m/z for the unheated sample.

For the unheated sample, the largest peak is seen at 683.83 m/z for the monomer as expected (theoretical is 683.8303 u). For both of the heated samples, the largest peak is seen at 1241.77 m/z which corresponds to the dimer with an extra iodine ($C_{48}H_{31}I_5$ - 1241.7645 u). This species may have formed during the SIMS process or may have been present on the surface, however it contains a hypervalent iodine thus may form a transition stage of the dimerisation process. The trimer with additional iodine ($C_{72}H_{45}I_6$ - 1670.78 u) is also a more intense peak than the trimer with the expected iodine ($C_{72}H_{45}I_5$ - 1543.87 u) which supports a model wherein a stable intermediate is

formed prior to full dehalogenation. A peak corresponding to the monomer missing an iodine was seen in all spectra, including the unheated. This suggests that a portion of the molecules have enough energy in solution or from deposition to lose an iodine without heating although this may have also been due to the ionisation beam for the SIMS process. Molecular iodine is absent from these spectra as it has previously only been seen in the negative ion spectra.

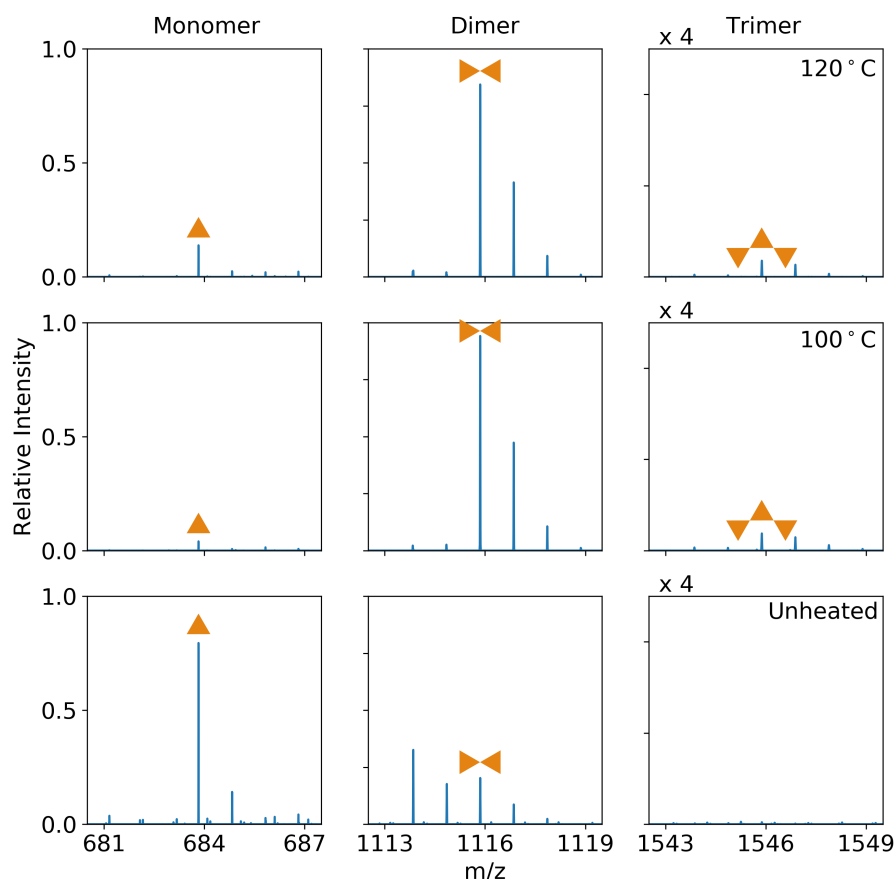


Figure 4.12 Selected mass spectrometry results for all three samples with isotopic resolution. The highest peaks corresponding to the monomer, dimer and trimer are marked with orange triangles. Spectra are normalised to the summed area under the monomer, dimer, and trimer peaks.

Figure 4.12 shows a section of the spectra at m/z values for the TIPB monomer ($C_{24}H_{15}I_3$ - 683.83 u), dimer ($C_{48}H_{30}I_4$ - 1113.853 u), and trimer ($C_{72}H_{45}I_5$ - 1543.874 u) with isotopic resolution. The main dimer peak is actually seen for the dimer with two extra hydrogens ($C_{48}H_{32}I_4$ - 1115.855 u) as for the main trimer peak ($C_{72}H_{47}I_5$ - 1545.890 u). This is believed to be an artifact of the SIMS ionisation process as it is common to gain extra hydrogen atoms. Interestingly, the mass spectra reveal that there

is dimer present for the unheated sample which may have been formed in solution or immediately after deposition on the surface.

	m/z	Theory	Unheated	100 °C	120 °C
Monomer $C_{24}H_{15}I_3$	683.83	100	100	100	100
	684.83	26.13	17.26	15.99	16.74
	685.83	3.273	2.97	34.39	13.77
Dimer + 2H $C_{48}H_{32}I_4$	1115.868	100	100	100	100
	1116.872	52.28	41.92	50.01	49.16
	117.875	13.39	10.66	11.35	11.02
Trimer + H $C_{72}H_{46}I_6$	1241.765	100	100	100	100
	1242.768	52.27	48.26	52.00	50.29
	1243.772	13.38	10.73	11.57	11.41

Table 4.4 The theoretical and experimental isotopic distributions.

The isotopic distributions for the different molecular species can be used to confirm the peak assignment. The isotopic distributions shown in Table 4.4 show some good agreement to support the assignments, particularly for the trimer species. The differences in the distribution around the monomer peak suggests that a second species is present around this mass. This is likely to be due to the BN or alkyl periodic peaks at the lower mass range seen in Figure 4.11. There is also some difference in the dimer distributions as expected given the additional peaks seen in Figure 4.12. This is caused by the overlapping distributions for the dimer, dimer + H, and dimer + 2H.

To obtain comparative results, the spectral data were normalised to the height of the monomer peak and the normalised peak intensity data is shown in Table 4.5. The normalised data clearly shows that the 100 °C sample contains the most dimer and trimer relative to the amount of monomer. The 120 °C sample was expected to have more dimer and trimer than the 100 °C sample, however, the SIMS results suggests that, at this anneal temperature, the reaction rate is limited which may be because the molecules have enough energy to leave the surface rather than migrate across the surface. The proportional amount of monomer minus iodine is the same on both the unheated and the 100 °C sample suggesting that the dehalogenation process does not solely rely on the additional energy from annealing. It is also possible that iodine is removed during the ionisation process and is a stable gas-phase complex if not already stable on the surface. This could be checked by increasing the ionisation energy of the

Species	m/z (ppm)	Unheated	100 °C	120 °C
Monomer - I + H $C_{24}H_{16}I_2$	557.93 (0.16)	0.77	0.75	0.92
Monomer $C_{24}H_{15}I_3$	683.83 (0.18)	1.00	1.00	1.00
Monomer + phenyl $C_{30}H_{21}I_3$	761.86 (16)	0.07	6.61	1.45
Dimer - I + 3H $C_{48}H_{33}I_3$	989.96 (12)	0.05	6.11	1.57
Dimer $C_{48}H_{30}I_4$	1113.85 (3.7)	0.40	0.54	0.19
Dimer + 2H $C_{48}H_{32}I_4$	1115.86 (11)	0.25	23.53	6.02
Dimer + I + H $C_{48}H_{31}I_5$	1241.75 (11)	0.34	31.71	8.87
Trimer + 2H $C_{72}H_{47}I_5$	1545.88 (7.55)	0.00	0.46	0.12
Trimer + I + H $C_{72}H_{46}I_6$	1671.78 (1.83)	0.01	0.89	0.22

Table 4.5 The peak intensities normalised to the monomer peak for each sample with the parts-per-million error on the m/z .

primary ion beam on an unheated sample. Alternatively, these results could be due to variation within the samples as repeats were not carried out.

The mass spectrometry results agree with the XPS results that dehalogenation and polymerisation are taking place. However, these results also suggest that the some of the dimers are forming with an extra iodine attached. This supports the dimer structure for the 120 °C and may give an explanation for the extended intra-row distance suggested by the model in Figure 4.5 (d) if the iodine is between the two monomers forming the dimer. The presence of trimer species support the polymer structure in Figure 4.6 (d), however, as a spectra was not taken on a 140 °C sample, this was not fully confirmed. The unheated TIPB results agree with the proposed structure in Figure 4.4 (b) with the monomer peak dominating the spectra.

4.2 Vacuum Deposition of TIPB onto hBN

In addition to depositing TIPB from solution, the deposition of TIPB in vacuum was also investigated. This also allowed vacuum AFM to be carried out on the sample

within the same system as the deposition which reduced contamination particularly water.

TIPB was loaded into a Knudsen cell in a vacuum system with a base pressure of 1×10^{-9} mbar. Before the vacuum deposition, the hBN/SiO₂ sample was heated to 456 °C for 1 h to remove any surface contamination. The TIPB was then deposited from a Knudsen cell at 183 °C for 15 min. This deposited a large amount of material. After initial AFM imaging, the sample was heated to 80 °C for 30 min and then to 115 °C for another 30 min. This reduced the amount of material on the boron nitride surface to a few layers.

4.2.1 Results

After the initial deposition of TIPB, a hBN flake was imaged with the vacuum AFM (Omicron VT). The imaging was complicated by the lack of an optical microscope attached to the system. An optical image of the sample was taken prior to insertion into the vacuum system to display the positions of the hBN flakes which was used to judge the correct positions to approach the tip. However, the surface had to be approached and imaged to check whether a hBN flake had been approached. The images of an area around a hBN flake are shown in Figure 4.13.

Despite the tip artifact (appearing as a triangle with bright dots), the image shown in Figure 4.13 (a) shows that the TIPB did not deposit as a thick film on the hBN, rather it preferentially adsorbed onto the surrounding SiO₂ surface. An area over the flake was imaged repeatedly; one of these images is shown in Figure 4.13 (b). As seen in Figure 4.13 (c), the scanning removed material from the area surrounding the flake although the height across the flake appears consistent suggesting that material was not removed from the hBN surface. This shows that the molecules were not strongly bound to the surface of the SiO₂ or in large networks. The sample was then heated in two stages as described above. This resulted in a sample surface as shown in Figure 4.14.

The steps resolved in Figure 4.14 (a) are 0.3 ± 0.1 nm high corresponding to monolayer steps of the hBN substrate. The lattice vectors on the upper and lower steps are similar in dimension (2.20 ± 0.05 nm and 1.90 ± 0.05 nm) although the angle

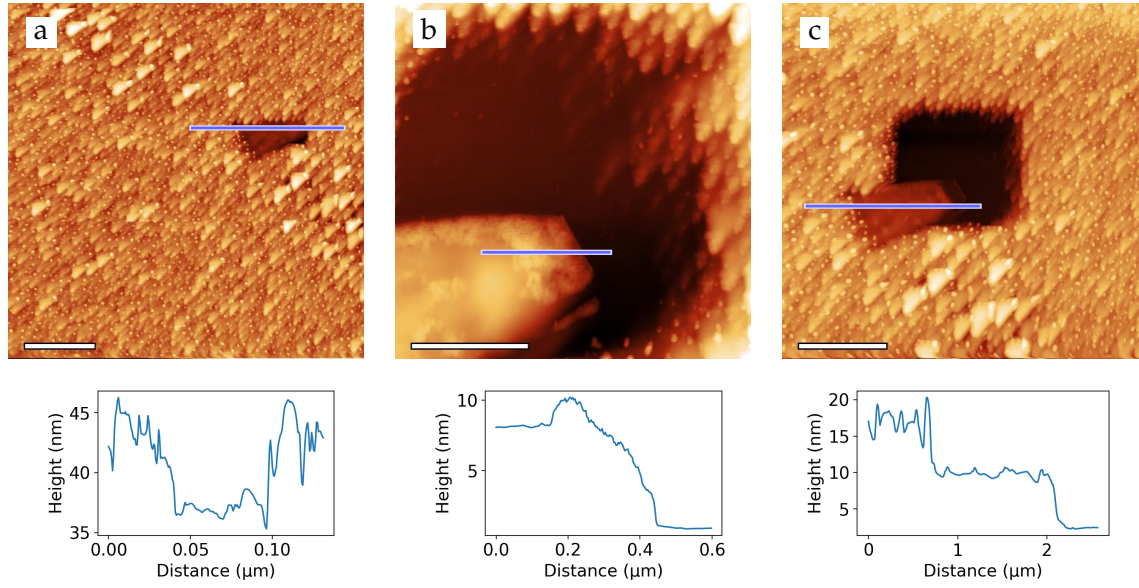


Figure 4.13 Topographic images after deposition of the thick film: (a) hBN flake 7 ± 2 nm below height of TIPB deposition with profile along the blue line shown below [scale bar is 1 μ m]; (b) hBN flake 8 ± 1 nm high with surrounding TIPB removed with profile along the blue line shown below [scale bar is 500 nm]; (c) 13.6 ± 0.7 nm deep area of damage from previous scans (1.44 ± 0.01 μ m by 1.31 ± 0.02 μ m) with profile along the blue line shown below [scale bar is 1 μ m].

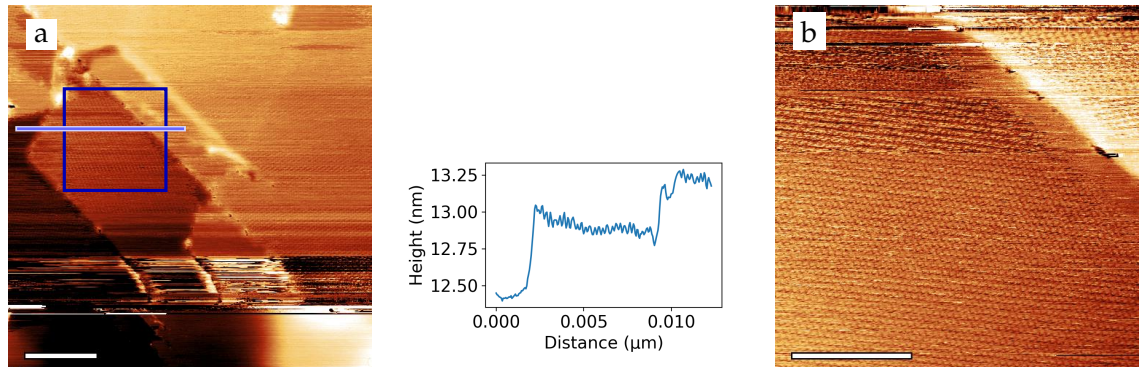


Figure 4.14 Topographic images taken on a hBN flake post annealing: (a) lattices visible on upper (height 0.3 ± 0.1 nm) and lower (height 0.4 ± 0.1 nm) steps with lattices of 2.19 ± 0.04 nm by 1.91 ± 0.02 nm ($78 \pm 2^\circ$) and 2.24 ± 0.05 nm by 1.9 ± 0.2 nm ($71 \pm 3^\circ$) respectively with profile along the blue line shown below [scale bar is 48 nm]; (b) zoom of blue square on (a) showing a lattice of 1.88 ± 0.02 nm by 1.93 ± 0.01 nm ($76 \pm 1^\circ$) [scale bar is 33 nm].

between the vectors differs. The lattice is clearer in (b) which shows the difference between the upper and lower step orientations. This lattice is explored further in Table 4.6 as Phase I. Although the surface was more stable under scanning than prior to annealing due to the reduction in material, the tip often changed during scanning as seen by the changes across both images in Figure 4.14.

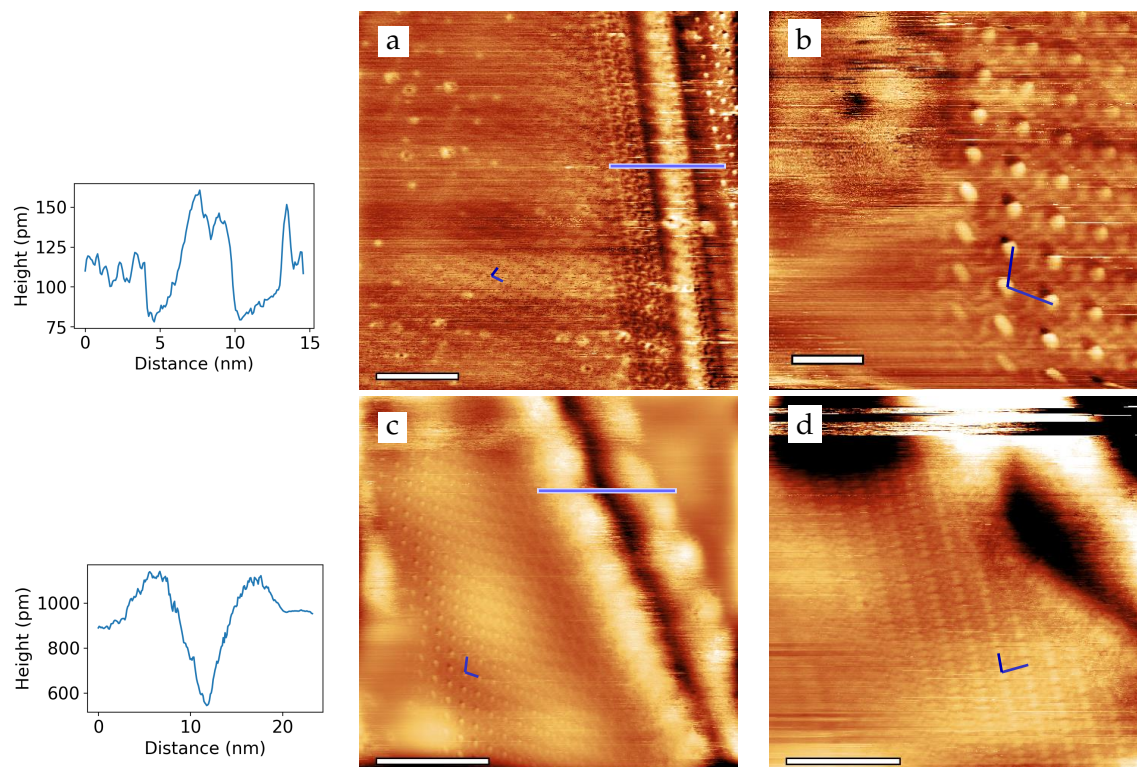


Figure 4.15 Topographic images taken on different areas of a hBN flake post annealing: (a) lattice at bottom of image is 1.84 ± 0.02 nm by 1.87 ± 0.02 nm ($67.3 \pm 0.8^\circ$) with bright band 3.7 ± 0.5 nm wide and a lattice on the right of 1.90 ± 0.01 nm by 2.15 ± 0.02 nm ($60 \pm 3^\circ$), left is a profile along the blue line [scale bar is 10 nm]; (b) lattice of 1.96 ± 0.05 nm by 1.70 ± 0.01 nm ($82 \pm 4^\circ$) [scale bar is 3 nm]; (c) crack across hBN flake 0.64 ± 0.07 nm deep with a lattice on the left of 2.05 ± 0.01 nm by 1.95 ± 0.02 nm ($77.8 \pm 0.7^\circ$), left is a profile along the blue line [scale bar is 18 nm]; (d) large ordered island of TIPB extending to hBN step with lattice of 0.74 ± 0.02 nm by 2.21 ± 0.04 nm ($86.7 \pm 0.8^\circ$) [scale bar is 10 nm].

The bright line along the edge of a hBN step seen in Figure 4.15 (a) has large ordered structures on each side. At the right edge of the lattice to the left of the line, molecular structure can be resolved which is then shown in detail in Table 4.7 as Phase IV. The molecular structure to the right of the line is also shown in Figure 4.15 (b) and (c) and is outlined as Phase III in Table 4.6. In a different area on the hBN flake, the lattice shown in Figure 4.15 (d) was observed. As with the earlier images, there are areas of tip changes at the top of the image. This lattice is explored further in Table 4.6 as Phase II.

The three phases shown in Table 4.6 all contain the sine-wave structure within each row with equally spaced TIPB molecules. Phases I and II have aligned rows as the sine-wave structure in Table 4.1 does with similar lattice dimensions between rows although

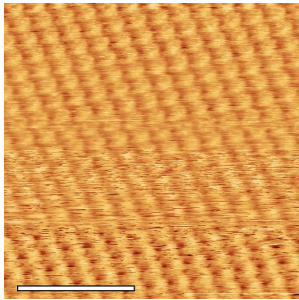
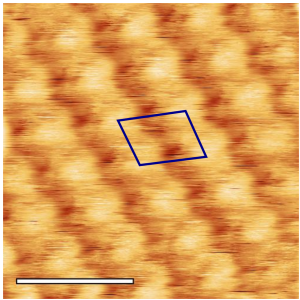
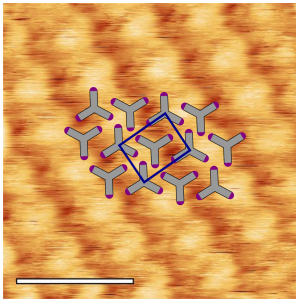
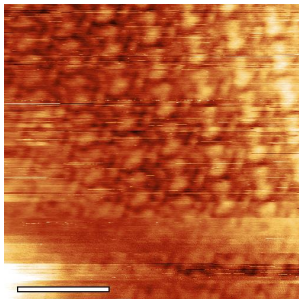
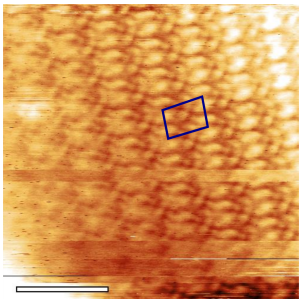
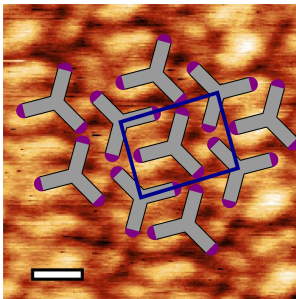
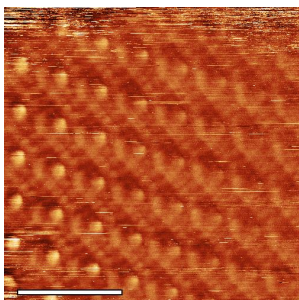
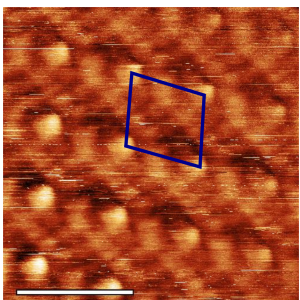
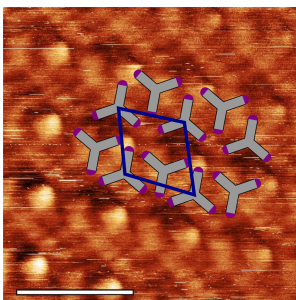
Lattice Phase	AFM Images		Model
Phase I			
	[scale bar is 12 nm] 2.25 ± 0.02 nm by 1.71 ± 0.01 nm ($76 \pm 1^\circ$)	[scale bar is 4 nm] 2.21 ± 0.05 nm by 1.61 ± 0.05 nm ($69 \pm 2^\circ$)	[scale bar is 4 nm] 1.90 ± 0.04 nm by 1.55 ± 0.04 nm ($89 \pm 5^\circ$)
Phase II			
	[scale bar is 5 nm] 2.2 ± 0.1 nm by 1.8 ± 0.2 nm ($86 \pm 4^\circ$)	[scale bar is 5 nm] 2.2 ± 0.1 nm by 1.8 ± 0.2 nm ($86 \pm 4^\circ$)	[scale bar is 1 nm] 2.0 ± 0.1 nm by 1.6 ± 0.1 nm ($87 \pm 3^\circ$)
Phase III			
	[scale bar is 5 nm] 1.99 ± 0.05 nm by 2.14 ± 0.02 nm ($85 \pm 1^\circ$)	[scale bar is 3 nm] 1.71 ± 0.01 nm by 2.25 ± 0.01 nm ($76 \pm 1^\circ$)	[scale bar is 3 nm] 1.83 ± 0.03 nm by 2.0 ± 0.1 nm ($67 \pm 5^\circ$)

Table 4.6 The three areas of sine-wave like structure observed using vacuum AFM for vacuum deposited TIPB on hBN post-anneal. The differences in unit cell dimensions between the AFM images demonstrate the drift in the instrument between up and down scans as well as changes to tip geometry.

these structures are closer packed within the rows. Unlike the other two phases, phase III has misaligned rows with similar inter-row distance as the other phases but wider

spaced molecules within the rows. This structure corresponds to the structure seen for the unheated solution deposited structure shown in Figure 4.4.

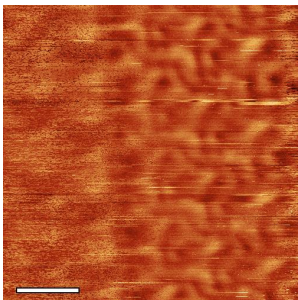
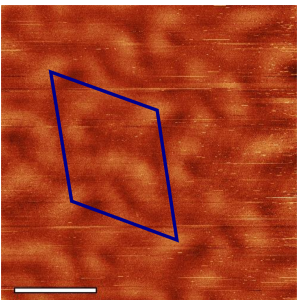
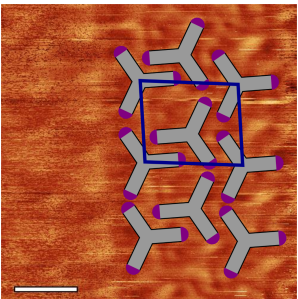
Lattice Phase	AFM Images		Model
Phase IV	 <p>[scale bar is 1 nm] 0.88 ± 0.02 nm by 1.05 ± 0.01 nm $(73 \pm 2^\circ)$</p>	 <p>[scale bar is 0.5 nm] 0.68 ± 0.05 nm by 0.75 ± 0.05 nm $(68 \pm 2^\circ)$</p>	 <p>[scale bar is 1 nm] 1.24 ± 0.06 nm by 1.56 ± 0.02 nm $(85 \pm 1^\circ)$</p>

Table 4.7 An area of skewed sine-wave structure observed using vacuum AFM for vacuum deposited TIPB on hBN post-anneal.

In addition to structures with equally spaced TIPB molecules within each row, a structure with unequally spaced TIPB molecules was resolved and is shown in Table 4.7. This structure contains elements of the sine-wave structure and the bow-tie structures outlined in Table 4.1 and is similar to the structure observed on the 120°C solution deposited sample shown in Figure 4.5 although much closer packed. This structure is very close-packed which may suggest that the molecules are non-planar in a 3D multilayer structure. This is also supported by the additional lines not explained by the model which may be an underlying layer.

4.3 Deposition of TIPB onto HOPG

In addition to investigating the structures formed by TIPB on hBN, TIPB was also studied on HOPG although this work did not look at the polymerisation reaction. As with the earlier work on hBN, TIPB was deposited by immersion in solution. The graphite surface was prepared as described in Subsection 3.6.1. Immediately after exfoliation, the graphite was immersed into a freshly prepared solution of TIPB in toluene (0.5 mg ml^{-1}) for 100s. After removal from the solution, the sample was

dried with nitrogen to reduce drying effects on the surface. This deposition time and concentration were chosen to give a minimal coverage.

4.3.1 Results

Post deposition, large ordered domains were visible with ambient STM as shown in Figure 4.16 (a) with two different domain orientations seen on the different steps. High-resolution images of these domains in Figure 4.16 (b) and (c) show detailed structures.

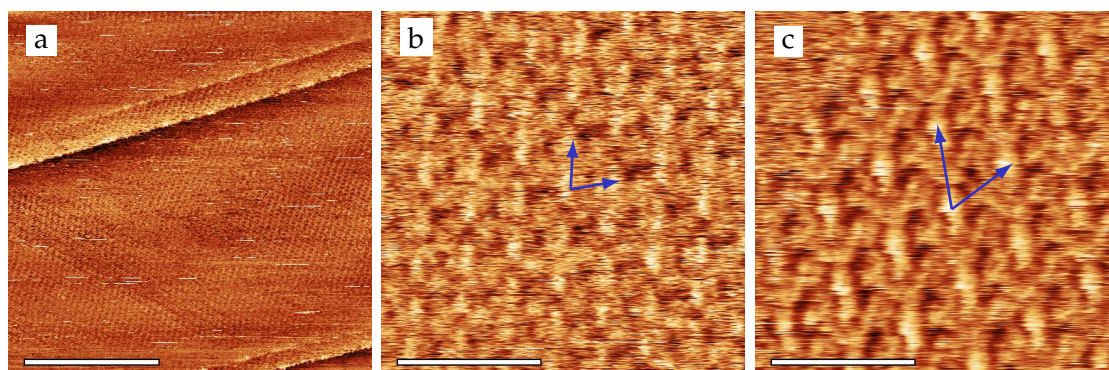


Figure 4.16 Ambient STM images for TIPB on graphite: (a) large domain of ordered TIPB on graphite steps with a step height of 0.36 ± 0.07 nm [scale bar is 30 nm]; (b) lattice with unit cell of 1.30 ± 0.01 nm by 1.34 ± 0.02 nm ($72.7 \pm 0.8^\circ$) [scale bar is 4 nm]; (c) lattice with unit cell of 2.17 ± 0.02 nm by 1.91 ± 0.02 nm ($63 \pm 1^\circ$) [scale bar is 4 nm]. All images obtained with bias voltage of -1 V and current of 35 pA.

The sample had approximately a monolayer coverage and domains were modified with continual scanning. The lattices seen in Figure 4.16 are extended between step edges forming large ordered domains. Several different structures were seen on the surface. The lattices observed in Figure 4.16 (b) and (c) were modelled as a packing of TIPB monomers in Figure 4.17. The structure seen in Figure 4.17 (a) is similar to phase III shown in Table 4.6 and the unheated solution deposited sample shown in Figure 4.4 although the molecules are much wider spaced to give a very low packing density of 0.40 nm^{-2} .

There are two possible structures overlaid on Figure 4.16 (c). The first, shown in Figure 4.17 (b), places TIPB monomers over the arrowheads, however, this gives a very low packing density of $0.37 \pm 0.01 \text{ nm}^{-2}$ which, whilst similar to the density for the model in Figure 4.17 (a), is extremely low suggesting that the apparent arrowheads are not the individual monomers. An alternative packing is shown in Figure 4.17

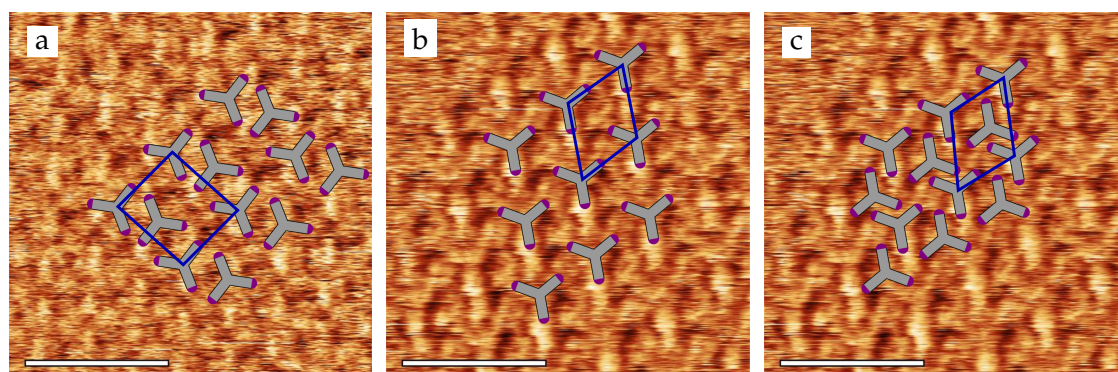


Figure 4.17 Images shown in Figure 4.16 with overlays of the theorised molecular structures: (a) structure with unit cell 2.49 ± 0.05 nm by 2.18 ± 0.02 nm ($84 \pm 2^\circ$); (b) structure with unit cell 2.10 ± 0.02 nm by 1.90 ± 0.02 nm ($43 \pm 2^\circ$); (c) structure with unit cell 1.87 ± 0.01 nm by 2.15 ± 0.01 nm ($51 \pm 2^\circ$) [scale bars are 4 nm].

(c) which is a halfway structure between the sine-wave and the bow-tie structures seen in Table 4.1. The packing density of this structure is 0.64 ± 0.01 nm⁻² which is much closer to the packing density seen for the hybrid dimer structure. The change in molecular arrangement could be due to interactions with the underlying surface or a loss of iodine. Unlike the other structure, this structure is not similar to any of those previously seen.

4.4 Summary

A variety of structures were formed by TIPB on HOPG and hBN surfaces. A summary of the structures seen on hBN is shown in Table 4.8. The majority of the monomer structures are minor alterations to the previously observed sine-wave structure named after the pattern formed by the iodine atoms under STM.

Following the AFM evidence of polymerisation around 120 °C and 140 °C, the dehalogenation of the molecules on the surface was investigated with XPS. This found evidence of the loss of iodine without equivalent proportional loss of carbon suggesting that the molecules were dehalogenating on the surface but not leaving the surface at the temperatures polymerisation was believed to be occurring at. OrbiSIMS was then carried out to investigate the polymerisation products. This confirmed the increased presence of dimer and trimer TIPB species for the 100 °C and 120 °C samples compared to the unheated sample. The SIMS also showed the presence of dimer and trimer

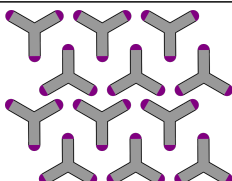
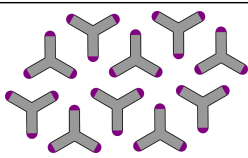
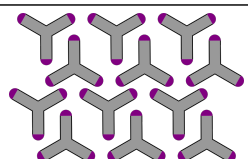
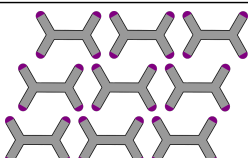
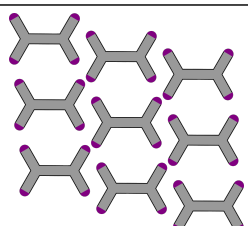
Lattice Phase	Unit Lattice	Model	Samples
Sine-Wave	2.0 ± 0.1 nm by 1.6 ± 0.1 nm		Vacuum Phase I & IV
Alternative Sine-Wave	2.00 ± 0.05 nm by 1.80 ± 0.06 nm		Solution - Unheated, Vacuum Phase III
Skewed Sine-Wave	1.7 ± 0.2 nm by 1.4 ± 0.2 nm		Solution - 120 °C, Vacuum Phase II
Linear Dimer	1.70 ± 0.05 nm by 2.35 ± 0.05 nm		Solution - 120 °C
Non-Linear Dimer	2.25 ± 0.05 nm by 1.95 ± 0.05 nm		Solution - 140 °C

Table 4.8 The structures formed by TIPB on hBN observed in this work.

species containing additional iodine which suggested the polymerisation reaction did not occur following loss of I_2 from neighbouring molecules but via a transition stage containing an additional iodine.

Further AFM work could be done at low temperature to investigate the structures formed by the annealing process as the reduced temperature should stabilise the structures. Higher resolution XPS work could be carried out to investigate the carbon 1s peak which should contain contributions from the C–C and the C–I bonds within the TIPB molecule; a reduction in the C–I contribution would be expected without equivalent reduction in the C–C contribution. The mass spectrometry results should be explored further by carrying out MS/MS to fragment selected peaks to investigate the structure of the dimer and trimer peaks containing additional iodine. This could

confirm the presence of a transition stage. Isolation of the dimer with additional iodine in the Orbitrap for an extended period of time would also indicate the stability of this species. Furthermore, the adsorption of TIPB onto the hBN surface should be modelled and the dehalogenation energy on the surface should be calculated.

The preliminary results obtained on HOPG provide a proof-of-concept for the deposition of TIPB from solution onto this surface and require further study.

5 The deposition of melamine on hexagonal boron nitride

Melamine (1,3,5-triazine-2,4,6-triamine) is a small highly symmetric triangular molecule as shown in Figure 5.1. It is a common precursor for materials such as formica laminate which has been widely used as electrical insulation. In surface science, melamine has been observed to form large hydrogen-bonded structures due to the high proportion of hydrogen-bonding atoms.

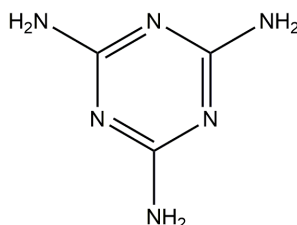


Figure 5.1 The structure of melamine.

Melamine has mostly been studied in hydrogen-bonded networks with other molecules such as cyanuric acid^{27,28} and perylenetetracarboxylic diimide (PTCDI)^{21,24,80}. Previous work done with melamine as a monomolecular network has generally involved solution deposition onto a metal^{30,31,81,82} or HOPG^{27,28} surface which is then imaged with STM. Three different melamine assemblies (α , β , γ) have been reported previously, as shown in Figure 5.2 and discussed fully in Subsection 2.2.1. The α porous structure is potentially of interest as a template for other molecular structures such as C_{60} . Additionally, melamine has been seen to adsorb vertically on Cu(111).³²

	α	β	γ
a (nm)	1.042	1.20	1.042
b (nm)	1.042	0.77	1.733
θ ($^\circ$)	120	65.3	106.1
Density (nm ⁻²)	2.123	2.382	2.306

Table 5.1 Lattice parameters for melamine assemblies shown in Figure 5.2.^{30,31}

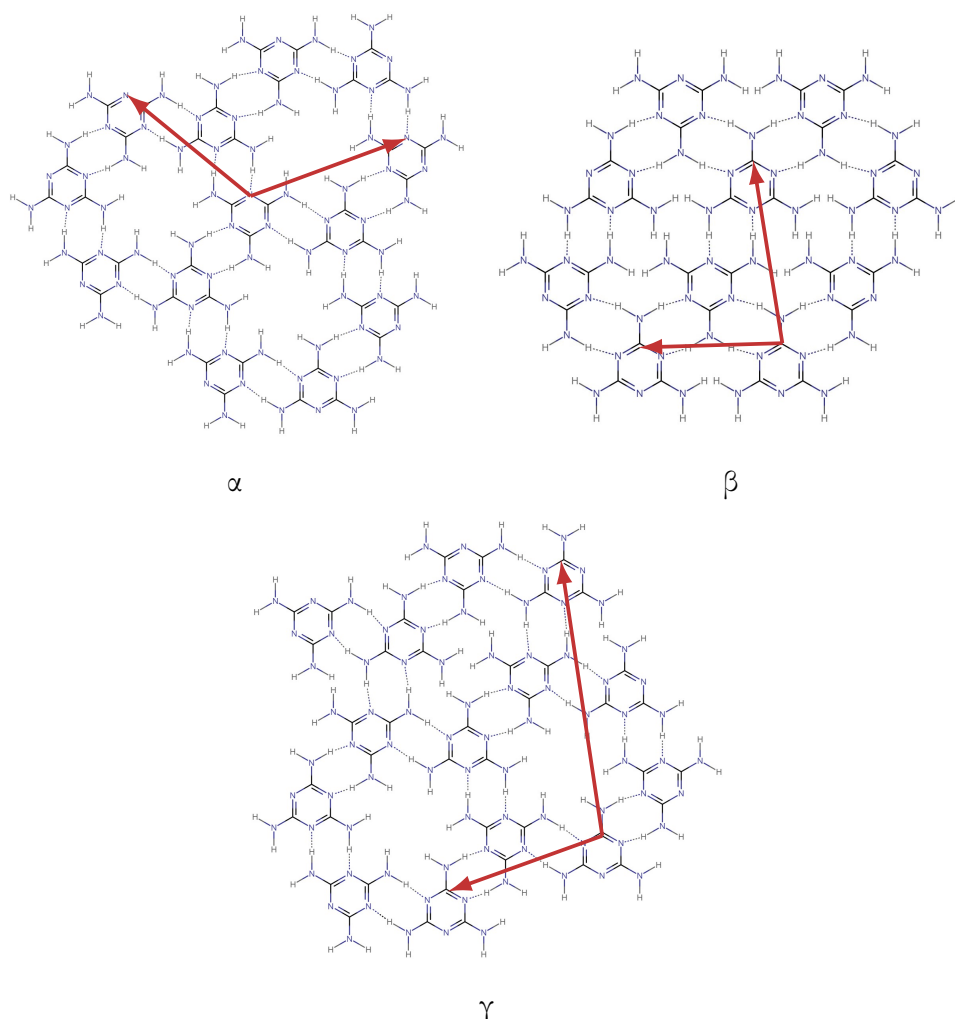


Figure 5.2 The α , β , and γ assemblies formed by melamine on Au(111) and Ag(111).^{30,31} Hydrogen bonds are denoted by dotted lines.

The melamine assemblies have different molecular densities which may cause distinct structures to be observed for specific preparation methods. The α structure has the lowest density and the β structure has the highest density. The substrate surface structure has also been observed to affect the molecular arrangements; melamine on the Ag(111) surface was seen to have preferential adsorption sites with the rings aligned to the silver adatoms.³¹

The adsorption of melamine on metal surfaces was modelled by Šimenas and Tornau⁸³ who found that the α assembly is the preferred outcome at low coverages as it has symmetric hydrogen bonding (a 120° angle between the central molecule and the three neighbouring molecules). At higher coverage, the β model was found to be favoured on the Ag(111) and Au(111) surfaces.

Melamine in Bulk

The 3D bulk structure of melamine has been studied with X-ray^{84,85} and neutron^{85,86} diffraction. The structure is shown in Figure 5.3. The molecule is nearly planar with pyrimidal amine groups that are disordered at room temperature and have been observed to break the symmetry of the molecule when studied at low temperature.⁸⁶ The observed bulk structure is very similar to the β assembly seen on surfaces. The main difference is the β assembly is believed to be fully planar due to surface-molecule interactions.

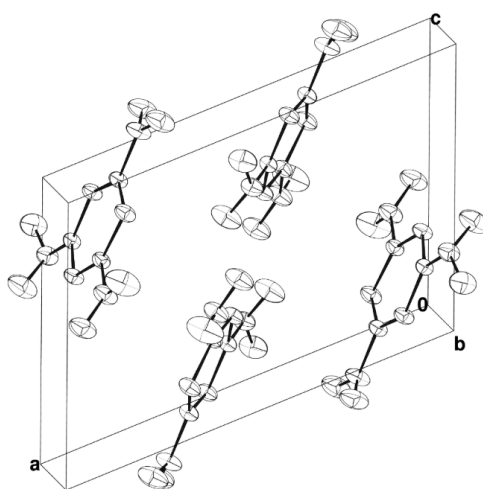


Figure 5.3 The bulk structure of melamine with $a = 1.0573 \pm 0.0006$ nm, $b = 0.7463 \pm 0.0006$ nm, $c = 0.7268 \pm 0.0005$ nm, and β (angle between b and c) = $112.4 \pm 0.2^\circ$ (at 293 K). Reproduced from reference 86.

5.1 Deposition of a Thick Film

Melamine (Sigma Aldrich 99% purity) was deposited onto hBN/SiO₂ in a vacuum system with a base pressure of $\sim 10^{-6}$ mbar. Initially, the melamine was placed in a Knudsen cell and annealed to 100 °C for 1 h to outgas any water. For the depositions, the Knudsen cell was heated to approximately 90 °C and a shutter was used to control the amount of material reaching the sample surface. The deposition rate was measured using a quartz crystal thickness monitor which was calibrated by depositing a thick film of melamine. As measured with the quartz crystal, 10 nm was deposited over 38 min which resulted in a surface as shown in Figure 5.4. From this, the island height

was measured to be 21 ± 4 nm. From the island height and the percentage coverage (70%), a tooling factor was calculated which was used to calculate the actual deposited thickness from the monitor for all subsequent samples.

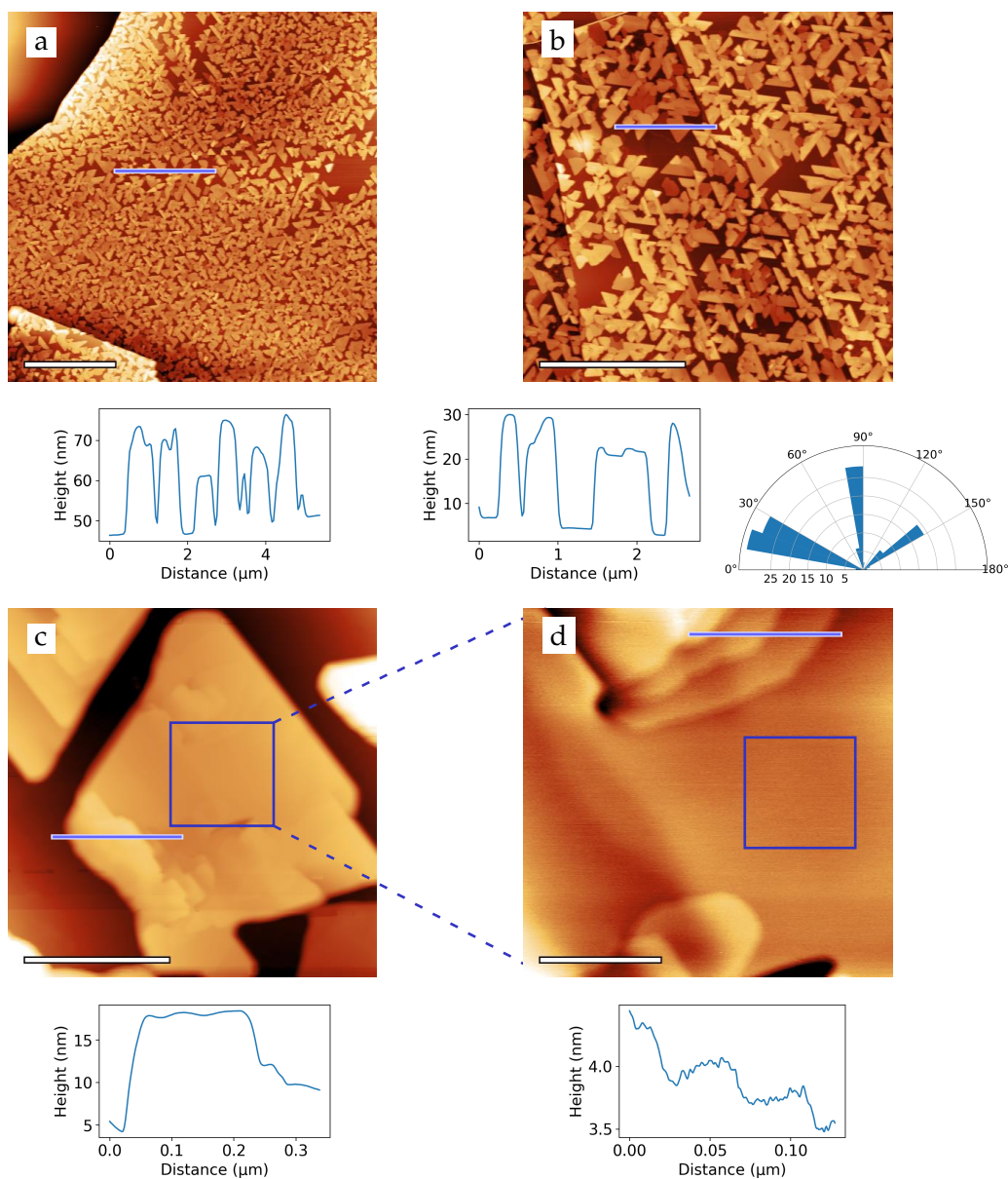


Figure 5.4 Topographic images of a thick film of melamine on the hBN surface: (a) the edge of the hBN flake 51 ± 1 nm and a hBN step of 48 ± 5 nm [scale bar is $5 \mu\text{m}$]; (b) melamine islands of varying height from 8 nm to 30 nm (average height of 21 ± 4 nm) with a profile across the blue line and a histogram of island orientation shown below [scale bar is $4 \mu\text{m}$]; (c) central 18 ± 1 nm high melamine island $0.69 \pm 0.01 \mu\text{m}$ by $0.7 \pm 0.1 \mu\text{m}$ and a bottom right island 10.3 ± 0.7 nm high with a profile across the blue line showing steps of 2.2 ± 0.4 nm and 5.8 ± 0.4 nm below [scale bar is 400 nm]; (d) the area in the blue square on (c) with steps 0.31 ± 0.08 nm high at the top of the image as shown in the profile below the image [scale bar is 100 nm].

The thick film islands show a triangular geometry with island edges subtended by $60 \pm 1^\circ$ matching the molecular structure and expected bonding (assuming the α structure). There is a preferential orientation for the islands relative to the substrate. The island orientations relative to the horizontal were measured on Figure 5.4 (b) and a histogram of these orientations is shown in Figure 5.4. This shows some equally spaced preferred orientations at approximately 20° , 80° and 140° with greatest spread around the 20° peak. The consistency in orientation suggest that the islands align with the underlying hBN lattice which also has a threefold symmetry.

The top surface of the islands were not completely flat; steps and facets are visible in Figure 5.4 (c). The minimum step height as shown in Figure 5.4 (d) was 0.31 ± 0.08 nm which matches the height generally observed on AFM for molecules lying flat on the surface.

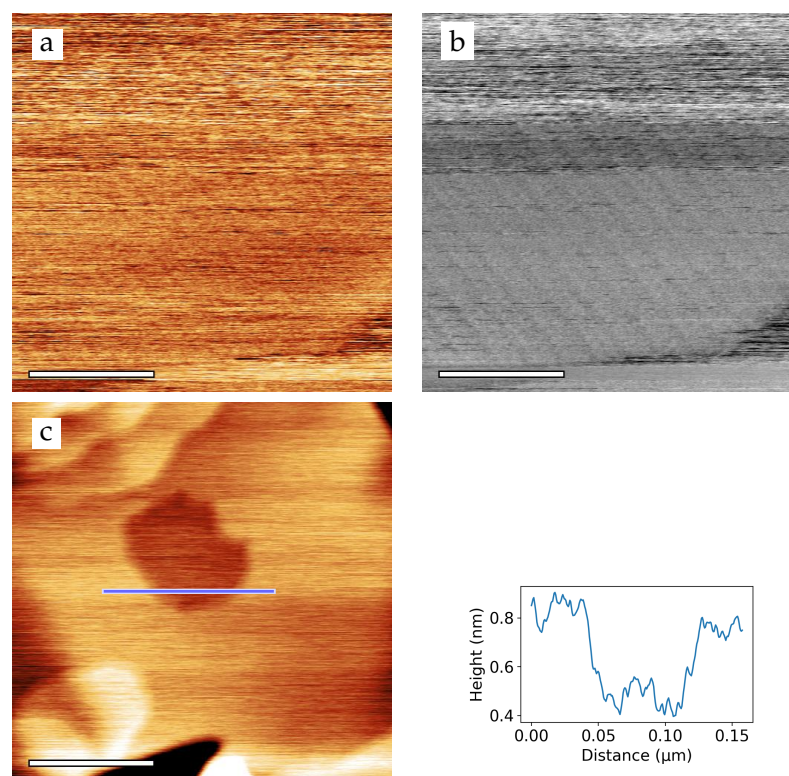


Figure 5.5 Images from a thick island of melamine: (a) topographic image and (b) phase image of detailed structure, lattice is 2.02 ± 0.06 nm by 0.77 ± 0.03 nm ($85 \pm 6^\circ$) [scale bar is 10 nm]; (c) topographic image showing a 0.38 ± 0.08 nm deep hole over area scanned, profile along the blue line shown to the right [scale bar is 100 nm].

Higher resolution scans acquired on top of the thick islands, shown in Figure 5.5, reveal a regular structure with lattice vectors of 2.02 ± 0.06 nm and 0.77 ± 0.03 nm

subtended by $85 \pm 6^\circ$. The larger lattice dimension is shown most clearly in the bottom half of the image and the smaller dimension is clearest at the top of the image where the AFM tip was in a slightly different condition. The smaller lattice dimension is similar to one of the dimensions seen for the unit cell in bulk however the other lattice dimension is approximately double the bulk unit cell. If the structure corresponded to the bulk, the doubling of the dimension may be due to a multi-layer effect. However, the dimensions and orientation of the bulk do not match the observed structure overall.

The imaging shown in Figure 5.5 (a) and (b) results in modification to the surface as shown in (c). The layer removed was 0.38 ± 0.08 nm deep which implies the removal of a monolayer, suggesting that the inter-layer bonding is fairly weak. This also indicates that the molecules are fairly mobile as there is no raised area on the sides of the hole as would be expected from the tip moving material to the edge of the scan. Another possible explanation for the lack of material build-up is that it is migrating to the AFM tip.

Melamine was also resolved as a thinner layer between the large islands shown in Figure 5.4 with structures seen most clearly in the phase images. The structure in Figure 5.6 (b) has two areas of periodic structure (2.3 ± 0.2 nm separation) indicated by the red lines. These areas are misaligned by an angle of $67 \pm 4^\circ$. The two structures in Figure 5.6 (d) are misaligned by $113 \pm 3^\circ$ corresponding to the same lattice alignment as $67 \pm 4^\circ$. The bottom lattice has lattice vectors of 2.22 ± 0.03 nm and 2.10 ± 0.09 nm subtended by $81 \pm 1^\circ$. This thin film was not very stable under scanning as is shown by the areas of tip changes on Figure 5.6 (a) and (b); this made obtaining high resolution images difficult.

5.2 Deposition of Thin Films

5.2.1 Square Lattice of Melamine on RT hBN

Thin films of melamine were deposited using the tooling factor found from the thick film deposition of 1.4 to calculate the thickness deposited. The thin films varied from 0.3 ML to 3 ML with short exposure times required due to the rate of sublimation of

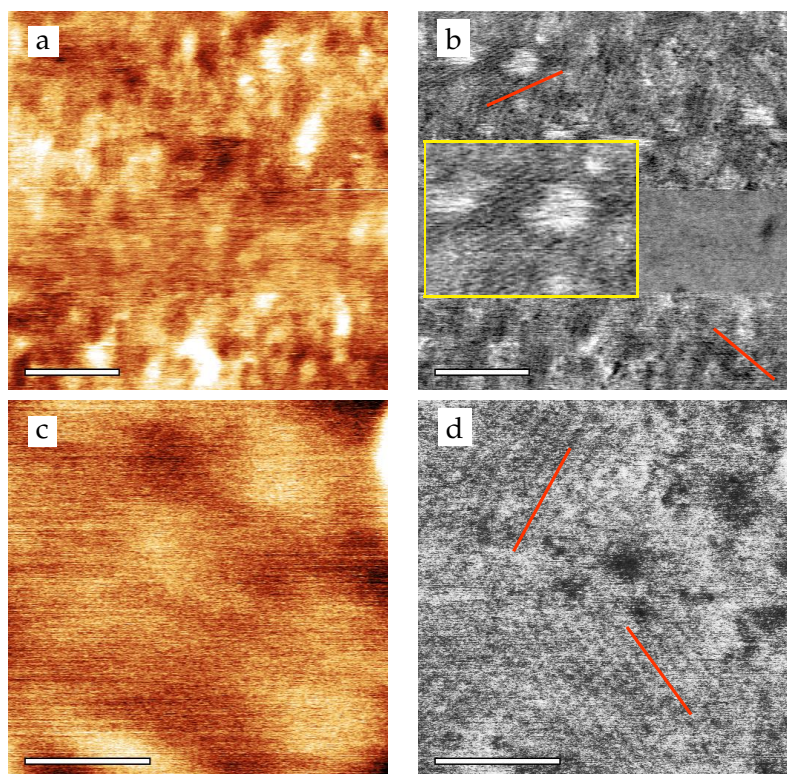


Figure 5.6 Images from areas between melamine islands: (a) topographic image showing a section of tip change mid-image [scale bar is 50 nm]; (b) phase image of the area in (a) showing periodic structure (indicated by red lines) separated by 2.3 ± 0.2 nm in the upper left area which is shown in yellow box and 2.2 ± 0.2 nm in the lower right area [scale bar is 50 nm]; (c) topographic image showing no clear structure [scale bar is 20 nm]; (d) phase image of (c) showing two areas of a lattice offset by $118 \pm 3^\circ$ with lattice vectors for the bottom lattice of 2.22 ± 0.03 nm and 2.10 ± 0.09 nm ($81 \pm 1^\circ$) and only one measureable lattice vector for the top lattice of 1.9 ± 0.2 nm [scale bar is 20 nm].

melamine from the Knudsen cell even at the low temperatures used. Firstly, a 3 ML film was deposited via a 2 minute exposure with the Knudsen cell held at 90°C . This formed a near continuous film with ordered growth as shown in Figure 5.7.

Figure 5.7 (a) shows a thin film of melamine 0.23 ± 0.04 nm high which covers 89% of the surface in a near continuous island. This height corresponds to a monolayer coverage rather than the expected 3 ML coverage however the measured thickness may be for the incomplete third layer on top of two underlying continuous layers or reflect an inaccuracy in the deposition parameters. Within this island, areas of ordered structure were seen with an average lattice of 2.20 ± 0.07 nm by 2.19 ± 0.02 nm subtended by $82 \pm 2^\circ$. In some of the images obtained the dominant lattice direction in the phase images was observed to be perpendicular to the dominant direction in

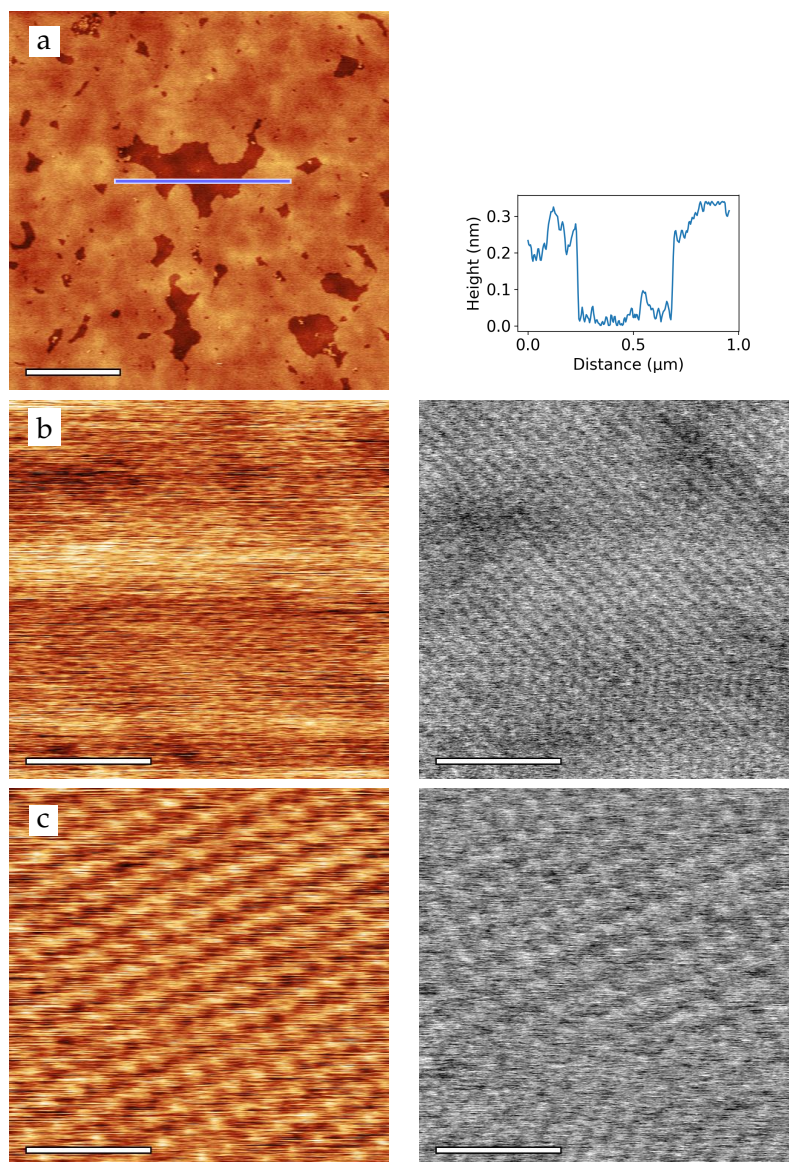


Figure 5.7 A 3 ML film of melamine deposited on hBN: (a) topographic image of island 0.23 ± 0.04 nm high with 89% coverage, inset is a profile along the white line [scale bar is 500 nm]; (b) topographic and phase images with lattice 2.119 ± 0.006 nm by 2.18 ± 0.05 nm ($80 \pm 3^\circ$) [scale bar is 20 nm]; (c) topographic and phase images with measured lattices of 2.25 ± 0.01 nm by 2.20 ± 0.01 nm ($83.5 \pm 0.3^\circ$) [scale bar is 10 nm].

the topographic images, as seen in Figure 5.7 (b), whereas in the majority of images, as seen in Figure 5.7 (c), the lattice seen in the phase was the same orientation and period as the topography.

Samples with sub-monolayer coverages were also grown. A sample with 0.5 ML was prepared from a 18 s exposure with the Knudsen cell held at 90°C . As expected, this formed a non-continuous layer with smaller islands as shown in Figure 5.8 with a coverage which ranged from 60% to 90% across different areas on the sample. At all

coverages, the islands appear quite square in geometry, with this being clearer in areas with lower observed coverage. Some variety in island height was observed, with island height varying from 0.3 nm to 0.6 nm corresponding to 1 ML and 2 ML respectively. This may be due to scanning conditions or it may suggest that the growth of a second layer occurs before a continuous monolayer has formed. The island edges also have some preferential orientation as shown by the histograms in Figure 5.8 although this is not as strong as for the thick film islands. Ordered structures were seen within these islands as shown in Figure 5.9 and Figure 5.10.

Figure 5.9 shows an intersection of three island lattices with different orientations. The orientations are separated by $24 \pm 1^\circ$ which is less than the expected 30° if all islands were aligned with the underlying hexagonal boron nitride surface. The three lattices are consistent in their dimensions with average lattice vectors for all orientations of 2.19 ± 0.03 nm and 2.20 ± 0.03 nm subtended by $88 \pm 6^\circ$. The fast Fourier transform also shows the consistency in lattice size between the orientations as they show up as points within the same ring but also shows the asymmetry in orientation. Higher resolution images of the lattice were obtained as shown in Figure 5.10. This lattice was stable under imaging and high quality images of the lattice could be obtained even in large scale images.

The lattices shown in Figure 5.10 measured in different areas of the sample are consistent with an average lattice of 2.22 ± 0.05 nm by 2.15 ± 0.09 nm subtended by $81 \pm 3^\circ$. This is close to that seen for the lattices in Figure 5.9 and the lattice seen in between islands in Figure 5.7. This implies that this is the preferred structure when the melamine is in a thin film on the boron nitride surface. This is a larger lattice than previously seen on other surfaces thus modelling proved difficult. Initially, a version of the γ structure shown in Figure 5.2 was believed to be a good model as this was observed to appear square in STM by Schmitz et al.³¹ however this model would be unlikely to give the lattice vectors and rotational symmetry observed. In the end, the observed square lattice was modelled as shown in Figure 5.11.

This structure has rings that are similar to the α structure, although the exact positioning is different in order to align the melamine molecules in an electrostatically

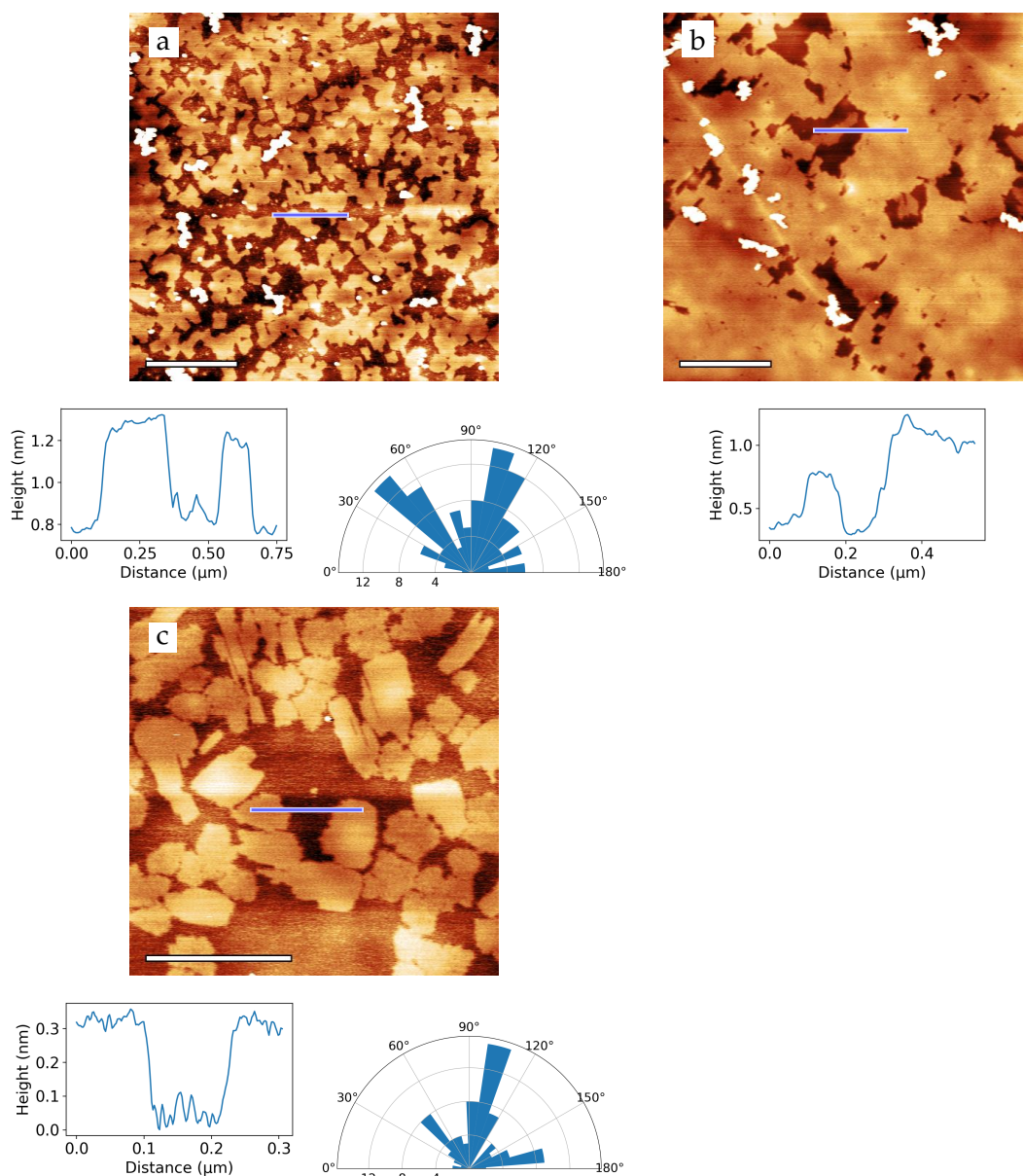


Figure 5.8 Topographic images of a 0.5 ML melamine film on the hBN surface: (a) islands 0.40 ± 0.07 nm high covering $\sim 90\%$ of the surface with a profile along the blue line and a histogram of island edge orientation below [scale bar is 1 μm]; (b) area of near continuous island 0.6 ± 0.1 nm high covering $\sim 88\%$ of the surface with a profile along the blue line below [scale bar is 500 nm]; (c) an area of more distinct square islands 0.27 ± 0.03 nm high covering $\sim 60\%$ of the surface, below is a profile along the blue line and a histogram of island edge orientation [scale bar is 400 nm].

favourable position over the hBN surface. In between the rings are small areas that correspond to the β structure. The lattice vectors with respect to the image in Figure 5.11 (b) are 2.52 ± 0.06 nm and 2.08 ± 0.05 nm which are slightly larger than those previously measured in Figure 5.10 but in good agreement with the image under the model.

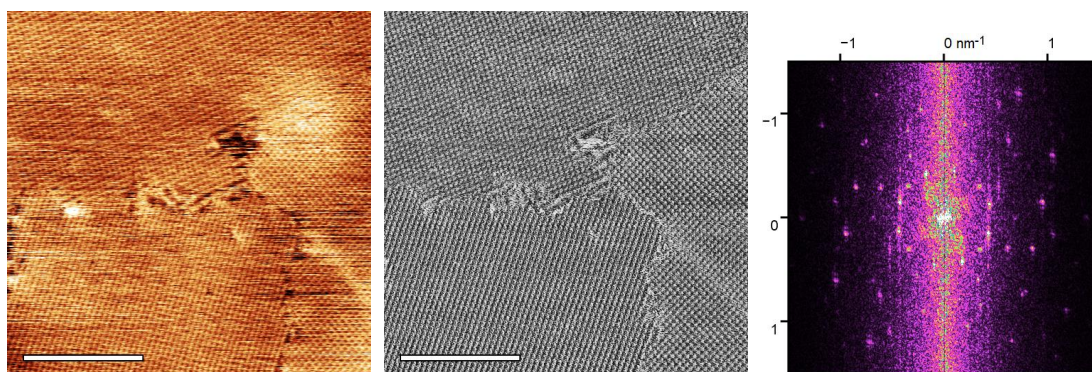


Figure 5.9 Topographic, phase, and FFT images of an area of the 0.5 ML melamine film showing three orientations ($23.0 \pm 0.3^\circ$, $71.0 \pm 0.3^\circ$, and $46 \pm 1^\circ$) of a lattice structure measured to be (from top anti-clockwise) 2.18 ± 0.04 nm by 2.20 ± 0.01 nm with $84 \pm 1^\circ$, 2.21 ± 0.03 nm by 2.18 ± 0.01 nm with $83 \pm 1^\circ$ and 2.21 ± 0.04 nm by 2.19 ± 0.03 nm with $86 \pm 2^\circ$ [scale bar is 50 nm].

The lattice vectors for the lattice measured with respect to the hBN lattice are 2.04 ± 0.01 nm and 2.37 ± 0.04 nm which has a much better agreement for the lattice vectors measured in Figure 5.10. This gives a packing density of $2.2 \pm 0.3 \text{ nm}^{-2}$ which is close to the γ structure previously seen. The overlay in Figure 5.12 also clearly shows that this arrangement can give electrostatically favourable positions with nitrogen atoms over boron in the underlying hBN wherever possible with electrostatically unfavourable positions avoided.

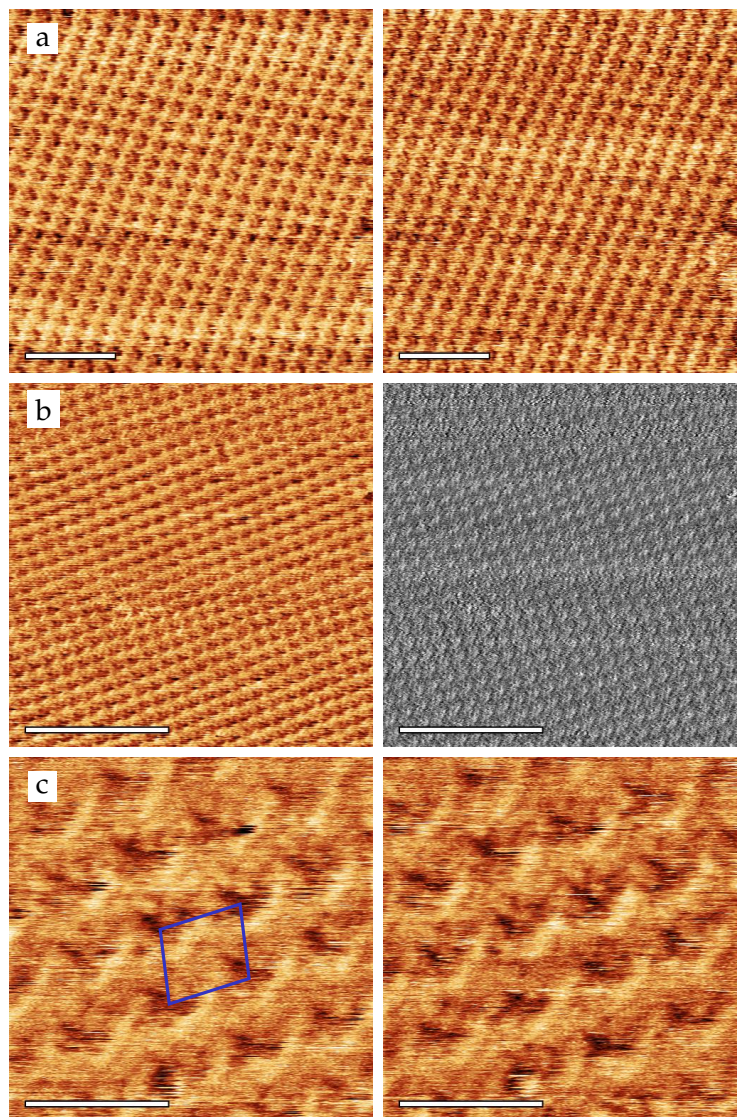


Figure 5.10 Higher resolution images of the 0.5 ML melamine film showing a square lattice structure: (a) topographic (trace and retrace) images with lattice measured to be 2.20 ± 0.01 nm by 2.18 ± 0.01 nm with $78.2 \pm 0.1^\circ$ [scale bar is 10 nm]; (b) topographic and phase images with lattice measured to be 2.21 ± 0.01 nm by 2.14 ± 0.01 nm with $83.7 \pm 0.2^\circ$ [scale bar is 20 nm]; (c) topographic (trace and retrace) images with lattice shown in blue measured to be 2.29 ± 0.02 nm by 2.02 ± 0.01 nm with $78 \pm 1^\circ$ [scale bar is 4 nm].

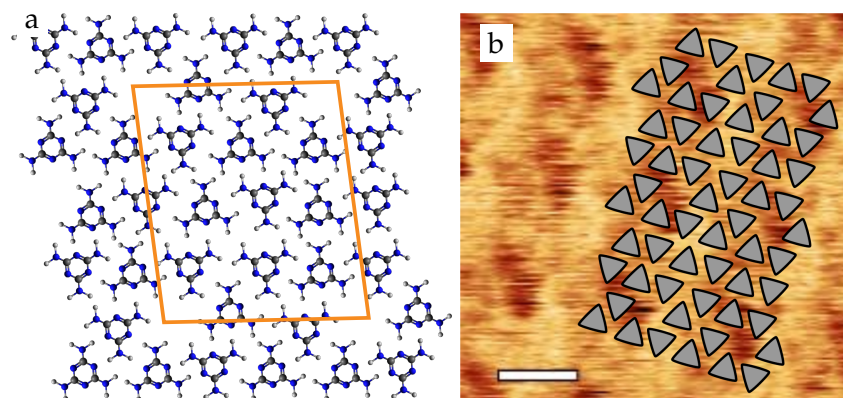


Figure 5.11 (a) The square model that fits the images shown in Figure 5.10 with the unit cell marked in orange; (b) the model overlaid on a topographic image of the 0.5 ML melamine film with lattice vectors of 2.52 ± 0.06 nm and 2.08 ± 0.05 nm ($98 \pm 1^\circ$) [scale bar is 1.6 nm].

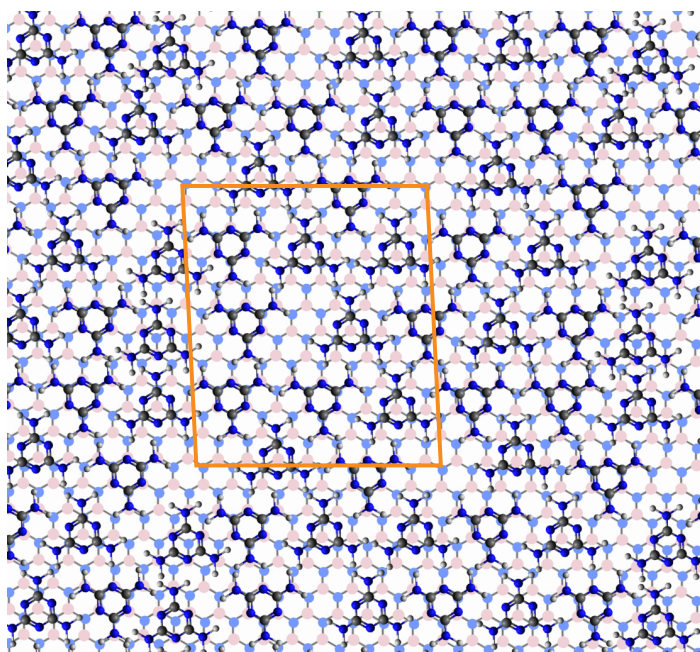


Figure 5.12 The square model seen in Figure 5.11 overlaid on a hBN lattice with lattice vectors of 2.04 ± 0.01 nm and 2.37 ± 0.04 nm ($85 \pm 1^\circ$).

5.2.2 Rhombic Lattice of Melamine on room temperature hBN

A sample with intermediate coverage, 1.5 ML, was prepared by exposing a hBN/SiO₂ sample for 16 s to a Knudsen cell held at 105 °C. The Knudsen cell was taken to a higher temperature in order to maintain a constant deposition rate. The resultant thin film had a lower apparent coverage (38%) than expected, as seen in Figure 5.13 (a), which could be explained as the growth of a second layer over a continuous monolayer. The island height in Figure 5.13 (a) corresponds to that of a monolayer of material. This, along with a lack of difference between the background and the upper layer in the phase images, supports the idea that this is the growth of a second layer.

The islands on the 1.5 ML sample are elongated with a preferential growth in one direction, shown clearly in Figure 5.13 (b). Within the islands a lattice, marked with a yellow rhombus in Figure 5.13 (c), was observed with lattice vectors of 0.87 ± 0.01 nm and 0.89 ± 0.01 nm subtended by $60.5 \pm 0.2^\circ$. This lattice also has periodic brighter line of 2.67 ± 0.01 nm which may be due to an interaction between the two layers of melamine. Submolecular resolution was achieved and shows three pronged units orientated in the same direction seen most clearly in the phase image. The average prong-to-prong distance is 0.62 ± 0.06 nm which is in good agreement with the van der Waals surface of the melamine molecule which is approximately 0.56 nm. This lattice could be explained by the proposed structure shown in Figure 5.14 which is also shown overlaid on the lattice in Figure 5.13 (c).

This structure shown in Figure 5.14 corresponds to a symmetry in which all melamine molecules have a common orientation. In this model, the molecules would be unlikely to be stabilised via hydrogen bonding as this requires a co-linear arrangement of donor and acceptor atoms which cannot be realised with molecules lying flat on the surface. Although unlikely to be this close, using known bond lengths for melamine⁸⁵ and the hydrogen bond length seen for base pair N...H bonds,⁸⁷ the theoretical minimum period of this lattice was estimated to be 0.74 nm. This is less than the period seen on the surface suggesting that other effects such as interactions with the substrate or lower layers dominate. The difference in lattice vectors between the theoretical minimum (0.74 nm) and those observed (0.88 ± 0.02 nm) suggests that some

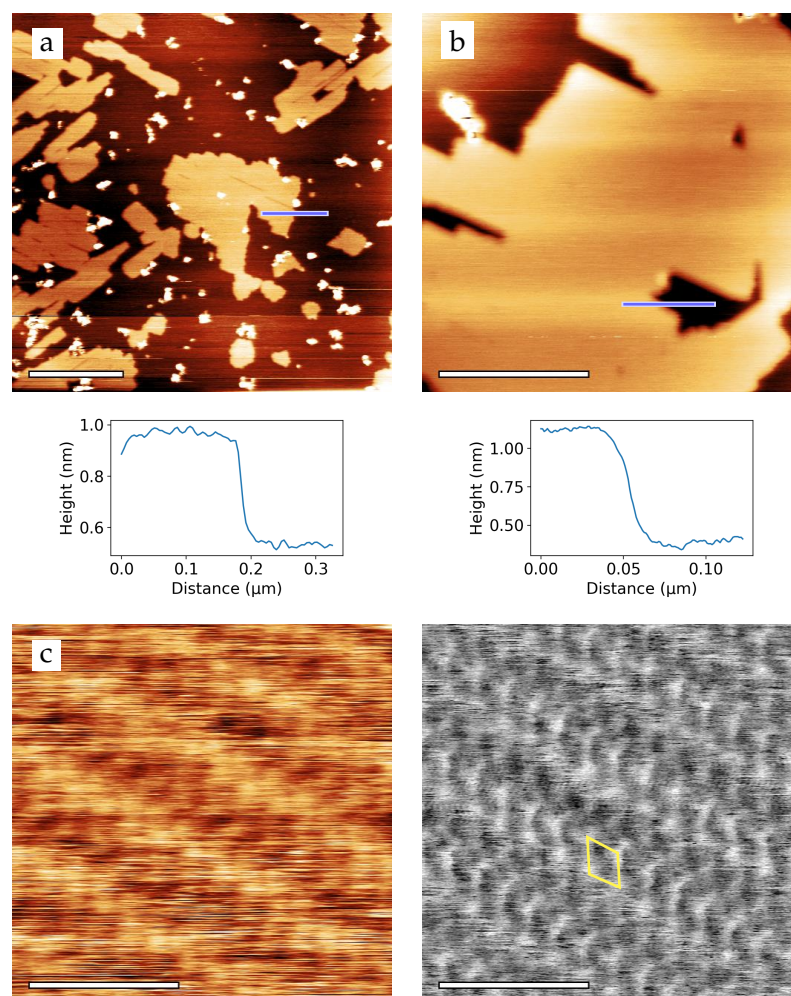


Figure 5.13 A 1.5 ML melamine film: (a) topographic image showing island 0.45 ± 0.04 nm high covering 38% with a profile along the blue line below [scale bar is 500 nm]; (b) topographic image showing island 0.61 ± 0.04 nm high covering 84% with a profile along the blue line below [scale bar is 200 nm]; (c) topographic and phase images with measured lattice of 0.87 ± 0.01 nm by 2.67 ± 0.01 nm ($60.4 \pm 0.2^\circ$) with a clearer lattice in the phase of 0.87 ± 0.01 nm by 0.89 ± 0.01 nm ($60.5 \pm 0.2^\circ$) [scale bar is 4 nm].

alignment with the hBN surface may be extending the lattice. To explore this, the model was overlaid with a hBN lattice. The arrangement that gives the correct alignment of the melamine molecules with threefold symmetry is shown in Figure 5.15. This arrangement has lattice vectors of 0.86 ± 0.02 nm subtended by $59.5 \pm 0.4^\circ$. The lattice has a lower packing density than any of the previous structures outlined in Table 5.1 with a packing density of 1.56 ± 0.06 nm⁻². This alignment places nitrogen atoms over the boron atoms and carbon over the nitrogen atoms which could provide electrostatic stabilisation.

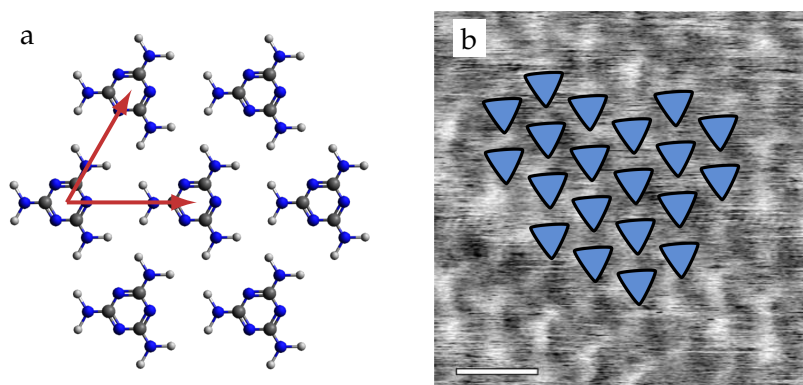


Figure 5.14 The possible molecular structure shown in Figure 5.13c: (a) the model as calculated from known bond lengths; (b) the melamine (represented as triangles) model overlaid on the phase image from Figure 5.13 (c) [scale bar is 1.4 nm].

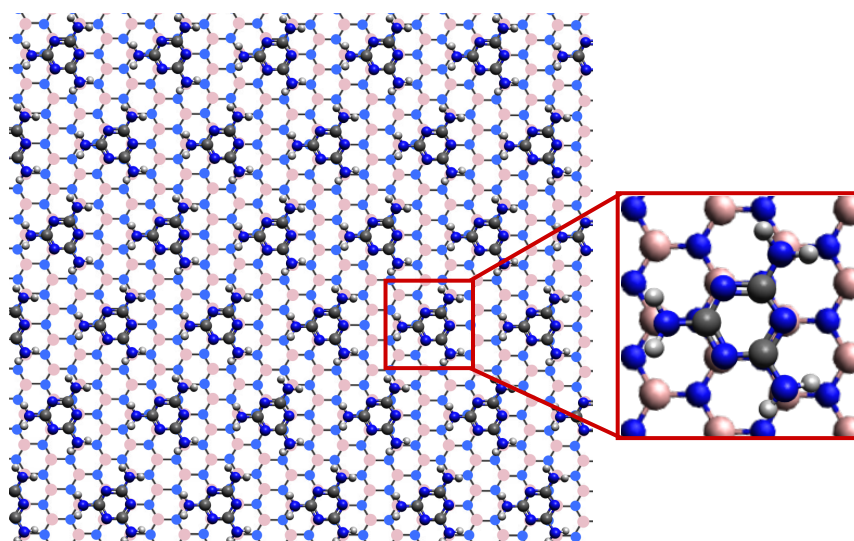


Figure 5.15 The melamine hexagonal lattice seen in Figure 5.14 overlaid on a hBN lattice (boron shown in pink, nitrogen in blue). A zoomed in view of a melamine molecule shows the arrangement over the boron nitride ring.

5.2.3 Observed Moiré Pattern for Melamine on room temperature hBN

Whilst trying to reduce the material deposited to further investigate the structure seen in Subsection 5.2.1, a sample was prepared by exposing a hBN/SiO₂ surface for 30 s to the Knudsen cell held at 90 °C to deposit 1 ML. This formed a continuous film with ordered growth as shown in Figure 5.16.

Figure 5.16 (a) shows the layer of melamine to be 0.18 ± 0.04 nm thick as measured using the cracks in the surface; this is slightly lower than the usual 0.3 nm expected for a monolayer, which may be due to the tip set-point. In this sample a continuous layer has formed with small areas of a second layer also present. Figure 5.16 (b) and (c) show a

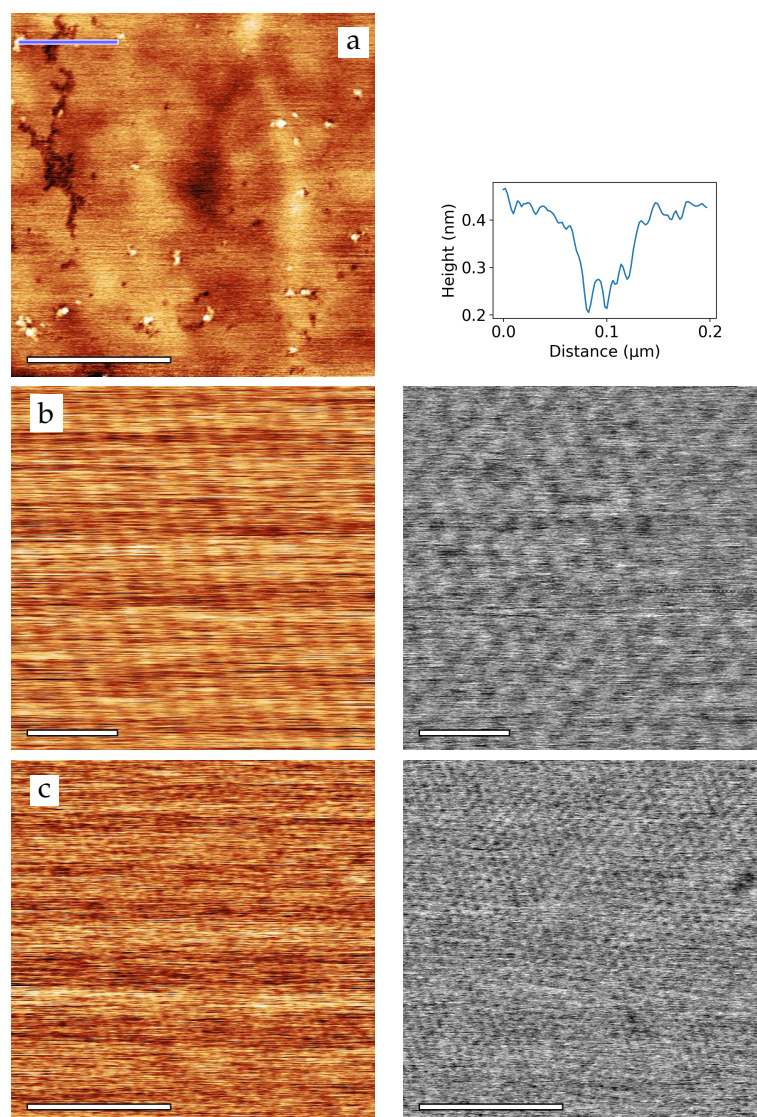


Figure 5.16 A 1 ML film of melamine deposited on hBN: (a) topographic image showing an island 0.18 ± 0.04 nm thick with a profile along the blue line to the right [scale bar is 400 nm]; (b) topographic and phase images with a lattice measured to be 3.18 ± 0.03 nm by 3.17 ± 0.01 nm with $119.7 \pm 0.7^\circ$ [scale bar is 10 nm]; (c) topographic and phase images with measured lattice of 3.20 ± 0.02 nm by 3.21 ± 0.02 nm ($60.3 \pm 0.5^\circ$) [scale bar is 40 nm].

hexagonal lattice of 3.19 ± 0.03 nm by 3.19 ± 0.02 nm subtended by $119.7 \pm 0.5^\circ$. It was initially unclear how an arrangement of melamine molecules could form an array with such a large lattice constant. However, it was then realised that the observed lattice could be a moiré pattern formed from the rhombic melamine lattice in Subsection 5.2.2 and the hBN lattice which could give a much larger lattice constant than the lattice vectors of either constituent lattice.

The lattice seen in Subsection 5.2.2 rotated with respect to the hBN surface could lead to the appearance of a moiré pattern in the AFM images of the system. To confirm whether this could lead to the lattice seen in Figure 5.16, a model was made by rotating the melamine hexagonal structure previously modelled aligned with the hBN lattice as shown in Figure 5.15. The resulting overlay at a rotation of 18.43° is shown in Figure 5.17. As with the model shown in Figure 5.15, the model has nitrogen atoms sitting over boron atoms in the aligned rings. This model of melamine is also overlaid on an area of Figure 5.16 (b). The implications of this are that the melamine formed a monolayer on the hBN surface with the same dimensions as for complete alignment of melamine rings to the hBN rings but with misalignment of some of the melamine rings. This may have been due to defects in either the hBN lattice or the melamine lattice which lead to an initial misalignment which then found an energy minima in this structure.

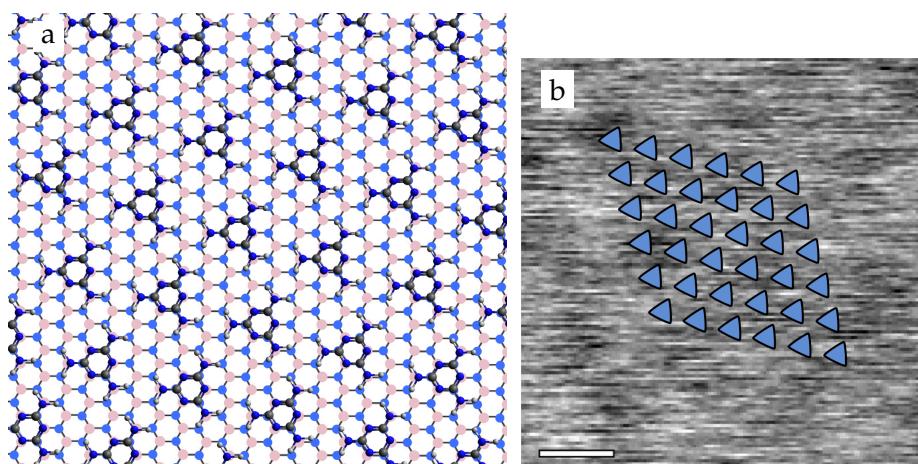


Figure 5.17 The structure seen as a moiré pattern: (a) the 18.43° rotation of the hexagonal melamine lattice adjusted to sit with nitrogen atoms over boron atoms; (b) an overlay of the melamine molecules on an area of the phase image from Figure 5.16 [scale bar is 2 nm].

Moiré patterns have previously been observed for melamine-cyanuric acid hexagonal complexes on HOPG by Zhang et al.²⁷ although they observed a much larger moiré period of 10.2 ± 0.4 nm which corresponded to a 1.4° offset between the lattices. Unfortunately, in this work the hBN lattice was not resolved so the true offset angle could not be found therefore the structure in Figure 5.17 is speculative.

5.2.4 Melamine Grown at Elevated Substrate Temperature

To investigate which of the the observed structures seen in Subsections 5.2.1, 5.2.2 and 5.2.3 the system would settle into if given energy with which to rearrange, melamine was deposited onto a hBN/SiO₂ surface that was held at an elevated temperature of approximately 30 °C. The expected preferred structure was that seen in Subsection 5.2.2 as the melamine deposited on this sample was inadvertently heated to a higher temperature, potentially giving the melamine system more energy to rearrange. The heated substrate also had the potential to lower the sticking coefficient for adsorption of melamine onto the surface which was hoped to give lower coverages. The first sample was made with the substrate held at 31 °C exposed for 20s with the Knudsen cell held at 90 °C in order to deposit 1 ML. The sample was left to cool to room temperature before it was removed from the vacuum system for imaging.

As seen in Figure 5.18, there was a range in island morphologies seen. Some areas, such as those in Figure 5.18 (a), had large islands bordered by smaller thin islands which appear to have preferred growth directions as shown by the histogram which has peaks at approximately 60° and 120° (although compared to the island orientations seen for the thick film the spread is much wider). The structure seen in Figure 5.18 (b) is nearer to a continuous island containing holes and some cracks, these may be due to different domains joining. The island is thicker than the expected monolayer thickness so may contain a second layer which is supported by the profile shown which has steps which could correspond to a single and a double layer. However, the other large holes in the island do not show the same steps. The islands seen in Figure 5.18 are much more mobile than on the samples prepared at room temperature as is seen by the change between Figure 5.18 (c) and (d). The steps seen on the mobile islands are also higher than expected but, in this case, can be attributed to the tip condition as it changed over the pore in the island. This can be indicative of a mobile species which is moved by the tip and adsorbs on and off of the tip with scanning therefore the scanning may have induced this mobility.

Due to the mobility of the molecules, observing a lattice was more difficult than for the room temperature prepared samples, however, a lattice was seen as shown in

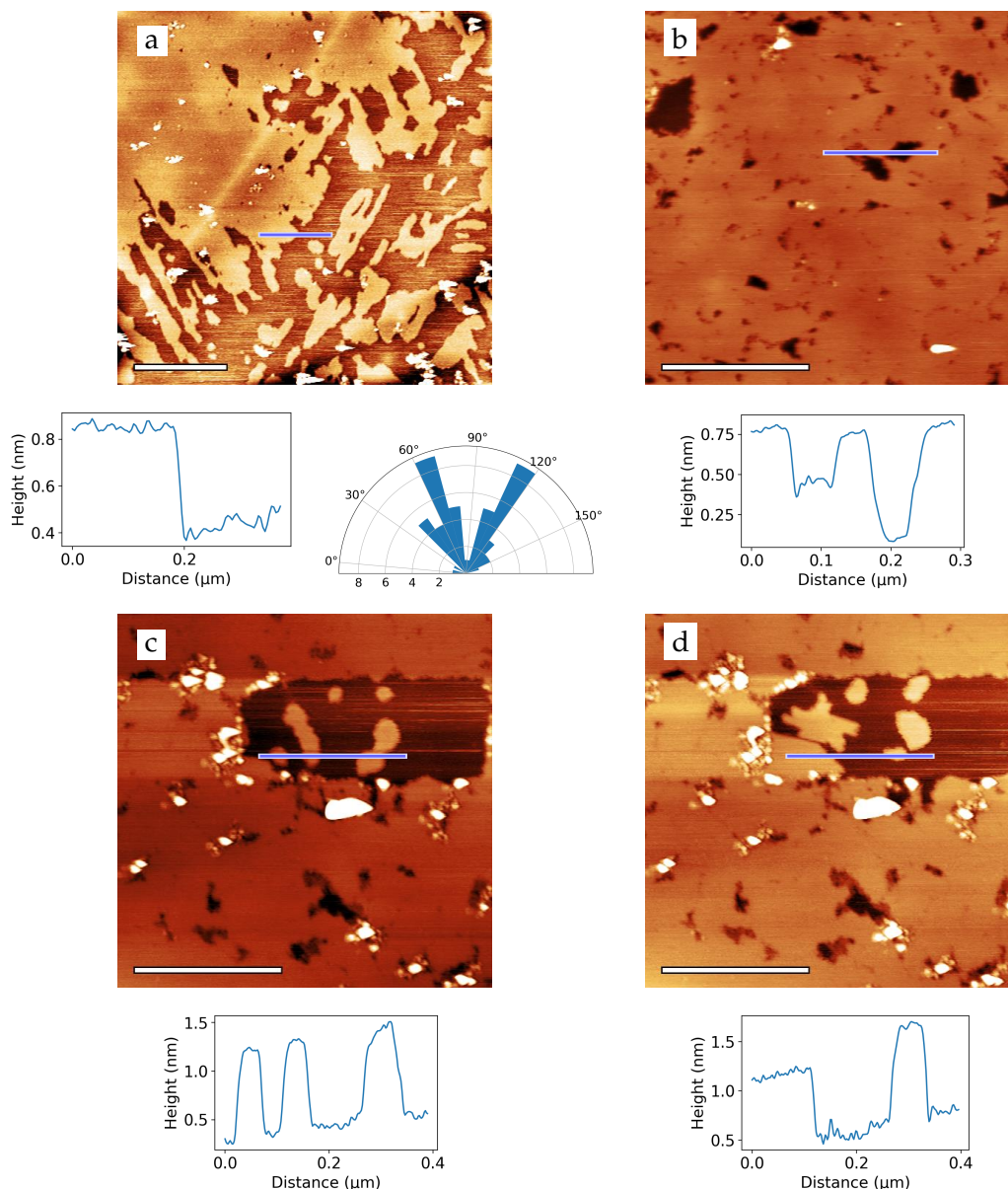


Figure 5.18 Overview topographic images for 1ML heated substrate: (a) a large area of island growth with smaller islands at its edge with coverage of $\sim 80\%$ and height of $0.46 \pm 0.06 \text{ nm}$, below is a profile along the blue line and a histogram of island edge orientation [scale bar is 500 nm]; (b) a near continuous island $0.5 \pm 0.1 \text{ nm}$ high with a profile along the blue line shown underneath [scale bar is 400 nm]; (c) and (d) sequential images of the same area on the surface showing mobility at the edges of the island with profiles along the same blue line shown under each image [scale bar is 400 nm].

Figure 5.19. This lattice is very similar to the square lattice seen on unheated samples as described in Subsection 5.2.1 but is slightly larger making it closer to the lattice dimensions predicted by previous studies on Ag(111).

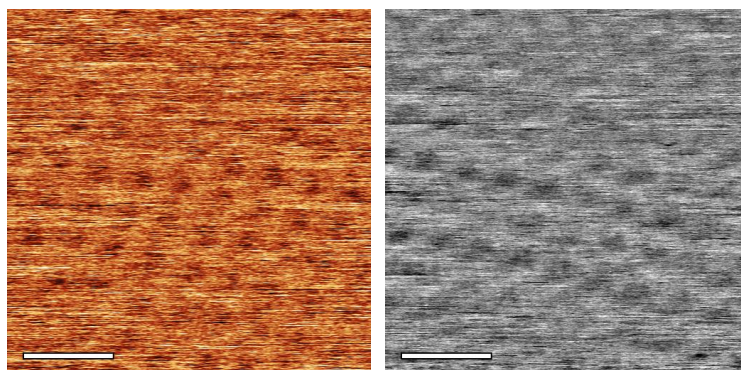


Figure 5.19 Topographic and phase images on the 1 ML melamine film deposited on the heated substrate showing a lattice of 2.23 ± 0.01 nm by 2.3 ± 0.1 nm with $82 \pm 2^\circ$ [scale bar is 5 nm].

An additional sample was made with the sample held at 32°C exposed for 9 s with the Knudsen cell held at 90°C to deposit $2/3$ ML. This resulted in a sub-monolayer coverage with an island structure closer to that seen in for the 0.5 ML room temperature deposition. The observed islands and the lattice seen within these islands are shown in Figure 5.20.

The islands in Figure 5.20 are similar to the square islands in Figure 5.8 (a) however they are elongated. As shown in the histogram, the islands have a dominant direction on the surface with some signs of threefold symmetry with small peaks $\sim 60^\circ$ from the main peak at $\sim 70^\circ$ however the peaks are not as clear as for the room temperature samples. The roughness of the edges of the islands also suggest that this structure is less stable than for the room temperature depositions. Higher resolution images were obtained of the molecular lattice although it was more difficult to image this structure than for a similar lattice on a room temperature sample and more drift was observed in the images.

The lattice seen in Figure 5.20 (b) and (c) is similar to that seen in Figure 5.13. The larger lattice vector of 2.6 ± 0.2 nm seen for this sample is in good agreement with the larger lattice vector of 2.67 ± 0.01 nm previously seen in Figure 5.13. This periodicity over the detailed structure may be due to interactions with the underlying substrate or, as suggested for the room temperature 1.5 ML sample, a second layer of growth although this is less likely given the deposition parameters used in this case. The smaller lattice vectors measured from the phase image in Figure 5.20 (c) are similar

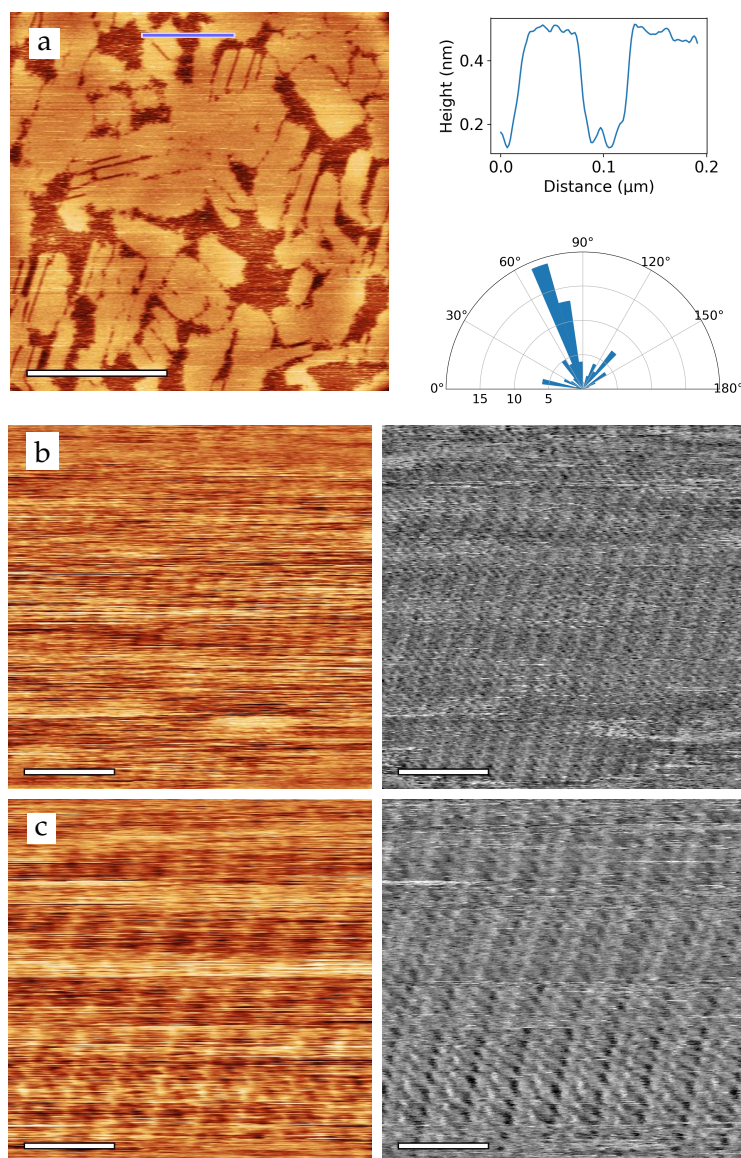


Figure 5.20 Images of 2/3 ML sample heated substrate: (a) topographic image with a rectangular deposition 0.31 ± 0.05 nm high with a profile along the blue line and a histogram of island orientation shown to the right [scale bar is 300 nm]; (b) topographic and phase images showing a lattice of 2.8 ± 0.2 nm by 0.91 ± 0.03 nm ($124 \pm 3^\circ$ as measured from the phase image [scale bar is 10 nm]; (c) topographic and phase images showing a lattice with vectors 2.5 ± 0.1 nm by 0.81 ± 0.03 nm ($115 \pm 3^\circ$) with the phase also showing a more detailed lattice with vectors of 0.84 ± 0.01 nm by 0.94 ± 0.01 nm ($62 \pm 3^\circ$) [scale bar is 5 nm].

to the smaller lattice seen for the 1.5 ML sample although there is a larger difference between the two vectors than previously measured. This lattice can be matched to the structure shown in Figure 5.14 as shown in Figure 5.21. This structure supports the idea that the previously observed line structure and the rhombic lattice may be formed from the same structure which was also suggested by the image seen in Figure 5.13.

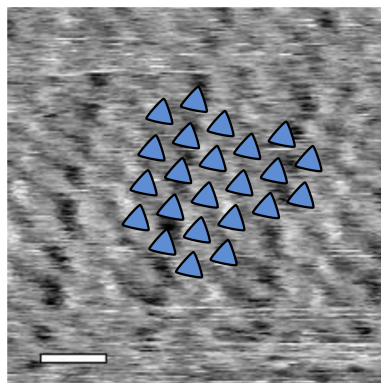


Figure 5.21 Melamine molecules overlaid on an area of Figure 5.20 (c) phase image. The orientation of the melamine molecules could be rotated by 30° in either direction to give the same packing structure.

5.3 Summary

Several different melamine structures were observed on the hBN surface. For a thick film, the expected triangular islands were seen with a preferential orientation that is believed to align with the underlying hBN lattice. A thin film between the islands was also seen which had a lattice different from that on the surface of the islands. The square lattice seen between islands was further seen for depositions of 3 ML, 1 ML and 0.5 ML. This lattice was rationalised as a combination of the α and β structures similar to the γ lattice seen by Schmitz et al.³¹. A hexagonal lattice was seen on top of the thick islands and as the second layer on a thin film deposition. This was fitted to a model which aligns the melamine rings to the rings in the hBN lattice. This structure was also given as an explanation for the rows observed on the thick film islands with an unexplained brightness on every third row. Both the hexagonal and square lattice were also observed on samples prepared on heated substrates with the hexagonal lattice seen for a lower coverage sample. A moiré pattern was also observed and rationalised as a rotation of the melamine hexagonal lattice with respect to the boron nitride lattice.

Molecular modelling work is required to confirm these structures as stable structures for the melamine/hBN system. It would be of particular interest to confirm the electrostatic interactions involved in the positioning of the melamine ring over the boron nitride ring to confirm the existence of an energetically preferable rotation. Further depositions should be carried out to confirm the coverage that leads to a

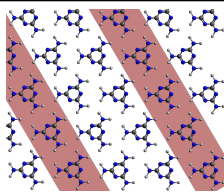
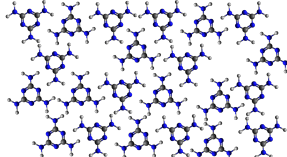
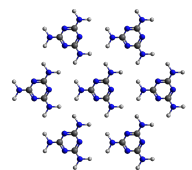
Phase	Structure	Unit Cell	Packing Density	Preparation Method
Phase I (row)		2.02 ± 0.06 nm by 0.77 ± 0.03 nm ($85 \pm 6^\circ$)	1.7 ± 0.1 nm ⁻²	Thick island, 2/3 ML Heated
Phase II (square)		2.22 ± 0.03 nm by 2.1 ± 0.1 nm ($81 \pm 1^\circ$)	2.2 ± 0.3 nm ⁻²	Between thick film island, 3 ML, 0.5 ML
Phase III (rhombic)		0.87 ± 0.01 nm by 0.89 ± 0.01 nm ($60.5 \pm 0.2^\circ$)	1.56 ± 0.06 nm ⁻²	1.5 ML, moiré, 2/3 ML Heated

Table 5.2

switching from one structure to the other and to confirm the combination of the row and rhombic phases.

The observed surface stabilised melamine structures could prove useful in the future as they are near room temperature depositions that give stable lattices. There is also a potential that similar lattice structures could be observed on a related surface to hBN – HOPG. If successful, this could provide a thin insulating layer on a conducting surface which would be a useful tool in producing electronic devices.

6 Deposition and Polymerisation of Porphyrins on Surfaces

Porphyrins are compounds with four pyrrolic rings linked by methine bridges to form a macrocycle. This central ring is extremely stable and can incorporate various metal atoms into the centre. Metals can substitute into the centre of the ring and there are twelve different substitution positions on the outside of the ring – eight *beta* positions on the pyrrolic rings and four *meso* positions on the methine bridges – as shown in Figure 6.1.

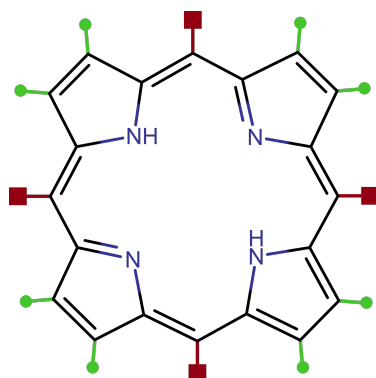


Figure 6.1 The central porphine ring with the *beta* and *meso* positions labelled with green circles and red squares respectively.

6.1 Porphyrins with increasing number of Reactive Groups

The porphyrin species investigated in this chapter have zinc in the central pore and are defined by the substituents at the four *meso* positions. The possible substituents for these porphyrins are a reactive ethyne group (ethynyl) or a bulky tertiary butylphenyl group (3,5-di-*tert*-butylphenyl). The porphyrins are thus defined by the number of reactive ethynyl groups: from 1R to 4R as shown in Figure 6.3. The tertiary butyl groups provide steric hinderance to the packing of the molecules on the surface and the ethynyl group allows the molecules to undergo Glaser coupling as discussed fully in Section 2.3. In short, Glaser-type coupling in surface science follows the reaction

shown in Figure 6.2, where terminal alkynes are coupled accompanied by the loss of H_2 .

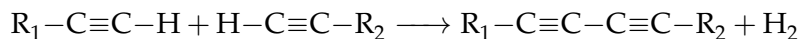


Figure 6.2 The reaction scheme for the Glaser-type coupling on metal surfaces.

The coupling reaction can be utilised with a variety of monomeric units – previously Glaser-type coupling has been used to form nanowires.⁴⁴ Glaser coupling can often lead to side products by reacting elsewhere than the end of the terminal alkyne. Work by Gao et al.⁴³ showed that Ag(111) led to a lower proportion of byproducts than Au(111) and was more efficient than Cu(111). The reaction pathway for the coupling of 1,3,5-triethynyl-benzene molecules on Ag(111) was modelled by Björk et al.⁸⁸ and found to involve transition states that include the surface. Organometallic complexes involving the substrate surface can also form during Glaser coupling. Nanowires have previously been formed by 2,5-diethynyl-1,4-bis(phenylethynyl)-benzene with Glaser-type coupling dominating on the Ag(111) surface but organometallic structures were formed on Ag(110) and Ag(100) which the authors linked to a lattice matching of the molecules with the underlying silver lattice.⁸⁹ Work by Wang et al.⁹⁰ found that organometallic complexes formed as a transition stage for Glaser-type coupling for 1,1'-biphenyl-4-bromo-4'-ethynyl on the Ag(111) surface but as a terminating step on the Cu(111) surface.

The potential structures formed by the covalent coupling of the ethynyl groups varies with the number of reactive groups on the monomer unit. The 1R porphyrin can only form very limited extended structures from two monomer units.⁹¹ There are several possible structures that the 2R porphyrin can form depending on the position of the reactive groups, however, the 2R porphyrin shown in Figure 6.3 can only form 1D wires. The 4R porphyrin can form ordered 2D arrays assuming all ethynyl groups undergo a coupling reaction. The 3R porphyrin can theoretically form various structures including straight ladders, stepped edges, squares, and zig zags. These structures assume that ideal Glaser-type coupling takes place, however, as mentioned above, previous work by Gao et al.⁴³ found that, in addition to the expected dehydrogenative homocoupling, hydroalkynylation leading to an aromatic junction

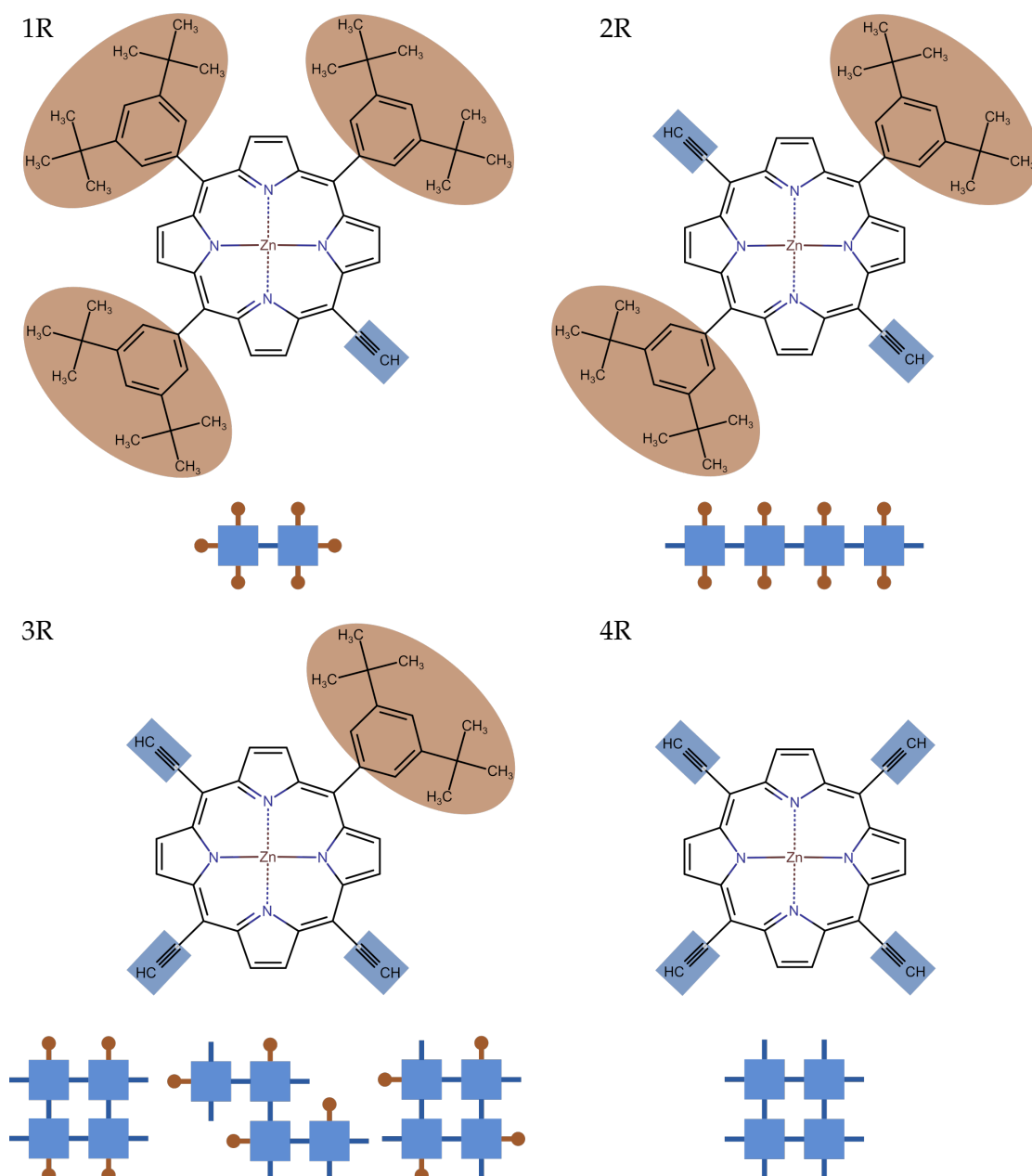


Figure 6.3 The structures of 1R porphyrin (zinc [5,10,15-tris(3,5-di-*tert*-butylphenyl)-20-ethynyl-porphyrin]), 2R (1D) porphyrin (zinc [5,15-bis(3,5-di-*tert*-butylphenyl)-10,20-diethynyl-porphyrin]), 3R porphyrin (zinc [5-(3,5-di-*tert*-butylphenyl)-10,15,20-triethynyl-porphyrin]), and 4R (2D) porphyrin (zinc [5,10,15,20-tetraethynyl-porphyrin]) with some examples of the structures they can form with Glaser coupling.

formed of three monomers. These trimer structures are unlikely to arise from the porphyrin monomers used in this work due to the steric hinderance of the porphyrin ring, however, non-linear structures are theoretically possible.

6.2 Polymerisation of 2R Porphyrin on Ag(111) in UHV

Due to the reactive terminal alkynes on opposite sides and the bulky tertiary butyl groups on the other two sides of the 2R porphyrin shown in Figure 6.3, this molecule is an ideal candidate for the formation of 1D molecular wires, hence the alternative name for this molecule – 1D porphyrin. This polymerisation was investigated using vacuum STM.⁹² A sample of Ag(111) on mica was inserted into a room temperature UHV STM system with a base pressure of 4×10^{-10} mbar. It was then cleaned by sputtering the surface with an argon ion gun for 60 min with a measured current of $\sim 1.1 \mu\text{A}$, accelerating potential of 0.75 keV, and a pressure of $\sim 2.5 \times 10^{-5}$ mbar. This was followed by annealing the surface to 400 °C for 30 min.

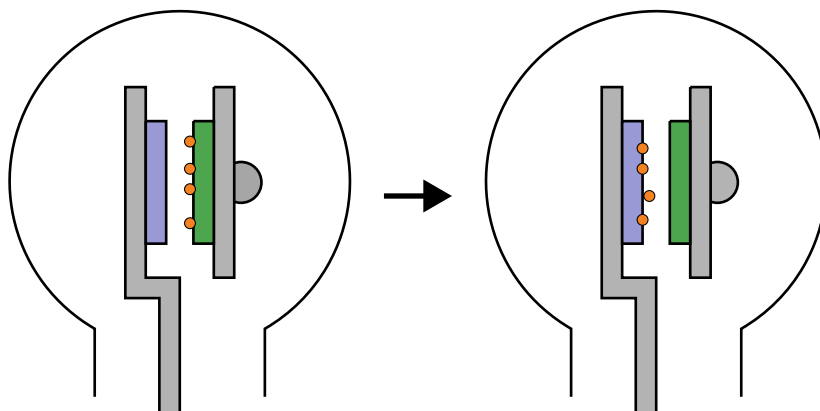


Figure 6.4 The vacuum transfer process for porphyrin units. The silicon sample with molecules drop deposited onto it (shown on the right) is heated to transfer the molecules onto the Ag(111) surface (shown on the left) which can then be moved into the neighbouring chambers ready for imaging.

An indirect deposition method was used to deposit the 2R porphyrin onto the clean Ag(111) surface, as shown in Figure 6.4. This method involved first drop-depositing a solution of the porphyrin in toluene with 1% pyridine (1 mg ml^{-1}) onto a piece of clean silicon wafer. This was placed in the vacuum system along with the Ag(111)/mica sample and the two samples were positioned so the sample surfaces were facing each other. The silicon wafer was heated rapidly to 500 °C which transferred the molecules directly onto the Ag(111) surface which was held at room temperature. The sample was imaged after deposition and corrected for a polynomial distortion arising from the non-perpendicular alignment of the xy axes as shown in Figure 6.5.

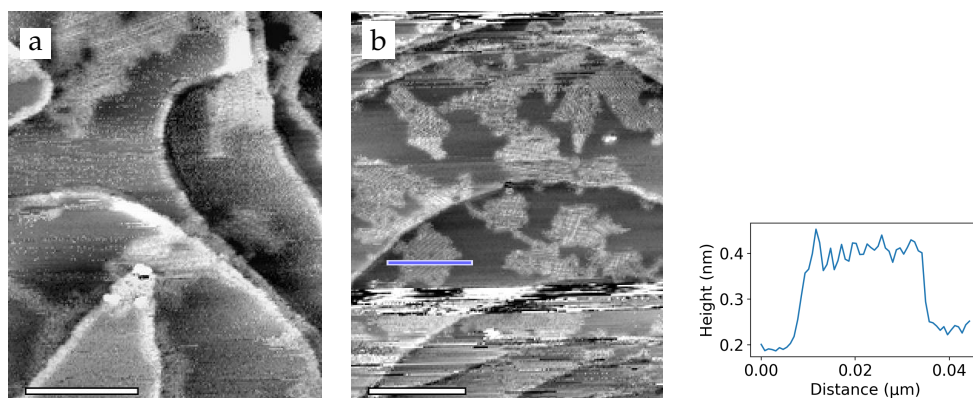


Figure 6.5 Vacuum STM images for 2R porphyrin post-deposition: (a) islands at the top and right of the image 29 ± 3 nm and 17 ± 1 nm wide [scale bar is 30 nm]; (b) islands 13 nm to 37 nm wide with an average width of 24 ± 7 nm, profile along the blue line shown to the right [scale bar is 50 nm].

The images taken after the deposition shown in Figure 6.5 show islands of reacted 2R porphyrin on the Ag(111) surface. These islands were not particularly stable under the STM imaging as seen in Figure 6.5 (b) where the centres of the islands appear clear but the edges are not. These structures were highly mobile and led to changes in the tip state. Figure 6.5 (a) shows areas of the Ag(111) surface where ordered islands are visible but the surface around them appears rough. This is believed to be due to unreacted porphyrin monomers moving on the surface. After this initial imaging, the surface was annealed to 120°C for 15 min. This resulted in more stable molecular structures under scanning as shown in Figure 6.6.

The islands in Figure 6.6 are very variable in size with an average island size of (8.1 ± 0.7) nm to (36 ± 5) nm. The chains are longer than the islands with bends visible at the island edges; a selection of these are denoted with red arrows. The chains are variable in length with the longest chain measured to be 40 ± 4 monomeric units long which corresponds to a length of 53 ± 8 nm. Near step edges, as in Figure 6.6 (a), (b), and (c), the porphyrin chains align with the step edge, however, away from the edges the alignment does not have a dominant orientation. A variety of features are seen within and at the edge of the islands; higher resolution images of islands are shown in Figure 6.7.

From the images in Figure 6.7, the unit cell is measured to be 1.33 ± 0.05 nm by 1.9 ± 0.1 nm with an angle of $81 \pm 4^\circ$ between the two as marked in blue on Figure 6.7

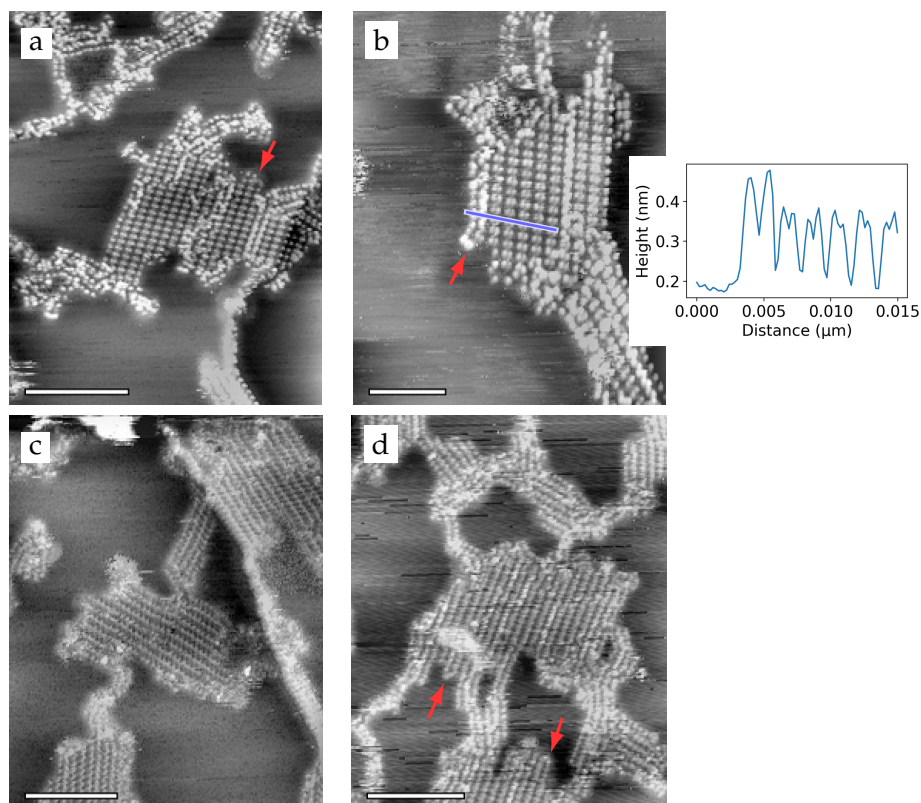


Figure 6.6 Vacuum STM images for 2R porphyrin post-anneal with 180° bends in the porphyrin chains indicated by red arrows: (a) island size 29 ± 5 nm [scale bar is 20 nm]; (b) island width 17.7 ± 0.3 nm with an average chain length of 14 ± 1 units [scale bar is 10 nm]; (c) island size 36 ± 5 nm [scale bar is 20 nm]; (d) island 28 ± 5 nm by 33.7 ± 0.8 nm [scale bar is 20 nm].

(b). The shorter distance is the intra-chain length between the coupled monomers, which provides evidence for the covalent nature of the bonding along the chain as it corresponds to the distance seen for similar covalently bonded structures of 1.33 ± 0.07 nm.⁹³ The longer length is the distance between the reacted chains which are separated by the tertiary butyl groups. The suggested structure of the chains is shown in Figure 6.7 (d). Within the porphyrin chains shown in Figure 6.7, each monomeric component shows up as two neighbouring bright features which together form a feature 1.32 ± 0.09 nm by 0.78 ± 0.09 nm. These correspond to the two tertiary butyl groups on the porphyrin ring which can rotate freely around the C–benzene bond in solution and has rotational conformational freedom on the surface. Detailed images show brighter lines within the islands denoted with green arrows which correspond to domain boundaries with interdigitated tertiary butyl groups. These

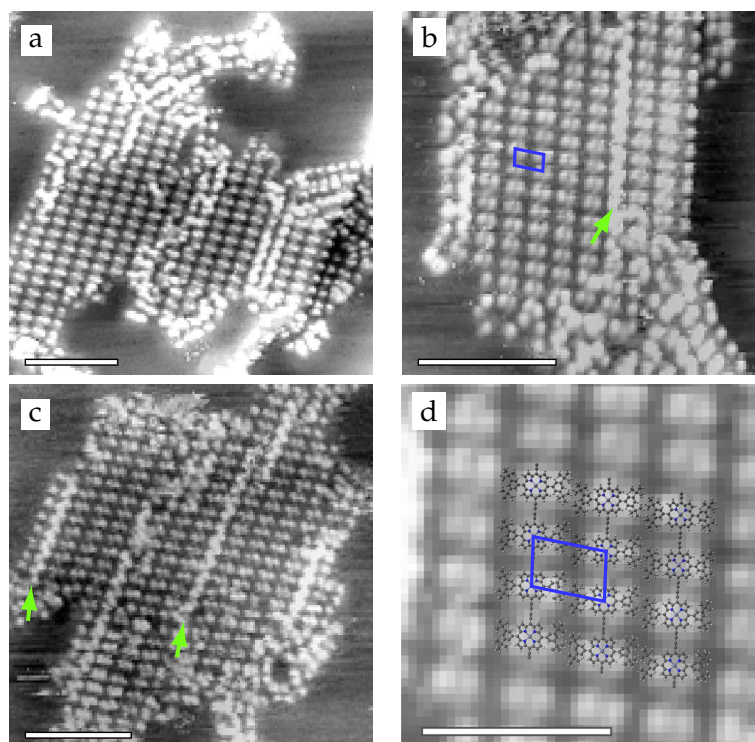


Figure 6.7 Details from STM images for 2R porphyrin post-anneal: (a) porphyrin inter-row separation is 1.9 ± 0.1 nm and intra-row separation is 1.35 ± 0.05 nm; (b) porphyrin inter-row separation is 1.83 ± 0.08 nm and intra-row separation is 1.35 ± 0.02 nm ; (c) distance between bright line features is 8.9 ± 1.0 nm, porphyrin units are separated by 1.28 ± 0.02 nm within the row and 1.95 ± 0.06 nm between rows [all scale bars are 10 nm]; (d) a suggested molecular structure for a smoothed area of (b) showing a section of the reacted 2D chains [scale bar is 5 nm].

tertiary butyl groups have fixed orientations under the time span of imaging whereas in areas without the interdigitation the groups are mobile during scanning.

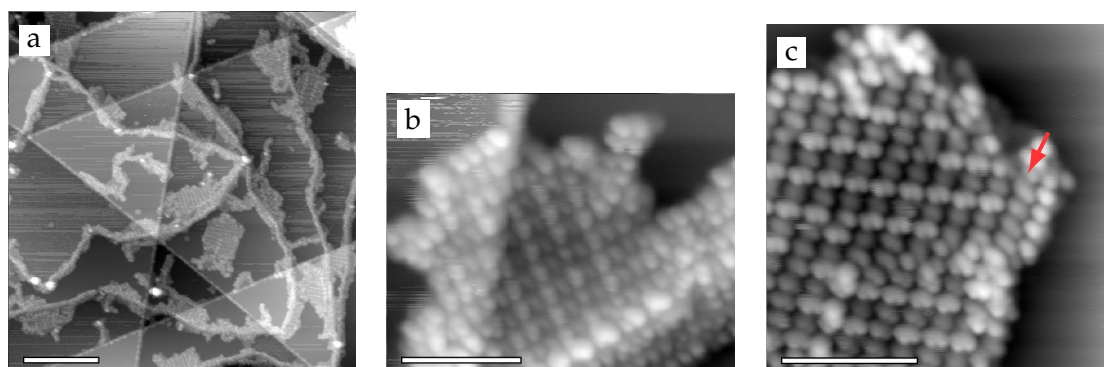


Figure 6.8 LT-STM images for the 2R porphyrin: (a) islands of porphyrin chains 13 nm to 37 nm wide with an average width of 21 ± 6 nm [scale bar is 50 nm]; (b) the porphyrin chain island with inter-chain distance of 1.29 ± 0.02 nm and intra-chain distance of 1.88 ± 0.02 nm with alternate rows bright and separated by 2.6 ± 0.1 nm [scale bar is 10 nm]; (c) porphyrin island with lattice of 1.32 ± 0.05 nm by 2.01 ± 0.07 nm with distance between alternate bright rows is 2.8 ± 0.1 nm [scale bar is 10 nm].

Images revealing the structure of the chains on the samples above were obtained by Dr Alex Saywell using LT-STM with a base pressure of 10^{-11} mbar at 78 K after transfer from the UHV STM system used above via a 'vacuum suitcase'. Figure 6.8 (a) shows thin chains along the Ag(111) step edges and islands that are smaller than those seen with RT STM. These smaller islands are more mobile at RT so are not observed. The islands shown in Figure 6.8 (b) and (c) are highly ordered with intra-chain separations of 1.29 ± 0.02 nm and 1.32 ± 0.05 nm respectively, which is in good agreement with the separation measured at RT. The porphyrin chains are aligned differently which gives rise to different chain separations within the islands: Figure 6.8 (b) has rows aligned perpendicular to the chains giving rise to a separation of 1.88 ± 0.02 nm whereas Figure 6.8 (c) has a slightly larger separation of 2.01 ± 0.07 nm. The alternating brightness along the porphyrin chain corresponds to two rotations for the tertiary butyl groups attached to the monomeric unit. These can either be in an upright or a tilted arrangement as illustrated in Figure 6.9 (a) and (b). The lattices in Figure 6.8 (b) and (c) have areas of alternating upright and tilted tertiary groups which is likely to be an energetically favourable arrangement and is shown in Figure 6.9 (c). The tertiary butyl arrangements may also explain the different inter-row packing between the two images as there are two options for the tilted position which, if combined, would increase the space between chains.

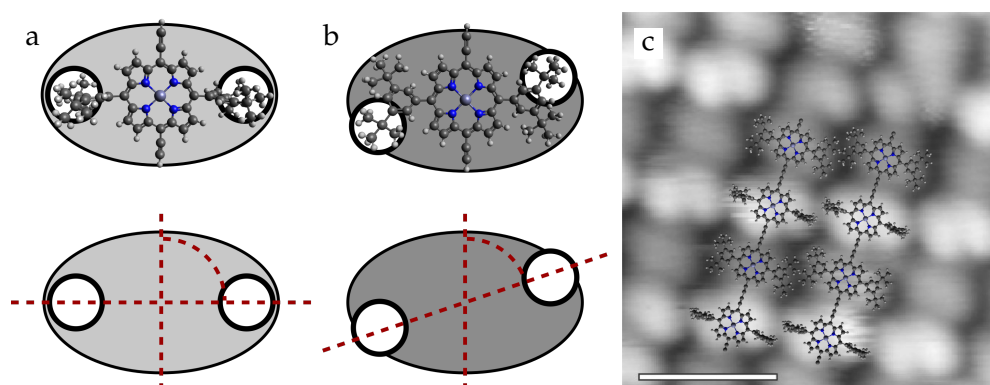


Figure 6.9 The two positions of the tertiary butyl groups on the 2R porphyrin monomer: (a) the upright position with the tertiary butyl groups perpendicular to the porphyrin ring; (b) the tilted position with the tertiary butyl groups 60° to the porphyrin ring; (c) chains with alternating upright and tilt tertiary butyl groups overlaid on Figure 6.8 (c) [scale bar is 3 nm].⁹²

In addition to the alternating tilted and upright positions within the chains, chains with greater rotations are seen on the edge of the island in Figure 6.8 (c) as marked by the red arrow. The molecules will have greater freedom to rotate when near the edge of an island or when independent of a chain. Furthermore, there are bright circular features visible in the bottom of Figure 6.8 (b) and (c) which may be silver adatoms that have been incorporated into the porphyrin chain between porphyrins. Alternatively, this may be a stacking of porphyrin monomers or chains.

6.3 Polymerisation of 4R Porphyrin on Ag(111) in UHV

Following on from the work with the 2R porphyrin, the 4R porphyrin was investigated on Ag(111). This structure has the potential to form square grids if fully reacted. As with the 2R porphyrin, a sample of Ag(111) on mica was inserted into a room temperature UHV STM system with a base pressure of 4×10^{-10} mbar. It was then cleaned by sputtering the surface with an argon ion gun for 30 min. The measured current was $\sim 1.1 \mu\text{A}$ with 0.75 keV and a pressure of $\sim 2.8 \times 10^{-5}$ mbar. This was followed by annealing the surface to 400 °C for 30 min. An indirect deposition method was used to deposit the 4R porphyrin onto the clean Ag(111) surface as described above in Section 6.2. This consisted of flash heating for 60 s a silicon sample that the molecules had been drop deposited on. As with the 2R porphyrin, the molecules were too mobile after the initial deposition to be imaged so the sample was annealed to 90 °C for 15 min. After the initial anneal, low resolution images were obtained which are shown in Figure 6.10 after a polynomial distortion correction.

As with the 2R porphyrin above, the surface initially appeared clean as seen in Figure 6.10 (a), however, areas of material were seen (as identified by the red arrow on Figure 6.10 (b)). The annealing temperature was lower than that used for the 2R porphyrin sample and did not lead to long-range covalent coupling so these areas were not stable under imaging as the molecules were mobile on the surface. The sample was subsequently annealed further to 120 °C for 15 min which lead to a more stable surface as shown in Figure 6.11.

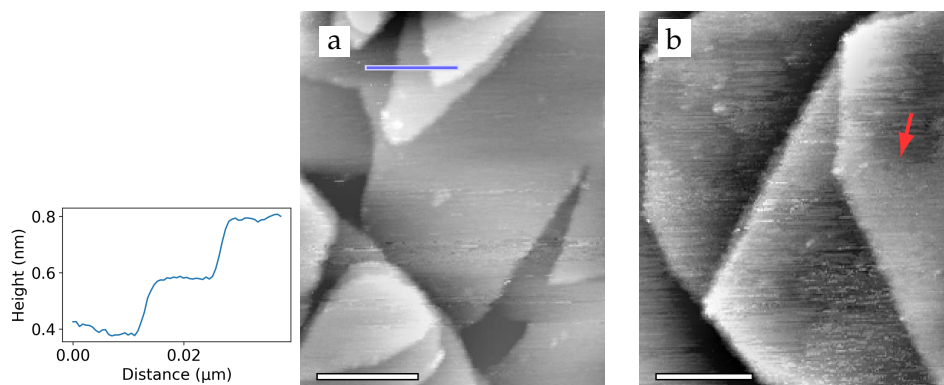


Figure 6.10 Vacuum STM images obtained for 4R porphyrin post-anneal to 90 °C for 15 min: (a) steps in the Ag(111) surface with no sign of molecules, profile along blue line is to the left [scale bar is 40 nm]; (b) steps in the Ag(111) surface with some signs of molecules although unstable under scanning [scale bar is 50 nm].

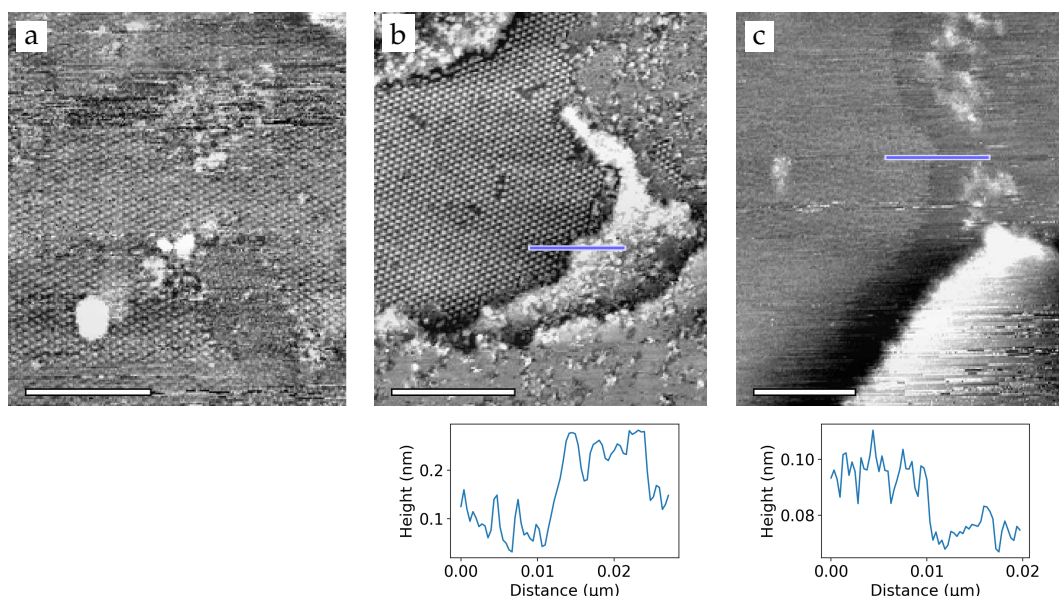


Figure 6.11 Vacuum STM images obtained for 4R porphyrin post second anneal to 120 °C for 15 min: (a) a lattice of 1.64 ± 0.05 nm by 1.73 ± 0.04 nm ($61 \pm 4^\circ$) [scale bar is 30 nm]; (b) a lattice of 1.68 ± 0.02 nm by 1.64 ± 0.02 nm ($56 \pm 2^\circ$) with an island step of 0.16 ± 0.03 nm shown in the profile along the blue line [scale bar is 30 nm]; (c) large island 0.021 ± 0.004 nm high with a 10 ± 1 nm gap between island edge and step edge [scale bar is 20 nm].

The surface appears to have a large amount of material deposited. Some material is in ordered islands, however, large amounts of material have formed islands as seen at the bottom on Figure 6.11 (b). The ordered islands are flat and only 0.16 ± 0.03 nm high, which is likely due to disordered molecules at the edge of the islands increasing the apparent height of the Ag(111) surface. Figure 6.11 (a) and (b) show a hexagonal lattice with an average lattice vector of 1.67 ± 0.05 nm subtended by $58 \pm 4^\circ$.

High resolution images were obtained for the lattices in Figure 6.11 (b) and (c) and these are shown in Figure 6.12. The intramolecular resolution in the lattices appear different, however, the structure seen in Figure 6.12 (b) is also visible at the top of (a) above the lines where the tip changed. The features in Figure 6.12 (b) appear to have three lobes rather than the expected four; this can be explained as one of the three lobes being two ethynyl groups from neighbouring porphyrin molecules that have reacted to form the chain. Alternatively, the appearance of the molecules on the surface may be caused by a porphyrin from the surface attaching to the tip with three dangling ethynyl groups creating the observed three-fold symmetry.

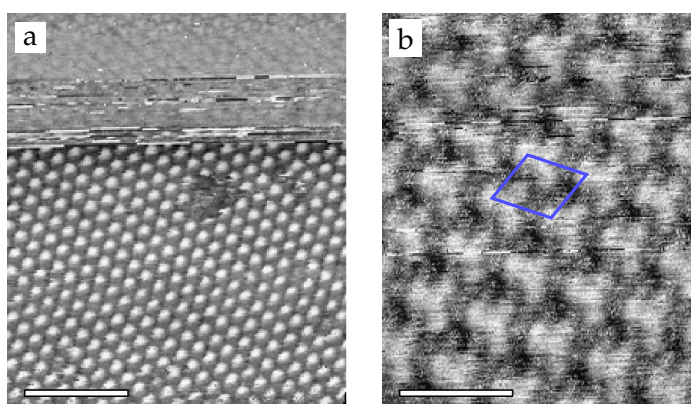


Figure 6.12 High resolution vacuum STM images obtained in areas shown in Figure 6.11: (a) image of Figure 6.11 (b) with a lattice of 1.50 ± 0.02 nm by 1.80 ± 0.02 nm ($65 \pm 2^\circ$) [scale bar is 10 nm]; (b) image of Figure 6.11 (c) with a lattice of 1.53 ± 0.03 nm by 1.68 ± 0.02 nm ($71 \pm 2^\circ$) shown with the blue outline [scale bar is 3 nm].

These chains have a longer porphyrin–porphyrin distance (1.53 ± 0.03 nm) than the distance measured for the 2R porphyrin chains in Figure 6.7 (1.33 ± 0.05 nm); this may be due to the inclusion of a silver adatom in the chain. In work on Ullmann coupling by Eichhorn et al.⁹⁴, the inclusion of a silver atom in an organometallic complex extended the chain length by 0.26 ± 0.10 nm which is similar to the difference between these chain length observed here (0.20 ± 0.05 nm) and to that observed by Wang et al.⁹⁵. Additionally, Wang et al.⁹⁵ observed that the angle of alkynl-Ag-alkynl bonds on the Ag(111) surface is 160° , which may explain the apparent rotation of the molecules relative to the chain direction. A suggested model for the structure seen in Figure 6.12 is shown in Figure 6.13. This model has the chains at an offset from the alignment required to form the 2D grid. Energetically, under the anneal parameters used, the

monomers may have been unable to reconstruct into a packing that would support the formation of the 2D grid. An alternative model could have the molecules unreacted and lying at an angle to the surface or bound by one ethyl group to the surface, however, these structures would not explain the relative stability of the structure under scanning compared to pre-anneal.

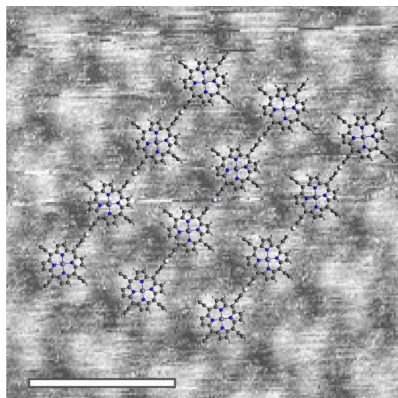


Figure 6.13 Model overlaid on Figure 6.12 (b) with the porphyrin 4R reacted to form closely packed chains with silver atoms at the joins [scale bar is 3 nm].

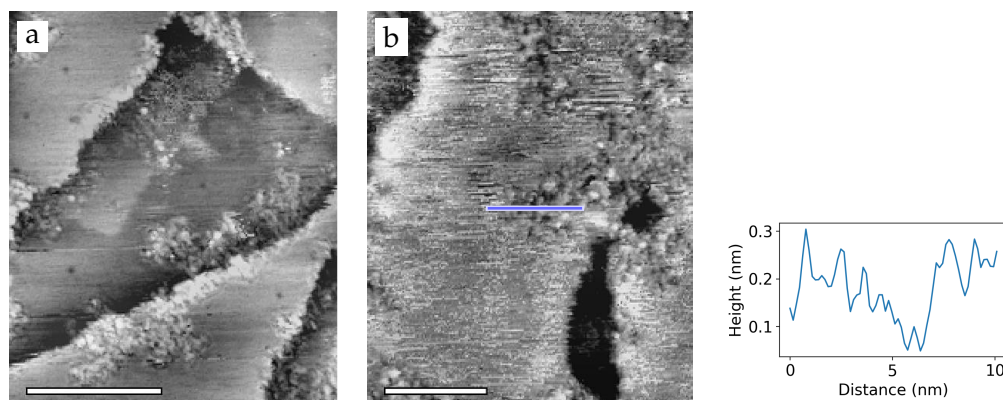


Figure 6.14 Vacuum STM images of the 4R porphyrin obtained after third anneal to 180 °C: (a) Ag(111) surface with steps 0.25 ± 0.04 nm high and material 0.11 ± 0.03 nm high [scale bar is 20 nm]; (b) step in Ag(111) 0.29 ± 0.03 nm high at top left, profile along the blue line is shown to the right [scale bar is 10 nm].

The sample was then heated further to 180 °C for 15 min to determine the change in structure corresponding to further Glaser coupling between the chains. This resulted in the images shown in Figure 6.14. The higher temperature of the anneal appears to have damaged the ordered structure on the surface with an increase in the roughness on the surface. The areas of molecules visible are disordered and denote boundaries within a film across the surface. This could suggest that the porphyrin has reacted to

form a flat layer, however, this was not directly imaged with the STM and, given the stability of the 1D chains formed from the 2R and 4R porphyrin, it would be expected to be clearly resolved in the STM images. It is more likely that the molecules have broken down to leave a layer of carbon structures covering the Ag(111) surface.

6.4 Deposition of 3R Porphyrin on Ag(111) in UHV

An investigation was also carried out with the 3R porphyrin shown in Figure 6.3. The Ag(111) surface was prepared as for the 4R and 2R samples by a cycle of sputtering and annealing. The 3R porphyrin was deposited using the same indirect method as in Section 6.2 from a drop of toluene with 1% pyridine solution on a silicon surface. Instead of imaging with RT STM, after deposition the sample was transferred in vacuum using a 'vacuum suitcase' into a low temperature (77 K) STM without an anneal stage. For the 2R and 4R porphyrins, the anneal stage was necessary to stabilise the molecules into a structure that could be imaged whereas the low temperature allowed the molecules to be imaged prior to reacting to see how they initially deposited onto the surface.

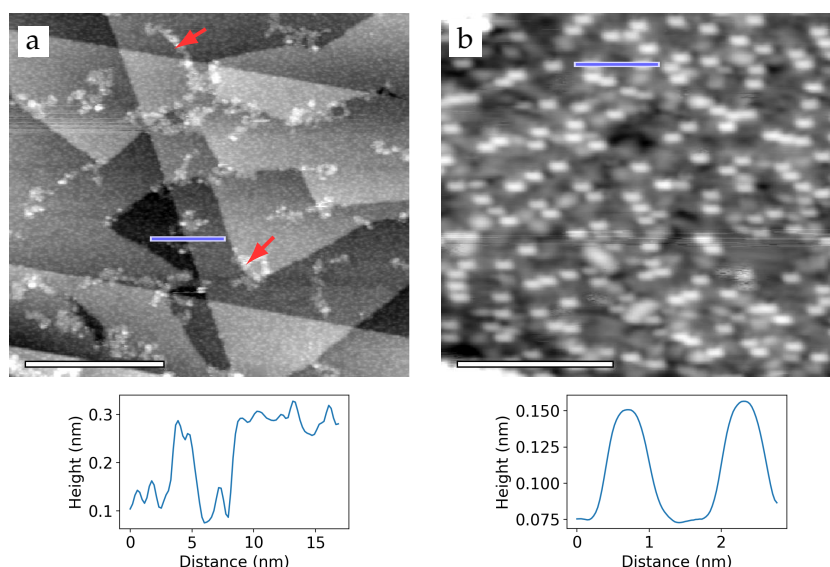


Figure 6.15 LT-STM images of 3R porphyrin: (a) near full coverage of the Ag(111) surface with bright features 0.20 ± 0.07 nm high as shown in profile along blue line below [scale bar is 30 nm]; (b) rectangular features (0.50 ± 0.04 nm by 0.27 ± 0.03 nm) are 0.075 ± 0.009 nm high, profile along blue line across two bright features below [scale bar is 5 nm].

Figure 6.15 (a) shows a high coverage of 3R porphyrin on the surface. Steps in the Ag(111) surface are visible as are brighter areas of the 3R porphyrin marked with red arrows, which are assumed to be stacked molecules. These features may also consist of small chains of coupled porphyrins that formed during the deposition. The rectangular features in Figure 6.15 (b) are believed to be the tertiary butyl groups of the porphyrin molecules as in Figure 6.7 although these are smaller as they are a singular tertiary butyl group rather than a pair, however, these may be a tip artefact so the shape will be ignored in the analysis.

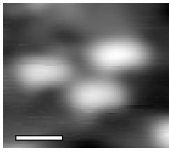
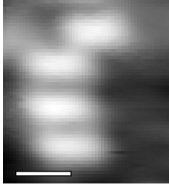
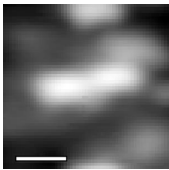
Category	Example	Percentage
Diagonal		$53 \pm 5\%$
Stacked		$21 \pm 9\%$
Side-by-side		$29 \pm 2\%$

Table 6.1 The three main arrangements of the rectangular features and their percentage of the total feature distribution [scale bars are 0.5 nm].

The bright features are arranged in a wide range of positions which were broadly categorised into three groups – diagonal, stacked, side-by-side – for a range of images. Examples of these are shown in Table 6.1 along with their percentage of the distribution on features in each image. The diagonal features were the most common arrangement in all images forming half of the assigned features. It is difficult to link these features to chemical structures, however, can be assumed that these common features are reacted monomers in short chain structures. The structure of these features is difficult to determine as the distance between features is much lower than expected for a coupled chain so the features are unlikely to be the tertiary butyl groups unless there is some

rotation of the groups. Due to the multitude of bonding arrangements available for the 3R porphyrin, these features are unable to be modelled without further imaging.

6.5 Solution Deposition of 4R Porphyrin on HOPG in Ambient

In addition to the work on the Ag(111) surface, the 4R porphyrin molecules shown in Figure 6.3 (d) were imaged on a HOPG surface. For this they were dissolved in toluene (1% pyridine) as for the vacuum deposition then diluted to $\sim 0.5 \text{ mg ml}^{-1}$ before being deposited onto freshly cleaved HOPG by immersion in the solution for ~ 40 min followed by drying the surface with nitrogen. A drop of nonanoic acid was then placed on the surface and the samples were imaged using ambient STM.

From the images in Figure 6.16, it is apparent that the deposition procedure gave close to a complete monolayer coverage. The porphyrins formed large ordered arrays that appear to be predominantly linear with a row separation of $1.7 \pm 0.2 \text{ nm}$. This structure was easily damaged by scanning as shown in Figure 6.16 (d) which is of the same area as Figure 6.16 (c) after several scans showing the removal of a large amount of material. This suggests that the molecules were unreacted and held in place with relatively weak van der Waals forces as expected for an unheated sample. The solvent used to improve the imaging may also affect the mobility of the islands. Some islands, such as that shown in Figure 6.16 (b), initially appear continuous over step edges but there is actually an $11.1 \pm 0.8^\circ$ rotation between the lattice on the upper and lower sides of the step – this indicates that the porphyrin lattice is not preferentially aligned with the underlying graphene lattice. A possible molecular models for the packing seen in Figure 6.16 (c) and (d) are shown in Figure 6.17. The model gives a rectangular lattice rather than the hexagonal lattice seen for the UHV Ag(111) sample. This may be because the HOPG sample had more mobile porphyrin monomers as they were completely unreacted, which may have given the molecules more rotational freedom. This lattice is well spaced to support Glaser coupling which could be carried out by heating the sample on a hotplate, by exciting the surface with a laser, or by chemical treatment of the surface.

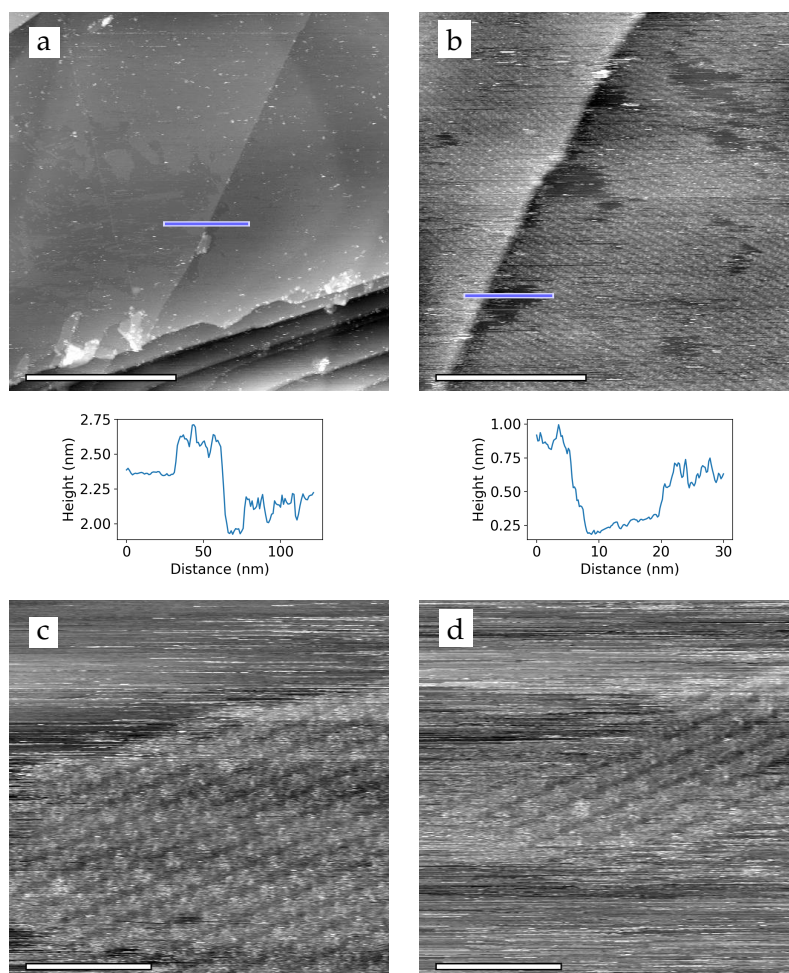


Figure 6.16 The structure formed by 4R porphyrin on HOPG: (a) HOPG steps of 1.9 ± 0.4 nm, below is a profile across the blue line showing a step across the surface and the porphyrin layer 0.26 ± 0.05 nm high [scale bar is 200 nm]; (b) porphyrin island 0.26 ± 0.05 nm high over a HOPG step of 0.4 ± 0.1 nm with line separation of 1.6 ± 0.1 nm on the upper step and 1.9 ± 0.2 nm on the lower step, below is a profile along the blue line [scale bar is 40 nm]; (c) area of 4R porphyrin with a lattice of 1.78 ± 0.03 nm by 1.28 ± 0.03 nm ($84 \pm 1^\circ$) [scale bar is 10 nm]; (d) the same area as (c) showing the destruction of the porphyrin island by the tip, the lattice is measured to be 1.80 ± 0.02 nm by 1.27 ± 0.01 nm with $85 \pm 1^\circ$ [scale bar is 10 nm].

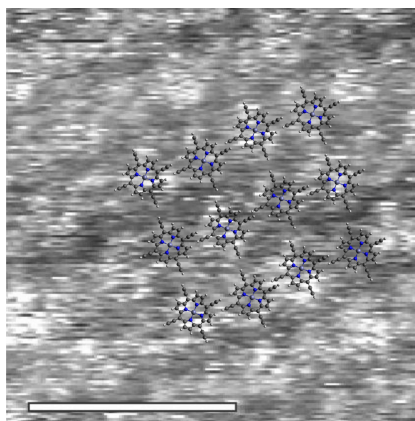


Figure 6.17 A suggested model for Figure 6.16 (c) with an inter-row distance of 1.74 ± 0.03 nm and an intra-row distance of 1.44 ± 0.02 nm subtended by $86 \pm 1^\circ$ [scale bar is 5 nm].

6.6 Summary

The porphyrin monomers utilised in this chapter are ideal candidates for surface polymerisation. This work utilised a novel deposition technique involving rapid heating of molecules on a silicon wafer to sublime them onto a Ag(111) surface. The technique was shown to be a viable alternative to electrospray for deposition, which could be expanded further to include surfaces more challenging for electrospray. It could also provide an alternate deposition method for molecules that are suitable for solution deposition onto surfaces which are not stable in the solvent. The viability of this technique should be tested further with different molecules of a variety of sizes and onto a range of surfaces.

Glaser coupling was observed for the 2R and 4R porphyrins into 1D chains, with the 4R porphyrin not observed to fully react into a 2D grid. Future work should look to reduce the coverage and improve the anneal protocol to encourage 2D grids to form. It is probable that the temperature used for the second anneal to form the chains (120 °C) could lead to 2D grids with increased anneal time and slightly lower coverage. The coupling reaction of the 3R porphyrin should also be investigated although this is likely to lead to a variety of structures as the molecules were not seen to have a preferred packing of monomers.

Further work on the HOPG surface should also be carried out with the aim of forming the 1D chains from the 2R porphyrin and the 2D grids from the 4R porphyrin. This could be achieved by following the deposition method outlined above then annealing to the temperatures used in vacuum to promote Glaser coupling. The observed structure for the 4R porphyrin on HOPG suggests that large ordered domains could be formed if coupling was promoted by heating.

7 Formation of Molecular/2D Hybrid Heterostructures by Mechanical Transfer

The formation of 2D heterostructure devices is of great interest in many different fields owing to their potential in producing novel properties and effects.⁸ The focus of this chapter involves the encapsulation of molecules between sheets of 2D materials. These structures potentially allow molecular islands to be studied in various ways that are not possible for molecular islands on a substrate including TEM and electrical transport studies.⁹⁶ The encapsulated molecules can also undergo reactions when exposed to energy via an electron beam or other penetrating radiation, with the enclosing sheets acting as a nanoreaction chamber in which the molecular reaction can be confined to 1D or 2D.^{14,97} Molecules could also theoretically be used to chemically modify the enclosing layers. The formation of heterostructures relies on the reliable production of clean, well-ordered layers and on incorporating them into heterostructures. This chapter looks at a new technique for the transfer and formation of heterostructures.

There are two methods to forming heterostructures: mechanical transfer of the layers and in situ growth of the layers. In situ growth is generally achieved using chemical vapour deposition (CVD) or epitaxial growth. These techniques have been used to form complex structures, but are limited by the growth mechanisms and high temperatures required, which restricts the substrate and the inclusion of weaker bound networks (e.g. hydrogen-bonded networks). Mechanical transfer methods allow for the inclusion of molecular structures that would be damaged by the temperatures and pressures involved in CVD or epitaxial growth, however, these methods often lead to higher amounts of contamination on a sample. There are two general mechanical transfer methods which are shown in Figure 7.1: (a) wet-transfer where the flake is prepared on a transfer layer on a water soluble layer allowing it to be floated off

the support and transferred to another 2D material after which the transfer layer is removed; (b) pick-up and transfer method where a flake on a membrane is used to pick up other flakes into a stack and then placed on a support surface.⁸

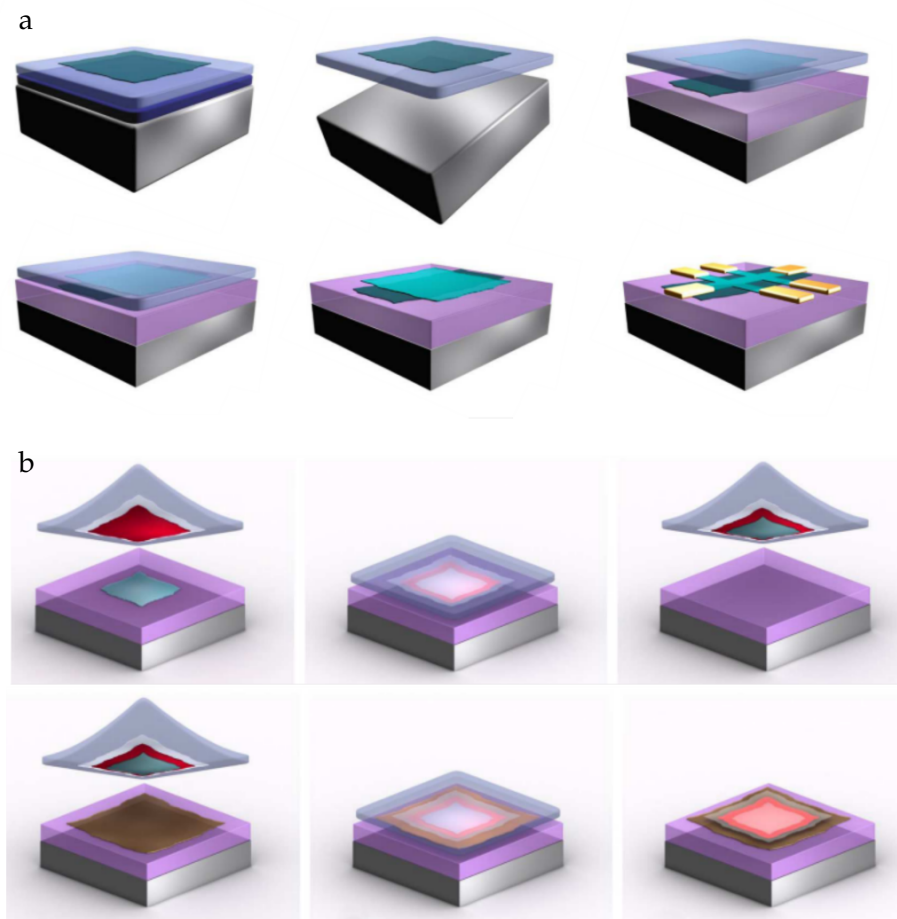


Figure 7.1 An overview of the two main mechanical transfer methods: (a) wet-transfer with the flake floated off of a support surface, flipped and transferred onto a different surface where the transfer layer is removed and contacts attached; (b) pick-up and transfer where a membrane is used to create a stack of flakes and then placed on a support surface where the membrane is removed. Adapted from reference 8.

Previously, mechanical transfer has allowed for the formation of multilayer heterostructure devices containing mono- and bi-layer graphene crystals interlaid between atomically thin hBN crystals. In work by Haigh et al.⁹⁸ a heterostructure stack was formed by first preparing hBN and graphene flakes on separate SiO₂ and poly(methyl methacrylate) (PMMA) surfaces. The target graphene flakes were transferred by floating off the PMMA layer from the support to allow the graphene flakes to be deposited onto the target hBN flakes. This was repeated multiple times with an anneal step between each transfer (300 °C in Ar–H mixture) to remove

contaminants. The resulting device was investigated with cross-sectional TEM which revealed trapped contaminants forming thin layers between the hBN and graphene layers, as seen in Figure 7.2. This method had been previously used to form devices for electrical measurements.⁹⁹ An alternative transfer method for forming hBN based structures was outlined by Kim et al.¹⁰⁰ and allows for accurate rotational alignment. This method was used to form a graphene bilayer structure with an interlayer of hBN for study with Raman and electrical measurements.

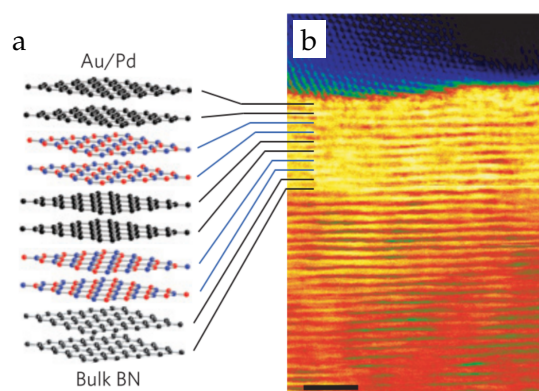


Figure 7.2 A heterostructure formed from bilayer graphene and hBN: (a) a model of the heterostructure; (b) bright-field cross sectional STEM of the heterostructure stack. Adapted from reference 98.

For the work in this chapter, C_{60} islands on hBN were chosen as the molecular network to transfer. C_{60} growth on hBN surfaces has been studied within the Beton group by Kerfoot et al.¹⁰¹ and found to form irregular shaped monolayer islands with the C_{60} packed in a hexagonal arrangement. For the same amount of material, a transition to faceted bilayers at a substrate growth temperature of 178 °C was reported. Additionally, C_{60} has been previously used as a protective layer for mechanical transfer. In work by Wieland et al.¹⁰², a thin film of C_{60} 10 nm to 100 nm thick was found to promote adhesion between a PDMS transfer layer and a gold supporting layer for the transfer of molecular films.

C_{60} has previously been encapsulated in carbon and boron nitride nanotubes by Hernández et al.⁹⁷, Trave et al.¹⁰³, Khlobystov et al.¹⁰⁴. Whilst encapsulated in single-walled carbon nanotubes, the fullerenes have previously been irradiated with electrons to induce coalescence to form carbon nanotubes 0.5 nm to 0.7 nm in diameter.⁹⁷ More recently, C_{60} has been incorporated into mixed dimension 2D heterostructures.¹⁴ These

heterostructures consisted of fullerenes held between two graphene layers and resulted in areas of clean and ordered C_{60} islands as shown in Figure 7.3. The graphene layers were found to shield the fullerenes from radiation damage during STEM and allow the analysis of the structure and dynamics of the C_{60} molecules with atomic resolution.¹⁴

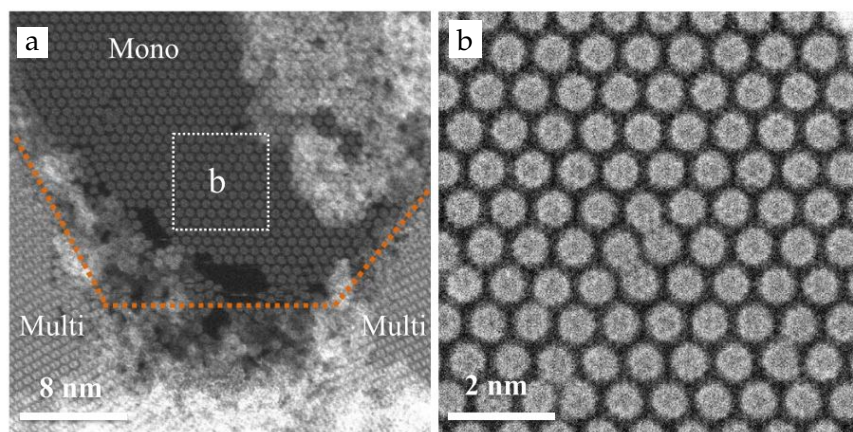


Figure 7.3 STEM images of an area of encapsulated C_{60} with (a) showing areas of multilayer and monolayer with the detail in the monolayer shown in (b) including areas of apparent coalescence between neighbouring molecules. Adapted from reference 14.

In this chapter, the compatability of mechanical transfer with molecular monolayers on a supporting surface was investigated in addition to using the technique to form structures of hBN encapsulated C_{60} . If it can be demonstrated that C_{60} molecules can be encapsulated in hBN pristinely then the techniques used for the nanotube encapsulated C_{60} could be used in future to create pristine mono- or bi-layer graphene encased by hBN.

7.1 Flake Transfer Methodology

The method used for transferring thin hBN flakes to form layered structures encapsulating molecules with minimal contamination follows the approach of Kim et al.¹⁰⁰. Firstly, 'stamps' with which to pick up the hBN flakes were manufactured as shown in Figure 7.4. The stamps consisted of a clean glass slide onto which a small drop of PDMS (polydimethylsiloxane, 10:1 elastomer to curing agent) was placed using a thin wire. This was baked at 110 °C for 15 min to harden. Once hardened, this was covered with a small square of PDMS (approximately 4 mm by 4 mm) using tweezers,

minimising air-bubbles between the film and the glass slide. Some of the samples were then treated in an O₂ plasma oven for 3 min. Immediately after removal from the plasma oven, the stamps had a single drop of PPC (polypropylene carbonate, 15% w.t. in anisole) deposited and were then spin coated (1K RPM for 30 s) to ensure even distribution. Following this, the stamps were placed on a hot plate held at 80 °C for 5 min to dry the PPC. At this point, the stamps could be stored for future use.

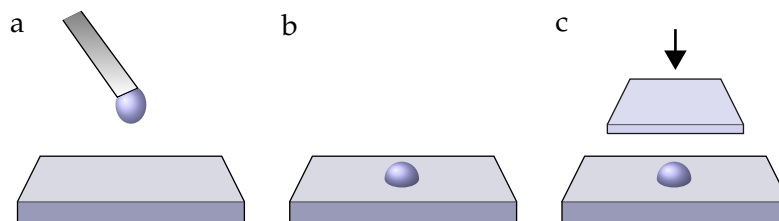


Figure 7.4 The formation steps to produce a PDMS flake pick-up stamp: (a) a drop of PDMS (10:1 elastomer to curing agent) is dropped from a wire onto the glass slide; (b) the droplet is then baked at 110 °C for 15 min to harden; (c) a square of PDMS is placed over the droplet before being spin coated and heat treated.

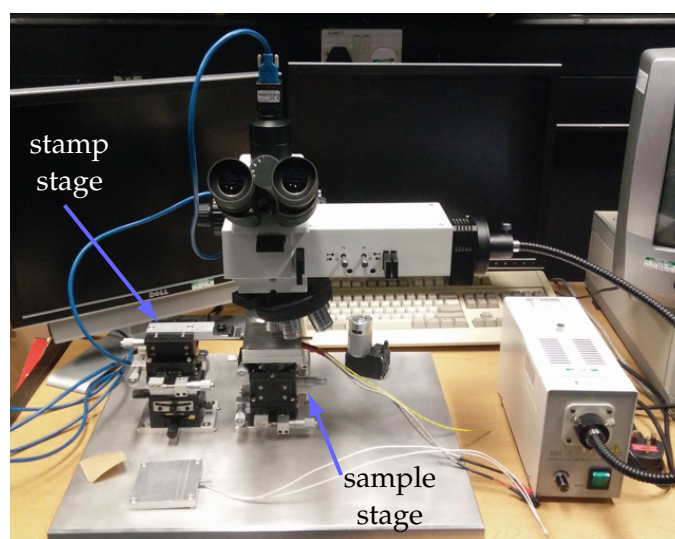


Figure 7.5 The set-up used for the flake pick-up and transfer.

A hBN on SiO₂ sample was prepared as described in Subsection 3.6.1 and mounted on the stage shown in Figure 7.5 where it was secured in place using a vacuum pump. The glass slide containing the stamp was held in place above the sample. The hBN sample was heated to 40 °C using the metal stage. Once at the target temperature, the stamp was lowered gently until in contact with the required flake which had been identified optically or via previous AFM imaging. Once the stamp and target flake had been held together for a few minutes, the heater was either turned off or the

temperature reduced to reharden the stamp to allow the stamp to be pulled away. The sample could then be removed and the target bottom layer sample placed on the stage.

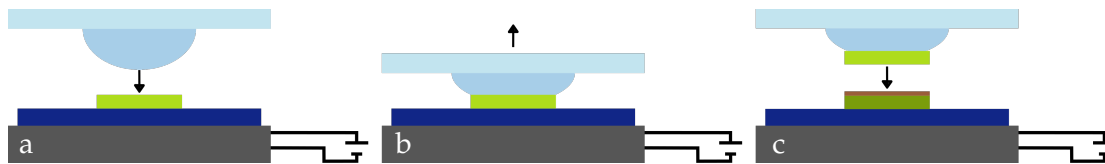


Figure 7.6 The steps required to pick up a flake from a surface: (a) the PDMS/PPC stamp is brought into contact with the target flake at an elevated temperature; (b) the temperature is lowered and the stamp pulled away; (c) the process is repeated to pick up multiple flakes or to deposit the flake.

In order to deposit the flake, two different methods were used. In the first, the stamp was heated to the temperature ($>80^{\circ}\text{C}$) at which the PPC delaminated from the PDMS leaving a large amount of polymer which required removal with acetone. The solvent removal process might modify or even remove the encapsulated molecules or the deposited flakes. To reduce the steps required, a different flake deposition method was created - the soft deposition method. In this method a plasma treated stamp was approached in the same way as for flake pick-up. Once in contact with the surface, the heater was turned off and a small amount of tension placed in the stamp by moving the glass slide holding the stamp away from the surface by approximately $5\text{ }\mu\text{m}$. As the stamp cooled, the PPC front on the surface gradually moved into the centre. If this process was carried out slowly, the flake attached to the stamp adhered more to the lower flake and surface than to the stamp and would remain on the surface. This reduced the amount of PPC contamination on the surface and meant the cleaning stages could be skipped.

7.2 Preservation of C_{60} Islands During Mechanical Transfer

In order to investigate the compatability of mechanical transfer with molecular monolayers on a supporting surface, hBN flakes with C_{60} islands were transferred between SiO_2 substrates.

The C_{60} samples were prepared by James Kerfoot within the Beton group by first preparing hBN/ SiO_2 samples as outlined in Subsection 3.6.1. The samples were loaded into a vacuum chamber with a base pressure of 10^{-8} mbar and annealed at

approximately 450 °C. The C_{60} was sublimed at 374 °C with the sample substrate held at different temperatures to produce different island morphologies. Two different C_{60} island morphologies prepared by depositing the same amount (equivalent to 0.3 ML) were used in this work: a sample with a monolayer covering a third of the surface was prepared with the substrate held at 178 °C and a sample with a bilayer covering approximately a sixth of the surface was prepared with the substrate held at 217 °C. The resulting islands for these two samples are shown in Figure 7.7 and show a significant difference in island morphology. The island heights are higher than would be expected for monolayer and bilayer depositions; the apparent height of C_{60} islands is highly dependent on the set-point of the AFM with a lower set-point giving higher islands. The samples are determined to be monolayers and bilayers according to the deposition parameters, island morphology, and absence of features indicative of multilayers (e.g. step edges).¹⁰¹

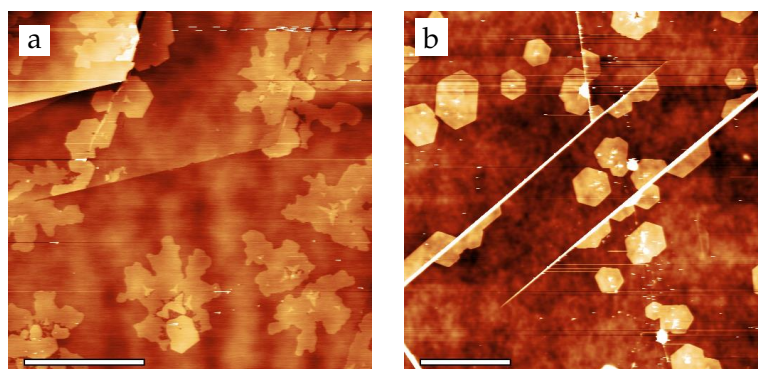


Figure 7.7 The island morphologies for the monolayer and bilayer C_{60} samples: (a) monolayer sample prepared with a substrate temperature of 178 °C with dendritic islands 1.0 ± 0.3 nm high and faceted islands 1.8 ± 0.3 nm high [scale bar = 5 μ m]; (b) bilayer sample prepared with a substrate temperature of 217 °C with faceted islands 2.5 ± 0.3 nm high [scale bar = 5 μ m]. Images acquired by James Kerfoot.¹⁰¹

From the two C_{60} samples with island morphologies shown in Figure 7.7, target flakes were selected and imaged with AFM. These flakes were then picked up using the stamping method outlined in Section 7.1 and deposited using the soft deposition method. This process had a low success rate with many stamps breaking during pick up or deposition likely due to defects in the stamp formation. Additionally some of the hBN flakes tore during pick up or deposition, however, these flakes could still be compared to their pre-transfer structures if there were identifying features such as flake

shape and prominent hBN steps on the surface. The flakes were imaged optically and with AFM before and after transfer. Optical images of the flakes show changes in colour which are due to the optical set up changing and do not reflect a change to the flake thickness.

First a flake from the monolayer sample grown at a substrate temperature of 178 °C was transferred between SiO₂ supports. The monolayer C₆₀ islands shown in Table 7.1 have small amounts of polymer present as circular features on the surface post-transfer but no major change to the C₆₀ island morphology as seen by the comparison of the two islands marked in green. The circular polymer contaminants have an average diameter of 0.32 ± 0.06 nm and may represent contact fronts for the PPC on the transfer stamp. There are some difficulties measuring C₆₀ island height as discussed above, however, the monolayer island height is relatively constant between the two images with 2.1 ± 0.4 nm before transfer and 2.4 ± 0.5 nm after transfer. The bright and dark features on the post transfer image show a change in the hBN flake due to deformation in the supporting SiO₂ or particles that have inadvertently been picked up under the hBN flake. These changes do not appear to have altered the island morphology.

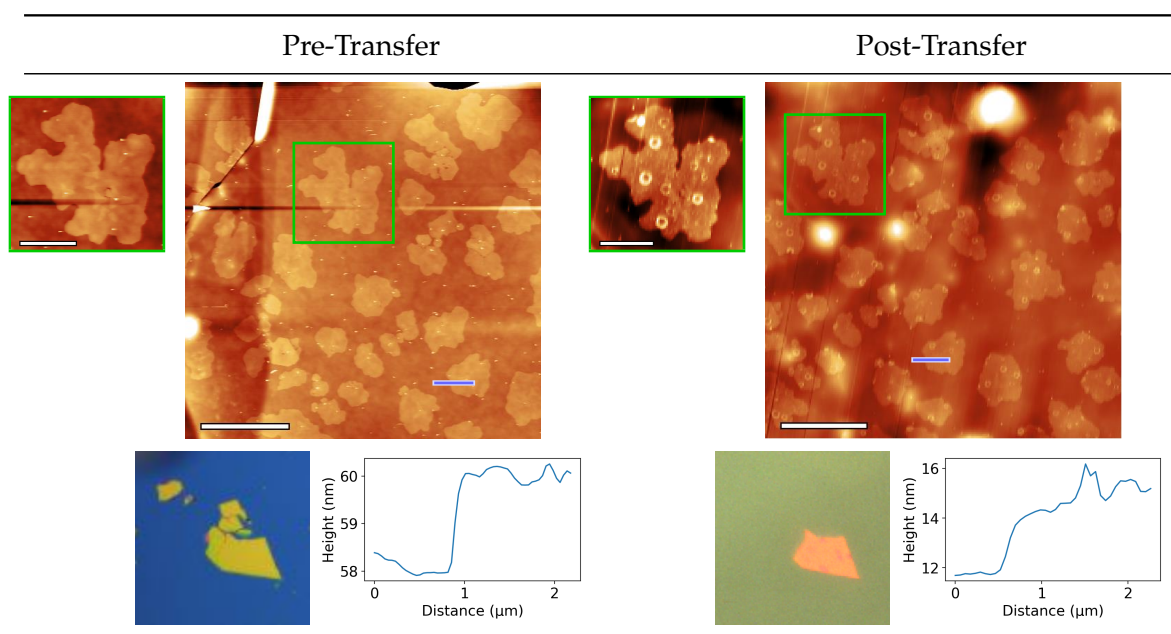


Table 7.1 Monolayer C₆₀ islands supported on hBN before and after transfer with a PPC/PDMS stamp. The profiles along the blue lines are across the same island before and after transfer as do the green squares with this island also shown to the left. Scale bars are 5 μm for the larger images and 2 μm for the smaller. Note: the post-transfer image is rotated from the imaging direction, diagonal lines are changes to the set-point.

Flakes from the bilayer C_{60} sample grown at a substrate temperature of 217 °C were then transferred between substrates to investigate whether the monolayer and bilayer behave differently due to different adhesion forces between C_{60} layers, compared to C_{60} with the hBN surface. The first transferred bilayer flake is shown in Table 7.2 (1) and reveals that much more polymer contamination is present on the transferred bilayer than was seen on the monolayer in Table 7.1. This is reflected by the measured island heights which are 3.8 ± 0.5 nm before and 5 ± 1 nm after transfer. Whilst the height measurements cannot be directly compared due to their dependence on the set point as discussed above, the increase in the variance of the island height indicates a rougher surface which is due to the increased polymer presence. This may reflect a minor difference in stamp preparation or temperature of transfer as more material is also visible on the background hBN, however, it may also be due to a greater adhesion to the bilayer C_{60} than the monolayer C_{60} . In addition, there are folds in the hBN flake visible prior to transfer that are removed post transfer as indicated by the dashed line. This indicates the flexibility of the flake during the transfer process. The bilayer C_{60} islands had grown constrained by these folds and remain in their constrained shape post-transfer.

The second transferred bilayer flake shown in Table 7.2 (2) broke during transfer along a fault line seen before transfer at the top of the image. The fold on the left hand side of the image reduced in height from 63 ± 5 nm to 48 ± 3 nm. In the pre-transfer image, it appears that there is a large step edge on the bottom right of the flake, however, this step disappears post-transfer. This is explained as the initial flake lying on top of a second flake which is creating a false step edge as the C_{60} island present across the apparent step is unchanged in the post-transfer image. The AFM image post-transfer also shows damage to the hBN surface with the formation of a dark pore 3.4 ± 0.7 nm deep on the surface. This was the only sample to display damage to the hBN surface which may suggest that there were defects in the hBN flake. This sample showed much less polymer contaminant on the hBN surface but a similar amount on the C_{60} islands to the first transferred bilayer sample, which suggests the polymer

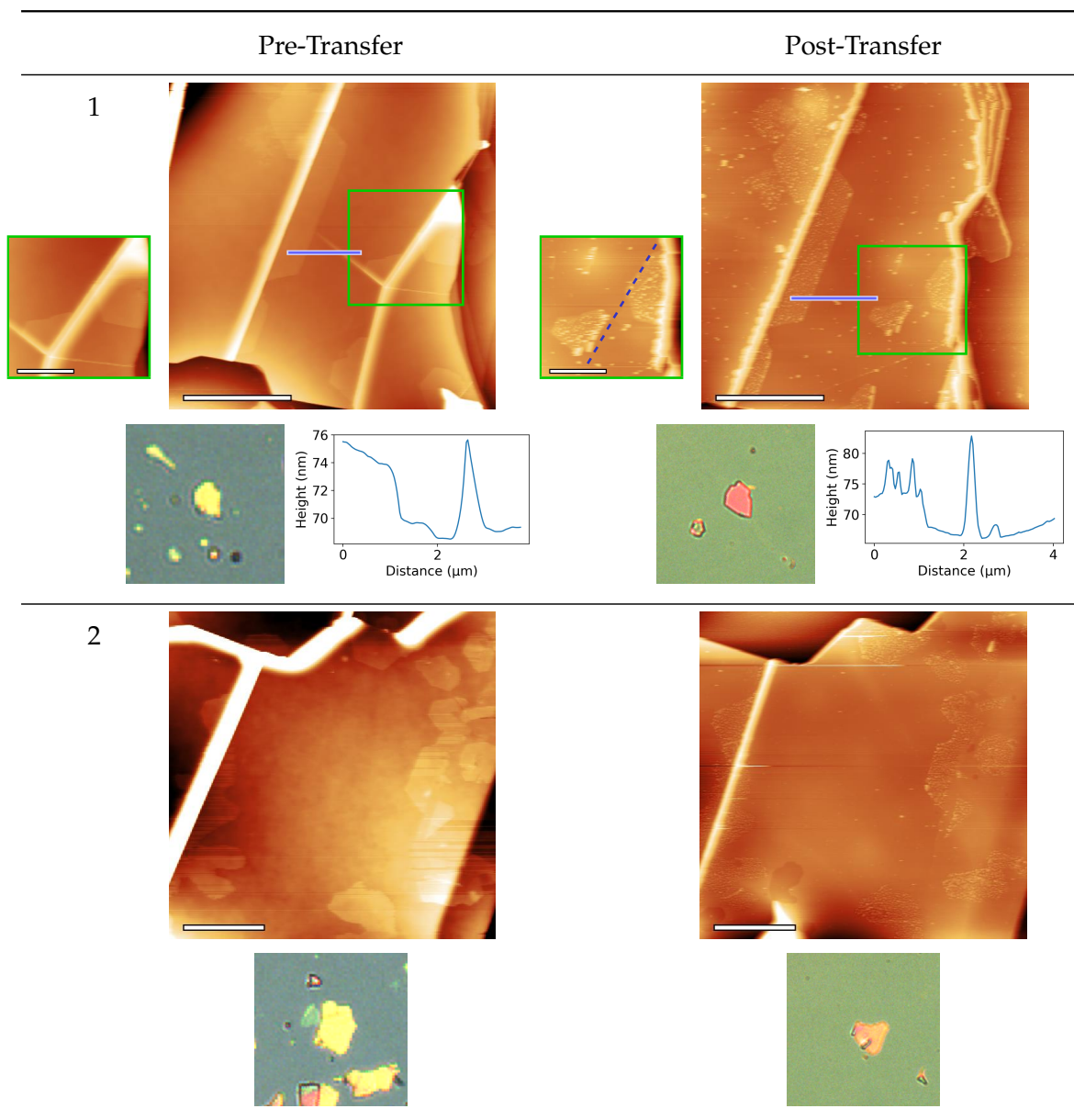


Table 7.2 Bilayer C_{60} islands on hBN before and after transfer between SiO_2 substrates. Scale bars are $5\ \mu m$ for the larger images and $2\ \mu m$ for the smaller.

contamination is associated with the C_{60} islands rather than being a fault in the stamp production.

These transferred C_{60} on hBN flakes demonstrate that the monolayer C_{60} appears more compatible with mechanical transfer than C_{60} bilayers. This may be connected to the percentage coverage so, in future, a bilayer structure covering more of the surface should be investigated as should a lower monolayer coverage.

7.3 Preparation of hBN Encapsulated C_{60} islands

Following on from the successful transfer of C_{60} /hBN flakes between SiO_2 substrates, hBN flakes were transferred onto C_{60} /hBN flakes to form heterostructures of encapsulated C_{60} ready for imaging with AFM and future transfer to electron-transparent grids for imaging with TEM. For this work a 0.3 ML C_{60} sample prepared with the substrate at room temperature prepared by James Kerfoot was used. Images showing the island morphology are shown in Figure 7.8 and show a high coverage (44%) with islands 1.6 ± 0.2 nm high.

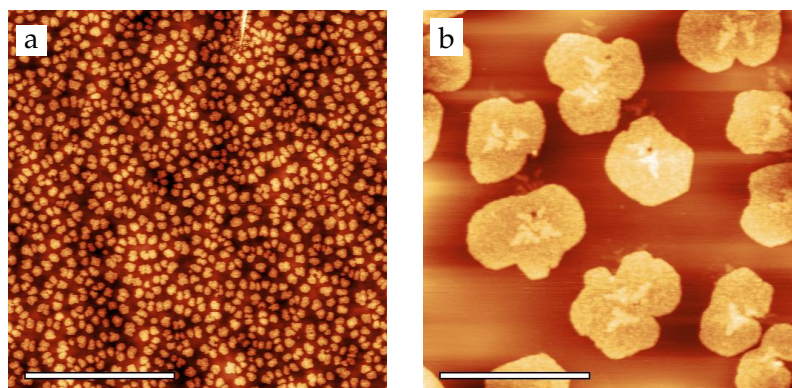


Figure 7.8 Island morphology for C_{60} islands deposited onto a substrate held at room temperature: (a) average island height 1.6 ± 0.3 nm [scale bar = $4 \mu m$]; (b) average island height 1.6 ± 0.1 nm [scale bar = 400 nm]. Images acquired by James Kerfoot.¹⁰¹

After optical inspection of a clean hBN/ SiO_2 sample, a thin hBN flake as shown in Figure 7.9 (a) was picked up using the method outlined in Section 7.1. A similar inspection process was carried out on the sample of C_{60} on hBN shown in Figure 7.8 to select a flake onto which to deposit the upper flake. This led to the formation of a heterostructure as seen in Figure 7.9 (b) and (d). The stamp used for deposition survived the process and it can be seen in Figure 7.9 (c) with additional flakes picked up from the C_{60} sample; additionally an undeposited hBN flake is seen both before and after deposition and is circled in blue. Due to the soft method used to create the heterostructure, no cleaning steps were taken post deposition. The heterostructure was then imaged using ambient AFM.

From the image in Figure 7.10 (a), the heights of the two flakes forming the heterostructure were measured to be 27 ± 5 nm and 43 ± 3 nm. There are C_{60} islands

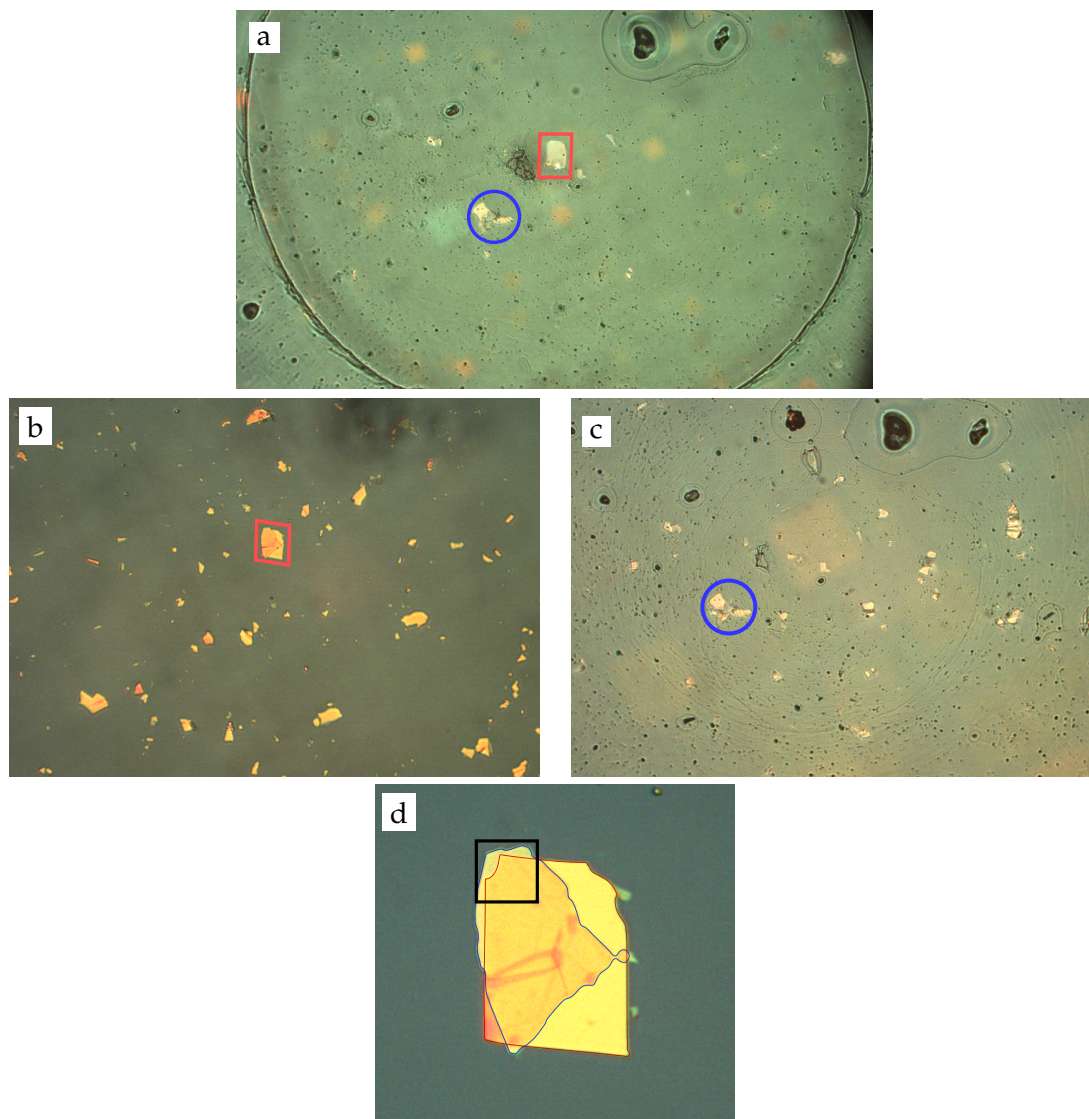


Figure 7.9 Optical images of the formation of a hBN/C₆₀/hBN heterostructure: (a) the target hBN flake on the PDMS/PPC stamp outlined with a red box; (b) the flake deposited onto the C₆₀/hBN sample to form a heterostructure outlined with a red box; (c) the stamp post drop-off of the selected flake showing that extra flakes were picked up from the C₆₀ sample and that one of the original flakes remained on the stamp; (d) optical image with the two flakes forming the heterostructure outlined in red and blue.

visible on the lower flake which have an average height of 2.3 ± 0.7 nm (from Figure 7.10 (a) and (b)), which corresponds to the C₆₀ island heights seen for the transferred C₆₀/hBN flakes above. As shown in Figure 7.10 (b), the upper flake mostly covers the underlying structure with a reduced roughness on the upper flake of 0.14 ± 0.03 nm (1.6 ± 0.7 nm on the lower flake). This also suggests that there are relatively low amounts of polymer from the transfer process. Figure 7.10 (a) also shows that large underlying flake structures can be seen through the upper flake with

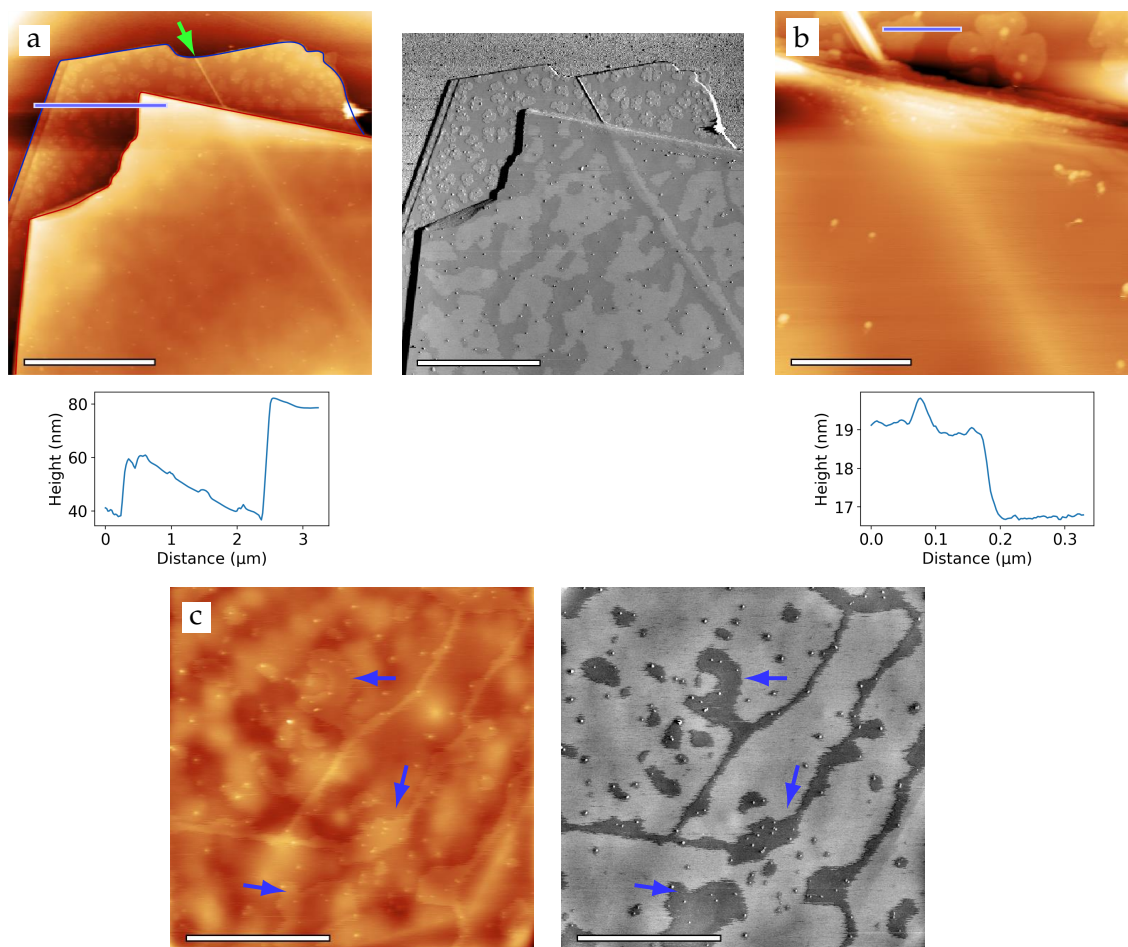


Figure 7.10 Ambient AFM images of the heterostructure: (a) height and phase images of area outlined by black line in Figure 7.9 of heterostructure comprised of lower flake 27 ± 5 nm high (blue) and upper flake 43 ± 3 nm high (red), below is a profile along the blue line [scale bar = $3 \mu\text{m}$]; (b) height image of top edge of heterostructure showing C_{60} islands on the lower flake 2.2 ± 0.4 nm high, below is a profile along the blue line [scale bar = 500 nm]; (c) height and phase images of an area on the upper flake below (a) showing changes in the flake corresponding to C_{60} islands on the underlying flake with the larger islands marked by blue arrows [scale bar = $2 \mu\text{m}$].

a diagonal line corresponding to a fold in the lower flake visible as a raised area in the upper flake as shown by the green arrow. This feature is visible in both the height and phase images. Figure 7.10 (c) shows areas of encapsulated material under the upper hBN flake which change between images. The bright lines may be due to folds in the bottom hBN layer or may denote boundaries of C_{60} islands. There are also areas visible in both height and phase images that are suggestive of C_{60} islands as marked by the blue arrows. These have a different morphology to the unencapsulated islands which may be due to an increase in pressure between the sheets. A pressure increase of 1–1.5 GPa has previously been observed within graphene encapsulated salts prepared

using a wet-transfer method by Vasu et al.¹⁰⁵. This increased pressure is believed to contribute to the removal of contaminants between layers but, in this case, may also be leading to a rearrangement or removal of C₆₀ islands although the pressures involved in the preparation for this heterostructure is unknown.

7.3.1 TEM of C₆₀ Heterostructures

Once the stamping method had been successfully used to create heterostructures encapsulating molecules, the AFM results suggested that the structure inside the heterostructure was different to that seen on the open surface. As seen above, there were limitations to the information obtained via AFM so an alternative method was used that would allow imaging through the hBN flake –TEM. In order to transfer the heterostructures to the TEM grids, a variation on the stamping method used to form the heterostructures was used. Silicon nitride grids (50 nm thick) containing a single 500 μm window with a labelled grid of 2 μm pores that had been coated with gold to reduce charging under the electron beam were used. Due to the fragile nature of the TEM grids, they were not held in place with the vacuum pump but were attached to a small square of PDMS which was placed on the sample stage.

Optical images taken at various stages of sample preparation are shown in Figure 7.11. A selection of heterostructures were prepared and deposited onto a clean SiO₂/Si surface as described in Section 7.2 (a). These were then picked up with a transfer stamp. It was clear by optical comparison of Figure 7.11 (a) and (b) that only a selection of the flakes and heterostructures were successfully picked up. A gold coated silicon nitride TEM was then held in place under the stamp using a PDMS film. The stamp was then gently lowered until in contact with the grid. The peel deposition method was not used due to the risk of removing the centre of the TEM grid from the brittle silicon nitride surround. The sample stage was then heated to 80 °C to deposit the flakes; this caused partial delamination of the PPC from the stamp which led to less polymer on the surface than for full delamination as seen in Figure 7.11 (d). The remaining polymer was then removed by placing the grid in acetone for several days

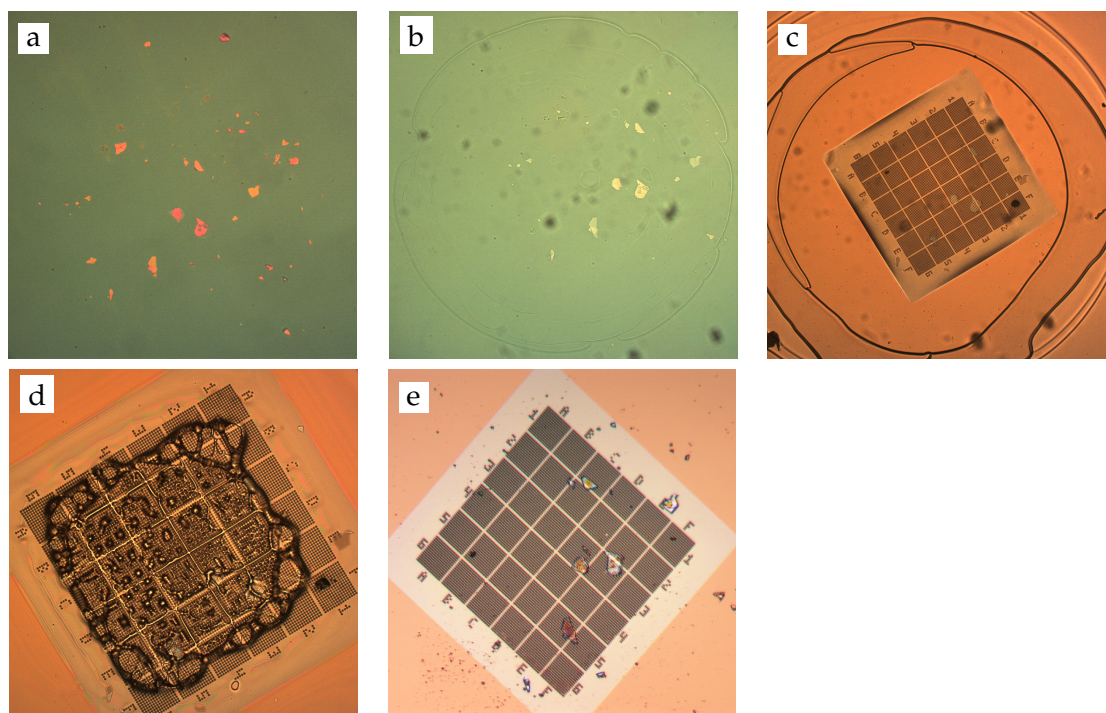


Figure 7.11 Optical images of the transfer of heterostructures to a TEM grid: (a) the heterostructures on a silicon substrate prior to transfer; (b) the heterostructures on the transfer stamp; (c) the TEM grid during the transfer process; (d) the TEM grid post transfer with polymer present on the surface; (e) the TEM grid post cleaning with acetone.

resulting in the clean grid seen in Figure 7.11 (e). An additional heterostructure was lost in the cleaning process.

This sample was then imaged in a JOEL 2100F FEG-TEM with the locations denoted by the grid reference system. The resulting images in Figure 7.12 were obtained with magnification between 100x and 1000x. As can be seen in Figure 7.12 (a), the focal plane for the hBN heterostructures was difficult to find due to the thickness of the hBN flakes and their non-planar positioning on the TEM grid. Circles between $0.17 \pm 0.01 \mu\text{m}$ and $0.91 \pm 0.03 \mu\text{m}$ are visible on the TEM images in Figure 7.12 (d) and (e). These are likely to be pockets of the remaining solvent from the cleaning process post transfer onto the TEM grid. Alternatively, these circular features could be areas of C_{60} , however, this is unlikely given the island morphologies seen previously. If the solvent did penetrate the heterostructures, it may have removed or led to a rearrangement of the C_{60} . The lines across the heterostructure Figure 7.12 (c) are folds in one of the flakes forming the structure.

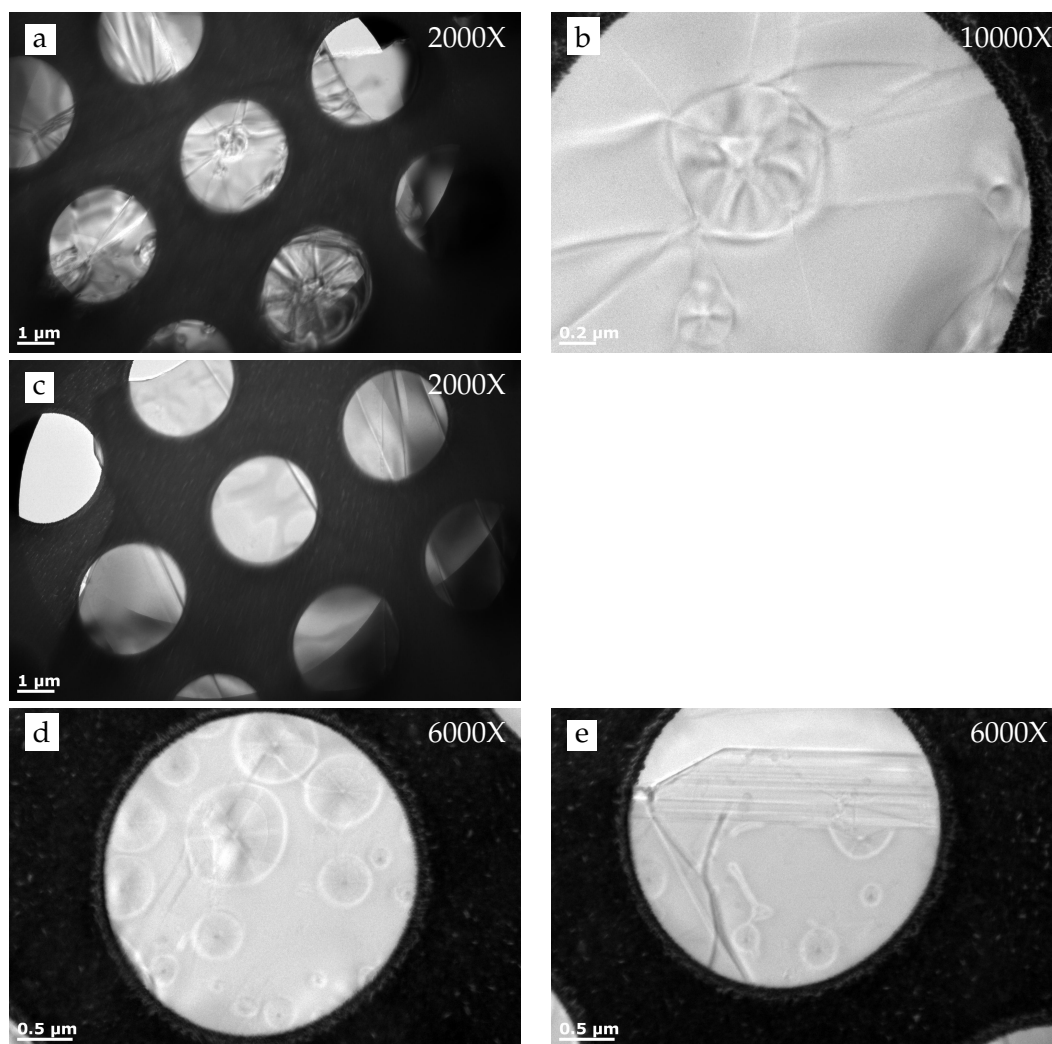


Figure 7.12 Low magnification images of the TEM grid: (a) 2000x image of the heterostructure in E5 showing the distortion in the sample, the ring edges on the right hand side show that the focal plane is beyond the TEM grid; (b) 10000x image of the heterostructure in E5; (c) 2000x image of the heterostructure in E3 showing a much flatter flake with lines across it; (d) 6000x image of heterostructure in D3 with circles of radius $(0.17 \pm 0.01) \mu\text{m}$ to $(0.91 \pm 0.03) \mu\text{m}$; (e) 6000x image of the edge of heterostructure in D3.

Higher magnification images were obtained in flat areas of interest on the heterostructures. Figure 7.13 (a) shows the edge of the heterostructure in E5 with the change in contrast representing hBN steps. The dark features on the edge step are metal particles from the grid coating or from polymer contamination. Also on the heterostructure in E5, a pattern with a period of $1.02 \pm 0.02 \text{ nm}$ was seen. This was too large to be the hBN lattice (0.250 nm) and was determined to be a moiré pattern by the FFT showing two hexagonal patterns. A moiré pattern was also observed on a different area of this heterostructure with a period of $0.95 \pm 0.02 \text{ nm}$ and is shown in Figure 7.13

(c). This image also shows the edge of one of the flakes forming the heterostructure as highlighted with the red dashed line. The moiré pattern is only seen in the area to the left of this line; this is confirmed using the fast fourier transforms (FFT): the FFT on the area on the right reveals a lattice vector of 0.21 ± 0.02 nm and the FFT of the area on the left shows a complex structure formed from the overlay of two different orientations of hBN lattice. The difference between the true hBN lattice (0.250 nm) and the measured lattice (0.21 ± 0.02 nm) is likely due to distortion in the TEM or the focus being incorrect for the hBN lattice plane.

Additional moiré patterns with periods of 0.97 ± 0.04 nm and 4.4 ± 0.3 nm were seen on the heterostructures in E3 and D3 respectively (Figure 7.13 (d-f)). Once again, the FFT of the image in Figure 7.13 (f) shows the hBN lattice as well as the moiré pattern with the hBN lattice measured to be 0.22 ± 0.02 nm. This is consistent with the hBN lattice constant measured above suggesting a consistent distortion or error in focal point of the TEM for the hBN lattice plane. The image in Figure 7.13 (e) shows the large scale of the moiré pattern observed on the surface as well as an area where the moiré pattern is absent (outlined in yellow). This oval area likely represents an area of encapsulated cleaning solvent or other material preventing the two flakes from interacting to form a moiré pattern. The absence of the C_{60} islands in the TEM images may be due to their removal during the cleaning stage, however, the solvent used does not have high C_{60} solubility. The signal from the C_{60} islands is likely hidden by the signal from the hBN flakes due to their similar atomic masses but large difference in layer thickness.

Heterostructure Location	Moiré Period	Rotation
E5	1.02 ± 0.02 nm	$14.1 \pm 0.5^\circ$
E3	0.97 ± 0.04 nm	$14.8 \pm 0.6^\circ$
D3	4.4 ± 0.3 nm	$3.3 \pm 0.3^\circ$

Table 7.3 The measured moiré patterns and the corresponding relative rotation between hBN flakes calculated using a rearrangement of Equation 2.1 ($\phi = 2 \sin^{-1}(d/2D)$) and the known value for the hBN lattice ($d = 0.250$ nm).

The observed moiré patterns in Figure 7.13 can be mathematically modelled using Equation 2.1 to give the relative rotation between the two hBN flakes¹⁵ which are

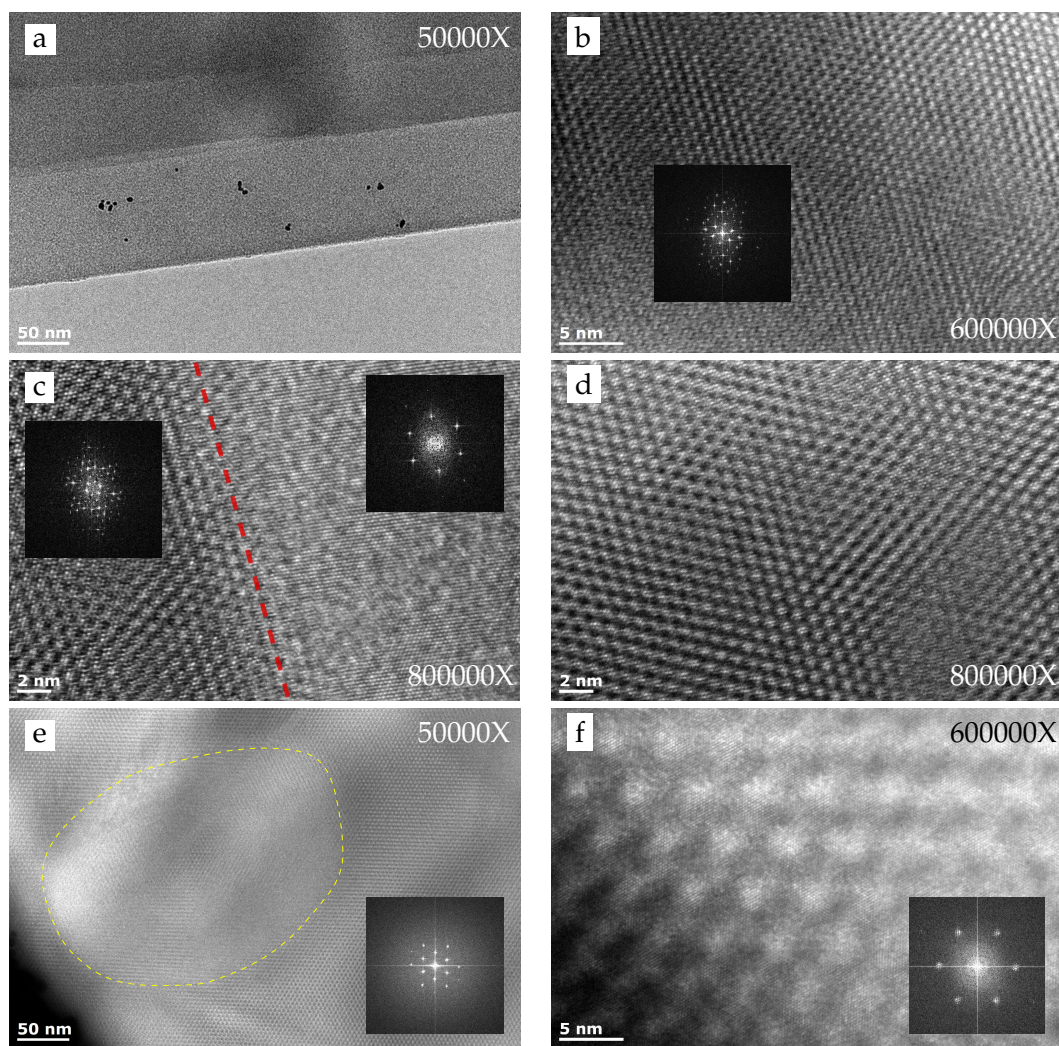


Figure 7.13 High magnification images of the TEM grid: (a) 50000x image of the edge of the heterostructure in E5; (b) 600000x image of the lattice with period of 1.02 ± 0.02 nm from the FFT on the flake seen in (a); (c) 800000x image of an area of heterostructure on the edge of one of the flakes with the FFT area on the right having a lattice vector of 0.21 ± 0.01 nm and the FFT on the left having a complex structure; (d) 800000X image of lattice from E3 with a lattice of 0.97 ± 0.04 nm; (e) 50000x image of a moiré pattern of 4.1 ± 0.2 nm for the heterostructure in D3 with a oval of absent moiré pattern; (f) 600000x image of a moiré pattern with period 4.6 ± 0.2 nm for the heterostructure in D3, inset is the FFT which also reveals a lattice with period 0.22 ± 0.02 nm.

shown in Table 7.3. This gives similar rotations for the heterostructures in E5 and E3 and a much smaller rotation for the heterostructure in D3. The rotations for the E5 and E3 structures are much larger than the rotations seen by Liao et al.¹⁵ due to better instrumental resolution to separate the smaller moiré patterns from the hBN lattice. This modelling assumes no influence from the C_{60} layer which could have contributed

to the observed moiré pattern, however, no evidence of the C_{60} islands was seen with the TEM.

7.4 Summary

The technique used in this chapter is an ideal technique for the transfer of 2D materials, particularly hBN due to the low levels of contamination when the slow, low temperature removal is used. This was demonstrated by the successful transfer of C_{60} islands on hBN flakes between SiO_2 substrates.

The transfer method was also used to prepare heterostructures for TEM study. This demonstrated that the technique can be used on delicate substrates although for these the high temperature PPC delamination technique was required.

The results in this chapter demonstrate the successful formation and transfer of heterostructures for TEM imaging. Unfortunately, the encapsulated C_{60} islands were not visible with TEM but were studied with AFM. Future work should investigate molecules containing metal atoms as these are more likely to be visible with TEM due to higher contrast - ideal candidates would be zinc-porphyrins or endohedral fullerenes. The possibility of using thinner hBN flakes should be investigated as this would increase the contrast in TEM and perhaps allow for the coalescence of the C_{60} into mono- and bi-layer graphene.

References

1. Geim, A. K.; Novoselov, K. S. [The rise of graphene](#). *Nature Materials* **2007**, *6*, 183–191.
2. Wiesendanger, R.; Anselmetti, D. In *Scanning Tunnelling Microscopy I*, 2nd ed.; Guntherodt, H.-J., Wiesendanger, R., Eds.; Springer-Verlag, 1994; Chapter STM on Lay, pp 131–175.
3. Lin, Y.; Connell, J. W. [Advances in 2D boron nitride nanostructures: nanosheets, nanoribbons, nanomeshes, and hybrids with graphene](#). *Nanoscale* **2012**, *4*, 6908.
4. Zhi, C.; Bando, Y.; Tang, C.; Kuwahara, H.; Golberg, D. [Large-Scale Fabrication of Boron Nitride Nanosheets and Their Utilization in Polymeric Composites with Improved Thermal and Mechanical Properties](#). *Adv. Mater.* **2009**, *21*, 2889–2893.
5. Du, M.; Wu, Y.; Hao, X. [A facile chemical exfoliation method to obtain large size boron nitride nanosheets](#). *CrystEngComm* **2013**, *15*, 1782.
6. Golla, D.; Chattrakun, K.; Watanabe, K.; Taniguchi, T.; Leroy, B. J.; Sandhu, A. [Optical thickness determination of hexagonal boron nitride flakes](#). *Appl. Phys. Lett.* **2013**, *102*.
7. Kim, D. H.; Kim, S. J.; Yu, J. S.; Kim, J. H. [Measuring the thickness of flakes of hexagonal boron nitride using the change in zero-contrast wavelength of optical contrast](#). *Journal of the Optical Society of Korea* **2015**, *19*, 503–507.
8. Novoselov, K. S.; Mishchenko, A.; Carvalho, A.; Neto, A. H. C.; Road, O. [2D materials and van der Waals heterostructures](#). *Science* **2016**, *353*, aac9439.
9. Geim, A. K.; Grigorieva, I. V. [Van der Waals heterostructures](#). *Nature* **2014**, *499*, 419–425.
10. Gorbachev, R. V.; Geim, A. K.; Katsnelson, M. I.; Novoselov, K. S.; Tudorovskiy, T.; Grigorieva, I. V.; MacDonald, A. H.; Morozov, S. V.; Watanabe, K.; Taniguchi, T.; Ponomarenko, L. A. [Strong Coulomb drag and broken symmetry in double-layer graphene](#). *Nature Physics* **2012**, *8*, 896–901.
11. Britnell, L.; Gorbachev, R. V.; Jalil, R.; Belle, B. D.; Schedin, F.; Mishchenko, A.; Georgiou, T.; Katsnelson, M. I.; Eaves, L.; Morozov, S. V.; Peres, N. M. R.; Leist, J.; Geim, A. K.; Novoselov, K. S.; Ponomarenko, L. A. [Field-Effect Tunneling Transistor Based on Vertical Graphene Heterostructures](#). *Science* **2012**, *335*, 947–950.

12. Roy, K.; Padmanabhan, M.; Goswami, S.; Sai, T. P.; Ramalingam, G.; Raghavan, S.; Ghosh, A. Graphene-MoS₂ hybrid structures for multifunctional photoresponsive memory devices. *Nature Nanotechnology* **2013**, *8*, 826–830.
13. Woessner, A.; Lundeborg, M. B.; Gao, Y.; Principi, A.; Alonso-González, P.; Carrega, M.; Watanabe, K.; Taniguchi, T.; Vignale, G.; Polini, M.; Hone, J.; Hillenbrand, R.; Koppens, F. H. Highly confined low-loss plasmons in graphene-boron nitride heterostructures. *Nature Materials* **2015**, *14*, 421–425.
14. Mirzayev, R.; Mustonen, K.; Monazam, M. R. A.; Mittelberger, A.; Pennycook, T. J.; Mangler, C.; Susi, T.; Kotakoski, J.; Meyer, J. C. Buckyball sandwiches. *Sci. Adv.* **2017**, *3*, e1700176.
15. Liao, Y.; Cao, W.; Connell, J. W.; Chen, Z.; Lin, Y. Evolution of Moiré Profiles from van der Waals Superstructures of Boron Nitride Nanosheets. *Scientific Reports* **2016**, *6*, 26084.
16. Schreiber, F. Structure and growth of self-assembling monolayers. *Progress in Surface Science* **2000**, *65*, 151–256.
17. Atkins, P.; De Paula, J. *Atkins' Physical Chemistry*, 9th ed.; Oxford University Press, 2009.
18. Kawai, T.; Tanaka, H.; Nakagawa, T. Low dimensional self-organization of DNA-base molecules on Cu(111) surfaces. *Surface Science* **1997**, *386*, 124–136.
19. Furukawa, M.; Tanaka, H.; Kawai, T. The role of dimer formation in the self-assemblies of DNA base molecules on Cu(111) surfaces: A scanning tunneling microscope study. *Journal of Chemical Physics* **2001**, *115*, 3419–3423.
20. Otero, R.; Schöck, M.; Molina, L. M.; Løegsgaard, E.; Stensgaard, I.; Hammer, B.; Besenbacher, F. Guanine quartet networks stabilized by cooperative hydrogen bonds. *Angewandte Chemie - International Edition* **2005**, *44*, 2270–2275.
21. Griessl, S.; Lackinger, M.; Edelwirth, M.; Hietschold, M.; Heckl, W. M. Self-assembled two-dimensional molecular host-guest architectures from trimesic acid. *Single Molecules* **2002**, *3*, 25–31.
22. Dmitriev, A.; Lin, N.; Weckesser, J.; Barth, J. V.; Kern, K. Supramolecular assemblies of trimesic acid on a Cu(100) surface. *Journal of Physical Chemistry B* **2002**, *106*, 6907–6912.
23. Spitzer, S.; Helmle, O.; Ochs, O.; Horsley, J.; Martsinovich, N.; Heckl, W. M.; Lackinger, M. What can be inferred from moiré patterns? A case study of trimesic acid monolayers on graphite. *Faraday Discuss.* **2017**, *204*, 331–348.

24. Perdigão, L. M. A.; Perking, E. W.; Ma, J.; Staniec, P. A.; Rogers, B. L.; Champness, N. R.; Beton, P. H. [Bimolecular networks and supramolecular traps on Au\(111\)](#). *Journal of Physical Chemistry B* **2006**, *110*, 12539–12542.
25. Madueno, R.; Räisänen, M. T.; Silien, C.; Buck, M. [Functionalizing hydrogen-bonded surface networks with self-assembled monolayers](#). *Nature* **2008**, *454*, 618–621.
26. Korolkov, V. V.; Svatek, S. A.; Allen, S.; Roberts, C. J.; Tendler, S. J. B.; Taniguchi, T.; Watanabe, K.; Champness, N. R.; Beton, P. H. [Bimolecular porous supramolecular networks deposited from solution on layered materials: graphite, boron nitride and molybdenum disulphide](#). *Chem. Commun.* **2014**, *50*, 8882–8885.
27. Zhang, H. M.; Pei, Z. K.; Xie, Z. X.; Long, L. S.; Mao, B. W.; Xu, X.; Zheng, L. S. [Preparing self-assembled monolayers of cyanuric acid and melamine complex on HOPG surfaces](#). *J. Phys. Chem. C* **2009**, *113*, 13940–13946.
28. Zhang, X.; Chen, T.; Chen, Q.; Wang, L.; Wan, L.-J. [Self-assembly and aggregation of melamine and melamine–uric/cyanuric acid investigated by STM and AFM on solid surfaces](#). *Phys. Chem. Chem. Phys.* **2009**, *11*, 7708.
29. Korolkov, V. V.; Timokhin, I. G.; Haubrichs, R.; Smith, E. F.; Yang, L.; Yang, S.; Champness, N. R.; Schröder, M.; Beton, P. H. [Supramolecular networks stabilise and functionalise black phosphorus](#). *Nature Communications* **2017**, *8*, 1–8.
30. Silly, F.; Shaw, A. Q.; Castell, M. R.; Briggs, G. A. D.; Mura, M.; Martsinovich, N.; Kantorovich, L. [Melamine Structures on the Au \(111\) Surface](#). *J. Phys. Chem. C* **2008**, *112*, 11476–11480.
31. Schmitz, C. H.; Ikonov, J.; Sokolowski, M. [Two commensurate hydrogen-bonded monolayer structures of melamine on Ag\(111\)](#). *Surface Science* **2010**, *605*, 1–6.
32. Wang, L.; Li, P.; Shi, H.; Li, Z.; Wu, K.; Shao, X. [Thickness-Dependent Adsorption of Melamine on Cu/Au\(111\) Films](#). *J. Phys. Chem. C* **2017**, *121*, 7977–7984.
33. Ciesielski, A.; Colella, S.; Zalewski, L.; Bruchmann, B.; Samorì, P. [Nanopatterning the graphite surface with ordered macrocyclic or ribbon-like assemblies of isocytosine derivatives: an STM study](#). *CrystEngComm* **2011**, *13*, 5535.
34. Bao, M.; Wei, X.; Cai, L.; Sun, Q.; Liu, Z.; Xu, W. [Self-assembly of melem on Au\(111\) and Ag\(111\): the origin of two different hydrogen bonding configurations](#). *Phys. Chem. Chem. Phys.* **2017**, *19*, 18704–18708.

35. Silly, F. Selecting Two-Dimensional Halogen Halogen-Bonded Self-Assembled 1,3,5-Tris(4-iodophenyl)benzene Porous Nanoarchitectures at the Solid-Liquid Interface. *J. Phys. Chem. C* **2013**, *117*, 20244–20249.
36. Gutzler, R.; Fu, C. Y.; Dadvand, A.; Hua, Y.; MacLeod, J. M.; Rosei, F.; Perepichka, D. F. Halogen bonds in 2D supramolecular self-assembly of organic semiconductors. *Nanoscale* **2012**, *4*, 5965–5971.
37. Russell, J. C.; Blunt, M. O.; Garfitt, J. M.; Scurr, D. J.; Alexander, M. R.; Champness, N. R.; Beton, P. H. Dimerization of tri(4-bromophenyl)benzene by aryl-aryl coupling from solution on a gold surface. *J. Am. Chem. Soc.* **2011**, *133*, 4220–3.
38. Lackinger, M. Surface-Assisted Ullmann Coupling. *Chem. Commun.* **2017**, *53*, 7872–7885.
39. Cai, J.; Ruffieux, P.; Jaafar, R.; Bieri, M.; Braun, T.; Blankenburg, S.; Muoth, M.; Seitsonen, A. P.; Saleh, M.; Feng, X.; Müllen, K.; Fasel, R. Atomically precise bottom-up fabrication of graphene nanoribbons. *Nature* **2010**, *466*, 470–473.
40. Blunt, M. O.; Russell, J. C.; Champness, N. R.; Beton, P. H. Templating molecular adsorption using a covalent organic framework. *Chem. Commun.* **2010**, *46*, 7157–7159.
41. Franc, G.; Gourdon, A. Covalent networks through on-surface chemistry in ultra-high vacuum: state-of-the-art and recent developments. *Phys. Chem. Chem. Phys.* **2011**, *13*, 14283.
42. Lindner, R.; Kühnle, A. On-Surface Reactions. *ChemPhysChem* **2015**, *16*, 1582–1592.
43. Gao, H. Y.; Franke, J. H.; Wagner, H.; Zhong, D.; Held, P. A.; Studer, A.; Fuchs, H. Effect of metal surfaces in on-surface glaser coupling. *J. Phys. Chem. C* **2013**, *117*, 18595–18602.
44. Cirera, B.; Zhang, Y. Q.; Björk, J.; Klyatskaya, S.; Chen, Z.; Ruben, M.; Barth, J. V.; Klappenberger, F. Synthesis of extended graphdiyne wires by vicinal surface templating. *Nano Letters* **2014**, *14*, 1891–1897.
45. Gao, H. Y.; Zhong, D.; Mönig, H.; Wagner, H.; Held, P. A.; Timmer, A.; Studer, A.; Fuchs, H. Photochemical glaser coupling at metal surfaces. *J. Phys. Chem. C* **2014**, *118*, 6272–6277.
46. Giessibl, F. J. Advances in atomic force microscopy. *Rev. Mod. Phys.* **2003**, *75*, 949–983.
47. Tersoff, J.; Hamann, D. R. Theory of the scanning tunneling microscope. *Physical Review B* **1985**, *31*, 805–813.
48. Magonov, S. N.; Whangbo, M.-H. *Surface Analysis with STM and AFM*; VCH Verlagsgesellschaft mbH, 1996.

49. Abel, M.; Clair, S.; Ourdjini, O.; Mossoyan, M.; Porte, L. [Single Layer of Polymeric Fe-Phthalocyanine: An Organometallic Sheet on Metal and Thin Insulating Film](#). *J. Am. Chem. Soc.* **2011**, *133*, 1203–1205.
50. Eigler, D. M.; Stroscio, J. A. Atomic and Molecular Manipulation with the Scanning Tunneling Microscope. *Science* **1991**, *125*, 1319–1326.
51. Li, B.; Li, Z.; Yang, J.; Hou, J. G. [STM studies of single molecules: Molecular orbital aspects](#). *Chemical Communications* **2011**, *47*, 2747–2762.
52. H.C., H. [The London—van der Waals attraction between spherical particles](#). *Physica* **1937**, *4*, 1058–1072.
53. García, R.; Perez, R. [Dynamic atomic force microscopy methods](#). *Surface Science Reports* **2002**, *47*, 197–301.
54. García, R. *Amplitude Modulation Atomic Force Microscopy*, 1st ed.; John Wiley & Sons, 2010.
55. Attard, G.; Barnes, C. *Surfaces*, 1st ed.; Oxford University Press: Oxford, 1998.
56. Briggs, D. In *Surface Analysis by Auger and X-Ray Photoelectron Spectroscopy*; Briggs, D., Grant, J. T., Eds.; IM Publications and SurfaceSpectra Limited: Chichester, 2003; pp 31–56.
57. Jenkins, R.; Manne, R.; Robin, R.; Senemaud, C. [Nomenclature system for X-ray spectroscopy](#). *Pure & Appl. Chem.* **1991**, *63*, 149–155.
58. Friedbacher, G.; Bubert, H. In *Surface and Thin Film Analysis*, 2nd ed.; Friedbacher, G., Bubert, H., Eds.; Wiley-VCH Verlag GmbH & Co. KGaA: Weinheim, Germany, 2011.
59. Hofmann, E. *Mass spectrometry: principles and applications*, 3rd ed.; John Wiley & Sons: Chichester, 2007; p 502.
60. Vickerman, J. C.; Briggs, D. *ToF-SIMS: Surface Analysis by Mass Spectroscopy*, 1st ed.; IM Publications: Chichester, 2001.
61. de Hoffmann, E.; Stroobant, V. *Mass Spectrometry: Principles and Applications*, 3rd ed.; John Wiley & Sons: Winchester, 2013.
62. Chescoe, D.; Goodhew, P. *The Operation of Transmission and Scanning Electron Microscopes*; RMS Microscopy Handbooks: London, 1990.
63. Agilent Technologies, *High and Ultra-High Vacuum for Science Research*; 2011; pp 1–136.

64. Taniguchi, T.; Watanabe, K. Synthesis of high-purity boron nitride single crystals under high pressure by using Ba-BN solvent. *Journal of Crystal Growth* **2007**, *303*, 525–529.
65. Asylum Research, Cypher SPM User Guide USER GUIDE 2 Asylum Research Cypher Scanning Probe Microscope. 2013.
66. PREVAC, PREVAC - flag style sample holders. 2012; <https://www.prevac.eu/en/2,offer/36,sample-holders/339,flag-style-sample-holders.html>.
67. Horcas, I.; Fernandez, R.; Gomez-Rodriguez, J.; Colchero, J.; Gomez-Herrero, J.; Baro, A. WSXM: A software for scanning probe microscopy and a tool for nanotechnology. *Review of Scientific Instruments* **2007**, *78*.
68. Nečas, D.; Klapetek, P. Gwyddion: An open-source software for SPM data analysis. *Central European Journal of Physics* **2012**, *10*, 181–188.
69. Gutzler, R. Band-structure engineering in conjugated 2D polymers. *Phys. Chem. Chem. Phys.* **2016**, *18*, 29092–29100.
70. Morchutt, C.; Björk, J.; Krotzky, S.; Gutzler, R.; Kern, K. Covalent coupling via dehalogenation on Ni(111) supported boron nitride and graphene. *Chem. Commun.* **2015**, *51*, 2440–2443.
71. Eder, G.; Smith, E. F.; Cebula, I.; Heckl, W. M.; Beton, P. H.; Lackinger, M. Solution preparation of two-dimensional covalently linked networks by polymerization of 1,3,5-Tri(4-iodophenyl)benzene on Au(111). *ACS Nano* **2013**, *7*, 3014–3021.
72. Schlögl, S.; Heckl, W. M.; Lackinger, M. On-surface radical addition of triply iodinated monomers on Au(111) - The influence of monomer size and thermal post-processing. *Surface Science* **2012**, *606*, 999–1004.
73. Zhao, W.; Dong, L.; Huang, C.; Win, Z. M.; Lin, N. Cu- and Pd-Catalyzed Ullmann Reaction on a Hexagonal Boron Nitride Layer. *Chem. Commun.* **2016**, *52*, 13225–13228.
74. Eichhorn, J.; Nieckarz, D.; Ochs, O.; Samanta, D.; Schmitt, M. On-Surface Ullmann Coupling : The Influence of Kinetic Reaction Parameters on the Morphology and Quality of Covalent Networks. *ACS Nano* **2014**, *8*, 7880–7889.
75. Cavallo, G.; Metrangolo, P.; Milani, R.; Pilati, T.; Priimagi, A.; Resnati, G.; Terraneo, G. The halogen bond. *Chem. Rev.* **2016**, *116*, 2478–2601.

76. Peyrot, D.; Silly, F. On-Surface Synthesis of Two-Dimensional Covalent Organic Structures versus Halogen-Bonded Self-Assembly: Competing Formation of Organic Nanoarchitectures. *ACS Nano* **2016**, *10*, 5490–5498.
77. Gatti, R.; Macleod, J. M.; Lipton-Duffin, J. A.; Moiseev, A. G.; Perepichka, D. F.; Rosei, F. Substrate, Molecular Structure, and Solvent Effects in 2D Self-Assembly via Hydrogen and Halogen Bonding. *J. Phys. Chem. C* **2014**, 25505–25516.
78. Gutzler, R.; Walch, H.; Eder, G.; Kloft, S.; Heckl, W. M.; Lackinger, M. Surface mediated synthesis of 2D covalent organic frameworks: 1,3,5-tris(4-bromophenyl)benzene on graphite(001), Cu(111), and Ag(110). *Chem. Commun.* **2009**, 4456–4458.
79. Passarelli, M. K. et al. The 3D OrbiSIMS - Label-free metabolic imaging with subcellular lateral resolution and high mass-resolving power. *Nature Methods* **2017**, *14*, 1175–1183.
80. Korolkov, V. V.; Mullin, N.; Allen, S.; Roberts, C. J.; Hobbs, J. K.; Tendler, S. J. B. The structure and formation of hydrogen-bonded molecular networks on Au(111) surfaces revealed by scanning tunnelling and torsional-tapping atomic force microscopy. *Phys. Chem. Chem. Phys.* **2012**, *14*, 15909.
81. Uemura, S.; Aono, M.; Komatsu, T.; Kunitake, M. Two-dimensional self-assembled structures of melamine and melem at the aqueous solution-Au(111) interface. *Langmuir* **2010**, *27*, 1336–1340.
82. Okada, A.; Nakata, Y.; Minou, K.; Yoshimura, M.; Kadono, K. Effect of Solvent Evaporation Temperature on the Structure of Two-Dimensional Melamine Networks on Au(111). *Japanese Journal of Applied Physics* **2016**, *55*, 1–22.
83. Šimenas, M.; Tornau, E. E. A model of melamine molecules ordering on metal surfaces. *Journal of Chemical Physics* **2014**, 141.
84. Hughes, E. W. The crystal structure of melamine. *Journal of the American Chemical Society* **1941**, *63*, 1737–1752.
85. Varghese, J. N.; O'Connell, A. M.; Maslen, E. N. The X-ray and neutron crystal structure of 2,4,6-triamino-1,3,5-triazine (melamine). *Acta Crystallographica Section B Structural Crystallography and Crystal Chemistry* **1977**, *33*, 2102–2108.
86. Cousson, A.; Nicolai, B.; Filiaux, F. Melamine (1,3,5-triazine-2,4,6-triamine): A neutron diffraction study at 14 K. *Acta Crystallographica Section E: Structure Reports Online* **2005**, *61*, 222–224.

87. Heyrovská, R. Dependence of the length of the hydrogen bond on the covalent and cationic radii of hydrogen, and additivity of bonding distances. *Chemical Physics Letters* **2006**, *432*, 348–351.
88. Björk, J.; Zhang, Y. Q.; Klappenberger, F.; Barth, J. V.; Stafström, S. Unraveling the mechanism of the covalent coupling between terminal alkynes on a noble metal. *J. Phys. Chem. C* **2014**, *118*, 3181–3187.
89. Liu, J.; Chen, Q.; Xiao, L.; Shang, J.; Zhou, X.; Zhang, Y.; Wang, Y.; Shao, X.; Li, J.; Chen, W.; Xu, G. Q.; Tang, H.; Zhao, D.; Wu, K. Lattice-Directed Formation of Covalent and Organometallic Molecular Wires by Terminal Alkynes on Ag Surfaces. *ACS Nano* **2015**, *9*, 6305–6314.
90. Wang, T.; Lv, H.; Feng, L.; Tao, Z.; Huang, J.; Fan, Q.; Wu, X.; Zhu, J. Unravelling the Mechanism of Glaser Coupling Reaction on Ag(111) and Cu(111) Surfaces: A Case for Halogen Substituted Terminal Alkyne. *Journal of Physical Chemistry C* **2018**, *122*, 14537–14545.
91. Heim, D.; Seufert, K.; Auwärter, W.; Aurisicchio, C.; Fabbro, C.; Bonifazi, D.; Barth, J. V. Surface-assisted assembly of discrete porphyrin-based cyclic supramolecules. *Nano Letters* **2010**, *10*, 122–128.
92. Saywell, A.; Browning, A. S.; Rahe, P.; Anderson, H. L.; Beton, P. H. Organisation and ordering of 1D porphyrin polymers synthesised by on-surface Glaser coupling. *Chemical Communications* **2016**, *52*, 10342–10345.
93. Saywell, A.; Sprafke, J. K.; Esdaile, L. J.; Britton, A. J.; Rienzo, A.; Anderson, H. L.; O'Shea, J. N.; Beton, P. H. Conformation and Packing of Porphyrin Polymer Chains Deposited Using Electrospray on a Gold Surface. *Angew. Chem Int. Ed.* **2010**, *49*, 9136–9139.
94. Eichhorn, J.; Strunskus, T.; Rastgoo-Lahrood, A.; Samanta, D.; Schmittle, M.; Lackinger, M. On-surface Ullmann polymerization via intermediate organometallic networks on Ag(111). *Chem. Commun.* **2014**, *50*, 7680.
95. Wang, T.; Fan, Q.; Feng, L.; Tao, Z.; Huang, J.; Ju, H.; Xu, Q.; Hu, S.; Zhu, J. Chiral Kagome Lattices from On-Surface Synthesized Molecules. *ChemPhysChem* **2017**, *18*, 3329–3333.
96. Jariwala, D.; Marks, T. J.; Hersam, M. C. Mixed-dimensional van der Waals heterostructures. *Nature Materials* **2017**, *16*, 170–181.

97. Hernández, E.; Meunier, V.; Smith, B. W.; Rurali, R.; Terrones, H.; Buongiorno Nardelli, M.; Terrones, M.; Luzzi, D. E.; Charlier, J. C. [Fullerene coalescence in nanopeapods: A path to novel tubular carbon](#). *Nano Letters* **2003**, *3*, 1037–1042.
98. Haigh, S. J.; Gholinia, A.; Jalil, R.; Romani, S.; Britnell, L.; Elias, D. C.; Novoselov, K. S.; Ponomarenko, L. A.; Geim, A. K.; Gorbachev, R. [Cross-sectional imaging of individual layers and buried interfaces of graphene-based heterostructures and superlattices](#). *Nature Materials* **2012**, *11*, 764–767.
99. Ponomarenko, L. A.; Geim, A. K.; Zhukov, A. A.; Jalil, R.; Morozov, S. V.; Novoselov, K. S.; Grigorieva, I. V.; Hill, E. H.; Cheianov, V. V.; Fal'Ko, V. I.; Watanabe, K.; Taniguchi, T.; Gorbachev, R. V. [Tunable metalinsulator transition in double-layer graphene heterostructures](#). *Nature Physics* **2011**, *7*, 958–961.
100. Kim, K.; Yankowitz, M.; Fallahazad, B.; Kang, S.; Movva, H. C. P.; Huang, S.; Larentis, S.; Corbet, C. M.; Taniguchi, T.; Watanabe, K.; Banerjee, S. K.; LeRoy, B. J.; Tutuc, E. [Van der Waals Heterostructures with High Accuracy Rotational Alignment](#). *Nano Letters* **2016**, *16*, 1989–1995.
101. Kerfoot, J.; Korolkov, V. V.; Svatek, S. A.; Alkhamisi, M.; Taniguchi, T.; Watanabe, K.; Parkinson, P. W.; Beton, P. H. [Two-Dimensional Diffusion of Excitons in a Perylene Diimide Monolayer Quenched by a Fullerene Heterojunction](#). *The Journal of Physical Chemistry C* **2019**, *123*, acs.jpcc.9b01413.
102. Wieland, M. B.; Slater, A. G.; Mangham, B.; Champness, N. R.; Beton, P. H. [Fullerenes as adhesive layers for mechanical peeling of metallic, molecular and polymer thin films](#). *Beilstein Journal of Nanotechnology* **2014**, *5*, 394–401.
103. Trave, A.; Ribeiro, F. J.; Louie, S. G.; Cohen, M. L. [Energetics and structural characterization of C60 polymerization in BN and carbon nanopeapods](#). *Physical Review B* **2004**, *70*, 1–7.
104. Khlobystov, A. N.; Porfyrakis, K.; Kanai, M.; Britz, D. A.; Ardavan, A.; Shinohara, H.; Dennis, T. J. S.; Briggs, G. A. D. [Molecular motion of endohedral fullerenes in single-walled carbon nanotubes](#). *Angew. Chem Int. Ed.* **2004**, *43*, 1386–1389.
105. Vasu, K. S.; Prestat, E.; Abraham, J.; Dix, J.; Kashtiban, R. J.; Beheshtian, J.; Sloan, J.; Carbone, P.; Neek-Amal, M.; Haigh, S. J.; Geim, A. K.; Nair, R. R. [Van der Waals pressure and its effect on trapped interlayer molecules](#). *Nature Communications* **2016**, *7*, 1–24.

8 Appendix

8.1 Additional Data for Chapter 4

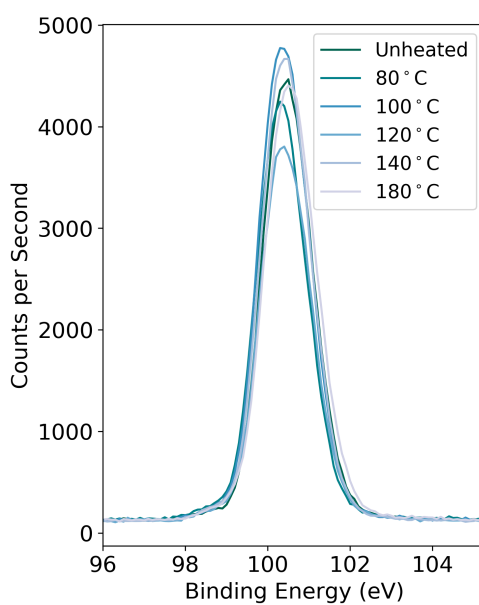


Figure 8.1 The XPS peak corresponding to Si 2p for a range of anneal temperature TIPB samples.

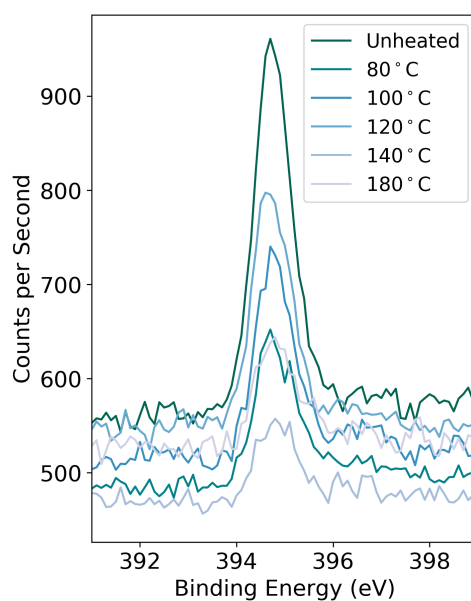


Figure 8.2 The XPS peak corresponding to N 1s for a range of anneal temperature TIPB samples.

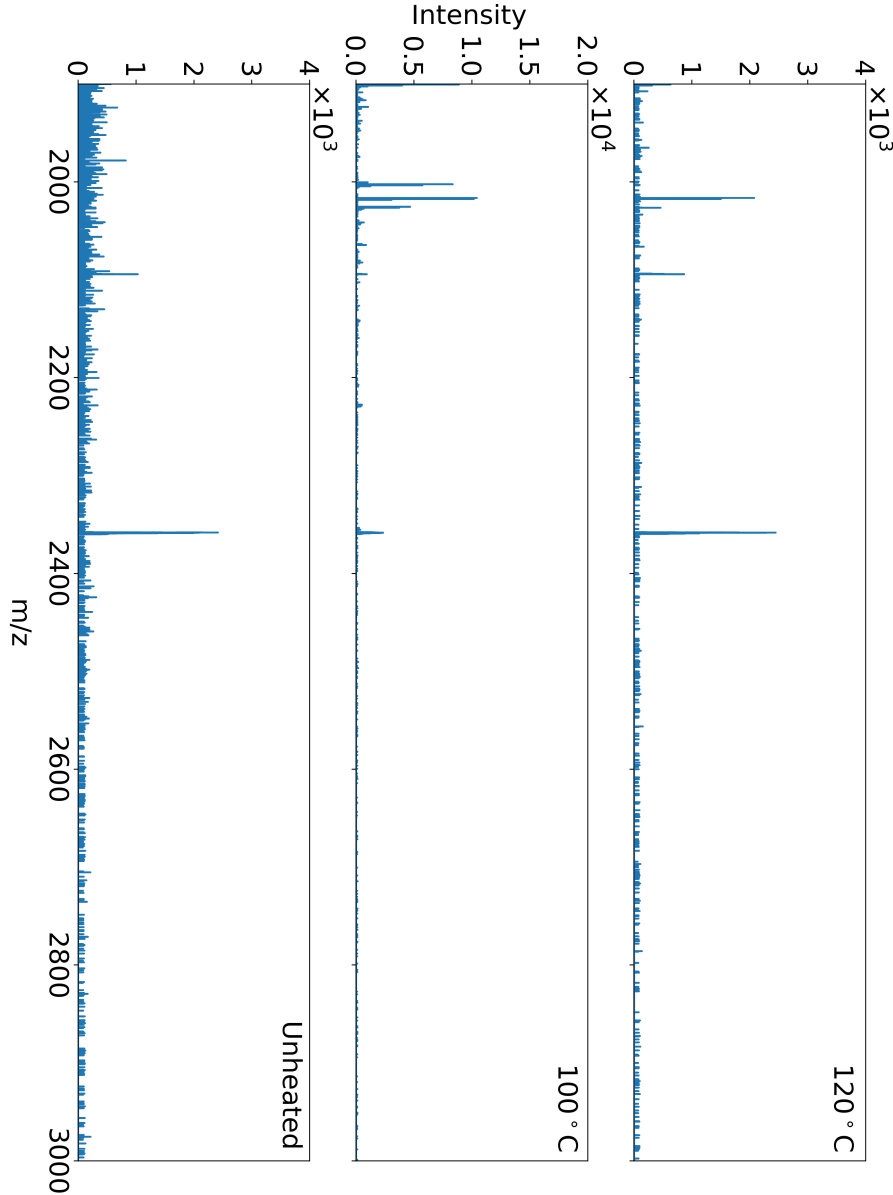


Figure 8.3 The mass spectrometry data for the range 1900 to 3000. The peak at 2094 m/z is an artefact of the instrument.

8.2 Additional Data for Chapter 6

The calibration factor for RT UHV STM images:

$$X = -0.1 + 1.0664x + 0.1558y$$

$$Y = 0.005 + 0.0215x + 0.9011y$$

The calibration factor for the LT UHV STM images:

$$X=1.168$$

$$Y= 1.284$$